# Structural and Thermoelectric Properties of Binary and Ternary Skutterudite Thin Films

## Marcus Daniel

**von der Fakultät für Naturwissenschaften der Technischen Universität Chemnitz genehmigte Dissertation zur Erlangung des akademischen Grades**

**doctor rerum naturalium**

**(Dr. rer. nat.)**

**Abstract**

Increasing interest in an efficiency enhancement of existing energy sources led to an extended research in the field of thermoelectrics. Especially skutterudites with their high power factor (electric conductivity times Seebeck coefficient squared) are suitable thermoelectric materials. However, a further improvement of their thermoelectric properties is necessary. The relatively high thermal conductivity can be decreased by introducing loosely bound guest ions, whereas atom substitution or nanostructuring (as thin films) could yield an increased power factor.

The present work proves the feasibility to deposit single phase skutterudite thin films by MBE technique. In this regard $CoSb_y$ and $FeSb_y$ film series were deposited with three different methods: i) codeposition at elevated temperatures, ii) codeposition at room temperature followed by post-annealing, and iii) modulated elemental reactant method. The structural and thermoelectric properties of these films were investigated by taking the thermal stability of the film and the substrate properties into account. Compared to the stoichiometric Sb content of skutterudites of 75 at.%, a small excess of Sb is necessary for achieving single phase skutterudite films. It was found, that the deposited single phase $CoSb_3$ films reveal bipolar conduction (and therefore a low Seebeck coefficient), whereas $FeSb_3$ films show p-type conduction and very promising power factors at room temperature.

The need of substrates with a low thermal conductivity and a suitable thermal expansion coefficient is also demonstrated. A high thermal conductivity influences the measurements of the Seebeck coefficient and the obtained values will be underestimated by thermal shortening of the film by the substrate. If the thermal expansion coefficient of film and substrate differ strongly from each other, crack formation at the film surface was observed.

Furthermore, the realization of controlled doping by substitution as well as the incorporation of guest ions was successfully shown. Hence, this work is a good starting point for designing skutterudite based thin film structures. Two successful examples for such structures are given: i) a thickness series, where a strong decrease of the resistivity was observed for films with a thickness lower than $10\,nm$, and ii) a $Fe_xCo_{1-x}Sb_3$ gradient film, for which the gradient was maintained even at an annealing temperature of $400\,°C$.

**Keywords:** skutterudites, thermoelectric, thin films, molecular beam epitaxy (MBE), Seebeck coefficient, ZT, $CoSb_3$, $FeSb_3$, gradient films, van der Pauw, thermal expansion coefficient, antimony, modulated elemental reactant method, semiconductor

# Contents

# 1 Introduction

Thermal and electric properties of a material are linked to each other. An electric current could for instance originate from a temperature gradient, while an electric field can also generate an heat flux [1]. The field of thermoelectrics describes all phenomena that are connected to the interaction of thermal and electric material properties. The first thermoelectric phenomenon was observed by Thomas Seebeck in 1821. He observed the generation of a voltage in a material by applying a temperature gradient. If a temperature gradient is present, charge carriers will move by thermal diffusion from the hot to the cold side yielding a thermovoltage [1, 2]. This effect is nowadays known as Seebeck effect and the magnitude of the generated thermovoltage is described by the material specific Seebeck coefficient $S$. The Seebeck effect could be applied to convert thermal energy in electric power, which is thought to be used in thermoelectric generators recovering waste heat. The field of thermoelectric power generation becomes more and more important, since new energy sources have to be found and existing energy sources have to be used more efficient. The waste heat recovery is also under investigation by the automotive industry in order to decrease the fuel consumption and thus to reach the $CO_2$ emission limits set for 2020 in Europe [3]. For this goal mainly three directions were investigated: i) light weight construction, ii) lower friction by new oils and fluid types and iii) thermoelectric waste heat recovery [3].

Thermoelectric generators are only well established for space probes, where the radioactive decay heat is used to produce power on missions far away from the sun [4]. For commercial application the use of thermoelectric materials was not competitive for decades, since the efficiency of these materials was very low. A good thermoelectric material has to have a large Seebeck coefficient $S$, a high electric conductivity $\sigma$, and a low thermal conductivity $\kappa$, which can be summarized in the dimensionless figure of merit: $ZT = S^2 \sigma T / \kappa$. A $ZT$ value which equals unity corresponds to an efficiency of $\sim$10 %, which was the upper limit between 1950 and 1990 for the established materials $Bi_2Te_3$, SiGe, and PbTe. To be competitive $ZT$ has to reach values between 2 and 3.

Recently, this research field was renewed by the introduction of nanostructuring approaches and new technologies, as well as the development of new material groups. The main challenges for enhancement of $ZT$ arise from the coupling of the transport coefficients $\sigma$, $S$ and $\kappa$. Nanostructured materials give the opportunity to decouple this coefficients partially and to optimize them individually [5]. Different approaches were introduced: i) increase of electric conductivity/Seebeck coefficient by quantum

confinement in one or more dimensions [6, 7, 8, 9]; ii) decrease of the phononic part of the thermal conductivity by scattering at grains or at introduced interfaces, particles, and defects, while maintaining the electronic properties [10, 11, 12]; iii) energy filtering at introduced barriers (e.g. interfaces, modulations) or by designed energy transitions using band structure modeling [13, 14]; and iv) combined approaches [15, 16, 17].

New materials like clathrates [18] and skutterudites [19, 20] were found, for which special properties of the crystal structures can be used to enlarge $ZT$. Guest ions can be incorporated into the voids of the crystal structure yielding a lower phononic thermal conductivity. This approach is called phonon glass-electronic crystal (PGEC) and was first introduced by Slack [21]. The material should behave glass-like for phonons exhibiting a low thermal conductivity and as an ordered crystal for electrons with large $S$ and $\sigma$.

In this work a systematic route from the deposition of thermoelectric skutterudite thin films towards nanostructured thin film structures will be provided. In literature several publications for skutterudite thin films can be found, but most of them describe films thicker than $150\,\mathrm{nm}$, which is in a range, where the benefits due to nanosize effects are not observed. Therefore skutterudite thin films ($CoSb_3$, $FeSb_3$, $Fe_xCo_{1-x}Sb_3$, $Yb_z(CoSb_3)_4$) in the thickness range between $2\,\mathrm{nm}$ and $150\,\mathrm{nm}$ were deposited by MBE technique and the structural and thermoelectric properties have been investigated. Even though the integration of such thin films in thermoelectric modules is a challenge, several additional applications exist for thin films, like usage in the field of microelectronics and optoelectronics, for microcoolers and thermal management of chips, for small scale or implanted sensors or for low power generators [22, 23]. In these cases bulk materials cannot be used.

The experimental results of the present work are structured as follows. In chapter 6 and 7 the peculiarities occurring during the deposition of skutterudite thin films are discussed and it is explained, how the different deposition methods influence the film structure. Many difficulties for achieving single phase skutterudite films have been reported in the literature. The presented results should give further insights to explain and overcome these problems and demonstrate ways to achieve high quality single phase films. In chapter 8 the thermoelectric properties of the deposited skutterudite films will be shown. Here the dominating transport mechanism and the influence of different compositions have been investigated.

A critical point for the properties of thin films is the choice of the substrate. The film morphology can be changed by the substrate during thermal treatments, which could alter the film properties and influence the thermal stability. Furthermore the measured thermoelectric properties are usually always a combination of the used substrate and the film. Suitable substrates are introduced in chapter 9.

Frequently, the intrinsic properties of a thermoelectric material do not exhibit its best thermoelectric properties and an additional optimization is needed. In most

cases controlled doping is used to optimize $S$ and $\sigma$, which can be done by a gradual substitution of atoms in the lattice. The successful realization of the substitution is discussed in chapter 10. The second possibility for skutterudites to improve the thermoelectric properties, is the reduction of the thermal conductivity by the incorporation of filling ions as mentioned above, which was also investigated in the present work by using Yb as filler (chapter 11).

Finally the achieved results were used to demonstrate different nanostructure thin film approaches. The benefit of a film thickness below 10 nm for the electric conductivity is shown as well as the successful deposition of skutterudite gradient films (see chapter 12).

# 2 Nanostructured thermoelectric materials

## 2.1 Thermoelectric materials and ZT

The main goal of recent thermoelectric research is the improvement of the thermoelectric efficiency of a material. The efficiency $\eta$ of a thermoelectric material exhibiting a temperature gradient $\Delta T = T_H - T_C$ at a given average temperature $T = (T_H + T_C)/2$ can be described with the following formula:

$$\eta = \eta_C \frac{\sqrt{1 + ZT} - 1}{\sqrt{1 + ZT} + \frac{T_C}{T_H}}. \tag{2.1}$$

$T_H$ and $T_C$ are the temperatures at the hot and the cold side of the material, $\eta_C$ is the Carnot efficiency and $Z$ is the figure of merit. The corresponding function is plotted for $T_C = 400\,\text{K}$ in figure 2.1 (a) in dependence of $\Delta T$. The efficiency is dependent on the size of the temperature gradient present and on the material parameter $ZT$. The upper limit is the Carnot efficiency. However, the Carnot efficiency is not the desired goal, since it does not correspond to the maximum achievable power output, which is the more important parameter for practical use [24]. The optimum efficiency for the maximum power was described by Carzon and Ahlbeck ($\eta = 1 - \sqrt{T_C/T_H}$) [24, 25]. Based on the close connection between the dimensionless figure of merit $ZT$ and the efficiency $\eta$ shown in equ. 2.1, $ZT$ is usually used to characterize the quality of a thermoelectric material at a given working temperature $T$. Many established materials achieve a $ZT$ close to unity, which corresponds to an efficiency of 5% to 15% depending on the usable gradient (see fig. 2.1 (a)). A further increase was a challenge for decades, but in the most promising materials a value up to 1.8 is confirmed [27]. As already mentioned, $ZT$ is linked to the electric conductivity $\sigma$, the Seebeck coefficient $S$ and the thermal conductivity $\kappa$ in the following way:

$$ZT = \frac{\sigma S^2}{\kappa} T = \frac{PF}{\kappa} T. \tag{2.2}$$

Here the power factor $PF = \sigma S^2$ is introduced, which is strongly connected to the achievable power output and needs to be optimized first for promising thermoelectric materials [28]. The electric conductivity $\sigma$ describes how good a material transports electric current and is related to the electric resistivity by $\rho = 1/\sigma$. In this work $\rho$ is mainly used to describe the quality of the electric conduction and respectively
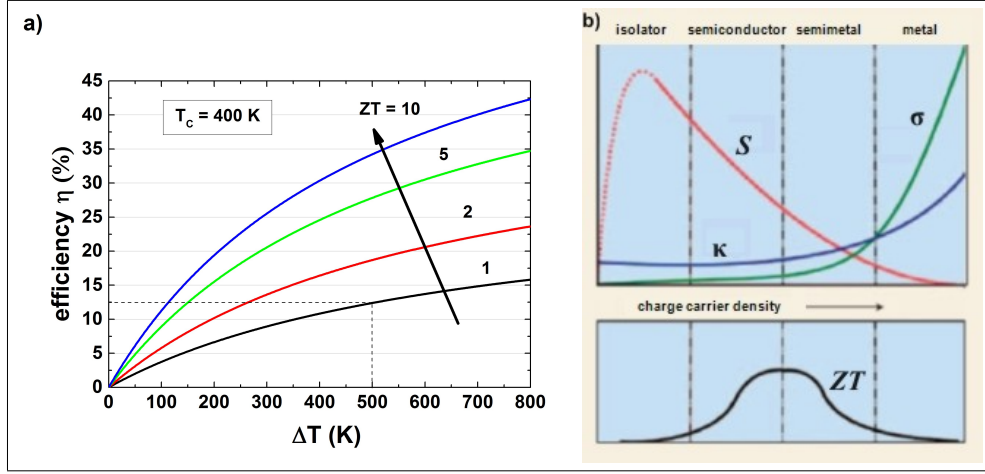
Figure 2.1: a) Efficiency $\eta$ in dependence on $ZT$ and $\Delta T$. The dashed line demonstrates the achieved efficiency of $\sim 12.5\%$ for $ZT = 1$ and $\Delta T = 500\,\mathrm{K}$. A $ZT$ of 2 - 3 is needed to reach an efficiency of 20% required for commercial applications [26] b) Dependence of the transport coefficients on the charge carrier density $n$, revealing semiconductors as possible thermoelectric material with high $ZT$ values [4].

$PF = S^2/\rho$ for the power factor. The Seebeck coefficient $S$ characterizes the actual thermoelectric properties of the material. It is a measurement for the created thermovoltage $U_{Th}$ in a material by applying a temperature gradient $\Delta T$:

$$S = \frac{U_{Th}}{\Delta T}. \tag{2.3}$$

The main driving force for the occurrence of the thermovoltage is the thermodiffusion and not, as often explained, contact potentials between different materials [2]. A more detailed description can be found in chapter 3. The thermal conductivity $\kappa$ gives the quality of the heat conductance in a material, which can be carried by lattice vibrations ($\kappa_L$) and by electrons ($\kappa_e$).

The difficulties for enhancing $ZT$ arise from the fact, that all these electronic transport coefficients are coupled to each other. The simplest coupling is described by the Wiedemann-Franz law for metals, which connects $\sigma$ and $\kappa_L$ linearly at a given temperature $T$ by the Lorentz number $L$:

$$\kappa_L = LT\sigma. \tag{2.4}$$

In contrast to metals, the Lorentz number of semiconductors is not constant (see ch. 3.1). Further coupling relation between $S$, $\sigma$ and $\kappa_e$ can not be given in such simple expressions and a more general consideration is needed as introduced in chapter 3.1. Nevertheless, it can be shown that all coefficients are related to the charge
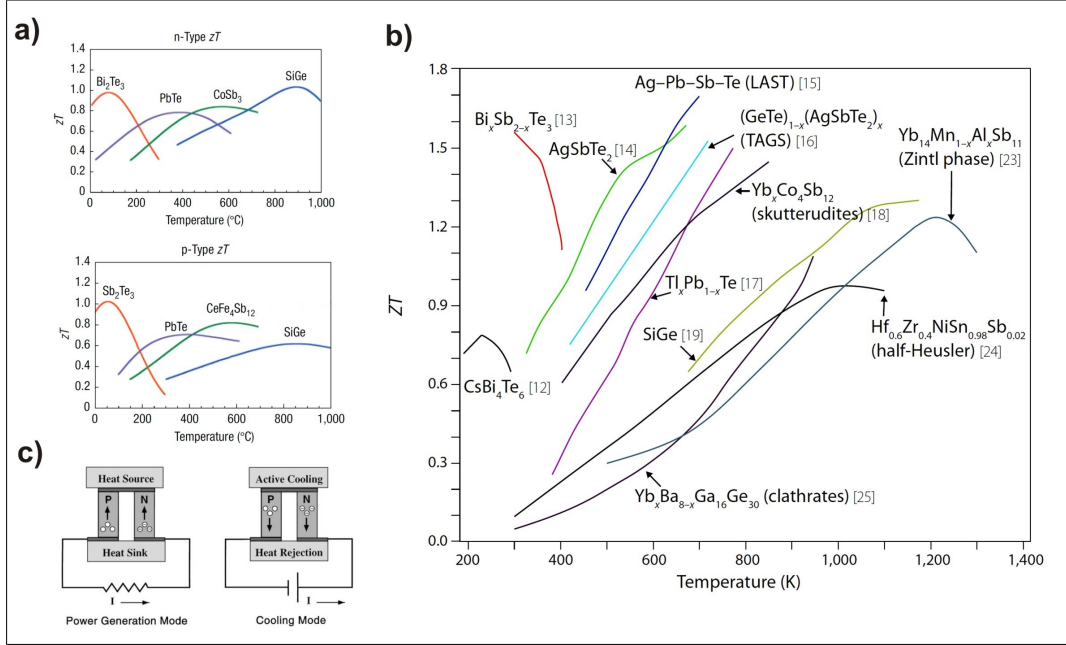
Figure 2.2: a+b) Temperature dependence of $ZT$ for established n-type and p-type thermoelectric materials. Additional the skutterudites $CoSb_3$ and $CeFe_4Sb_3$ is added [29]. b) Overview over promising novel materials actually investigated in the field of thermoelectrics [30] c) Principle of a thermoelectric module for power generation (left) and of a peltier element for heating or cooling (right). Both setups are based on a p- and a n-type material [20].

carrier density $n$. While a high carrier density yield a large electric conductivity, the Seebeck coefficient is low (or vice versa). By using this considerations suitable thermoelectric materials can be found as presented in fig. 2.1 (b). Isolators have large $S$, but negligible $\sigma$. In metals the conditions are opposite. Semimetals provide two species of charge carrier, competing for the Seebeck effect. Therefore semiconductors are preferred, which are usually strongly degenerated with a charge carrier density in the range of $10^{19}\,\mathrm{cm}^{-3}$ to $10^{20}\,\mathrm{cm}^{-3}$.

For given thermoelectric materials, it is necessary to control $n$ accurately for achieving optimized power factors. This can be simply realized for semiconductors by doping and offers also the possibility to produce p-type and n-type materials, which are needed for the fabrication of thermoelectric modules. Modules usually consist of p-type and n-type legs, connected to a serial circuit as shown in fig. 2.2 (c). To provide thermal stability both legs should have the same mechanical properties (for instance thermal expansion coefficient), which can be easily fulfilled, if the basic material is the same and only the doping species differs.

In fig. 2.2 (a) and (b) an overview of typical thermoelectric materials and novel alloys is given for both, p-type and n-type materials. The established material in the room temperature range is $Bi_2Te_3$, while for elevated temperatures PbTe and for high temperatures SiGe are used. All these materials do not exhibit $ZT$ values noteworthy above 1, even though they have been optimized for many years. A large increase is therefore not expected in future and new routes have to be found to decouple the individual transport coefficients. This goal can be reached either by nanostructuring (see chapter 2.2) or by novel material groups, which are also added in fig. 2.2 (b). Slack [21] has provided a guideline for finding suitable new materials. Complex unit cells in combination with large atomic masses and low electronegativity differences of the individual atoms, as well as large carrier mobilities are needed for high $ZT$ values [20, 21]. This results finally in the framework of "Phonon Glass-Electron Crystal" (PGEC) materials [21]. The electric properties of these materials should behave metal-like, while the thermal properties should show characteristics of a glass. This approach is nicely represented for instance in filled skutterudites and clathrates. Other promising material groups are for examples LAST (lead-antimony-silver-tellurium) and Zintl compounds or chalcogenides [18, 29, 30, 31].

## 2.2 Recent developments in improving ZT in thin films

The difficulties by increasing the thermoelectric figure of merit $ZT$ arise from the coupling of the transport coefficients $\sigma$, $S$, and $\kappa$. Nanostructuring is believed to be a promising way to decouple the individual coefficients. The following nanostructure approaches are used to enhance $ZT$ and will be explained in detail below:

- Decrease of phononic thermal conductivity $\kappa_L$ by the "PGEC" principle

- Increase of $\sigma$ by quantum confinement

- Increase of $S$ or $\sigma$ by energy filtering

- carrier pocket engineering, semimetal-semiconductor transition, modulation doping, and others

In this work thin films are investigated with a thickness in the nanometer range, which is equivalent to a 2D structure with confinement in one dimension. Therefore examples of the approaches listed above will be given mainly for thin films. In other nanostructures like nanowires, quantum dots, nanoinclusion or composites these approaches can be also adopted.

In 1995, Slack introduced his principle of PGEC [21]. One way to achieve such a system is to lower the phononic part of the thermal conductivity $\kappa_L$ of a proper thermoelectric material further, while maintaining the electronic properties. This can be
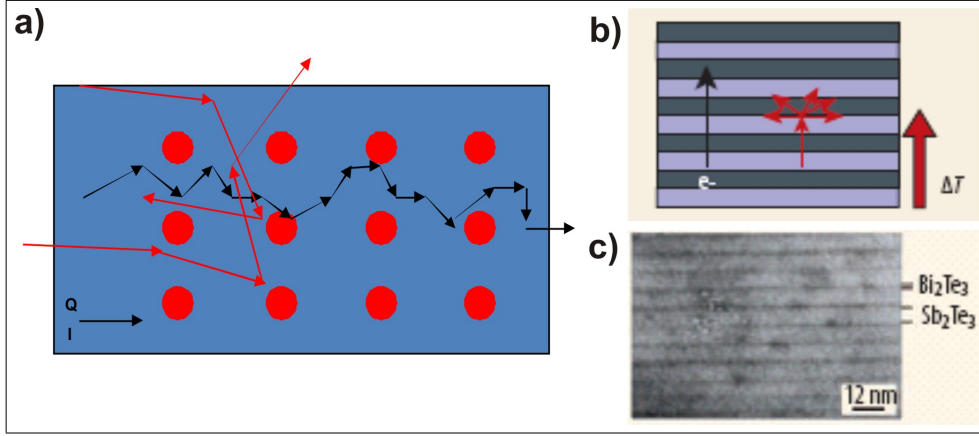
Figure 2.3: Realizations of the "Phonon Glass-Electron Crystal" principle. a) The distance between scattering centers is in the range of the phonon mean free path (red arrows) and larger than the one of electrons (black arrows). Phonons get scattered, while the electrons can pass. b) Schematical realization as cross-plane multilayer structure [4] c) TEM image of a $Bi_2Te_3$/$Sb_2Te_3$ cross-plane multilayer based on this approach [10].

realized by introducing additional scattering centers with size or spacings in the range of the mean free paths of phonons, but larger than the mean free paths of electrons. In that case phonons will get scattered and electrons could pass. The principle is sketched in fig. 2.3 (a). For grain sizes in the nanometer range, the grain boundaries could act as such scattering centers. Another possibility are thin films arranged in a multilayer structure for conduction in cross-plane direction. By choosing a proper thickness of the individual layers, the phonons get scattered at the interfaces, while the electrons are not affected (see fig. 2.3 (b) and (c)). A famous example is the $Bi_2Te_3$/$Sb_2Te_3$ multilayer structure of Venkatasubramanian et al. [10], for which a $ZT$ of 2.4 was reported.

By decreasing the dimension of thermoelectric structures, quantum confinement occurs, which could yield a higher electric conductivity. This was predicted by M. Dresselhaus and L. D. Hicks for the in-plane conductivity of thin films and along nanowires [6, 7] and some results of their work are shown in fig. 2.4 (a). For multilayer structures not only scattering at the interfaces could be utilized to enhance $ZT$, but also changing the arrangement from cross-plan to in-plane geometry and using quantum confinement effects to increase $ZT$ by an enlarged electric conductivity (fig. 2.4 (b). Two effects contribute to the higher conductivity [4, 5]. The energy level will shift for low dimensional samples to higher energies in comparison to bulk samples. The strength is depending on the effective mass of the charge carriers and for thin films on the film thickness. The lower both parameter are, the higher shift

9
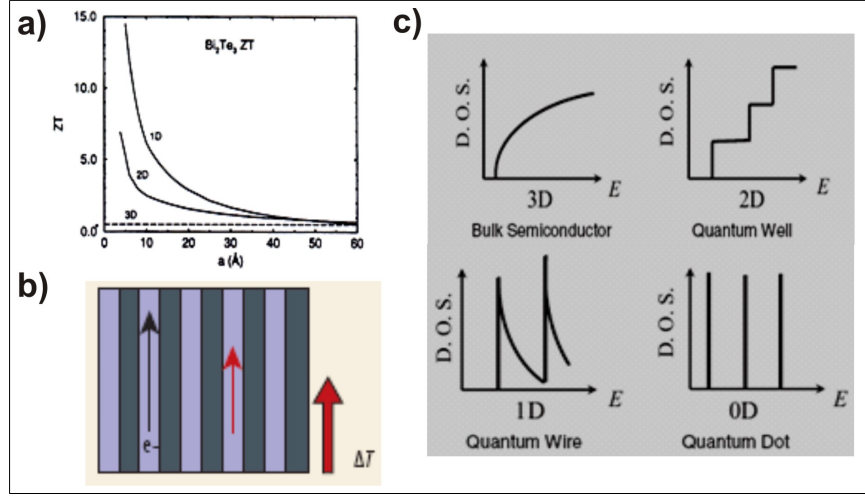
Figure 2.4: a) Theoretical calculation of $ZT$ for low dimensional $Bi_2Te_3$ systems by Dresselhaus et al. [32]. b) Illustration of a multilayer structure with in-plane conduction as a possible realization of a system with quantum confinement [4]. c) Energy dependence of the density of states for low dimensional systems [5].

the energy levels [4]. Additionally, the density of states is changed for low dimensional systems from a root function for 3D systems to discrete states for 0D quantum dots (see fig. 2.4 (c)). If these discrete energy states are close to the Fermi energy an increased charge carrier density and therefore a higher $\sigma$ follows [4, 5].

A third possibility to take benefit of nanostructured materials is energy filtering for an enhancement of $\sigma$ or $S$. The principle is visualized in fig. 2.5. The challenge for this approach is to create special barriers, where low energy charge carrier are scattered and only high energy charge carrier can pass [5]. By filtering the low energy charge carriers mainly the Seebeck coefficient $S$ is affected. Anno et al. [33] demonstrated for instance huge Seebeck coefficient above $600\,\mu V/K$ due to energy filtering at the grain boundaries in skutterudite thin films. Barriers can be also created by special super lattices [14], resonant tunneling through quantum dots, geometric modulations or heterostructure nanowires [34].
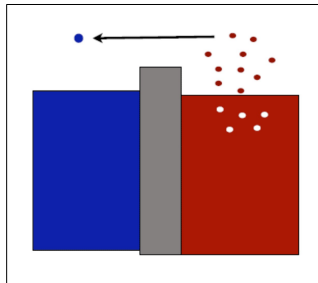


Figure 2.5: The principle of energy filtering is demonstrated. By introducing a barrier or interface, that only high energy charge carriers can pass, the Seebeck coefficient is increased [13].

# 3 Thermoelectric transport theory

## 3.1 Electronic transport coefficients

The connection between the band structure of a material (which is based on its structural properties) and the electronic transport coefficients is usually derived by the Boltzmann transport theory. The following derivations for the electric current and for the electronic heat current are based on this theory and can be found in more detail in "Prinzipien der Festkörpertheorie" of J. M. Ziman [1]. The equilibrium Fermi distribution, which describes the concentration of charge carriers in the state $k$, can be distorted by external fields, changes in the chemical potential or local temperature gradients. Scattering causes the relaxation back to the equilibrium state. The scattering processes are usually described by the constant relaxation time approach, which reveals an exponential relaxation. The relaxation time $\tau$ is introduced, which can be interpreted as time between two scattering events and defines the strength of the corresponding scattering processes. Following this consideration the electric current density $j$ and the heat flow density $q$ of a material can be derived in the cgs unit system as [1]:

$$\boldsymbol{j} = e^2 \boldsymbol{K}_0 \cdot \boldsymbol{E} + \frac{e}{T} \boldsymbol{K}_1 \cdot (-\nabla T) \; , \tag{3.1}$$

$$\boldsymbol{q} = e^2 \boldsymbol{K}_1 \cdot \boldsymbol{E} + \frac{1}{T} \boldsymbol{K}_2 \cdot (-\nabla T) \; . \tag{3.2}$$

Here $e$ is the electron charge, $E$ the electric field, and $\nabla T$ the temperature gradient. The different coefficients $K_n$ are tensors depending on the band structure at the Fermi energy [1]:

$$\boldsymbol{K}_n = \frac{1}{4\pi^3} \frac{\tau}{\hbar} \int \int \boldsymbol{v_k} \boldsymbol{v_k} (\varepsilon - \zeta)^n \left( -\frac{\partial f^0}{\partial \varepsilon} \right) \frac{\mathrm{dS}}{v_{\boldsymbol{k}}} \mathrm{d}\varepsilon \; . \tag{3.3}$$

$\boldsymbol{v_k}$ is the drift velocity of a charge carrier in state $k$, $\varepsilon$ is the energy, $\zeta$ the reduced Fermi energy and $f^0$ the equilibrium distribution function. It can be seen by analyzing equations 3.1 and 3.2, that the electric and thermal material properties are interconnected. Equation 3.1 implies, that an electric current can be caused by a temperature gradient, while from equation 3.2 follows, that a thermal flux can also be generated by an electric field. This interconnection is the origin of thermoelectric effects.

## Conductivity

Using equation 3.1 in absence of a thermal gradient together with the general expression $j = \sigma E$, it follows:

$$\boldsymbol{\sigma} = e^2 \boldsymbol{K}_0 \ . \tag{3.4}$$

For isotropic materials this equation can be simplified to an integral over the Fermi surface [1]:

$$\boldsymbol{\sigma} = \frac{1}{12\pi^3} \frac{e^2 \tau}{\hbar} \int \boldsymbol{v_k} dS_{Fermi} \ . \tag{3.5}$$

This equations implies, that only the charge carriers at the Fermi surface are responsible for the conductivity. Low energetic electrons cannot be accelerated due to the Pauli principle [1]. Furthermore the assumption of a free electron gas with uniform effective mass $m^*$ can be made for metals. The Fermi velocity is therefore given by $\boldsymbol{v_{k,Fermi}} = \frac{\hbar k_{Fermi}}{m^*}$, the Fermi surface by $S_{Fermi} = 4\pi k_{Fermi}^2$ and the corresponding Fermi vector by $k_{Fermi}^2 = 3\pi^2 n$. Using this equation in 3.5 yields:

$$\boldsymbol{\sigma} = \frac{ne^2\tau}{m^*} = ne\mu \ , \tag{3.6}$$

where $n$ is the charge carrier density and and gives the number of charge carriers contributing to the conduction process in a material. $\mu$ is the charge carrier mobility and characterizes, how good the carriers can move through the material. Furthermore, it can be shown in general, that equation 3.6 is also valid for non-degenerated semiconductors with a dominant species of charge carriers [1]. In case of different species, the equations have to be modified by considering the density and the effective mass of each species. From equation 3.6 follows the general expression for the mobility:

$$\mu = \frac{e\tau}{m^*} \ . \tag{3.7}$$

The mobility depends therefore on the effective mass $m^*$ of the charge carriers and on the relaxation time $\tau$. While $m^*$ is connected to the band structure, $\tau$ is defined by the occurring scattering processes.
From equation 3.6 follows, that $\sigma$ is only depending on the charge carrier density and on the mobility, but not explicitly on temperature. However both, the charge carrier density and the mobility exhibit strong temperature dependences discussed in the following. Metals, highly doped or degenerated semiconductors reveal only a weak temperature dependence of the charge carrier density, while for non-degenerated semiconductors in the intrinsic range, the charge carrier density varies for instance exponentially as [35]

$$n = n_0 \cdot e^{\frac{-E_g}{2k_B T}} = 2 \left( \frac{k_B T}{2\pi\hbar} \right)^{3/2} (m_n^* m_p^*)^{3/4} e^{\frac{-E_g}{2k_B T}} \ , \tag{3.8}$$

where $E_g$ is the size of the band gap, $k_B$ the Boltzmann constant, $m_n^*$ and $m_p^*$ the effective electron/hole mass and $h$ the Planck constant. For low temperatures the charge carrier density and the conductivity approaches zero. Is the thermal energy $k_B T$ large enough to overcome the band gap, charge carriers can be excited from the valence band into the conduction band yielding an exponential increase of $n$ and $\sigma$. A more general relation can be derived from equation 3.3, 3.4, and 3.6 by using the Fermi integral $F_{1/2}(\zeta)$ [36]:

$$n = \frac{4\pi(2m^*k_BT)^{3/2}}{h^3}F_{1/2}(\zeta) \ . \tag{3.9}$$

The temperature dependence of $\mu$ is dominated by the relaxation time, which depends on the occurring scattering mechanism of the charge carriers, like neutral and ionic impurity scattering, point defect scattering, electron-phonon scattering or grain boundary scattering. The individual processes reveal different temperature dependences. Furthermore, the dominant scattering process changes for different temperature regimes and its temperature dependence therefore dictates the characteristic behaviour of $\mu$ in this regime. If more than one mechanism is present, the overall relaxation time is described as [37]:

$$\frac{1}{\tau} = \frac{1}{\tau^{(1)}} + \frac{1}{\tau^{(2)}} + ... \tag{3.10}$$

The identification of the occurring scattering mechanism gives feedback for the present microstructure and important information for adjusting the material properties. Temperature dependent measurements of conductivity, charge carrier concentration and mobility are therefore necessary to extract band structure properties (for instance band gap, density of states, Fermi energy) and microstructural properties like scattering mechanism (examples in [38, 39, 40]). In table 3.1 the typical observed behaviour of $\sigma(T)$, $\mu(T)$ and $n(T)$ is summarized for the different temperature regimes.

**Seebeck coefficient**

The following expression can be derived by using equation 3.1 and 3.2 for an open circuit, where no current flows ($j = 0$) [1]:

$$\boldsymbol{E} = \frac{1}{eT}(\boldsymbol{K_0}^{-1}\boldsymbol{K_1}) \cdot \nabla T = \boldsymbol{S} \cdot \nabla T \ . \tag{3.11}$$

The temperature gradient yields an electric field, whose magnitude is defined by the Seebeck coefficient $S$. The generated voltage can be calculated by integration of the electric field over the entire conductor and equation 2.3 is derived. The process of generating a thermovoltage by a temperature gradient is called Seebeck effect. If two materials A and B are in contact forming a ring structure as shown in fig. 3.1 and
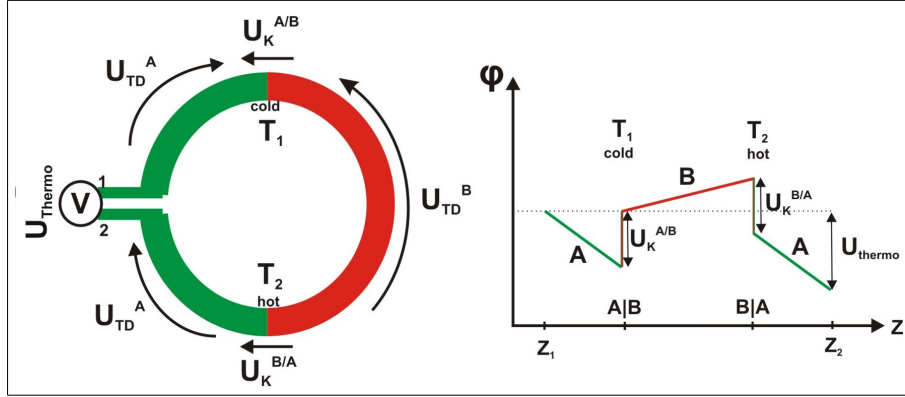
Figure 3.1: a) Ring structure of two materials A and B, where the contacting points exhibit different temperatures [2]. b) Integrating the potential along the ring structure. Contact potentials $U_K^i$ have no influence on the resulting thermopower. Only the difference of the thermodiffusion processes $U_{TD}^i$ in both materials contribute to the occurring thermovoltage [2].

both contacts exhibit different temperatures, the measured thermal voltage is given by [2]

$$U_{Thermo} = \int (S_A - S_B)dT \ . \tag{3.12}$$

The contact potentials exhibit only a weak temperature dependence and have no influence to the occurring thermovoltage as demonstrated in fig. 3.1. In many studies the formula 3.11 is rewritten by using the Fermi integral $F_r(\zeta)$ with the scattering parameter $r$ [36]:

$$S = -\frac{k_B}{e} \left( \frac{(2+r)F_{1+r}(\zeta)}{(1+r)F_r(\zeta)} - \zeta \right) \ . \tag{3.13}$$

This equation can be used to extract the reduced Fermi level $\zeta$ from the measurements. The scattering parameter depends on the occurring scattering mechanism and can be found in table 3.1 for some cases. If the charge carrier density is known the effective mass $m^*$ can be determined by using $\zeta$ in equation 3.9 [36].

The link of $S$ to $\sigma$ was determined for semiconductors and partially degenerated semiconductors by Ioffe as [41]:

$$
\begin{aligned}
S &= \frac{k_B}{e} \left[ A + \ln \left\{ \frac{2(2\pi m^* k_B T)^{3/2} e\mu}{h^3} \right\} \right] - \frac{k_B}{e} \ln ne\mu \\
&= \frac{k_B}{e} \left[ A + \ln \left\{ \frac{2(2\pi m^* k_B T)^{3/2} e\mu}{h^3} \right\} \right] - \frac{k_B}{e} \ln \sigma \ .
\end{aligned}
\tag{3.14}
$$

This equation predicts a low Seebeck coefficient for metals due to the large conductivity in the second term compensating the first one. For semiconducting materials and small temperatures the absolute value of the Seebeck coefficient increases with $T$ and the first term dominates, which describes the average energy per carrier [1]. In case of intrinsic conduction the second term compensates the first term by the increasing conductivity, which results in a decrease of $S$ and thus in the characteristic maximum of $S$ found for intrinsic semiconductors at larger temperatures.

**Electronic contribution of the thermal conductivity**

If no electric field is present, equation 3.2 reveals the electronic thermal conductivity $\kappa_e$ as:

$$\boldsymbol{q} = \frac{1}{T}\boldsymbol{K}_2 \cdot (-\nabla T) = \boldsymbol{\kappa}_e \cdot (-\nabla T) \ . \tag{3.15}$$

Nevertheless, this expression is a simplification and agrees only with measured data in case of metals. In practical measurements, a contribution of parasitic electric fields has always to be taken into account. Therefore only an open circuit with $j = 0$ can be realized and the equations 3.1 and 3.2 reveal [1]:

$$\boldsymbol{q} = \frac{1}{T}(\boldsymbol{K}_2 - \boldsymbol{K}_1 \boldsymbol{K}_0{}^{-1} \boldsymbol{K}_1) \cdot (-\nabla T) \ . \tag{3.16}$$

The coupling between $\sigma$ and $\kappa_e$ for metals (Wiedemann-Franz law, equation 2.4) can be determined performing some additional steps [1]:

$$\boldsymbol{\kappa}_{e,metal} = \frac{1}{T}\boldsymbol{K}_2 = \frac{\pi^2 k_B^2}{3e^2}T\boldsymbol{\sigma} = LT\boldsymbol{\sigma} \ . \tag{3.17}$$

It has to be considered, that L is only constant for metals. In case of semiconductors corrections have to be applied [40]. A possibility to calculate the real Lorentz number is given by the following expression [40, 42]:

$$L = \frac{k_B^2(1+r)(3+r)F_r(\zeta)F2 + r(\zeta) - (2+r)^2 F_{1+r}(\zeta)^2}{e^2(1+r)^2 F_r(\zeta)^2} \ . \tag{3.18}$$

If the conductivity and the overall thermal conductivity is measured, one of the given equations can be used to determine $\kappa_L$ and $\kappa_e$.

Table 3.1

| Transport parameter | Origin | Temperature dependence | Typical plot (for linearization) | Requirements/ remarks | References |
|---|---|---|---|---|---|
| **low temperature** | | | | | |
| $\rho(T)$ | variable range hopping (VRH) | $\sim e^{-(T_0/T)^{1/4}}$ | $\ln \rho$ over $(1/T^{\frac{1}{4}})$ | $n(T)$ decreases, $\mu(T)$ increases | [43, 44, 45] |
| | extended VRH | $\sim e^{-(T_0/T)^{1/2}}$ | $\ln \rho$ over $(1/T^{\frac{1}{2}})$ | $n(T)$ decreases, $\mu(T)$ increases | [43] |
| | phonon scattering of electrons | $\sim T^5$ | $\ln \rho$ over $\ln T$ | Bloch Grüneisen, simple met. | [46, 42] |
| $\mu(T)$ | neutral impurities $(r=\frac{1}{2})$ | $=$ constant/$\sim (m^*)^2$ | $\mu(T)$ | - | [37, 42] |
| | ionized impurities $(r=2)$ | $\sim T^{3/2}(m^*)^{1/2}$ | $\ln \mu$ over $\ln T$ | non-deg sc | [46, 42] |
| | dislocations/point defects | $\sim T^{-1/2}$ | $\ln \mu$ over $\ln T$ | only observable if all other suppressed | [42] |
| | electron-electron | $\sim T^{-2}$ | $\ln \mu$ over $\ln T$ | - | [37] |
| | grain boundaries | $\sim L T^{-1/2} e^{-E_b/k_B T}$ | $\ln (\mu T^{1/2})$ over $1/T$ | - | [22] |
| | grain boundaries with variable barrier height | gauss function for barrier height | - | curved $\ln \rho$ over $1/T$ | [47] |
| $\kappa(T)$ | specific heat, Debye theory | $\sim T^3$ | $\ln \kappa$ over $\ln T$ | sc (moderate doping), T<$\Theta_D$/2, $\kappa = \kappa_l$ | [48] |
| | specific heat, free el. gas | $\sim T^1$ | $\ln \kappa$ over $\ln T$ | met.;deg: sc(pb band); T<$\Theta_D$/2, $\kappa = \kappa_e$, boundary scatt. | [48] |
| **high temperature (T>$\Theta_D$)** | | | | | |
| $\rho(T)$ | ionized impurities | constant | $\mu(T)$ | met | [1] |
| | phonon scattering | $\sim T^{-5}$ | $\ln \mu$ over $\ln T$ | met., T<$\Theta_D$ | [1] |
| | intrinsic bandgap | $= \rho_0 \cdot e^{E_g/2k_B T}$ | $\ln \rho$ over $(1/T)$ | phonon scatt., single band, pb | [22] |
| | phonon scattering of electrons | $\sim T$ | $\rho(T)$ | Bloch Grüneisen, simple met. | [35] |
| $R_H(T)$ | intrinsic bandgap | $\sim T^{-3/2} e^{E_g/2k_B T}$ | $\ln (|R_H|T^{3/2})$ over $(1/T)$ | semiconductor | [1, 42] |
| $\mu(T)$ | acoustic phonon scattering $r=0$ | $\sim T^{-\frac{3}{2}}(m^*)^{-\frac{5}{2}}$ | $\ln \mu$ over $\ln T$ | metal | [49] |
| | phonon scattering | $\sim T^{-1}$ | $\mu(T)$ | - | [48] |
| $\kappa(T)$ | point defect | $\sim T^{1/2}$ | $\ln \kappa$ over $\ln T$ | - | [48] |
| | Umklapp scattering | $\sim T^{-1}$ | $\ln \kappa$ over $\ln T$ | sc (moderate doping),T>$\Theta_D$, $\kappa = \kappa_l$ | [48] |
| | electron-phonon scattering | $=$ constant | $\kappa(T)$ | met.;deg: sc(pb band); T>$\Theta_D$/2 $\kappa = \kappa_e$, boundary scatt. | [48] |
| **general** | | | | | |
| $\rho(T)$ | extrinsic excitation | $\sim T^{3/4} \cdot e^{\frac{E_d}{2k_B T}}$ | $\ln (\rho T^{-\frac{3}{4}})$ over $(1/T)$ | sc, phonon scatt., single band, pb | [35] |
| $R_H(T)$ | extrinsic excitation | $\sim T^{-3/4} e^{E_d/2k_B T}$ | $\ln (|R_H|T^{\frac{3}{4}})$ over $(1/T)$ | sc, no intrinsic excitation | [35] |

Table 3.1: Temperature dependences of the transport coefficients for typical cases. Metal like behaviour is colored gray. met:metal; sc:semiconductor; bg:bandgap; pb:parabolic; deg:degenerated; $\Theta_D$:Debye temperature; $m^*$:effective mass; $E_g$:gap energy; $E_d$:transition energy corresponding to doping state; $k_B$:Boltzmann constant; $L$:grain size.

## 3.2 Lattice thermal conductivity

The lattice thermal conductivity $\kappa_L$ is based on lattice vibrations, which can be described as quasi-particle called phonon. Phonons are divided into optical and acoustic phonons. Acoustic modes correspond to a low frequency oscillation with atoms oscillating in phase, while optical modes exhibit higher frequencies and the atoms oscillate in phase opposition. The theoretical derivation of $\kappa_L$ can be performed in a similar way, as for the electronic parameters. First the phonon dispersion $\omega(q)$ for a given crystal structure has to be determined. $\omega$ is the oscillation frequency and $q$ the wave vector. The phonon dispersion is the link of the thermal transport to the actual material, analogous to the bandstructure for electronic transport. For a lattice with $N$ atoms, 3 acoustical modes and $3N$-1 optical ones exist. The dispersion of acoustic modes exhibits a larger slope and is nearly linear for low $q$ values. It converges to zero for q approaching zero. The optical modes are flat, correspond to higher $\omega$ (and therefore higher energy) and become nonzero for all wave vectors. The differences can be seen for example in fig. 3.2.

If the phonon dispersion relation is known, the thermal conductivity is derived analogous to the Boltzmann theory [46]. However, phonons are bosons and no particle conservation can be assumed. Therefore the average number of phonons is analyzed instead of the distribution function [46]. For an isotropic system the following expression is found [48]:

$$\kappa_L = \frac{1}{3}Cv(\boldsymbol{q})\Lambda(\boldsymbol{q}) \ . \tag{3.19}$$

C is the specific heat of the materials. $v(\boldsymbol{q}) = \frac{\partial \omega}{\partial q}$ is the phonon group velocity and corresponds to the slope of the phonon dispersion and therefore on the crystal properties. This implies, that the main contribution to the thermal conductivity arises from the acoustic modes with low wave vectors and long wavelength. Optical modes and phonons at the zone boundaries have only a small contribution. To decrease the thermal conductivity, scattering mechanism for long wavelength phonon have to be introduced. The influence of the scattering processes on the thermal conductivity is described by $\Lambda(\boldsymbol{q})$, the phonon mean free path. Different scattering mechanisms are known (for instance at impurities and defects, point defects, electron-phonon and Umklapp scattering) [48]. As already explained for electrons, each scattering mechanism shows different temperature behaviour and becomes dominant in specific temperature regime. Some of these processes are also included in table 3.1.

The temperature dependence of the specific heat dominates usually at low temperatures, while at higher temperatures mainly scattering processes are found, such as electron-phonon scattering for metals and Umklapp scattering for semiconductors [48].
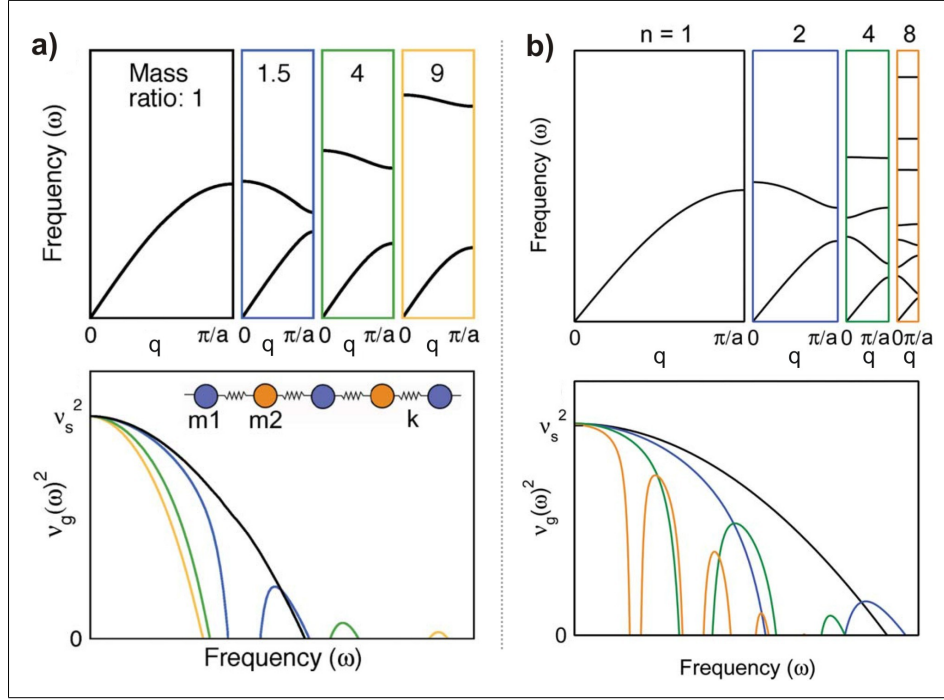
Figure 3.2: The influence of the unit cell properties on the phonon dispersion [50]. a) Large mass differences yield a strong separation of the modes and flat acoustic modes. This can be seen in the suppressed high frequency range of $v_g^2$ in the bottom graph. $\kappa_L$ is linearly dependent on $v_g^2$. b) A large number of atoms results also in a flattening of the modes especially in the acoustic branch.

For achieving materials with low lattice thermal conductivity, materials with heavy constituents, complex structures with many atoms and a large amount of scattering centers have to be synthesized [21]. While the latter one decreases the phonon mean free path, the former requirements decrease the phonon group velocity. Heavy elements flatten the phonon dispersion, compress the acoustic modes to lower frequency and shift the optical modes to higher energies as can be seen in fig. 3.2 (a) [50]. A large number of atoms also yield flat acoustic modes and a smaller acoustic contribution in the high frequency range (fig. 3.2 (b)) [50]. Both conditions are fulfilled for skutterudites, which is the material investigated in this work. The basic properties of this material group are introduced in the next chapter.

# 4 Skutterudites as promising thermoelectric material

Skutterudites are promising candidates as future material for thermoelectric applications in the medium temperature range around $800\,K$. The material group got its name from the town Skutterut in Norway, where the first representative $CoAs_3$ was found. Skutterudites are in the focus of current research, since they provide $ZT$ values larger than unity over a broad temperature range around $800\,K$, which is suitable for the automotive industry [51]. Additionally the efficiency to cost ratio is one of the best known at the moment [51, 52]. In space application this material is thought for usage in segmented modules [53]. Skutterudites provide in general a high power factor, but its phononic thermal conductivity is relatively large. Therefore many approaches aim for lowering this parameter. Rogl et al. achieved this goal for example by high pressure torsion and a $ZT$ close to 2 is reported, which is to the best of my knowledge the highest confirmed value so far [27]. In this work the representatives $CoSb_3$ and $FeSb_3$ were investigated and both materials will be introduced in the next sections. However, $FeSb_3$ is a metastable compound and only a low number of publication for $FeSb_3$ thin films are existing. Therefore the chapter gives mainly an overview of the current state of research for $CoSb_3$ bulk materials and $CoSb_3$ thin films.

## 4.1 CoSb$_3$

### 4.1.1 Structural properties of skutterudites

Binary skutterudites can be described by the chemical formula $TX_3$. T is a transition metal of the $9^{th}$ subgroup of the periodic table and X a pnictogen of the $5^{th}$ main group [4]. Reported combination are for instance $CoP_3$, $CoAs_3$, $CoSb_3$, $RhP_3$, $RhAs_3$, $RhSb_3$, $IrP_3$, $IrAs_3$ and $IrSb_3$ [54, 19]. The most famous representative in the field of thermoelectrics is $CoSb_3$ and its modifications. The following discussion is therefore mainly focused on this alloy, however the basic principles can be overtaken to all other skutterudite alloys.

$CoSb_3$ exhibits a body centered cubic lattice with the Im-3 space group. The investigated lattice constant for bulk single crystals is $(9.0345 \pm 0.0003)\,\text{Å}$ [55]. In most cases the structure is visualized by a cubic unit cell with eight $CoSb_6$ octahedron (gray shaded in fig. 4.1 (a)) [4]. The Co atoms (red) are situated in the center of such an octahedron.
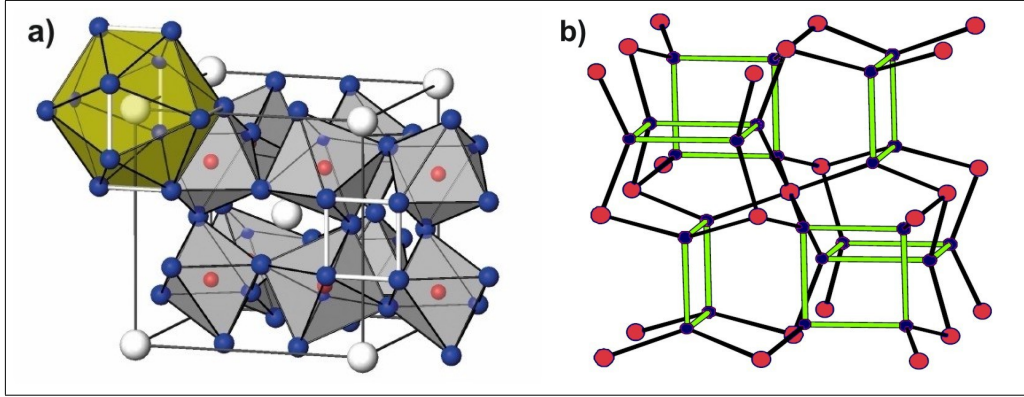
Figure 4.1: Crystalline structure of skutterudites ($CoSb_3$). Co atoms are red, Sb are blue and guest ions white. a) Possible illustration to emphasize the basic structural features: Sb octahedrons with Co in the center, large voids filled with guest ions, small voids with $Sb_4$-rectangles [19]. The large voids exhibit a diameter of $1.892\,\text{Å}$ for $CoSb_3$. b) Possible illustration to emphasize the Sb-Sb and the Co-Sb bonds [56].

Additionally two types of voids are formed in this structure. In the smaller voids planar rectangle shaped $Sb_4$ groups are formed, while the large voids (yellow shaded) could be filled with guest ions. For binary skutterudites the larger voids stay empty. The host lattice formed by Co and Sb exhibits only covalent bonds [4]. In fig. 4.1 (b) another scheme of the structure is shown, where the formed bonds can be seen more clearly [56]. Each Co atom is bonded to 6 Sb atoms, while each Sb atom exhibits two bonds to the neighboured Sb atoms in the rectangles and two to Co atoms. The mechanism behind the bonds are explained by Nolas et al. [20] as follows. Each Sb atom exhibits 5 electrons for bonds (three 5p- and two 5s-electrons). Two of them form the $\sigma$ bonds in the $Sb_4$ rectangle. The remaining 3 electrons provide the bonds to the two Co atoms, which results in a contribution of nine Sb electrons to the bond between the 6 Sb atoms to a single Co atom. Co contributes with nine electrons itself to this bonds (two 4s- and seven 4d-electrons). Due to the ligand field of the Sb octahedron, the Co d-level is separated into three low energy non-bonding states and two orbitals with higher energy, which hybridize with the s- and p-states of Sb. 6 of the 18 electrons fill the antibonding states and 12 the hybridized state providing mainly the $CoSb_6$ bonds. How the individual bonds correspond to the band structure is discussed in the next section. The crystal structure has three degrees of freedom, the lattice parameter $a_{latt}$ and two positional parameter $u$ and $v$, describing the exact position of the Sb atoms in the rectangles. This Co-Sb host lattice is the base for the promising thermoelectric properties. The physical properties for this alloy are summarized in table 4.1.

| Property | Value | Reference |
|---|---|---|
| Lattice constant | 9.0345 Å/9.0357 Å | [38]/[55] |
| $u$ (parameter for Sb position) | 0.3348 | [38] |
| $v$ (parameter for Sb position) | 0.1570 | [38] |
| Mass density | (7.582/7.69) g/cm$^3$ | [55]/[57] |
| Crystallization temperature | 153 °C/153 °C | [22]/[58] |
| Decomposition temperature | 1146 K | [55] |
| Thermal expansion coefficient | $(6,36/9.6/9.1) \cdot 10^{-6}$ K | [55]/[58]/[59] |
| Bulk modulus | 102 GPa, 90 GPa | [60],[61] |
| Shear sound velocity | 4590 m/s | [55] |
| Transversal sound velocity | 2643 m/s | [55] |
| Debye temperature | 307 K/321 K | [55],[62] |
| Grüneisen constant | 0.952 | [55] |
| Conduction type (intrinsic) | p-type | [55] |
| Magnetic type | diamagnetic | [20, 38, 39] |
| Calculated band gap size | 0.05 $e$V-0.2 $e$V | [60, 63] |
| Experimental band gap size | widely spread: 0.05 $e$V-1 $e$V | [33, 38, 39, 55, 64] |

Table 4.1: Physical properties of CoSb$_3$ bulk samples found in literature.

Furthermore, the host structure of skutterudites provides several opportunities for modifications, which are necessary for enhancing the thermoelectric properties. The charge carrier density $n$ is for instance a critical parameter, on which all other transport parameters rely on (see fig. 2.1). A controlled adjustment of $n$ is therefore essential for all possible thermoelectric materials. For CoSb$_3$ the charge carrier density can be controlled by substitution. In most cases Co is substituted by Fe (p-type doping) or Ni (n-type) [65, 66, 67, 23]. There are also several studies for the substitution of Sb for instance by Pd, Te or Sn [55, 68]. The main goal of the doping is to achieve a large power factor $S^2/\rho$ and to fabricate p-type and n-type skutterudites for final modules (see fig. 2.2 (c)). The substitution yield usually a change of lattice constant, while the basic crystal structure is maintained. By substitution also ternary skutterudites can be formed. Several examples are presented in literature [54]. Hereby the valence electron count (VEC) is helpful to predict the properties of possible ternary or binary skutterudites. If the number of valence electron in a unit cell (T$_4$X$_{12}$) is 72, semiconducting behaviour is expected [54]. This is for example true for CoSb$_3$ (Co$_4$Sb$_{12}$ = $4 \cdot 9$e$^-$+$12 \cdot 3$e$^-$ = 72e$^-$). If the alloy exhibits 68 or 76 valence electron like in NiP$_3$ or FeSb$_3$ metallic behaviour should occur.

Another structural feature for manipulating the properties of the skutterudites is provided by the large voids in the crystal structure. These ones can be filled by electro-positive guest ions R, as mentioned above, and filled skutterudites are formed with the sum formula R$_z$(TX$_3$)$_4$. $z$ defines the filling fraction and can be varied

between 0 and 1. A filling fraction of 1 means, that each void is filled by one guest ion. This filling ions are visualized in fig. 4.1 by the white balls. Several studies were performed to investigate, which elements could be used as fillers and a large variety containing rare-earth metals, alkaline-earth metals, thallium, uranium and thorium was found [19, 20, 54, 58, 69]. Filled skutterudites exhibit usually a silver-gray color and reveal different properties depending on the filler species, like super-conductivity, ferromagnetism, and heavy fermionic character [4, 20].

The bond between the guest ions and the skutterudite host lattice is ionic and acts electronically stabilizing. Some binary skutterudite alloys like $FeSb_3$ are even unstable until a filling ion is introduced. The fillers are only loosely bond and exhibit therefore huge thermal parameters (mean displacement parameter) [20, 70]. The smaller the ionic size is, the larger is the thermal parameter. The incorporation of fillers increases slightly the lattice constant compared to the corresponding binary alloy [71, 72]. This effect is small, since the binary host lattice has strong bonds and is very stiff. Additionally, changed intensity ratios of the individual peaks of the X-ray diffraction pattern (XRD) are obtained in dependence of the filling fraction $z$, which can be used to determine $z$ by Rietveld refinement [66, 70]. The thermal parameter of the filler can be also extracted with this method. More details are given in chapter 5.1.

Since the filling ion change the charge balance and the number of valence electrons as explained above, this approach is usually combined with a (partial) substitution of the transition metal element to keep the structural stability and the semiconducting behaviour (VEC around 72) or both [20, 54]. Otherwise the enlarged charge carrier concentration would also yield a larger electronic thermal conductivity and therefore partly compensate for the benefit achieved by the lower phononic thermal conductivity due to the filling approach.

## 4.1.2 Band structure of $CoSb_3$ and density of states

First band structure calculation of $IrSb_3$, $CoSb_3$ and $CoAs_3$ were performed by Singh and Pickett [63] by using the local-density approximation (LDA) together with the linearized augmented-plane-wave method (LAPW). They have described the formation of the valence and conduction band by hybridization of transition-metal d states and pnictide p-states and found for $CoSb_3$ an indirect pseudogap between the $\Gamma$ and the P point with an energy difference of $0.57\,eV$ and an direct pseudogap at the $\Gamma$ point with $0.8\,eV$. They introduced the pseudogaps since they calculated another gap-crossing band mainly formed by the pnictide p-states (see also in fig.4.2). For $IrSb_3$ and $CoAs_3$ this band closes the gap, but for $CoSb_3$ a small gap of $0.05\,meV$ is observed. This gap-crossing state exhibits a strong dispersion, is parabolic at the $\Gamma$ point and becomes linear for very small wave numbers (between 1% and 2% of the distance to the zone boundary), which makes this state very special. The linear
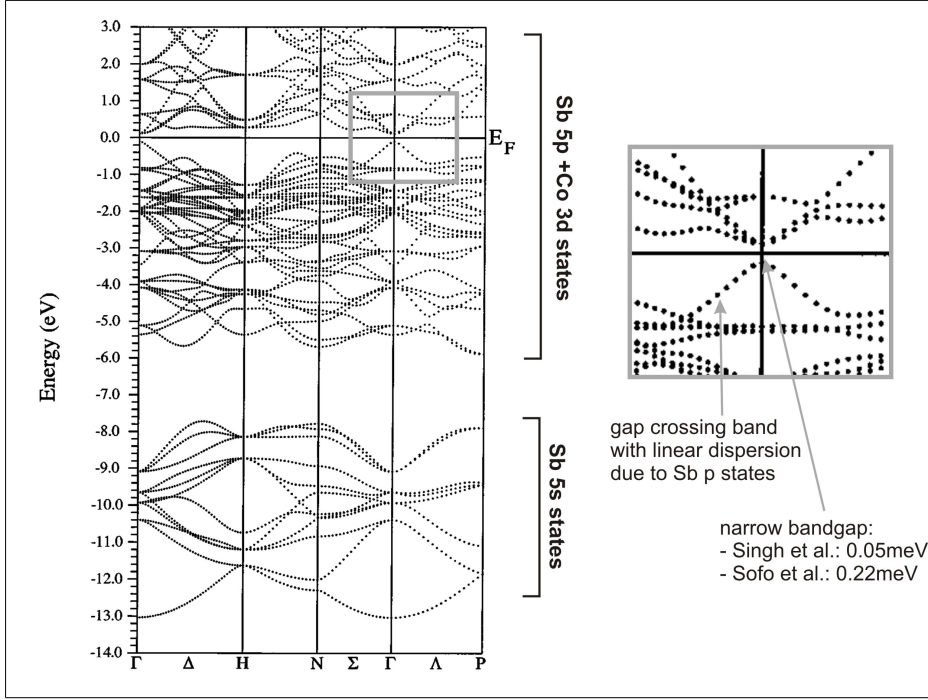
Figure 4.2: DFT band structure calculations of CoSb$_3$ performed by Sofo et al. [60]. The bandgap has a size of $50\,\mathrm{meV}$ and the valence band shows a linear dispersion. Therefore the effective mass of holes is much lower than for electrons, since a very flat conduction band is observed.

behaviour with a slope of $-3.1\,e\mathrm{V\AA}$ is therefore important for doping levels larger than $3\cdot10^{19}\,\mathrm{cm}^{-3}$. Nevertheless, the density of states (DOS) provided by this state is very small due to the large dispersion and due to the fact, that it is just a single band in a complex structure with a large amount of atoms in the unit cell [63]. The linear dependence effects the transport properties of CoSb$_3$ strongly. It changes the energy dependence of the DOS to quadratic and that one of the charge carrier density to cubic. The mass tensor reveals also an unusual behaviour, which results finally in a dependence of the hole mobility $\mu_p$ on the charge carrier density $n_p$ as $\mu_p \sim n_p^{-1/3}$ [63]. An approximation for the Seebeck coefficient for the constant relaxation time approach is also given there. $S$ depends in that case only on the slope $s$ of the linear band, on the temperature and on the charge carrier density:

$$S = -(2\pi k_B^2 T/3es)(\pi/3p)^{1/3}. \tag{4.1}$$

Further influence of the linear band on the transport parameter are discussed elsewhere [73].

**Table 1.** Band structure details, chemical bonds, molecule orbital and related substructure of $CoSb_3$.

| Energy band | No. | Chemical bonds | Molecule orbital | Substructure |
|---|---|---|---|---|
| Conduction band | Band-7 | $\sigma$-type antibonding Sb–Sb | Sb: 5s | $Sb_4$ ring |
| | Band-6 | $\pi$-type antibonding Sb–Sb | Sb: 5p | $Sb_4$ ring |
| | Band-5 | Nonbonding[a] | Co: $3d - e_g$ | $[CoSb_6]$ |
| Energy gap | | | | |
| Valence band | Band-4 | $\pi$-type antibonding $Sb_4$ hybridized with Co: 4p | Sb: 5p and Co: 4p | $Sb_4$ ring and $[CoSb_6]$ |
| | Band-3 | $\pi$-type bonding Sb–Sb | Sb: 5p | $Sb_4$ ring |
| | Band-2 | Nonbonding[b] | Co: $3d - t_{2g}$ | $[CoSb_6]$ |
| | Band-1 | $\sigma$-type bonding Sb–Sb | Sb: 5s | $Sb_4$ ring |

[a] This band is not distinguishable band but hybridizes strongly with band-6.
[b] This narrow nonbonding locates below the band-4 and overlaps with band-3.

Figure 4.3: The table summarizes the contribution of the different orbitals of Co and Sb to the Sb-Sb and Co-Sb bonds forming the band structure [74].

In the work of Sofo and Mahan [60], they improved the calculation further, nevertheless the basic features are preserved. Their calculated band structure is shown in fig. 4.2. They used the full-potential linearized augmented plane-wave method (FP-LAPW) and take additionally the internal structural parameters $u$ and $v$ into account, which describe the exact position of the Sb atoms in the $Sb_4$ rectangles. They achieved a band gap of $0.22\,eV$ for energy-minimized values of $u$ and $v$ and a gap of $0.05\,eV$ for experimental values of both parameters. This implies that the gap size is strongly dependent on the atom positions in the $Sb_4$ rectangles. It was shown that the top of the valence band is mainly influenced by the antibonding $\pi_4$ orbitals in the Sb rectangles [60, 75]. Furthermore, they have treated $CoSb_3$ as typical narrow-bandgap semiconductor and were applying the two-band Kane model to describe the bands close to the Fermi-level. The linear dispersion in the band at the top of the valence band yield light holes, while the bottom of the conduction band consists of a band with heavy electrons degenerated with a non parabolic band of light ones. By fitting the two-band Kane model, an effective mass of $0.071\,m_0$ for the light holes was determined and $0.35\,m_0$ for the heavy electrons [60]. The mass of the electrons in $CoSb_3$ is therefore about five times larger than that one of the holes, which has an strong influence on the mobilities of both charge carrier types.

A more detailed discussion, which bond contributes to which part of the bandstructure was given by Liu et al. [74] and the main results are summarized in the table in fig. 4.3 taken from their work. There is also explained, that the main contribution to the top valence band is from the Sb rings and the main contribution to the bottom of the conduction band arises from the Co 3d-states belonging to the Co-Sb bonds in the octahedra.

How strong the influence of the Sb rings on the top valence band really is, was demonstrated recently by Hammerschmidt et al. [61]. They calculated the band structure
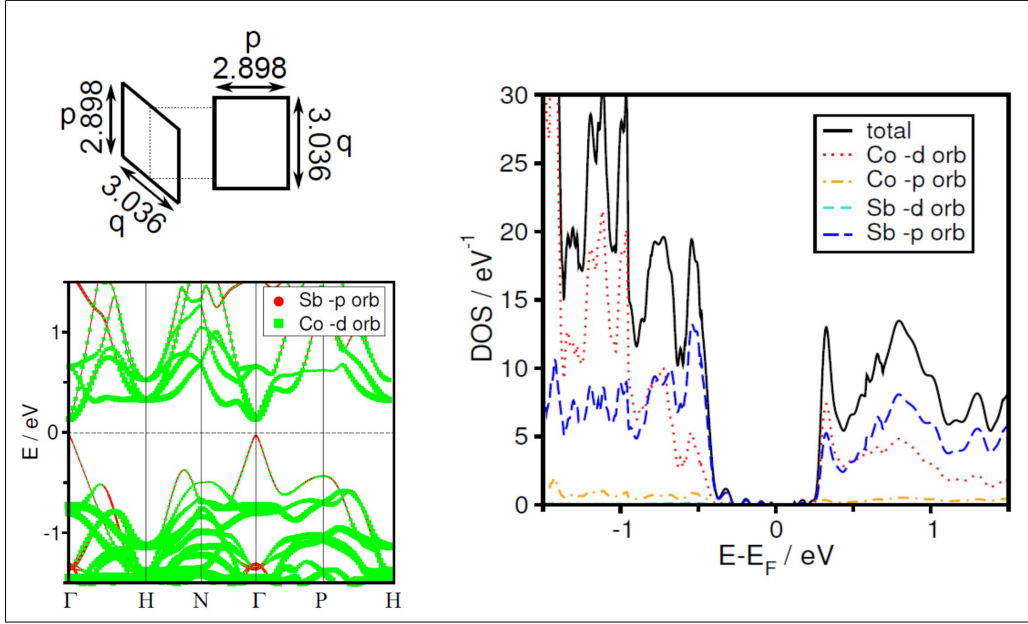
Figure 4.4: The band gap is very sensitive to the geometry of the Sb rectangles, since the Sb-Sb bonds in the rectangles are mainly responsible for the valence band [61]. The standard geometry is shown and the corresponding band structure calculated by PBE. The contribution of the atomic orbitals of Co and Sb is visualized by the green and red symbols, respectively. The projected density of states is also presented [61].

of CoSb$_3$ and the DOS with different DFT methods (density functional theory) and investigated the influence of the lattice parameter and different distortions of the Sb$_4$ rectangle on the bandgap. In fig. 4.4 their PBE[a] calculated band structure is shown close to the Fermi energy with the weighted contribution of the orbitals for the equilibrium Sb rectangle sizes of 2.898 Å x 3.036 Å and a equilibrium lattice constant of 9.1122 Å. The orbital contribution agrees well with the data given in table 4.3. The calculated total density of states and the individual orbital contribution is also shown. A band gap of 0.109 eV could be derived. If the lattice parameter is now varied between 8.8 Å and 9.2 Å, the gap varies between 0.4 eV and 0 eV, respectively. Furthermore it is possible by enlarging the long side of the rectangle (2.898 Å x 3.218 Å) to change the structure to an indirect band from N to Γ/H point with a gap width of 0.303 eV. The linear dispersion is also vanished in that case. By decreasing the long side until reaching nearly a square shape (2.898 Å x 2.854 Å), the linear dispersive band broadens and the gap is closed completely.

_____

[a]functional named after the physicists Perdew, Burke and Ernzerhof

### 4.1.3 Thermoelectric properties of CoSb$_3$

**Bulk properties**

Since skutterudites exhibit high power factors and show this promising opportunity of decreasing the thermal conductivity by the introduction of fillers, a lot of recent studies were performed on skutterudites. The main argument for skutterudites are the large achievable values of $ZT$ in a broad temperature range around 450 °C.

Thermoelectric investigations of CoSb$_3$ single crystals can be found in the work of Morelli et al. [39], Caillat et al. [55], Mandrus et al. [38], and Anno et al. [57]. In all publications similar features are observed and the connection of the calculated band structure to the thermoelectric transport properties could be shown.

*Low temperature measurements*
The measured low temperature curves of resistivity, hole mobility, thermal conductivity and Seebeck coefficient are shown in fig. 4.5 for CoSb$_3$ single crystals synthesized by Morelli et al. [39] and Mandrus et al. [38]. The investigated samples differ in purity and exhibit therefore different doping levels.

The resistivity of the samples investigated by Morelli et al. reveal a weak temperature dependence and metallic like behaviour. The samples are p-type and the carrier concentration is in the range of $10^{18}\,\mathrm{cm}^{-3}$ and nearly temperature independent (not shown). The expected intrinsic charge carrier density at $300\,\mathrm{K}$ by assuming a gap of $50\,\mathrm{meV}$ is in agreement to the observed values and should be around $10^{19}\,\mathrm{cm}^{-3}$. The mobility is constant at low temperatures, indicating only neutral impurity scattering, and decreases for temperatures larger than $100\,\mathrm{K}$ with a $T^{-3/2}$ dependence corresponding to acoustic phonon scattering (see table 3.1). The observed hole mobilities are comparably large, confirming the low effective mass of the holes found by the band structure calculations. The Debye temperature of CoSb$_3$ is $321\,\mathrm{K}$ (see table 4.1) and gives usually the borderline, where the dominant charge carrier scattering process changes from impurity scattering to acoustic-phonon scattering [22]. For scattering at ionized impurities a switch from a $T^{3/2}$ dependence of the mobility at low temperatures to a $T^{-3/2}$ is expected (see table 3.1). Therefore a maximum of the electric mobility should be found around room temperature for CoSb$_3$. Since these samples exhibit a high purity with low number of point defects and no ionic scattering occurs, the onset of phonon scattering could be already observed for much lower temperatures around $100\,\mathrm{K}$. This is different for the work of Mandrus et al. [38], which is also presented in fig. 4.5. Their crystals show semiconducting character of the resistivity and ionic impurity scattering for low temperatures. The expected maximum, where the slope of $\mu$ is changing, is observed at $250\,\mathrm{K}$ (see fig. 4.5). This value is fairly in agreement with the Debye temperature. Intrinsic excitation starts
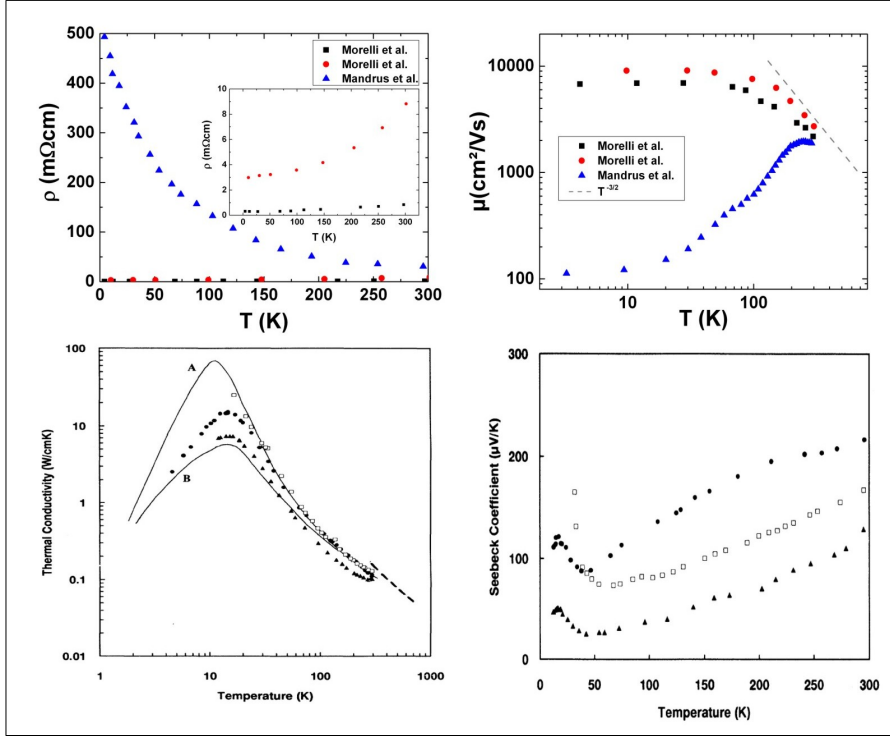
Figure 4.5: Low temperature transport measurement on p-type CoSb₃ single crystals published by Morelli et al. [39] and Mandrus et al. [38]. Two different characteristics (metal-like and semiconducting) occur for the resistivity $\rho$ and the mobility $\mu$. The temperature dependence of the Seebeck coefficient and the thermal conductivity were investigated only by Morelli et al.

for these samples at $150\,K$ and the determined band gap of $50\,meV$ is in agreement to the calculated value discussed in chapter 4.1.2.

Morelli et al. [39] have also investigated the low temperature thermal conductivity and the Seebeck coefficient. For the thermal conductivity a combination of boundary scattering and Umklapp scattering ($\sim T^{-1}$, see table 3.1) is assumed. The observed exponential decay towards higher temperatures can be only observed for a very low number of point defects and indicates the high purity of the single crystals. The Seebeck coefficient is positive and exhibits basically a linear slope with $T$. Below $100\,K$ a large increase due to phonon drag is observed [39].

Remarkably are the results of Anno et al. [57], who have synthesized p-type polycrystalline CoSb₃ bulk samples with different grain size of $3\,\mu m$ and $300\,\mu m$. The samples with a low grain size exhibit semiconducting properties of the films as discussed by Mandrus et al. (see fig. 4.5), while the large grain sizes yield film properties similar to the work of Morelli et al.. Even though they could not explain there results, both

characteristics seems to be typical for CoSb$_3$. This could also be confirmed by cold and hot pressed polycrystalline samples, which show these two types of conductivity characteristics at low temperatures [76].

*High temperature measurements*

Caillat et al. [55] have investigated room temperature and high temperature properties for p- and n-type CoSb$_3$ single crystals. The measured values for the p-type samples match very well the low temperature curves and the observed results vary only slightly due to the different doping concentration related to the individual fabrication processes. Typical room temperature values for very pure samples are therefore a resistivity of $1.9\,\mathrm{m\Omega cm}$, a hole density $n_p$ of $1.16 \cdot 10^{18}\,\mathrm{cm^{-3}}$, a mobility $\mu_p$ of $2835\,\mathrm{cm^2/Vs}$, a Seebeck coefficient of $220\,\mathrm{\mu V/K}$ and a thermal conductivity of $0.1\,\mathrm{W/Kcm}$ [55]. The n-type single crystals were synthesized by doping due to substitution of Sb by Pd or Te [55]. Comparing n- and p-type samples with the same charge carrier density shows that the hole mobility is much larger than the electron mobility ($2000\,\mathrm{cm^2/Vs}$ vs. $100\,\mathrm{cm^2/Vs}$), which is in agreement to the band structure calculations. The determined effective mass for the holes ($\sim 0.2\,m_0$) is larger than calculated and depends on the hole density $n_p$, while the electron mass is about 10 times larger, but independent on the electron density $n_n$. To compensate the influence of the low electron mobility on the resistivity, n-type samples need to be doped to the range of $10^{20}\,\mathrm{cm^{-3}}$. However, the room temperature Seebeck coefficient is larger for the n-type samples, due to the larger effective electron mass.

The measured high temperature curves are shown in fig. 4.6. The resistivity of the p-type samples increases slightly with $T$ until $300\,^\circ\mathrm{C}$ due to the decrease of the mobility by phonon scattering. Afterwards a strong decrease of resistivity occurs, which corresponds to the direct pseudogap found in the band structure ($0.8\,e\mathrm{V}$). For the n-type samples the same behaviour is observed, however the observed drop corresponds in that case to the indirect pseudo gap. The mobilities are not shown, but reveal also the $T^{-2/3}$ dependence for acoustic phonon scattering.

The Seebeck coefficient for the non-doped samples increases with $T$ up to $600\,\mathrm{K}$. For higher temperatures intrinsic conduction occurs and the value decreases. In the intrinsic case the Seebeck coefficient has necessarily to show a maximum and decreases afterwards as explained in chapter 3.1 by equation 3.14. The Seebeck coefficient rises nearly linearly before this maximum is reached. $S$ is the average energy of a charge carrier and before peaking it corresponds to a increasing number of charge carriers, excited from a narrow defect band with slightly higher energy than $k_B T$ [76].

Intrinsic excitation of holes leads for lightly n-type doped samples to a minimum of the Seebeck coefficient around $400\,\mathrm{K}$. Both carrier types compete for larger temperatures and the absolute Seebeck coefficient is lowered with increasing temperature. The compensation of both charge carrier species can be found around $600\,\mathrm{K}$ and for even larger temperatures the sample reveal quantitatively the same trends as the

28
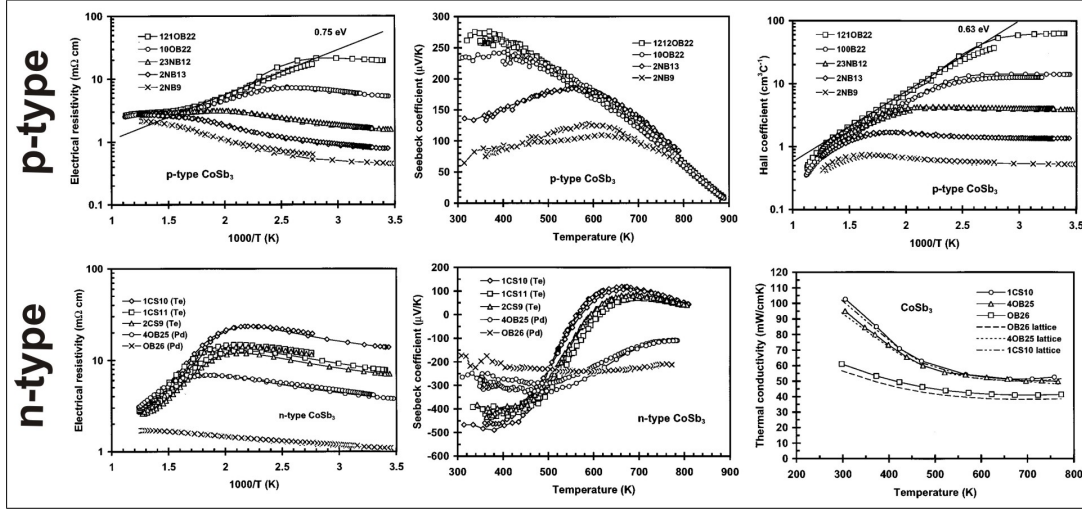
Figure 4.6: High temperature transport measurements of CoSb$_3$ single crystals published by Caillat et al. [55]. Two different types of crystals were prepared. Pure CoSb$_3$ p-type crystals with slightly different charge carrier density (top row) and n-type crystal by doping with Pd and Te (bottom row).

undoped samples. Highly doped n-type samples with large carrier density keep the negative sign and only the absolute value of the Seebeck coefficient is decreased by the bipolar conduction.

The thermal conductivity follows the trend of the low temperature data and mainly Umklapp scattering is observed. The electronic part has a small contribution ($< 10\%$) and the main thermal conductivity comes from phonons. Furthermore there are indications for electron-phonon coupling in this system [55].

In conclusion, CoSb$_3$ single crystals revealed the same trends for high temperatures: intrinsic hole excitation around 400 K-500 K, acoustic phonon scattering of charge carriers and Umklapp scattering of phonons. Differences occur between p-type and n-type samples due to the large differences in the effective mass of the electrons and the holes in this system. The doping level to optimize the power factor has therefore to be chosen quite differently for the different carrier species. Furthermore the influence of the linear dispersion in p-type samples could also result in "unusual" temperature dependences, which is discussed in none of these publications and can be found for instance in the work of F. Timmermann [73].

It is to note that room temperature measurements are very critical in this system for two reasons. First, the Debye temperature is close to room temperature and a change in the charge carrier scattering mechanism occurs here. Second, the onset of intrinsic hole excitation is usually observed around room temperature and bipolar

conduction could occur, making the interpretation of the measured data challenging. To further enhance the $ZT$ value of this material, two main routes are known: i) introduction of filler ions to lower the thermal conductivity, which changes the intrinsic crystal properties and ii) an extrinsic nanostructuring by lowered dimensions or artificial introduction of objects or structures with size in the nanoscale range. The change of thermoelectric properties by both routes are discussed next.

**Filled skutterudites - an intrinsic nanostructuring approach**

The incorporation of guest ions is a well-established method to lower the phononic thermal conductivity, while maintaining the basic features of the electric properties. In fig. 4.7 (a) the low temperature thermal conductivity is compared for unfilled and misch-metal filled $CoSb_3$ and a clear reduction of $\kappa_L$ is observed [77]. The mechanism behind the scattering of acoustic phonons due to the motion of the fillers as well as the interaction with the host lattice was intensively discussed. In many studies this fillers are described as independent Einstein oscillators that scatter the acoustic phonons incoherently. Heat transport is mainly carried by acoustic phonons, which could be described as plane waves traveling through a solid due to coherent vibrations. The freely oscillating fillers will scatter in all direction and disturb the plane wave propagation incoherently [78]. This is schematically illustrated in fig. 4.7 (b). Inelastic neutron scattering confirmed, that the vibrational states corresponding to the fillers are in the energy range of the acoustic phonons [77, 78]. Nevertheless broadening of the states provides hints for coupling of the fillers to the host lattice.
The general picture of independent Einstein oscillators explains the measurements of the specific heat sufficiently well [4, 78, 79]. However, it is more and more replaced by a model based on the interaction of the fillers with the host lattice [77, 79, 80]. Keppens et al. [79] demonstrated for La filled $CoSb_3$, discrepancies of the elastic constants by using the model of Einstein oscillators and they observed two filler modes by inelastic neutron scattering hybridizing with the phonon modes of Sb. Wang et al. [77] reported for large filling fractions the same frequency for the filler oscillation (measured by ultrafast optical measurements) and of a Sb oscillation mode (measured by Raman scattering), which indicates a coupling between both. In the work of Koza et al. [80] coherent coupling of the filler to the lattice was confirmed by inelastic neutron scattering where the explanation by Einstein oscillators does not hold. Since the detected filler modes have zero group velocity, they do not contribute to heat transfer and inelastic resonance effects can not occur [80]. The interaction of the filler and the host lattice, yield a strong flattening of the transversal and longitudinal acoustic branch at the energy of the filler state. The phonon dispersion reveal the so-called avoided-crossing of the acoustic phonon modes [81, 82], which is shown in fig. 4.8 (a) for clathrates, another material group with void filling. The decrease of the thermal conductivity by filling is therefore due to the band flattening by the avoided cross-
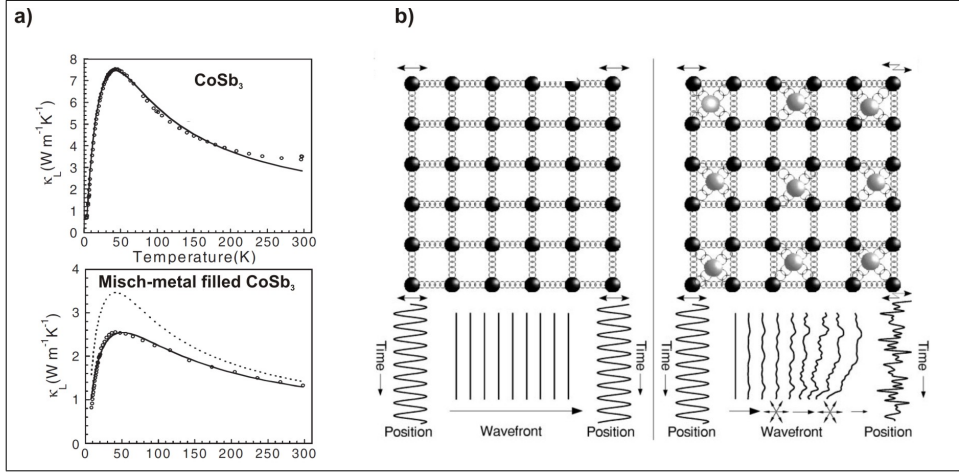
Figure 4.7: a) Experimentally observed decrease of the thermal conductivity by filling CoSb$_3$ with misch-metal [77]. b) Illustration of a model for the scattering process of acoustic phonons by the introduced fillers treated as Einstein oscillators [78]. The planar acoustic waves were incoherently and randomly scattered in all directions.

ing [81]. The basic principle can be explained by a simple spring model illustrated in fig. 4.8 (b), which gives the avoided crossing as solution for the dispersion spectrum of the shown spring arrangement [81]. Furthermore, the flattening of the acoustic modes enables Umklapp scattering already at low temperatures [80, 50]. Even though the avoided crossing was not yet shown for skutterudites, it is believed that this is the more realistic model. To point out the differences is difficult, since both concepts show features at the same energy in the phonon dispersion and frequency dependent measurements are necessary [50].

Many different studies were performed using the filling approach for lowering $\kappa_L$ [20, 83, 84]. Thereby partial filling is more effective than a complete incorporation of fillers [20], which is anyway not possible for all ion species [85]. How strong the decrease in thermal conductivity is, depends on the individual properties of the fillers. Small ions can oscillate stronger and introduce a higher degree of disorder giving rise to further reduction of $\kappa_L$ . Low-lying 4f-states (present for instance in Nd) give an additional scattering contribution [20]. Furthermore, the frequency of the scattered phonons is dependent on the mass of the filling ions, which results in the successful concept of multiple filling for scattering a larger bandwidth of phonons [86, 87, 77]. If the mass difference of the fillers is large (for instance Yb and Ba), a larger reduction of $\kappa_L$ is observed than for single filling, yielding a $ZT$ of 1.36 [86].

The incorporation of filling ions results also in a strong n-type doping, which has to be compensated for instance by substitution of Co or Sb as discussed in chapter 4.1.1.
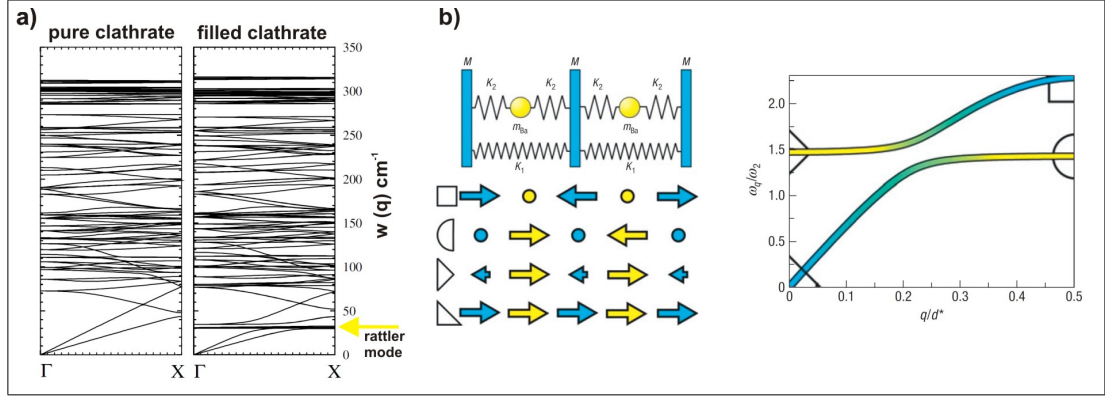
Figure 4.8: a) Theoretical calculation of the phonon spectra revealing avoided crossing in filled clathrates [82]. The acoustic branches are flattened at the energy of the filler mode (marked by arrow). b) Derivation of the avoided crossing by a simple spring model [81].

This substitution has an additional side-effect. Point defects were introduced due to the mass difference of the substituting element, which results in a further decrease of the thermal conductivity. The incorporation of filling ions and the additional point defects by substitution are an effective combination for scattering a wide bandwidth of acoustic phonons [20, 54]. It is further to note, that the substitution level can influence the maximum achievable filling fraction of a certain filling species [23, 54].

**Extrinsic nanostructuring and thin films**

The most common approach for extrinsic nanostructuring is currently the synthesis of nanocomposites offering the opportunity of nanostructured bulk samples. Since thermoelectric is in most cases connected to macroscopic heat transfer, this approach seems to be the most promising for large-scale applications. The samples are usually synthesized by several steps: i) mixing of powders with the right stoichiometry, ii) synthesizing the desired material by an annealing procedure, iii) grinding the material for instance by ball milling into fine powder with an appropriate grain size and, iv) sintering the powder by hot-pressing, cold pressing or spark plasma sintering (SPS). The challenge of the last step is to achieve bulk material without loosing the small grain sizes. SPS is therefore a widely used technique for the preparation of nanocomposites in the field of thermoelectrics. For skutterudites several studies exist and for instance a $ZT$ value of 1.7 is reported for n-type $Sr_{0.07}Ba_{0.07}Yb_{0.07}Co_4Sb_{12}$ [27]. This value is independently confirmed and the corresponding temperature dependences are shown in fig. 4.9. Compared to the thermoelectric bulk properties given in fig. 4.6, the main enhancement of $ZT$ for this composite is achieved by decreasing the thermal

conductivity due to the small grain size, the threefold filling and additional defects created by a high pressure torsion. While the Seebeck coefficient is in the range of bulk values, the resistivity is four times lower and the thermal conductivity is decreased by a factor of 3. Additionally another p-type composite (DD$_{0.6}$Fe$_3$CoSb$_{12}$, DD = didymium) with $ZT \sim 1.4$ is also added to the graph [27]. Further approaches for extrinsic nanostructuring are thin films, multilayers, nanowires, nanodots, nanoinclusions, and band structure architecture [5, 10, 15, 16, 17, 88, 89, 90].
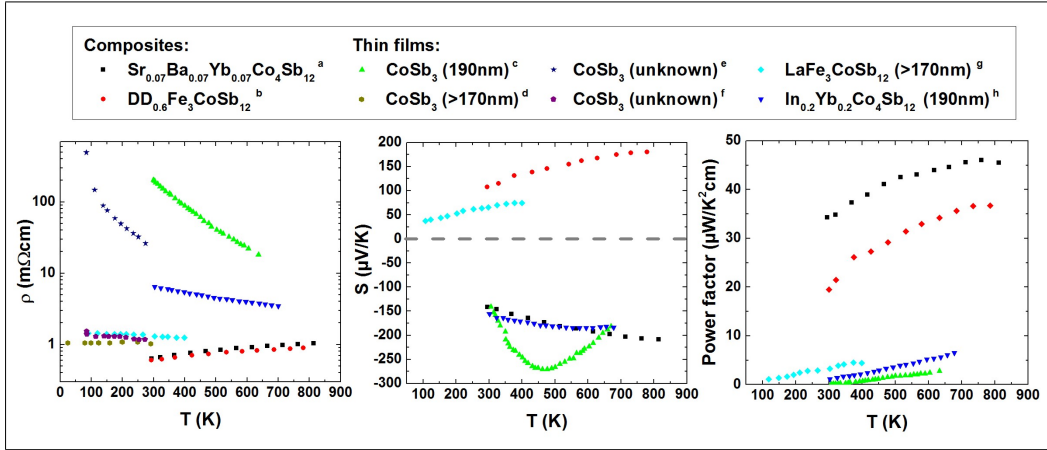


Figure 4.9: Overview of the measured temperature dependences of resistivity $\rho$, Seebeck coefficient $S$, and power factor $S^2/\rho$ for several skutterudite nanocomposites and thin films found in literature.

[a,b] Rogl et al. [27], [c] Savchuk et al. [22], [d,g] Suzuki et al. [23], [e,f] Anno et al. [91], [h] Kumar et al. [92]

In this work skutterudite thin films are investigated, for which the effects explained in chapter 2.2 can be utilized to enhance $ZT$. Several works are reported for skutterudite thin films deposited by sputtering [22, 33, 91, 93], pulsed laser deposition (PLD) [64, 90, 92, 94] or modulated elemental reactant method (MERM) [95, 96, 97, 98]. The measured temperature dependent transport coefficients of these studies are also shown in fig. 4.9 and fig. 4.10. The basic feature found in bulk samples for the resistivity and the Seebeck are also observed for thin films. While the Seebeck coefficient of the thin film samples is comparable to the measured values for bulk and nanocomposite samples, the resistivity is in general larger and thus the power factor lower. Since the charge carrier concentrations of the thin films is in many cases comparable or even larger compared to the results found for bulk materials (fig. 4.10), the main reason for the larger resistance is the lower mobility in thin films caused by smaller grain sizes, larger amount of point defects, intrinsic defects, and surface

roughness. Besides impurity scattering and acoustic phonon scattering found for bulk systems, additional scattering processes due to the changed microstructure have to be considered (see table 3.1) resulting in the extremely low mobilities (fig. 4.10 compared to fig. 4.5). Therefore the mobility is nearly constant over the entire temperature range and exhibits not the typical dependences found for bulk samples. The contribution of the individual scattering processes can be described by using equation 3.7 and 3.10. For high temperatures the mobility should still converge to the $T^{-3/2}$ dependence of acoustic phonon scattering.

Unfortunately the thermal conductivity is usually not investigated for the given examples due to the difficulties in performing the measurements for thin films. Nearly all methods reach their limits for thin films and established measurement techniques characterize the cross-plane conductivity ($3\omega$ method, thermoreflectance), while the Seebeck coefficient and electric conductivity are usually measured in-plane direction. One possibility for in-plane measurements of thin films is the Völklein method, for which film deposition on special membranes is required [9, 99, 100, 101]. However, without knowing the thermal properties, the potential of thin films can not be assessed. The smaller grain sizes should strongly decrease the thermal conductivity. If this effect compensates the lower power factor compared to bulk samples is still an open question for thin film thermoelectrics. Since nanocomposites also exhibit smaller grain sizes and therefore a strongly decreased thermal conductivity, comparable $ZT$ values should be obtained for thin films.
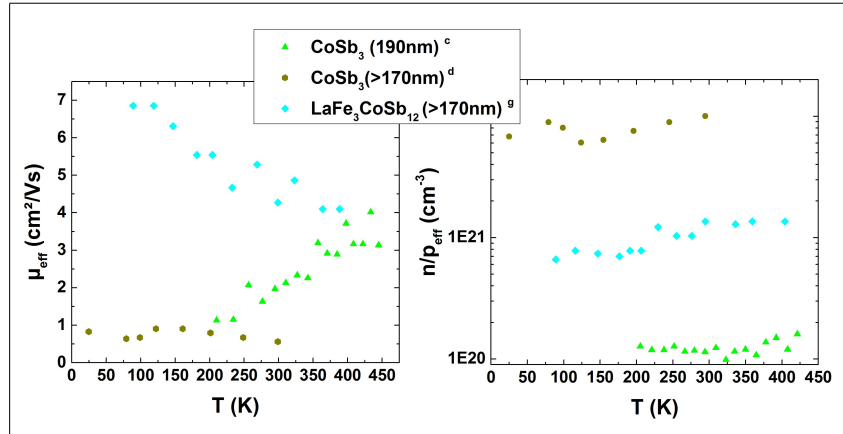


Figure 4.10: Temperature dependent mobilities $\mu$ and charge carrier densities $n$ for some thin film samples found in the literature. While the charge carrier density is quite large, the mobility exhibit low values due to the large number of different scattering processes occurring in thin films.

[c]Savchuk et al. [22], [d,g] Suzuki et al. [23].

34

Here is also to note that the presented results of thin films are mainly achieved without optimization of the power factor by adjustment of the charge carrier density as performed for the discussed composites. Furthermore only films thicker than 70 nm were prepared in all thin film studies based on CoSb$_3$ found in literature. This thickness is far above the range, where most of the effects described in chapter 2.2 arise. Thus further enhancement of the power factor should be possible. The ability to grow skutterudite films in the nanometer range is therefore a requirement to reach this goal and it is also the fundament for extrinsic nanostructuring approaches like geometric modulation (i.e. deposition on spheres or nanoperforations), multilayer structures or gradient layers. Additionally the structural, electrical, and stoichiometric properties of the material should be better controllable by thin film technology, which makes thin films also a good model system for basic research.

### 4.1.4 Synthesis of CoSb$_3$ thin films

The synthesis of single phase CoSb$_3$ thin films is a challenge. The phase diagram shown in fig. 4.11 reveals no homogeneity area for the single CoSb$_3$ skutterudite phase. The phase should be only observed for an accurate stoichiometry with 75 at.% Sb. For lower Sb content CoSb$_2$ is additionally formed, for higher Sb content pure Sb will be supplementary obtained.

As mentioned in the last section, skutterudite thin film preparation was already performed by PLD, sputtering and by the MERM method. Many difficulties are reported in these works for achieving single phase films. Caylor et al. [94] optimized the parameters for PLD and could achieve single phase films for a narrow range of the substrate temperature during deposition. By an excess of Sb in the targets, this temperature range can be shifted to higher temperatures. Colceag et al. [84] was not even successful to prepare skutterudite films by PLD, but in their work a lower substrate temperature around 200 °C leads to the skutterudite phase as major phase. Suzuki [23] was not able to find a systematic dependency of the phase formation on the laser fluence, substrate temperature or Sb content in films prepared by PLD. Nevertheless, he was able to synthesize single phase films at substrate temperatures below 250 °C. For very complex alloy targets (Ce$_{0.26}$Co$_{3.7}$Ni$_{0.26}$Ge$_{0.79}$Sb$_{11.21}$), the formation of diantimonides in the PLD prepared films is reported as long no additional Sb is used [90].

All these results indicate a strong dependence of the phase formation on the Sb content in the film. However, in most cases the Sb content was not determined for all samples, but rather for the single phase skutterudite films only. This is to my knowledge the main reason for the described difficulties. It will be shown in chapter 6.3, that for a successful preparation a slight excess of Sb and a low substrate temperatures should be preferred. This can be explained by the low sticking coefficient of Sb and its high vapour pressure resulting in Sb deficient films for higher temperatures. The first systematic investigation of the influence of the composition on the
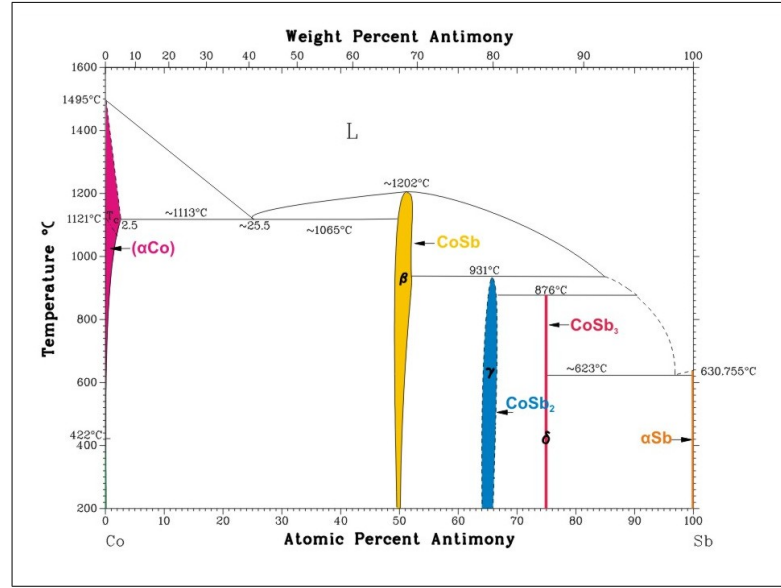
Figure 4.11: Co-Sb phase diagram [102].

phase formation was performed for MERM deposited films, where the composition was varied between 68 at.% and 81 at.% of Sb and the window for the formation of single phase skutterudites was found to be between 74 at.% and 78 at.% [95]. For sputtered films on non heated substrates, the additional formation of Sb is reported, even though the composition was in this range [58, 93]. The sputtering process might introduce more energy than the thermal evaporation used for MERM, which could result in the Sb phase during deposition.

To understand and overcome the described preparation problems, this work provides an extended investigation of the phase formation in dependence of i) the Sb content in the films, ii) the used deposition parameters and iii) the annealing temperature for post-treatment. Films were therefore deposited by MBE technique at different substrate temperatures, on non heated substrates with a post-annealing step or by using the MERM method. The results are discussed in chapter 6 and 7. For a comparison with other deposition methods such as sputtering, where a larger amount of energy is introduced, the influence of the chosen deposition rates was also investigated (chapter 7.1.3).

The deposition of CoSb$_3$ thin films reveals further advantages compared to bulk samples synthesized by equilibrium methods. Interesting results were for instance found for filled skutterudite thin film or skutterudites with partially element substitution. Schüpp et al. could for example achieve a substitution level of 20% for the substitution of Co by Fe, which is larger than the maximum solubility of 8% for bulk samples [58]. Additionally, very large filling fractions of 68% are reported by using

MERM method for Sn filled skutterudites, which is far above the bulk filling limit [96]. The lack of perfect filling for hot pressed bulk samples is for instance caused by the tendency of the fillers to oxidize due to their high reactivity [23]. This is supported for all synthesis techniques performed at high temperatures. Conventional bulk synthesis techniques exhibit therefore a limited ability to substitute atoms, to fill with guest ions or to prepare complex skutterudites, which is not the case for thin film preparation. Non equilibrium film deposition could be carried out for instance at low temperatures and under ultra high vacuum conditions [23].

Finally the influence of the substrate on the film growth has to be taken into account and several studies can be found in literature [23, 90, 91, 64]. First the grain size might be influenced by the substrate. On SiO$_2$/Si substrates columnar growth with a grain size of 50 nm was reported, while on Si$_x$N$_y$ a grain size of 250 nm was observed resulting also in a lower charge carrier density [23]. A few studies are also published on textured or epitaxial growth. Caylor et al. [90] reported an epitaxial growth by PLD on an InSb substrate along the (001) direction, while on polished and sputter-etched Si(100) substrates (310)-oriented CoSb$_3$ skutterudite films could be prepared via rf-sputtering [91]. However, epitaxial growth was not attempted in this study.

## 4.2 FeSb$_3$

### 4.2.1 Structural and thermoelectric properties of FeSb$_3$ thin films

The second investigated representative of the skutterudite alloys is FeSb$_3$. This compound is metastable and bulk material can not be synthesized. Only a few publications exist for the structural characterization of FeSb$_3$ thin films prepared via MERM method [97, 103, 98]. The most important physical properties from these studies are summarized in fig. 4.12 (a) and were mainly published by Möchel et al. [98]. Additionally, the resistivity and the lattice dynamics was investigated there. The



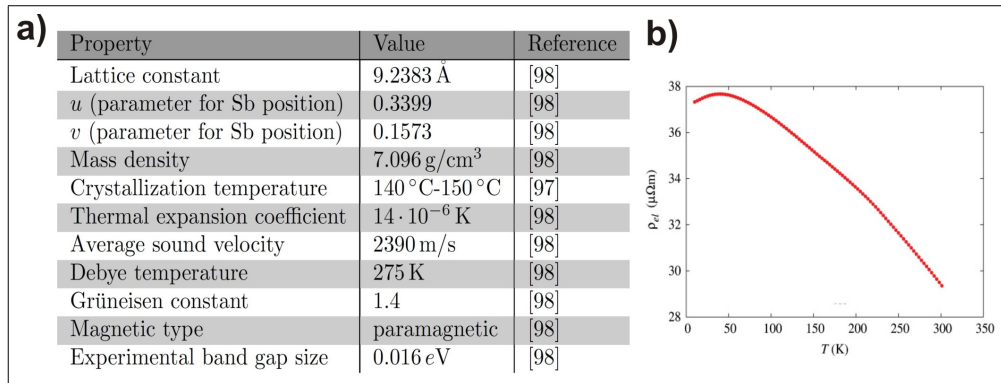| Property | Value | Reference |
|---|---|---|
| Lattice constant | 9.2383 Å | [98] |
| $u$ (parameter for Sb position) | 0.3399 | [98] |
| $v$ (parameter for Sb position) | 0.1573 | [98] |
| Mass density | 7.096 g/cm$^3$ | [98] |
| Crystallization temperature | 140 °C-150 °C | [97] |
| Thermal expansion coefficient | $14 \cdot 10^{-6}$ K | [98] |
| Average sound velocity | 2390 m/s | [98] |
| Debye temperature | 275 K | [98] |
| Grüneisen constant | 1.4 | [98] |
| Magnetic type | paramagnetic | [98] |
| Experimental band gap size | 0.016 eV | [98] |

Figure 4.12: a) Structural properties of FeSb$_3$ thin films found in literature. b) Temperature dependence of the resistivity for a FeSb$_3$ thin film [98].

37

temperature dependence of the resistivity is shown in fig. 4.12 (b) and exhibits semi-conducting character. A bandgap of $16\,$m$e$V could be extracted from this curve [98]. The investigation of the lattice dynamics reveals a softening of the phonon modes compared to $CoSb_3$. This indicates a lower speed of sound in $FeSb_3$ and thus a lower thermal conductivity [98]. Further thermoelectric characterizations do not exist.

### 4.2.2 Synthesis of FeSb$_3$ thin films

The $FeSb_3$ phase is no equilibrium phase and is therefore not present in the Fe-Sb phase diagram shown in fig. 4.13. As already mentioned, this phase is metastable and a special way of preparing far from equilibrium is needed to achieve this phase. The only successful approach reported in literature is based on the MERM method [97, 103], which will be introduced in chapter 6.2. The MERM method avoids the formation of more stable binary compounds as reaction intermediate and it was shown that single phase skutterudite films are only obtained for films with a Sb excess compared to the stoichiometric 75 at.% of $FeSb_3$. In this work it will be shown, that it is also possible to synthesize $FeSb_3$ skutterudite films by codeposition using molecular beam deposition. However, the metastable nature of this phase limits the thin film preparation to low temperatures combined with post-annealing.
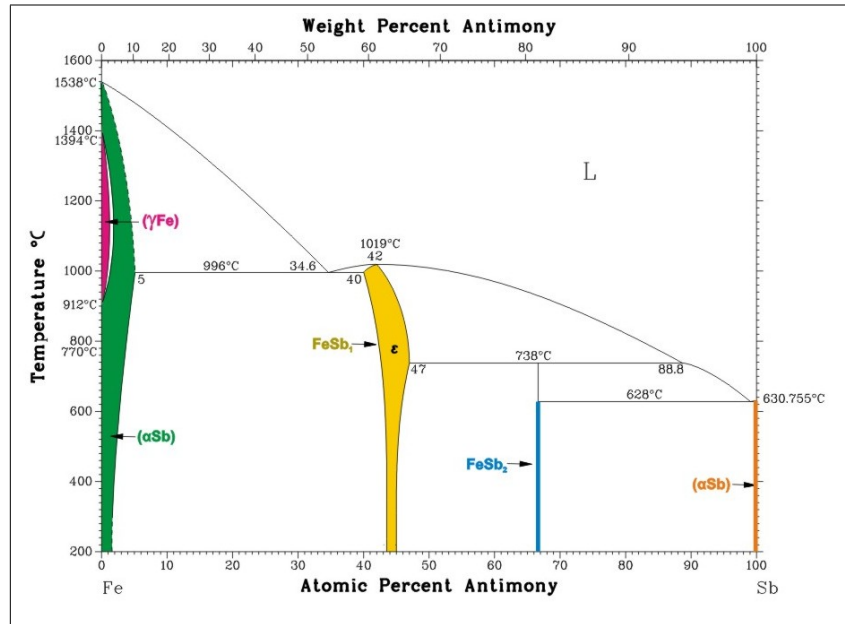


Figure 4.13: Fe-Sb phase diagram [102].

# 5 Experimental methods

## 5.1 Basic methods for structural characterization

For the structural characterization of the films several methods were used including RBS, XRD, XRR, AFM, DSC, SNMS, SEM and TEM. Since all this methods are well established in material science, a detailed description of the different techniques is abstained and mainly the measurement parameters will be given.

### Rutherford backscattering spectrometry (RBS)

RBS is a surface sensitive method for the investigation of the elemental constituents in a sample and for the determination of the composition. Usually accelerated He ions with a specific energy were shot on the sample and the energy of the backscattered ions is detected, which depends mainly on the mass of the scattering atom. Thus species and amount of the elements present in the sample can be identified. Further information can be found elsewhere [104, 105]. The experiments were performed in cooperation with the Helmholtz-Zentrum Dresden-Rossendorf (HZDR). He$^+$ ions were accelerated by a Van de Graaff generator to $1.7\,\mathrm{M}e\mathrm{V}$ and the used scatter angle was $170°$. The backscattered ions were detected with a multichannel semiconducting detector with a resolution of $13\,\mathrm{m}e\mathrm{V}$ and a covered room angle of $3.052\,\mathrm{msr}$. Usually the collected charge was $10\,\mathrm{\mu C}$. The data was analyzed by integration of the raw data or by using the simulation software SIMNRA [106, 107].

### X-ray diffraction (XRD)

XRD reveals mainly the crystal structure of a sample and is based on the coherent elastic scattering of X - rays in the sample and their interference afterwards. The diffracted X - rays are detected angle-resolved and constructive interference is observed for specific angles depending on the formed crystal phase, grain sizes and the orientation of the grains. These angles can be described in a first approximation by the Bragg condition for constructive interference [37]:

$$n\lambda = 2d_{hkl}\sin\theta. \tag{5.1}$$

$\lambda$ is the used wavelength of the used X - ray radiation, $d_{hkl}$ is the distance of specific crystal planes described by the Miller indices, and $\theta$ is half of the diffraction angle $2\theta$[a].

---

[a] $2\theta$ is defined as the angle between incident beam and diffracted beam

By analyzing all observed maxima, the corresponding phases can be identified and lattice parameter determined. Further details are discussed elsewhere [105, 108, 109]. In this work mainly the laboratory diffractometer XRD7 of the Seifert company was used, which is measuring in Bragg-Brentano geometry with point focus. The X - ray tube exhibit a Cu cathode generating X - rays with a wavelength of $1.5406\,\text{Å}$ (Cu K$\alpha_1$). A Ni filter on the primary side was used to decrease the Cu K$_\beta$ radiation, since no monochromator was available. On the secondary side a Soller collimator is installed. To increase the probed volume and to suppress the influence of the single crystalline substrates, usually a $2\theta$-scan (moving detector) was used and the incident angle was kept constant at $10°$. The data was afterwards corrected by the Rachinger algorithm [110]. To identify peaks and phases the literature data base [111] was used. Measurements were additionally performed at the synchrotron beamline G3 of HASY-LAB at DESY (Hamburg, Germany) with the corresponding wavelength of Cu K$\alpha_1$ and in some cases the one of Co K$\alpha_1$ ($1.7890\,\text{Å}$) to avoid X - ray fluorescence from Co in the samples. The desired wavelength was filtered by a double monochromator. Especially the XRD investigation of the Yb filled CoSb$_3$ films were investigated at the synchrotron by $\theta/2\theta$ scans, since Rietveld refinement was necessary for these films to extract the filling fraction (see chapter 11) and therefore larger intensity and resolution is needed. For the same reason the $\sin\chi^2$ stress measurements were performed at DESY.

**Rietveld refinement**

The Rietveld refinement is a method to analyze XRD patterns of powders or polycrystalline materials quantitatively. It is based on the refinement of the parameters of a underlying structure model. Thus the XRD pattern of corresponding phases with its crystal structure is calculated and compared with the measured pattern. Afterwards individual parameters of this structure model (for instance lattice constant, mass fraction of the phase, thermal parameters, peak shape, background, system parameter, occupation etc.) can be refined by the least square method until the calculated and the measured pattern agree to each other with the desired accuracy. The measured pattern has to fulfill several requirements. First several peaks (5 to 10) have to be measured with monochromatic radiation, adequate step size and a good signal to noise ratio. To fulfill the later requirement usually synchrotron measurements with higher intensities compared to the laboratory diffractometers are used. The quality of the performed refinement is additionally dependent on the initially used model and the choice of appropriate starting conditions is very important. Further information can be found elsewhere [112, 113]. The refinement was performed with the software FULLPROF [114, 115].

**Residual stress measurements via XRD**

By using XRD, the residual stress in a sample can be investigated with the $\sin \chi^2$-method. This method is based on measuring the shift of a specific peak as function of the tilting angle $\chi$ of the sample. The peak shift is caused by differences in the in - plane and cross - plane lattice constants caused by the residual stress. By performing $\theta/2\theta$ scans with different $\chi$, this change in lattice constant can be determined and thus the residual stress. Further details about the experimental procedure are given in chapter 9.1 and in the literature [108].

## X-ray reflectometry (XRR)

With XRR the thickness of thin films, the surface roughness, and the density of a material can be determined. For this method the interference of X - rays reflected at surfaces and interfaces is detected angle-resolved. The incident angle is thereby below $10°$. Further information are given elsewhere [108, 109]. This method is used in this work to characterize the initial state for the films deposited by the modulated elemental reactant method (see chapter 10.2). The corresponding low angle $\theta$ - $2\theta$ scans were performed in Eugene using a Bruker AXS D8 Discover XRD System with Cu K$\alpha_1$ radiation.

## Atomic force microscopy (AFM)

The surface structure of a sample can be imaged by AFM in the nanoscale range. An atomic sharp tip on a cantilever is rastered over the sample. If the tip is coming close to the sample it interacts with the surface structure by distracting short range atomic forces. These forces yield a deflection of the cantilever, which can be detected optically by a laser together with a multi-section diode. The deflection is a measure for the surface topography. The tip is usually used without permanent contact to the sample to avoid damage of both. In this mode the cantilever is vibrating and the interaction with the sample yield a change in oscillation frequency (tapping mode$^{TM}$). The achieved resolution is mainly determined by the sharpness of the tip and the force constant of the cantilever. Further information can be found elsewhere [116, 117, 105]. In this work an AFM of the type DI Dimension 3000 was used in the constant force tapping mode. The used tips NCH-W were fabricated by the Nanoworld company. Their force constant is about $42\,\mathrm{N/m}$ and the tip radius below $8\,\mathrm{nm}$. The Software Gwyddion was used for the data analysis, error correction and graphical revision [118]. To compare surfaces quantitatively, the so called rms-roughness (root-mean-squared roughness) can be determined. This value is the standard deviation from the mean surface height and counts therefore for both, elevations and depressions (e.g. surface cracks). Furthermore the mean surface height was set to zero, which results in a negative sign for surface depressions and positive sign for elevations.

## Differential scanning calorimetry (DSC)

DSC is a method for the thermal analysis of a sample and information about characteristic temperatures (e.g. crystallization temperatures, melting point), transition and reaction enthalpies, thermal stability, specific heat, etc. can be determined. The DSC system consists of a heat bath with furnace, two contact area and a sensor system. The sample material and a reference material are put in special pans, which were placed on the contact area. The contact areas are connected to a thermoelectric disc with high thermal conductivity. Thermocouples for each pan are mounted on the bottom side of the disc and can be used in combination with the disc itself to measure the temperature difference between sample and reference side and also the individual absolute temperatures of each side. The detected temperature difference can be converted to the corresponding heat flow through the disc after a calibration of the system. The setup is now heated with constant heating rate. Heat from the sample and from the reference is conducted through the disc and the heat flow between both pans can be measured. Since both materials got heated in the same way, the heat flow is usually zero. However if the sample undergoes a transition or reaction at a specific temperature, additional heat is produced or absorbed and a heat flow between both pans can be detected and related to the occurring process. Further information are given in literature [119, 120, 121, 122].
The measurements have been performed in Eugene with a Netzsch DSC 200 system. The used pans consist of Al and were weighted ($\sim$22 g) before performing the measurements to correct mass differences between sample pan and reference pan. The reference pan was used empty. The heat procedure was performed in $N_2$ atmosphere with a heating rate of 10 K/min.

## Secondary neutral mass spectroscopy (SNMS)

SNMS is a method to analyze the elemental depth profile of a sample. The sample surface is sputtered by bombardment with $Ar^+$ ions of low energy in the range of 100 eV and therefore only particles from a very narrow depth region are ejected. Most of these particles are neutrals, which are post-ionized afterwards. This can be done for instance by an interaction with the electrons of a rf-plasma. Finally the post-ionized particles can be detected by using a mass spectrometer and the elemental concentration in the sample can be given in dependence of the sample depth if the sputter rate is known. The achievable depth resolution is in the nanometer range.
There are several advantages of SNMS compared to the more common method secondary ion mass spectroscopy (SIMS). The lower energy usable for sputtering eliminates shadowing effects and preferential sputtering. Furthermore the separation of the ejection process of the particles from the ionization process avoids matrix effects occurring for SIMS. Additionally the ionization in the plasma is non selective to the

element species and finally a quite linear relationship between measured intensities and elemental concentration with large depth resolution is obtained. Further details of the SNMS method can be found elsewhere [123, 124, 125].

The measurements were performed by G. Katona in cooperation with the Group of Prof. D. Beke from the Department of Solid State Physics of the University of Debrecen. The measured system was an INA-X system of Specs GmbH Berlin. $Ar^+$ ions were extracted from a rf-Ar plasma and an ion energy of $100\,eV$ was used. For the post-ionization a rf-plasma is used in the system. The small energy together with the high lateral homogeneity of the ion current results in this system in a depth resolution of $2\,nm$ and a detection limit of 10 ppm.

## Scanning electron microscopy (SEM) and transmission electron microscopy (TEM)

SEM and TEM are microscopy methods based on electron beams. The lower wavelength of electrons compared to light results in a much higher resolution compared to optical microscopes.

The SEM is using an electron beam, which is rastered above the surface. Several processes occur due to the interaction with the sample, for instance backscattering of electrons or the generation of secondary electrons, X - rays and Auger electrons. Each process delivers different information about the rastered surface points and thus the surface topography, crystal structure or the elemental distribution in the sample can be investigated with spatial resolution [126, 127, 105]. In this work SEM was only used for EBSD investigation, which will be introduced latter.

In case of TEM the sample is measured in transmission and a direct image of the sample is produced. The samples have to be very thin and the corresponding preparation is relatively laborious. If the electrons pass the sample they were scattered and a contrast occurs due to scattering at different atoms or due to different sample thickness. If a crystalline sample is investigated, an additional contrast by diffraction can be observed. Furthermore the diffraction pattern of the electrons could be analyzed, which provides insights to the crystal structure and the phases, which can be found in the sample. Additional descriptions are given in literature [128, 129, 105]. The TEM study used in this work were performed by Z. Aabdin in cooperation with the group for "Elektronenmikroskopie und Angewandte Materialforschung" of Prof. O. Eibl at Universität Tübingen. The sample was prepared by making a sandwich with a Si dummy followed by cutting, grinding, polishing, and finally ion etching. The TEM of the type Zeiss 912$\Omega$ operated at $120\,kV$ was used. The shown energy-filtered bright and dark - field images (chapter 7.1.2, fig. 7.3) were acquired using an aperture of $750\,nm$ in size.

**Electron backscatter diffraction (EBSD)**

EBSD is an extension of the SEM and a scheme of the method is shown in fig. 5.1. The sample is rastered by the electron beam under relatively large incident angle. A smooth surface is required for applying this method. Some of the electrons of the incident beam get backscattered in the sample and are able to leave the sample afterwards. On their way through a crystalline sample the electrons get diffracted and interfere to the so-called Kikuchi pattern, which could be detected by a CCD camera. In that way information for each sample point can be collected, for instance if the investigated area is crystalline or amorphous, which crystalline phases contribute to the pattern and also the crystal orientation can be determined. The analysis of the Kikuchi pattern is usually done by computer software. Further information can be found in the review of F. J. Humphreys [130].

The measurements were performed at a the SEM Phillips Nano Nova by N. Jöhrmann in cooperation with the group for "Analytik an Festkörperoberflächen" of Prof. M. Hietschold at TU Chemnitz. The incident angle was 70°, the electron energy 15 keV, the detector a Nordlys II EBSD detector from HKL Technologies and the used Software was HKL Channel5 from Oxford Instruments [131].
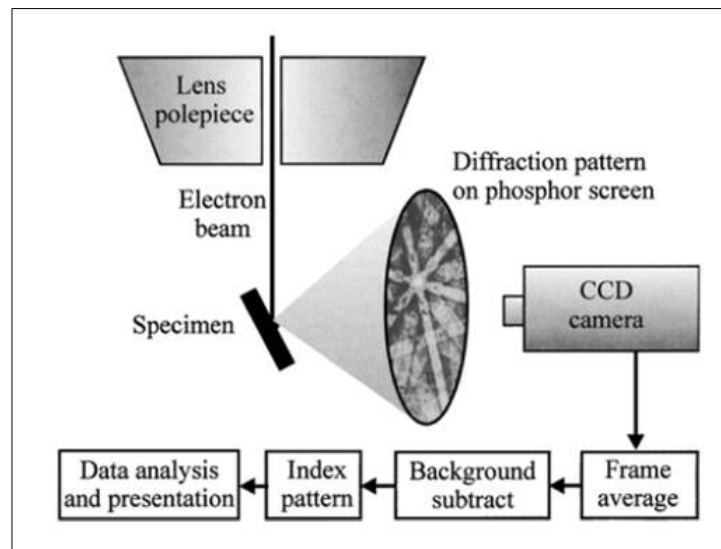


Figure 5.1: Scheme of electron backscatter diffraction (EBSD). [130]

## 5.2 Electric characterization: Resistivity and Hall measurements using van der Pauw geometry

For measuring the resistivity $\rho = 1/\sigma$ and the Hall constant $R_H$ a home-made room temperature setup based on the van der Pauw method and a cryostat with a home-made van der Pauw measurement rod for low temperature measurements was available. For the van der Pauw method four point contacts A, B, C, and D have to be made close to the edges of the film as shown in fig. 5.2.
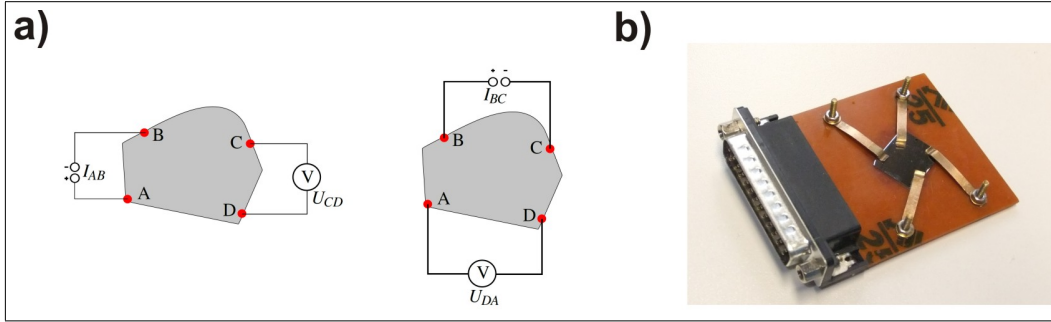


Figure 5.2: a) Scheme of the van der Pauw measurements for two different configurations. The contacts have to be made at the sample edges and the sample shape can be arbitrary. b) The sample holder of the home-made van der Pauw room temperature setup. The contacts are made by four CuBe springs.

If the sample is homogeneous, continuous without holes, and exhibits a constant thickness, the shape of the sample can be neglected for the determination of the resistivity. Van der Pauw has shown, that for this case the following expression is valid:

$$\rho = \frac{\pi d}{\ln 2} \frac{R_{AB,CD} + R_{BC,DA}}{2} f. \tag{5.2}$$

$d$ is the film thickness, $f$ the geometrical correction factor and $R_{ij,kl}$ pseudo resistances achieved by applying a current between the neighboured contact points i and j and measuring the voltage between k and l:

$$R_{ij,kl} = \frac{U_{k,l}}{I_{i,j}}. \tag{5.3}$$

Equation 5.2 implies that the pseudo resistances have to be measured for different circuit configurations (permutations), which is demonstrated in fig. 5.2 (a). The geometrical correction $f$ factor is depending on the ratio of both pseudo resistances and should be nearly constant during the measurements.

This contact geometry can be also used for Hall measurements, however different circuit configurations are necessary. In that case the current $I$ is applied diagonal through the sample ($I_{AC}$ or $I_{BD}$). Additionally a magnetic field $B$ orthogonal to the sample has to be applied. Due to the Hall effect, a Hall voltage U$_H$ perpendicular to the current lines ($= U_{BD}$ or $U_{AC}$) is measured and the following relation can be shown:

$$U_H = R_H \frac{IB}{d}. \tag{5.4}$$

$R_H$ is called the Hall constant and is connected to the charge carrier density $n$ of the film. In a single band model with parabolic band and one type of charge carriers the simple expression can be found:

$$R_H = \frac{r_H}{nq} \sim \frac{1}{nq} \tag{5.5}$$

Here q is the charge of the charge carrier (e for electrons, -e for holes) and $r_h$ the Hall factor. $r_h$ is usually taken as unity, which is only valid for degenerated systems, or systems where the relaxation time is energy independent [40]. In non-degenerated systems with acoustic phonon scattering it is 1.93, for ionized impurity scattering 1.18. However, in this work usually $r_H$ equals 1 is used due to the large charge carrier densities observed for the deposited films. With equation 5.5 it is possible to determine the charge carrier density by Hall measurements. The conductivity $\sigma$ is further given by the expression

$$\sigma = 1/\rho = ne\mu, \tag{5.6}$$

which was already derived in chapter 3.1 in case of one dominant species of charge carriers. Thus the Hall mobility $\mu$ is extractable from measurements of $R_H$ and $\rho$. These simple expressions are unfortunately in most cases not valid and only effective values averaging over charge carriers with different effective mass, relaxation time and species (electron or hole) can be derived. Therefore the effective charge carrier density $n_{eff}$ and the effective mobility $\mu_{eff}$ will be used in this work. Equation 5.5 fails completely for bipolar conduction with comparable charge carrier density of electrons and holes, and has to be extended to

$$R_H = \frac{r_{H,p}n_p\mu_p^2 - r_{H,n}n_e\mu_n^2}{e(n_p\mu_p + n_n\mu_n)^2} \sim \frac{n_p\mu_p^2 - n_e\mu_n^2}{e(n_p\mu_p + n_n\mu_n)^2}. \tag{5.7}$$

$R_H$ becomes dependent on the ratio of the mobilities of both carrier species. Furthermore equation 5.6 has to be also corrected to

$$\sigma = n_n e\mu_n + n_p e\mu_p. \tag{5.8}$$

In general the interpretation of the results of the electric measurements is complicated. Not only a single type of holes and a single type of electrons might contribute. In multivalley band structures both carrier types can exhibit different effective masses and relaxation times themselves. In that case also several bands could contribute to the conduction process. Furthermore a parabolic band is usually not observed, which gives rise to a change of the effective mass with larger excitation energies. Additionally not only one scattering mechanism dominates, but rather a combination of different ones depending also on the temperature regime of the measurements. In such complicated cases, the support of band structure calculations combined with the calculation of transport coefficients taking scattering into account is needed. Further information about the connection of the measured coefficients to the band structure, details about the performed Hall measurements, and the investigation of the contribution of different bands to the conduction process of $CoSb_3$ are described in the work of F. Timmermann [73].

**Room temperature van der Pauw setup**

The room temperature van der Pauw setup consist of a sample holder, where the contacts are made by four CuBe springs at the edge of the sample (see fig. 5.2 (b)). The different configurations needed for van der Pauw and Hall measurements are adjusted by a "Keithley 7001" switchbox with a "Keithley 7012" 4x10 matrix card. The current could be applied by a "Digistan BOP6-125MG" power supply, while the voltages were measured with a "Keithley 2000" multimeter. The necessary magnetic field was generated by two air cooled coils with Fe yoke. The sample holder was mounted in between with field perpendicular to the sample. The field could be varied between -1 T and +1 T. For the measurements the Hall voltage was measured during a magnetic field loop, while the applied current was kept constant. This procedure was repeated for different currents.

**Low temperature van der Pauw setup**

For the low temperature measurements in the range between 1.4 K and 300 K a Oxford Instruments $^4$He - cryostat was available. The sample can be cooled by pumping He through a needle valve from the He reservoir to an inner tube, which is surrounding the sample tube. The used measurement rod is situated in this sample tube. This arrangement is necessary to avoid direct contact of flowing gaseous or liquid He with the sample holder, which would yield a large sensitivity of the sample temperature on the He flow impeding an accurate temperature stabilization. The additional sample tube buffers the system. An heater close to the inner tube allows heating the sample up to 300 K and the corresponding temperature is measured by a Fe/Rh temperature resistance. For the temperature stabilization of the sample heating and cooling are performed simultaneously.

An existing home-made rod was used to determine resistivity and Hall constant at low temperatures. The rod provides an carbon glass temperature resistor to measure the temperature close to the sample and an additional heater to stabilize the temperature directly at the sample, which is necessary due to the buffering effect by the additional sample tube. The heater was controlled with a "Hameg HM8142" power supply. The different configurations needed for van der Pauw and Hall measurements are adjusted by a "Keithley 7001" switchbox with a "Keithley 7065" Hall effect card. The current could be applied by a "Keithley 236" source measure unit and the voltages were measured with a "Keithley 182" nanovoltmeter. The maximum perpendicular magnetic field provided by a superconducting magnet was 5 T.
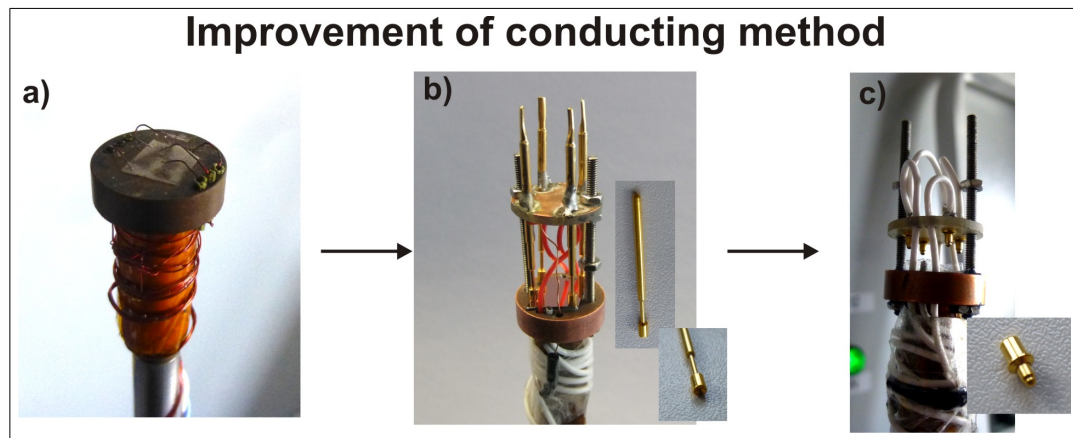


Figure 5.3: Contacting the skutterudite thin films was very challenging and the used method needed to be improved for achieving accurate results. a) Cu wires which were soldered to the sample with indium. b) spring loaded design with long dual pins, which yields contact jumps. c) This spring loaded design with short round pins was the best solution.

The sample contact with the Cu wires at the measurement head (see fig. 5.3 (a)) of the rod were first realized by soldering with indium or by using silver paste. Both methods did not work for skutterudite thin films. Indium sticks poorly on the film surface, which is also very sensitive to scratches. By using silver paste, the area around the contacts was torn out by cooling down, indicating also a low sticking between film and substrate. A possible influence of the silver paste solution on the film can not be excluded, even though only low amounts and different solutions were tried. Au/Cr contact pads made by a lithography process worked better, but turned out to be still not good enough for accurate Hall measurements. The design was therefore changed to a spring-loaded conducting method with different commercial

Au contact pins, which are consisting of two parts for an easy exchange of the actual pin with different contact probes (see fig. 5.3 (b)). With sharp probes many scratches occurred, while hollow semispheres were the most suitable probe design (insets fig. 5.3 (b)). However, this first measurement head with relatively long pins was finally exchanged by short pins with round probes, since the longer ones were sensitive to vibrations and contact jumps, which occurred quite regularly. The design is shown in fig. 5.3 (c) and is the best contact method achieved so far. No problems occur by cooling down and the geometry factor $f$ of the van der Pauw measurement is absolutely constant during the complete measurement.

The large charge carrier densities occurring in the measured films give rise to another difficulty. The Hall voltage exhibit values in the range of the thermal drift. Due to the interplay of the rod heater and the buffered outer heater it is not possible to stabilize the temperature by hand and a PID controller for the heating powers was programmed by LabView to keep the temperature during the measurement stable [132]. Two signals are therefore used: i) the measured temperature close to the sample and ii) the sample resistance [132]. Additionally the Hall curve is measured for each magnetic field in all 4 possible Hall configurations (current through both diagonals and in both current direction). By averaging all measurement offsets, small thermal drifts can be corrected. Details can be found in the work of F. Timmermann [73].

## 5.3 Thermoelectric characterization (Seebeck coefficient)

Within this work a low temperature Seebeck measurement rod for the existing cryostat and a room temperature setup was designed. The construction and the used measurement procedure are based on the work of E. Compans [133]. He introduced a concept, where two Cu blocks with integrated heater are separated by a slit. The sample is mounted with each side in thermal contact to a single Cu block overspanning the slit in between. If one of the Cu blocks is heated, a gradient evolves in the sample, mainly over the slit region. The created thermovoltage can be measured with contacts on each side of the sample and the temperature gradient simultaneously by using thermocouples. Afterwards the Seebeck coefficient can be calculated with equation 2.3.

Since this method is critical for eventually occurring offset voltages, a dynamical approach is used. For the measurements at room temperature one sample side is heated until a gradient of $2\,\mathrm{K}$ - $3\,\mathrm{K}$ is reached. Afterwards the thermovoltage and the temperature of each sample side is recorded during the relaxation back to room temperature. If the thermovoltage is now plotted over the temperature gradient, a linear curve is achieved and the occurring slope corresponds to the Seebeck coefficient (equation 2.3). Eventually occurring constant voltage offsets reveal no influence on
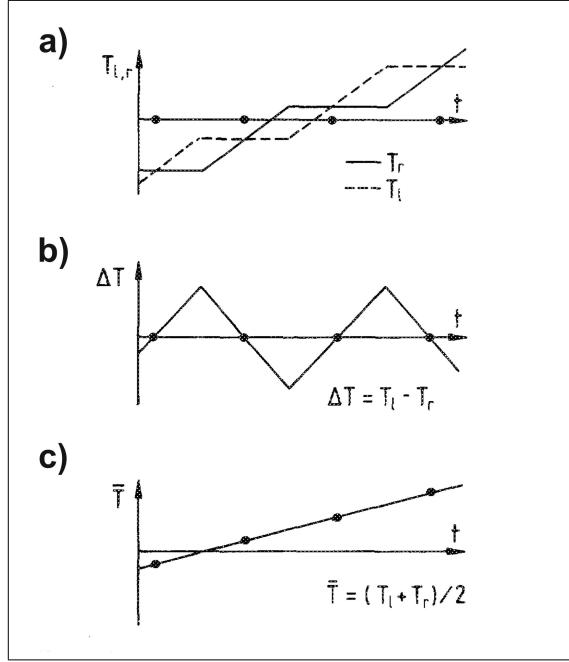
Figure 5.4: Ideal temperature evolution with time $t$ for the dynamical temperature dependent Seebeck measurement [133]. $T_l$ and $T_r$ are the temperatures of the left and right sample side, respectively. The temperature gradient is expressed as $\Delta T = T_l$ - $T_r$ and should vary alternately around zero. The average temperature $\bar{T} = (T_r + T_l)/2$ should linearly increase. The black dots mark the positions for which the Seebeck coefficients $S(\bar{T})$ are determined. For each $S(\bar{T})$ the measured data of the thermovoltage between two inflection points of $\Delta T$ is used.

the extracted value and yield only an offset of the complete curve. The contacting material has to be taken into account for the measurement of the thermovoltage according to equation 3.12.

For the low temperature setup this method can be also used. However, each desired measurement temperature has to be stabilized very accurately in that case, which is very challenging and time consuming. Therefore the procedure introduced in the work of E. Compans [133] is used. The principle is illustrated in fig. 5.4. In this approach first the left sample side ($T_l$) is heated and the temperature of the right sample side ($T_r$) is kept constant. Simultaneously the temperatures of each sample side and the thermovoltage is recorded. The heating process is continued until the desired gradient $\Delta T = T_l - T_r$ and the corresponding specific temperature $T_l$ of the left sample side is reached. Afterwards the temperature of the hot side is kept at this temperature $T_l$ and the heater of the right sample side is switched on until the

desired gradient is reached again, but with opposite sign (fig. 5.4 (a) and (b)). If the gradient exhibit the sign change, the thermovoltage $U_{Thermo}$ will change sign as well (delay due to offset voltages possible). Is $U_{Thermo}$ now plotted as function of $\Delta T$, the slope (derivation) of the curve can be determined and the Seebeck coefficients for the average temperature $\bar{T} = (T_l + T_r)/2$ can be extracted. Usually one value of the Seebeck coefficient is determined from all the data recorded during heating the left side ($T_l$) and one from the data obtained during heating the right one ($T_r$). The slope of the curve is therefore determined in all the points, for which the condition $T_l = T_r$ (or $\Delta T = 0$) is fulfilled, and thus the Seebeck coefficient can be given for the corresponding temperature. These points are marked in figure 5.4 as black dots. If this procedure is now periodically repeated (fig. 5.4 (a) and (b)), the average temperature is systematically increased (fig. 5.4 (c)) and the temperature dependence of the Seebeck coefficient can be investigated. Further information of the measurement methods to determine the Seebeck coefficient and the corresponding errors can be found in literature [134, 135, 136, 137]. It is to note, that according to equation 3.12 the contact material used to measure the thermovoltage has also to be taken into account. Only relative values can be measured and corrections are necessary. This will be discussed below.

**Room-temperature Seebeck measuring setup**

The room-temperature measuring setup was designed and built together with F. Timmermann and is shown in fig. 5.5 (a) and (b). It consists of a ground plate, where a larger aluminum block is mounted (left block in the figures). One insulated copper/constantan thermocouple is feed through it and fixed by thermal conductive and insulating glue. A stack consisting of a aluminum block, a Peltier element and another Al block (right side in the figures) is placed at a small distance forming the slit where the temperature gradient should arise. The Peltier element can be used to increase or decrease the temperature of this side. A second thermocouple is feed through this stack in the same way. The sample is mounted upside down but needs electric contact to the thermocouples.

The corresponding equivalent circuit is shown in fig. 5.5 (c). The thermocouples are used to measure the temperature of both sides of the sample ($\hat{=} U_{T1}/U_{T2}$ in the figure). Additionally the thermovoltage is measured in two ways over the appropriate legs of the thermocouples (first over the Cu wires of the left and the right thermocouples ($U_{Cu}$) and then over both constantan wires $U_{Ko}$). For both wire materials the Seebeck coefficients at room temperature are known (copper: 6.5 µV/K [139], constantan: -35 µV/K [139]), exhibiting opposite sign and can be corrected. Therefore absolute values of the Seebeck coefficient can be given and both have to reveal the same value within the error bars, which can be seen as cross check especially for small Seebeck coefficients of the sample.
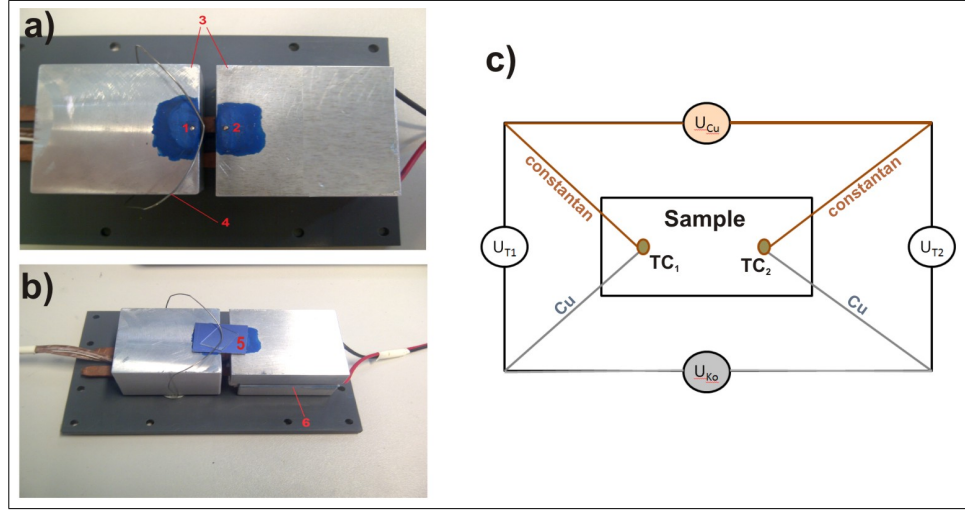
Figure 5.5: Room temperature Seebeck setup. a) Top view [138]: *1+2* copper/constantan thermocouple, *3* aluminum blocks, *4* spring for fixation of the samples. The blue regions are thermal conductive glue for insulating sample and aluminum blocks; b) Side view [138]: *5* sample, *6* Peltier element; c) Equivalent circuit of sample and thermocouples ($TC_1$ and $TC_2$). $U_{T1}$ and $U_{T2}$ are the thermovoltages of the thermocouples. $U_{Cu}/U_{Ko}$ is the thermovoltage of the sample measured either with the Cu wires or with the constantan wires of the thermocouples.

## Low-temperature Seebeck measuring rod

For the low-temperature measurements a new Seebeck measurement rod was constructed and designed within this work. The inner diameter of the sample tube (where the rod is introduced) is limited to 17 mm, which was also the limiting diameter of the designed low-temperature Seebeck measurement rod. The overall length of the rod with measurement head is about 1500 mm. The head design is based on the suggestion of E. Compans [133] and consists mainly of two sites separated by a slit as shown in figure 5.6.

The left side is connected to the rod and contains three sections (see fig. 5.6). A round section with small diameter is screwed to the rod and gives the opportunity to wrap the necessary cables and wires first to get them all on the same temperature and to store wires for eventually needed maintenance. It follows a more narrow round section with larger diameter. This section contains three special ceramic feed-throughs, each of them usable for 4 wires. These feed-throughs should bring the wires without stress to the sample and separate the wires geometrically. This section exhibits also the largest diameter along the rod and a cover shell surrounding the measurement head can be clipped over it. This shell should provide the guidance in the sample
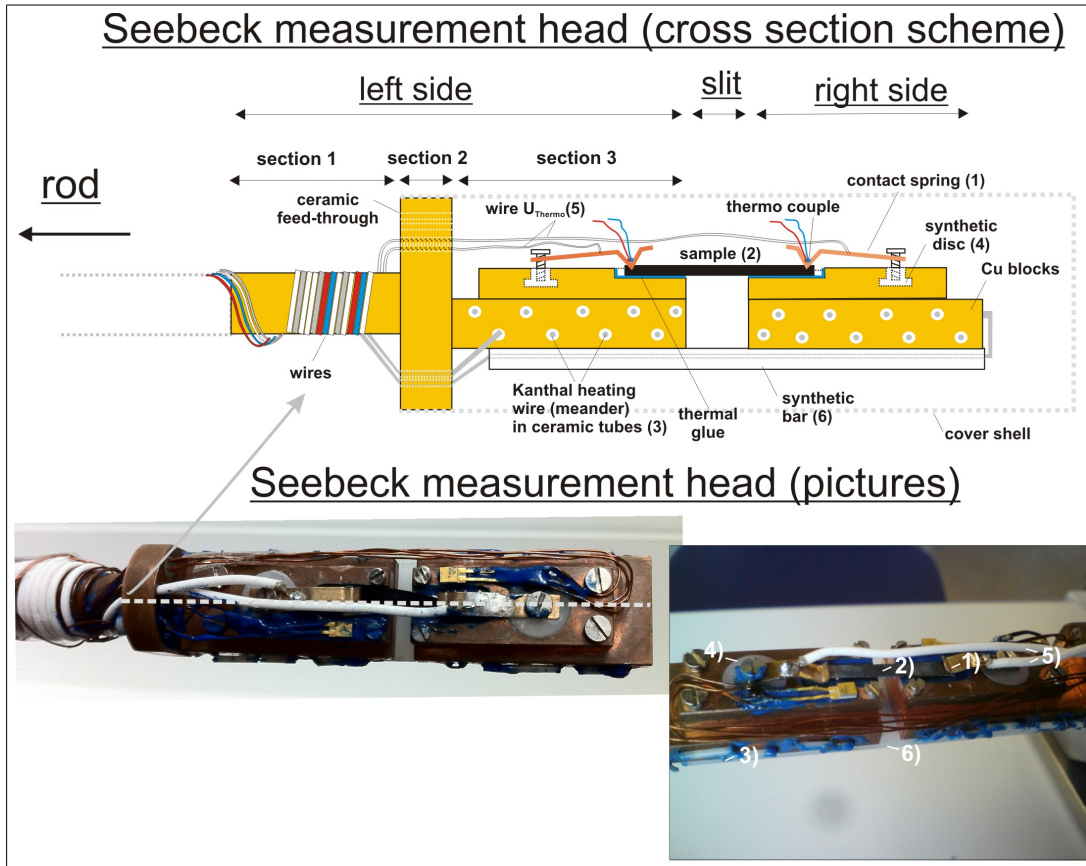
Figure 5.6: Low temperature rod for measurements of the Seebeck coefficient in the cryostat. Top: Scheme of the measurement head in cross section along the white dashed line marked in the bottom left picture. Bottom: Pictures of the measurement head. The added numbers correspond to the numbers used in the cross section scheme.

tube and a protection of the other parts from damage during the transfer into and out of the cryostat. The last section of the left side is a Cu block, which is drawn through meander-like by a Kanthal wire for heating (*3* in fig. 5.6). A smaller Cu block is mounted on top, which exhibits an indentation for the sample and serves as additional heat buffer. Heat conductive glue in the indentation isolates the sample from the Cu. The small block is partly replaced by a round synthetic disk containing a thread (*4*). Here a CuBe spring (*1*) can be fixed with a screw and is pressing on the sample to realize the electric contact to this sample side. The disk is made of synthetics to insulate spring and screw from the sample holder and the special shape

of the disk with two different diameters should avoid pulling out the disk by the forces caused by the spring and by thermal load. On top of the small Cu block, Si diodes (not marked in the figure)) were fixed by thermal glue to measure and control the temperature of both sample sites.

The right side of the sample holder is a copy of the third section of the left side and contains a large Cu block with heating wire, a small one with sample indentation, a synthetic disk with screw and a spring for conducting the other side of the sample. This right part is fixed to the left one by a thin synthetic bar (6) realizing the necessary slit for the temperature gradient between both parts. The thin synthetic material with low thermal conductivity decouples both sides of the measurement head thermally.

The sample (2) is placed for the measurements in the indentations of both Cu blocks overspanning the slit in between. This enables that each sample side can be heated separately by applying current through the Kanthal wire. The CuBe springs are pressed on the sample to give the electrical contact. Cu wires (5) soldered on top of the spring are used to measure the thermovoltage. The temperatures are measured by the Si diodes on the small Cu blocks. However it can be noted, that this position is not sufficient, since large temperature drops occur by the thermal glue between sample and block and additionally by the substrates [137]. Therefore thermocouples were additionally soldered on top of the springs, revealing much better agreement of measured temperature and real film temperature and providing both, a fast and durable way of mounting the sample [137]. The Seebeck coefficient was measured dynamically by an alternating and stepwise increase of the temperature of both sample sides as described above. To control this procedure a LabView program was written [135] and later extended by a proportional temperature controller to keep the unheated site constant in temperature [137]. The temperature of the "LakeShore DT-670B-SD" temperature diodes is measured with a "LakeShore 218 Temperature Monitor", the temperature of the thermocouples with a "Keithley 2000" multimeter and the thermovoltage with a "Keithley 182" nanovoltmeter. The current for the heater is supplied by a "Hameg HM8142" power supply.

Since the Seebeck coefficient of the measurement system (CuBe springs, screw, Cu wires...) is unknown and an additional temperature drop occurs due to the springs and the thermocouples, first Pb was investigated with the setup. The absolute Seebeck coefficient of Pb is well reported in literature [140] and the measured data of unknown materials can be corrected. It is therefore assumed that the contact area and contact pressure of the spring is always comparable and so the corresponding interface heat resistant. The recorded data were finally analyzed by a home-made program using LabView [135], which extracts the Seebeck coefficient for all temperatures, for which both sample sides are at the same temperature (see above).

## 5.4 Thermal characterization methods

### Time resolved X-ray diffraction (TRXRD)

TRXRD is a pump-probe experiment and can be used to investigate the temperature evolution in a sample. An ultrashort laser pulse heats the sample and the following relaxation with the corresponding change of the lattice constant can be measured as time dependent peak shift by XRD. Further discussions of the measurement principle and the achieved results are shown in chapter 11.

The measurements were performed at the beamline ID09B of the European Synchrotron Radiation Facility (ESRF) in Grenoble together with Dr. A. Plech from the Institute for Photon Science and Synchrotron Radiation(IPS)/Karlsruher Institut für Technologien (KIT). The laser was a fs-regenerative Ti:sapphire amplifier with 1 kHz repetition rate and a pulse length of 2 ps. The spot size was 450 µm and the pulse energy 10 mJ - 500 mJ. The used synchrotron radiation was pulsed by a chopper and the energy of 15 keV was filtered by a Si(111) monochromator. The X-ray pulses were synchronized with the laser pulses. The diffracted X-rays were detected by a scintillator together with a CCD camera (Frelon). It was measured in $\theta$ - $2\theta$ geometry with an incident angle of 10°. Further information can be found elsewhere [141].

### Asynchronous optical sampling (ASOPS)

ASOPS is an optical pump and probe method for characterizing the acoustic modes in a material and can be used to extract the speed of sound. Furthermore reflection of phonons at the interfaces can be investigated and information about phonon scattering can be extracted. The underlying principle of ASOPS is explained in more detail in chapter 11 and elsewhere [142, 143]. The measurements were performed by Chuan He in cooperation with the group "Moderne Optik und Photonik" of Prof. T. Dekorsy from the Universität Konstanz. Two mode-locked Ti:sapphire femtosecond lasers were used, which are operating at a repetition rate of ∼800 MHz. The frequency offset in the repetition rate of both laser was stabilized at 5 kHz and allows scans in a measurement window of ∼1.25 ns. The used wavelength is 790 nm for the pump and 820 nm for the probe laser. The nominal pulse length of both lasers is ∼50 fs. A collinear reflection geometry is chosen and it was measured in focus with a spot size of ∼2 µm.

### Raman spectroscopy

Raman spectroscopy is used to investigate the vibrational states of molecules or of solids. The sample is therefore irradiated with monochromatic laser light in the ultraviolet or in the visible range. The light is scattered in the sample and the detected light coming from the sample has two contributions [144]. The first contribution occurs due to Rayleigh scattering and has the same frequency $\nu_0$ as the initial light. If a

vibrational mode with the eigenfrequency $\nu_m$ is excited or annihilated in the sample, light with a frequency $\nu_0 - \nu_m$ or $\nu_0 + \nu_m$ can be detected. The second contribution are therefore lines with a frequency shift. The lines occurring at lower frequency are called Stoke lines and those ones with larger frequency anti-Stoke lines. Since the extractable information is equal for both, usually the Stoke lines are analyzed, since they exhibit the larger intensity [144]. Not all vibrational modes in a molecule or solid are Raman active. This is only the case if the vibration mode is polarizable [144]. How large the oscillation frequency is depends mainly on the bond (force constant) between the oscillating atoms and on their mass. Furthermore different vibrational modes exhibit different symmetries, which could be used to classify the modes with respect to their symmetry. The different classes ($E_g$, $F_g$ and $A_g$ modes) reveal different response to different polarization of the incident light, which can be used to achieve further information from the measured Raman spectra about the occurring vibrational modes. An extended discussion about the basics of Raman spectroscopy can be found in "Introductory Raman Spectroscopy" written by Ferraro, Nakamoto and Brown [144].

The measurements were performed together with Dr. O. D. Gordan and G. Tofighi in cooperation with the group for "Halbleiterphysik" of Prof. D. R. T. Zahn of TU Chemnitz. In the performed experiment, a Horiba LabRam HR800 confocal micro Raman system was used with a green laser of $532\,\mathrm{nm}$ wavelength and a power of around $2\,\mathrm{mW}$. It was measured in resonance (checked by ellipsometry) and with selection rules. The notation VV is thereby used for parallel and HV for perpendicular polarization.

# 6 Deposition of skutterudite thin films

## 6.1 Deposition chamber and deposition parameters

Most of the films were deposited in a ultra high vacuum (UHV) chamber for molecular beam epitaxy (MBE), equipped with a load lock, a transfer system to handle several samples and the main deposition chamber with a base pressure between $5 \cdot 10^{-11}$ mbar and $5 \cdot 10^{-10}$ mbar.

The used substrates (4" wafer or pieces) were first introduced in the load lock and baked at $200\,^\circ\mathrm{C}$ to remove water contamination. After reaching a pressure of $1 \cdot 10^{-8}$ mbar the samples were transfered to the manipulator in the deposition chamber. The main chamber is equipped with an electron beam evaporator for the evaporation of Co and three effusion cells for Sb, Fe and Yb. The flux of Co can be controlled instantaneously by an optical detector (via electron induced emission spectroscopy, EIES, see details in [105]), which was calibrated by depositing a Co film with a specific nominal thickness. The real thickness was afterwards investigated by RBS and the tooling factor determined. The deposition rates of Sb, Fe and Yb can be controlled by the temperature of the effusion cells. For calibration, three films of each element were deposited at different temperatures for a deposition time of $10\,\mathrm{min}$. Afterwards the thickness of each film was investigated by RBS allowing the calculation of the rate. By plotting the rates as function of the cell temperature, an exponential calibration curve is achieved.

The film composition of alloys can be controlled by adjusting the individual fluxes for codeposition (as described in chapter 6.2 and 6.3) or by adjusting the individual layer thicknesses for the modulated elemental reactant method (ch. 6.2 and 6.3). The Sb flux, which is the largest one, was chosen always smaller than $1.2\,\mathrm{\AA/s}$ (see ch. 7.1.3). To ensure homogeneous films, the sample holder is rotated during the deposition, which was verified by RBS. There are no detectable differences in thickness for Co and Sb over the entire area of the 4" wafers, however Fe reveals an decrease of thickness towards the edge of the wafer. Therefore the composition of Fe containing films has to be verified for each individual piece broken from the wafer. Furthermore a chamber wall cooling system prevents the film from contamination due to warmed-up side walls. For depositions at elevated substrate temperatures, the manipulator provides the possibility to heat the substrate from the backside of the sample holder up to $1000\,^\circ\mathrm{C}$. The temperature is also measured at the backside, which yields a difference compared to the real temperature on the substrate surface.

Additionally the MBE chamber was used for annealing under UHV conditions by using the sample heater of the manipulator. In most cases, the films were therefore deposited on wafers and afterwards shortly exposed to air for breaking the initial samples into pieces. Then pieces of different samples were mounted on a sample holder and reintroduced to the load lock. After reaching a proper pressure without baking, the samples were transfered from the load lock to the main chamber. The annealing process is therefore also performed in UHV by heating from the backside using a heating rate of $10 \, \text{K/min}$.

## 6.2 Deposition methods

In this work three different deposition approaches were performed to prepare skutterudite thin films:

- Codeposition of Co and Sb at elevated substrate temperatures

- Codeposition of Co/Fe and Sb on non-heated substrates followed by post-annealing

- Modulated elemental reactant method (layer by layer on non-heated substrate)

Details of the execution of this deposition methods will be discussed below. Since most of the results are valid for both transition metals Co and Fe, they are replaced by the more general expression $T$. The most important features of each method are also summarized in fig. 6.1 and the structural properties of the $TSb_3$ films achieved by the individual methods will be discussed in chapter 7.

### Codeposition at elevated temperatures

The codeposition of T-Sb films (with T = Fe or Co) at elevated temperatures is the fastest of the three approaches, since only a single step is needed. For this method the substrate is heated with a ramp of $10 \, \text{K/min}$ to a temperature above the crystallization temperature. The elements were afterwards deposited in parallel. To form $T_x Sb_y$ films with a ratio of T:Sb $= \frac{x}{y}$, the necessary T flux $\phi_T$ for a given Sb flux $\phi_{Sb}$ is calculated by:

$$\phi_T = \phi_{Sb} \frac{\rho_{Sb} M_T}{\rho_T M_{Sb}} \frac{x}{y}. \tag{6.1}$$

$\rho_i$ and $M_i$ is is the density and the atomic mass of the different elements. The film thickness is adjusted by the deposition time. Due to the heated substrate, the atoms have enough energy to diffuse on the surface and the film can crystallize already during the deposition (see 6.1, left column).
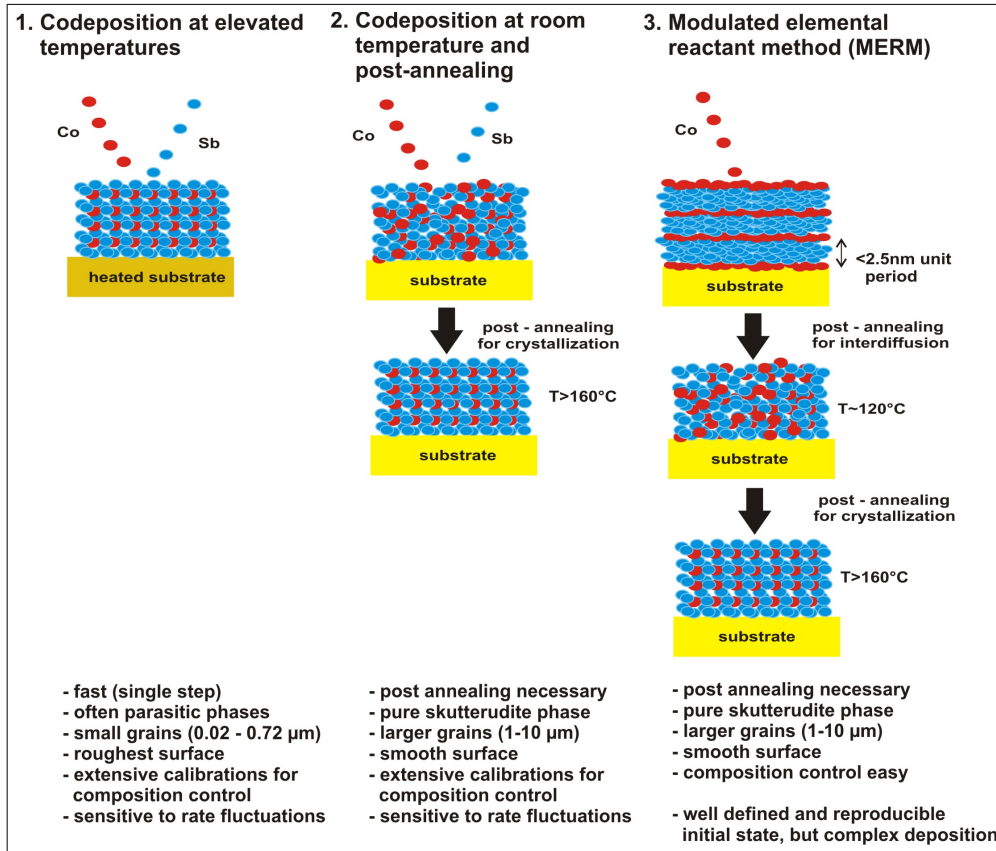
Figure 6.1: Overview of the used approaches for the deposition of skutterudite $TSb_3$ thin films. Exemplarily the synthesis of $CoSb_3$ is shown. Only method 2 and 3 should yield the metastable $FeSb_3$ skutterudite phase.

For the deposition of $CoSb_3$, the composition has to be adjusted accurately to the stoichiometric Sb content of 75 at.%. If deviations occur more stable phases will additionally form, since the $CoSb_3$ skutterudite phase has no homogeneity area in the phase diagram (see figure 4.11). This is a big disadvantage, especially in case of fluctuations of the fluxes during deposition.

It is to note, that it should not be possible to deposit a $FeSb_3$ skutterudite films at elevated temperatures, since this phase is metastable and the more stable $FeSb_2$ and Sb phases are expected to form due to the larger diffusion rate at the sample surface at higher temperatures (see fig. 4.13).

## Codeposition on non-heated substrates followed by post-annealing

With this approach the elements are codeposited at room temperature. The necessary fluxes for a desired composition are calculated with equation 6.1 and the film thickness is controlled by the deposition time. However, due to the non-heated substrate, the deposited films are amorphous and a further post-annealing step is necessary to get crystalline films. This is illustrated in the middle column of figure 6.1. XRD investigations reveal an amorphous structure for the films grown at room temperature, while TEM gives indications for a nanocrystalline structure [105]. The following post-annealing process is performed in UHV and the temperature is usually increased with a ramp of $10\,\mathrm{K/min}$ until the final temperature is reached. This temperature is kept for one hour. To obtain comparable crystallinity, the annealing temperatures need to be chosen always larger than the substrate temperatures used for the codeposition at elevated temperatures. The atoms get only embedded during the deposition at room temperature and to activate diffusion processes or to overcome existing bond or attraction forces during annealing, a higher energy is needed [105]. However the as-deposited initial state is exactly the advantage of this approach. The absence of diffusion processes during deposition results in this preordered state with locally bound atoms and a composition, which is everywhere close to the atomic ratio T:Sb of 1:3. This is supporting the skutterudite phase formation during annealing. Small fluctuations can be compensated by diffusion during the annealing process and should have a lower influence than for the codeposition at elevated temperatures, where deviation would immediately yield the formation of other phases. Thus this method might be also suitable for the stabilization of the metastable $FeSb_3$ skutterudite. Therefore it is important, that the local ordering (or the nanocrystallinity) of the as-deposited films is not connected with the creation of nucleation sites for more stable parasitic phases. The stabilization of $FeSb_3$ films via codeposition can be realized as will be shown in detail in chapter 7.2.

## Modulated elemental reactant method

The modulated elemental reactant method (MERM) was first introduced for skutterudite systems by Johnson et al. [95, 97]. For this approach the elements were deposited layer by layer on non-heated substrates. Double layer units, consisting of a T layer and a Sb layer with specific thickness ratio, are deposited alternately until the desired film thickness is reached. This amorphous initial state is a well defined starting point. After the deposition process, an annealing step is also necessary for this method to achieve crystalline films. It is believed that the multilayer structure of this T-Sb system mix first homogeneously by interdiffusion and the crystallization occurs afterwards (see fig. 6.1, right column) [97]. To guarantee a homogeneous mixing, the T/Sb unit thickness has to be thinner than a critical thickness, otherwise

composition gradients will form, which give rise to the formation of parasitic phases. A critical thickness between 2.5 nm and 3.5 nm is reported in literature [97, 145].

Due to the large amount of individual layers, the deposition process for the MERM method is rather complex and it is limited to room temperature to avoid interdiffusion during deposition. However, the advantages of this method are the well defined initial state and an easier way to control the composition by changing the layer thicknesses of a specific element, especially if complex skutterudites with several elements should be formed. For instance, $CoSb_3$ might be filled with two different filling ions and the charge carrier density should be controlled by doping due to substitution of Co with Fe ($=Y_{z1}Yb_{z2}(Fe_xCo_{1-x}Sb_3)_4$), thus five elements have to be deposited in parallel. To realize a good composition control and reproducible results, the MERM method should work much better than other deposition approaches. Additionally the synthesis of gradient films as demonstrated in chapter 12.2 is more simple to realize. It is further to note, that the MERM method is the only method reported so far in literature to achieve the $FeSb_3$ phase [97, 103].

## 6.3 Composition control of skutterudite films

The deposition of $TSb_3$ skutterudite films with the correct stoichiometry and a mass fraction of impurity phases smaller than 5% is challenging. One reason is the non-existence of a homogeneity area in the phase diagram for the investigated skutterudite phases $CoSb_3$ and $FeSb_3$ (fig. 4.11 and 4.13). The $TSb_2$ phases are the more stable phase. The second reason are the difficulties given by the very high vapour pressure of Sb and its low sticking coefficient. For depositions of elemental Sb on Si(100) at moderate temperatures like 300 °C, there is for example only one monolayer of Sb stable [146]. Therefore several aspects have to be considered for achieving skutterudite films with a desired composition.

### Composition control for codepositions

After calibrating the individual T and Sb flux (see chapter 6.1), both fluxes were adjusted by using equation 6.1 to achieve the desired stoichiometry. For the codeposition of Sb and T at room temperature, stoichiometries with a higher Sb content than the nominal one were achieved (fig. 6.2 (a)). This can be explained by the low sticking coefficient of Sb and/or its high desorption rate in case of the deposition of elemental Sb. In presence of the transition metal T either the sticking coefficient could be increased or the desorption rate decreased [105]. An ordering process like the observed nanocrystallinity (s. ch. 6.2) or a cluster formation could be therefore an explanation for a larger Sb content. Due to the ordering a larger number of Sb atoms can be bound instantaneously. In literature it is for instance discussed, that the triantimonide phase has a larger sticking coefficient than elemental Sb [94].
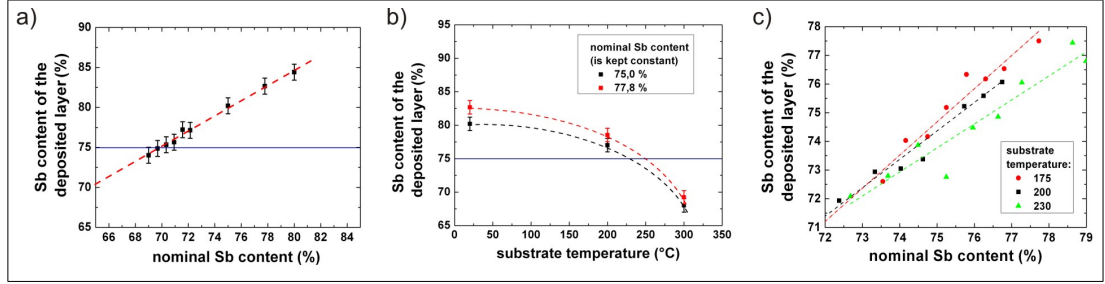
Figure 6.2: a) The Sb content of a Co-Sb film deposited at room temperature is higher than the nominal Sb content. It is to note that the Sb sticking coefficient is different for a codeposition of Co and Sb in parallel than for a deposition of elemental Sb alone. b) The Sb content of the films after deposition at different substrate temperatures. The rates of Co and Sb were kept constant. c) Change of the linear slope of the calibration curves by using different substrate temperatures.

The best procedure found to reach the correct stoichiometry was therefore to deposit at least three $TSb_y$ films with different Sb content $y$. The corresponding relationship of the nominal Sb content and the achieved one is almost linear, as shown in fig. 6.2 (a), and can be further used as calibration curve for future depositions [105]. This procedure has to be performed for each deposition temperature, since the sticking coefficient of Sb is further decreased with substrate temperature or the desorption rate of Sb strongly increased [105]. Caylor et al. explained this by a lower sticking coefficient of Sb [94]. They claim that Sb shows the tendency to form in the vapour additionally to monoatomic Sb, molecular $Sb_2$ and $Sb_4$ clusters, which exhibit a lower adsorbing probability for larger substrate temperatures than monoatomic Sb. Fig. 6.2 (b) shows, how the Sb content in the deposited films is decreased by increasing the substrate temperature during deposition, even though the Sb flux and the T flux (here Co) were kept constant. This effect changes the slopes of the linear calibration curves (fig. 6.2 (c)) and makes it necessary to perform the calibration for each temperature.

Similar effects have to be taken into account for the annealing process of samples grown at room temperature [105]. During the annealing, Sb is gassing out of the films and the Sb content decreases (s. fig. 6.3 (a)). For a moderate annealing temperature below 500 °C, the observed Sb loss is larger for films with a strong excess of Sb in comparison to the stoichiometric value of 75 at.%. The higher the annealing temperature the stronger is the Sb loss. For a Sb content close to 75 at.% no change can be detected within the error of RBS measurements [105]. Therefore it is a good starting point to deposit films with a small excess of Sb in comparison to the desired 75 at.% Sb and anneal the films afterwards. The composition will finally reach a Sb content very close to 75 at.%.
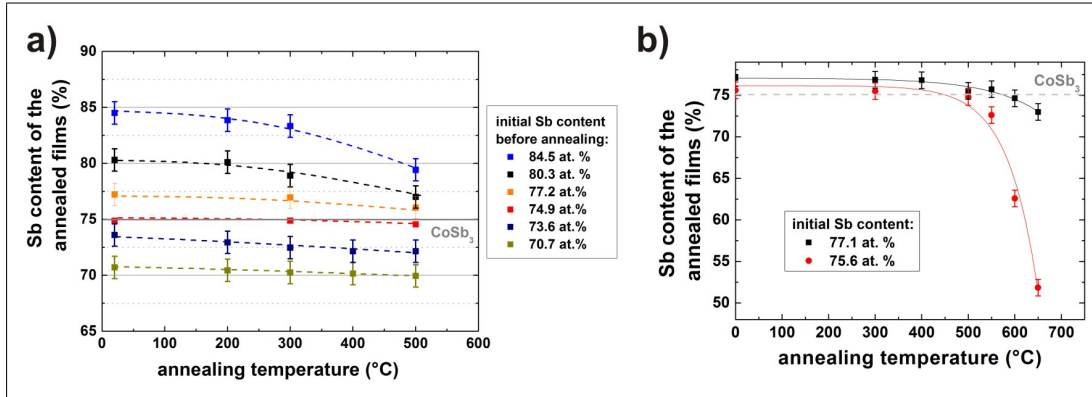
Figure 6.3: a) Sb content of Co-Sb films after annealing at different temperatures. The effect is stronger for higher initial Sb contents. b) Detailed analysis for higher temperatures than 500 °C for a sample with 75 at.% Sb and one with 77 at.% [147]. The sample with the excess Sb is thermally more stable

This work was further extended to temperatures above 500 °C for a film series with a Sb content of 75 at.% and one with 77 at.% [147]. In fig. 6.3 (b) the decrease of the Sb content of these films due to Sb evaporation is shown. Both curves agree nicely to exponential fits. Therefore the decrease of Sb can be related to the exponential character of the Sb vapour pressure with temperature, which was also observed by Durand et al. for pulsed laser deposition deposited films [148]. The decrease in Sb content is especially at larger temperature much weaker for the series with little Sb excess, which could be an indication that films of the other series are less thermally stable and start to decompose. This was confirmed by the XRD investigations presented in chapter 7.1.2. To conclude, a small excess of Sb in the initial films should be used to prepare post-annealed skutterudite films, which are stable up to 500 °C.

### Composition control for the MERM deposition method

The MERM deposition method provides an relatively easy way to control the composition compared to codepositions. For the MERM the composition is adjusted by the ratio of the individual thicknesses of the T and the Sb layer. It is to note that the MERM deposition is performed in a different high vacuum evaporation chamber with a base pressure of $10^{-6}$ mbar to $10^{-7}$ mbar and without wall cooling. Co and Fe were deposited by an electron beam evaporator, Sb by an effusion cell. Thickness and rates were measured in this chamber by quartz balances, that are positioned half way to the substrate.

The overall T-Sb double layer unit thickness was chosen as 1 nm. In case of T = Fe, the theoretical thickness of the Sb and Fe layer to achieve a composition of Fe:Sb = 1:3 has to be 0.98 nm and 0.129 nm respectively. The composition of a Fe/Sb double layer unit was calibrated by variation of the Fe layer between 0.06 nm and 0.16 nm and keeping the Sb layer thickness constant at 0.98 nm. Thickness and composition of the deposited film were afterwards investigated by Electron Probe Micro Analysis (EPMA). The found calibrations of composition and thickness for a Fe-Sb double layer unit is shown in fig. 6.4 in dependence of the Fe layer thickness. The composition can be therefore adjusted by different layer thicknesses of the transition metal T, while the overall double layer unit thickness can be changed by varying the T and the Sb layer thickness and keeping their ratio equal. The T flux and Sb flux were chosen in a way that the corresponding shutter opening times to achieve the necessary layer thicknesses are still in a well controllable range. For a unit thickness of 1 nm and a composition of 75 at.% Sb, the T rate was $0.2\,\text{Å/s}$ and the Sb rate $(0.3\,\text{Å/s})$, which corresponds to shutter times of around 5 s and 40 s, respectively.
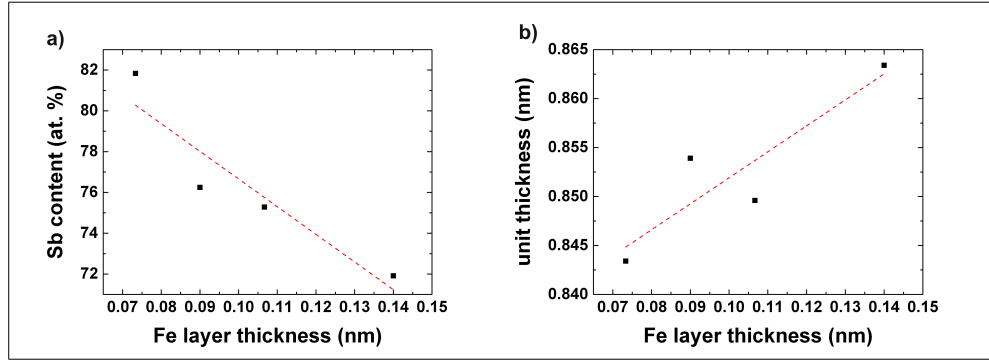


Figure 6.4: Calibration for a Fe/Sb double layer unit for MERM deposition of FeSb$_3$. The thickness of the Sb layer is kept constant, while the thickness of the Fe layer is varied. a) Overall Sb content in dependence of the Fe layer thickness; b) Fe/Sb unit thickness in dependence of the Fe layer thickness

# 7 Control of structural properties by the used deposition method

## 7.1 Structural properties of CoSb$_3$ thin films

### 7.1.1 Crystallization characteristics of CoSb$_3$ films

For the correct choice of proper deposition temperatures for the CoSb$_3$ films it is necessary to get insides how the film structure changes with increasing temperature starting from the amorphous phase. Therefore the crystallization process was investigated with differential scanning calorimetry (DSC). For this reason, a PMMA film was spin-coated on a Si wafer. Afterwards a Co-Sb film with a Sb content of 83 at.% and a thickness of 50 nm was deposited at room temperature on these wafers by the modulated elemental reactant method (double layer unit thickness 1 nm). By dissolving the PMMA layer in acetone, the deposited amorphous Co-Sb film can be lifted from the substrate and fished out. About 1.5 mg of the film is necessary for the DSC investigation. The measurement is performed under nitrogen atmosphere with a heating rate of 10 K/min. The sample was heated two times and the DSC voltage was measured. The second curve was subtracted from the first one to extract irreversible events.

In figure 7.1 (a) the measured difference curve for the Co-Sb sample is shown. The curve shows a very strong peak with a maximum at 161.4 °C and a small peak at around 300 °C. To clarify the origin of these transitions, pieces of the same sample without the PMMA layer were afterwards annealed in nitrogen atmosphere at specific temperatures below and above the DSC peaks. These temperatures are marked with the gray arrows in fig. 7.1 (a). The heating rate was chosen comparably to the DSC measurement and each sample was kept at the final temperature for 20 min. By measuring XRD of the annealed samples the peaks found by DSC can be related to the corresponding phase changes (s. fig. 7.1 (b)). The film annealed at 100 °C is amorphous. After annealing at 140 °C the CoSb$_3$ phase could be detected. Since the temperature measurement of the heating stage was less accurate, the peak at 160 °C can be related to the formation of the skutterudite phase. The observed crystallization temperature is in agreement to values given in the literature, which are in the range between 140 °C and 165 °C depending on the deposition technique [58, 93, 96]. The same phases are observed for films annealed at 180 °C and 250 °C. After annealing at 350 °C the Sb phase is found. Thus the broad peak observed in the DSC curve

at 300 °C can be attributed to the formation of the Sb phase, which can be explained with a relatively high Sb content of the investigated sample. It is unusual that the (012)-Sb main peak has the same intensity in the XRD pattern as the (003)-Sb peak. This indicates a preferred growth in (001) orientation (texture). After annealing at 450 °C only the Sb peaks corresponding to the (001) orientation are observed and they are sharper and more intense. Sb grows obviously with (001)-texture, which was observed in this work only for annealing in nitrogen but never in UHV.

The measurements show that the skutterudite phase crystallize at about 160 °C. This implies that the substrate temperature during the deposition or the temperature of the post annealing process has to be in the range of this value or larger to get crystalline films.
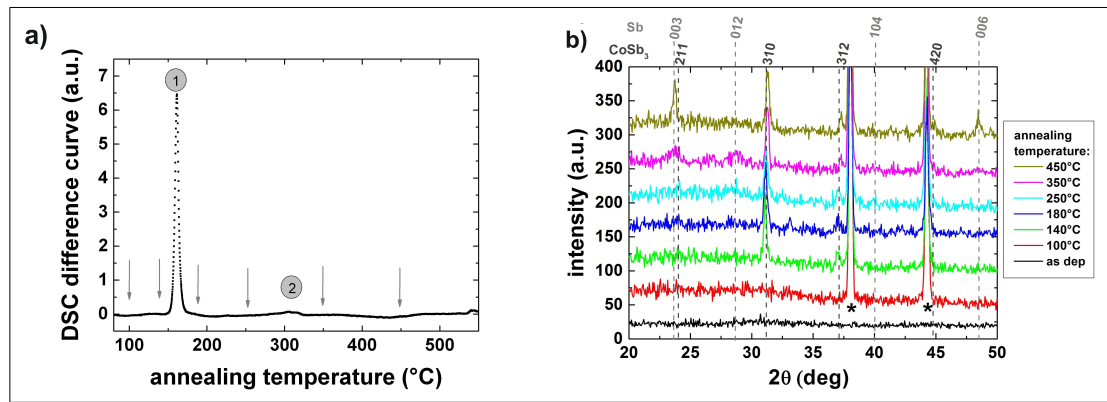


Figure 7.1: In (a) the DSC difference curve of a Co-Sb film deposited via the MERM method is shown. The initial Sb content was 82 at.%. The curve exhibit two exothermic crystallization processes (at 161.4 °C and around 300 °C). b) Similar samples were annealed at the temperatures marked with arrows. On these samples XRD was performed to clarify the origin of the exothermic processes. Peaks from sample holder are marked with asterisk.

### 7.1.2 Comparison of films deposited with different deposition methods

As described in chapter 6.2 three different deposition approaches were performed: (i) codeposition of Co and Sb at elevated substrate temperatures, (ii) codeposition of Co and Sb on non-heated substrates followed by post-annealing, and (iii) modulated elemental reactant method (layer-by-layer on non-heated substrates, s. fig. 6.1). The structural properties of the films prepared by applying these methods and the induced differences will be discussed in this chapter. It is to note that in the following "$CoSb_3$ films" is used as synonym for single phase Co-Sb films exhibiting the skutterudite phase, while the Sb content of these films is not necessarily 75 at.%.

**Structural properties of Co-Sb films deposited at elevated temperatures**

First the structural properties of films are discussed, which were prepared by code-position of Co and Sb on pre-heated substrates. If the substrate temperature is higher than 160 °C (crystallization temperature, ch. 7.1.1), the deposited films crystallize during the deposition and no further heat-treatment is necessary. In this study CoSb$_y$ films with different Sb content $y$ were deposited on SiO$_2$(100nm)/Si(100) substrates at three different substrate temperatures: 175 °C, 200 °C, and 230 °C. For larger temperatures the desorption rate of Sb gets too high (ch. 6.3).

| T$_S$ (°C) | Sb content (at.%) | | | | | | | |
|---|---|---|---|---|---|---|---|---|
| | 70-72 | 72 | 73 | 74 | 75 | 76 | 77 | 78 |
| 175 | amorph. | CoSb$_3$ | - | CoSb$_3$ | CoSb$_3$ | CoSb$_3$ | CoSb$_3$ | CoSb$_3$ +Sb |
| 200 | CoSb$_2$ | CoSb$_{2/3}$ | CoSb$_{2/3}$ +Sb | - | CoSb$_3$ | CoSb$_3$ | CoSb$_3$ | CoSb$_3$ (+Sb) |
| 230 | CoSb$_{2/3}$ | CoSb$_{2/3}$ | CoSb$_{2/3}$ +Sb | CoSb$_3$ | CoSb$_3$ | CoSb$_3$ | CoSb$_{2/3}$ +Sb | CoSb$_3$ +Sb |

Table 7.1: Phase formation of heated CoSb$_y$ films in dependence on the substrate temperature (T$_S$) during deposition and on the Sb content of the films. The Sb content was determined by RBS and the error is ±1 at.%. Due to the measurement position of the substrate temperature, the actual value are expected to be smaller than the given ones (ch. 6.1).

The films deposited at different substrate temperatures exhibit distinct differences with respect to impurity phase formation and grain size. The phase formation investigated by XRD is summarized in table 7.1. XRD reveals for films deposited at 175 °C only the skutterudite phase, if the Sb content is in the range between 72 at.% and 77 at.%. For higher Sb content the Sb phase was additionally detected. The CoSb$_2$ phase was present in none of these samples and the film with the lowest Sb content of 70 at.% was even amorphous. The temperature might not be high enough to activate the crystallization of this phase. However, to the best of my knowledge the crystallization temperature of the CoSb$_2$ phase was not yet reported in literature. Since single phase skutterudite films with a Sb content of 70 at.% are doubtful, the fraction of amorphous material in the samples is unknown and has to be checked by EBSD or TEM measurements to clarify the microstructure.

Films deposited at a substrate temperature of 200 °C reveal for a Sb content between 75 at.% and 77 at.% besides the skutterudite phase no impurity phases. This range

is narrower than for films deposited at 175 °C and also the $CoSb_2$ phase can be detected for Sb deficient films (<73 at.%) at this temperature. It is to note that neither films with a Sb content between 75 at.% and 73 at.% nor films with a Sb content larger than 78 at.% were investigated. Therefore the upper and lower limit for the formation of the skutterudite phase can not be given accurately, however the film with 77 at.% Sb shows already indications for the Sb phase. AFM studies reveal a considerable increase of roughness and the formation of large agglomerates on the surface, which is typical for the Sb phase formation (see ch. 8.1.1).

For a substrate temperature of 230 °C the situation is similar. The range, where only the skutterudite phase can be detected is even more narrow, mainly due to an augmented formation of the crystalline Sb phase. Here the single phase skutterudite films can be achieved between 73.5 at.% and 76 at.% Sb.

Further on, the lattice parameter of the single phase skutterudite films was extracted by analyzing the XRD peak positions but no change with substrate temperature could be found. The obtained lattice parameter has an average value of 9.010 Å and is smaller than the literature values of 9.032 Å/9.035 Å [93, 98].

One can conclude that the possibility to form impurity phases increases with higher substrate temperatures during deposition, which could be caused by two different processes. First, the larger temperature enables the formation of additional parasitic phases with larger crystallization temperature. Second, the surface mobility of the deposited atoms is larger for higher temperatures and the atoms could arrange themselves in a different configuration, forming clusters and finally crystallize in a more stable phase.

This second process has also an influence on the grain size, which was investigated by EBSD measurements. With increasing temperature the grain size decreases from 0.72 µm at 175 °C to 0.55 µm at 200 °C to <0.2 µm at 200 °C (s. fig. 7.2). This can
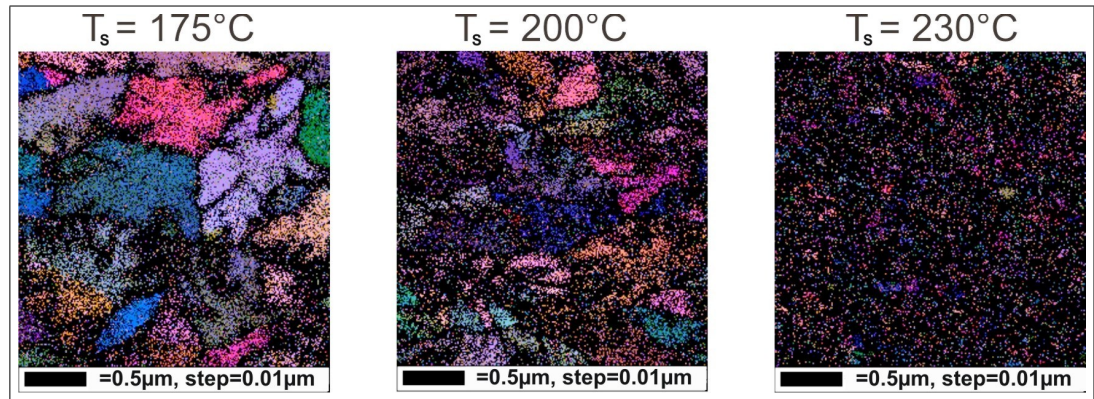


Figure 7.2: EBSD all Euler maps. The different colors indicate $CoSb_3$ grains with different orientations. The grain size decreases with increasing substrate temperature $T_S$ during deposition [149].

be explained again with the higher energy available for diffusion. Grain growth begins at a seed crystal and can proceed until two grains collide. The number of seed crystals, from where grain growth starts, increases with temperature and therefore a growing grain collides earlier with a neighboured one, which causes smaller grain sizes [149]. Since the grain size of the samples deposited at 230 °C was beyond the resolution of the EBSD measurements, a cross plane TEM investigation was performed and is shown in fig. 7.3. In the bright field image (BF) the CoSb$_3$ film with a thickness of around 30 nm and the corresponding grain boundaries can be seen. The grains, which correspond to specific diffraction reflexes, are brightened in the performed dark-field images (DF). By sizing up the lateral dimension of such a grain, a grain size of about 20 nm is determined. In the shown TEM images it is visible, that the individual grains form pillars from the bottom to the top of the film. The
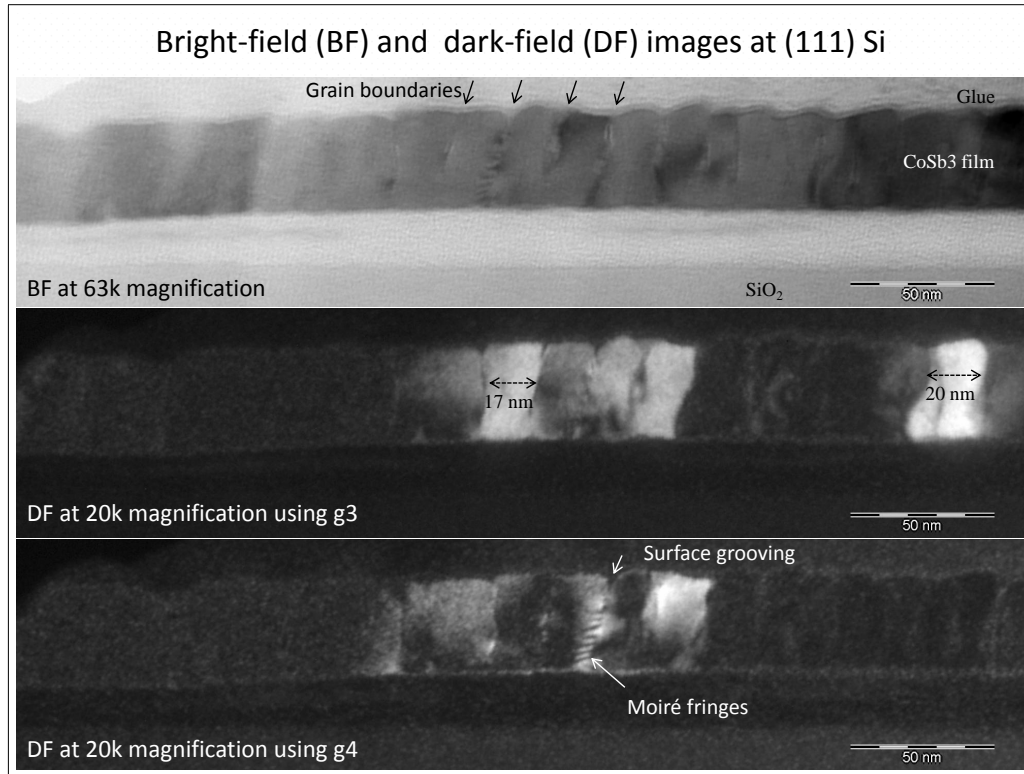


Figure 7.3: Cross-plane TEM images of a CoSb$_3$ film deposited at 230 °C. The bright field image (BF) shows the CoSb$_3$ film with a thickness of about 30 nm. With the dark-field image (DF) individual grains with different orientations are lighted. g3 and g4 correspond to different reflexes in the diffraction pattern of the CoSb$_3$ film.

cross plane grain size is therefore equivalent to the film thickness. This is supported by the XRD measurements, where the FWHM of the observed peaks is constant for all deposition temperatures indicating a constant cross plane grain size. It is to note that the difference in lateral grain size can not be investigated by a peak analysis in $\theta$ - $2\theta$ XRD scans. One has to perform $\omega$ scans (rocking curves) to achieve information about the different in-plane grain sizes.

A controllable grain size by changing the deposition temperature could be a key feature for the optimization of the thermoelectric properties, since especially the thermal conductivity should strongly depend on the grain size due to enhanced grain boundary scattering of phonons, if the grain size becomes the same order of magnitude as the phonon mean free path (see chapter 2.2). However, measurements of the thermal conductivity to prove this dependency were not yet performed.

If the grain size reaches the order of the electron mean free paths of this material (usually smaller than 50 nm, [150, 151]) the electric conductivity will be decreased as well. This effect can not be verified for the investigated films, since even small composition changes posses also a large influence on the electric conductivity (s. chapter 8.1.1). The resistivity values are in the range between 0.3 mΩcm and 92 mΩcm. A clear dependence on the deposition temperature was not observed.

Additionally, it was found by AFM that the average rms roughness increases with deposition temperature from 1.2 nm at 175 °C to 2.48 nm at 200 °C to 5.27 nm at 200 °C. Further details can be seen in chapter 8.1.1 and in figure 8.1. It is to note that these values are considerably larger compared to post-annealed films.

## Structural properties of post-annealed Co-Sb films deposited at room temperature

The second approach to form $CoSb_3$ thin films is to perform a codeposition at room temperature followed by a post-annealing step. Knowledge about the film properties after annealing in UHV at different temperatures provides important information about the stability at high temperatures, phase formation, and finally the maximum possible working temperature of these films before decomposition occurs. The as-deposited films are amorphous (XRD) and crystallize not until the following annealing process (see chapter 6.2), which is the main difference in comparison to the deposition at elevated temperatures and results in changed structural properties.

The phase formation of films deposited with this approach on $SiO_2(100nm)/Si(100)$ is less sensitive on composition changes and is summarized in table 7.2. The formation of the skutterudite phase without any impurity phases is found in a very broad composition range between 75 at.% and 82 at.% Sb [105], where a little excess of Sb is favourable. Therefore it is easier to get single phase films with this method, since the composition has not to be controlled that accurately. The reason for that (less diffusion, preordering) was already explained in chapter 6.2

| Annealing | Sb content (at.%) | | | | | | |
|---|---|---|---|---|---|---|---|
| temp. (°C) | 71 | 73 | 75 | 77 | 80 | 82 | 84 |
| 200 | CoSb$_3$ +CoSb$_2$ | CoSb$_3$ +CoSb$_2$ | CoSb$_3$ | CoSb$_3$ | CoSb$_3$ | CoSb$_3$ | CoSb$_3$ +Sb |
| 300 | CoSb$_3$ +CoSb$_2$ | CoSb$_3$ +CoSb$_2$ | CoSb$_3$ | CoSb$_3$ | CoSb$_3$ | CoSb$_3$ | CoSb$_3$ +Sb |
| 500 | CoSb$_3$ +CoSb$_2$ | CoSb$_3$ +CoSb$_2$ | CoSb$_3$ | CoSb$_3$ | CoSb$_3$ | CoSb$_3$ +Sb | CoSb$_3$ +Sb |

Table 7.2: Phase formation of UHV annealed CoSb$_y$ films in dependence on annealing temperature and Sb content. The Sb content was determined by RBS after the annealing process and the corresponding error is ±1 at.%.

In fig. 7.4 the XRD scans of a film series with a initial Sb content of 75 at.% and one with 77 at.% are shown, for which different post-annealing temperatures were investigated. The skutterudite phase is observed for both films already at an annealing temperature of 200 °C, which is in agreement to the work of Anno et al. [91] and to the obtained crystallization temperature of 161.4 °C (ch. 7.1.1).

The series with initially 75 at.% Sb shows no significant changes of peak positions or FWHM between 200 °C and 550 °C. The extracted lattice parameter is 9.0057 Å and the cross-plane grain size corresponds to the film thickness similar to the films deposited at elevated temperatures. Different grain sizes could therefore only occur in the in-plane direction. At 550 °C a shift to lower angles is observed. This could be an indication for the onset of the decomposition of the CoSb$_3$ skutterudite phase into CoSb and Sb and is supported by the fact, that the CoSb phase is indeed detected in the XRD scans of films annealed at higher temperatures. These films exhibit many small agglomerates at the surface as shown in fig. 7.5 for a film annealed at 600 °C, which might be attributed to the CoSb phase. The nascent Sb evaporates, which is the reason why no Sb phase is detected by XRD (marked in fig. 7.4 with asterisk). RBS measurements confirm these results. While the Sb content determined after annealing at 550 °C reveal 72.5 at.%, it is strongly decreased down to 62 at.% after annealing at 600 °C.

For the sample series with initially 80 at.% different results are obtained for low annealing temperatures. The peaks shift first towards higher angle with increasing annealing temperature, which corresponds to an decrease of the lattice constant. After annealing at 600 °C the same lattice constant is approached as found for the other sample series with 76 at.% Sb. This shift was already reported in former studies in case of Sb rich films [105] and occurs due to the evaporation of the excess of Sb and defect healing. However, it was not clarified, if distortion of the lattice due to the additional Sb or Sb incorporated in the voids of the structure causes the increased
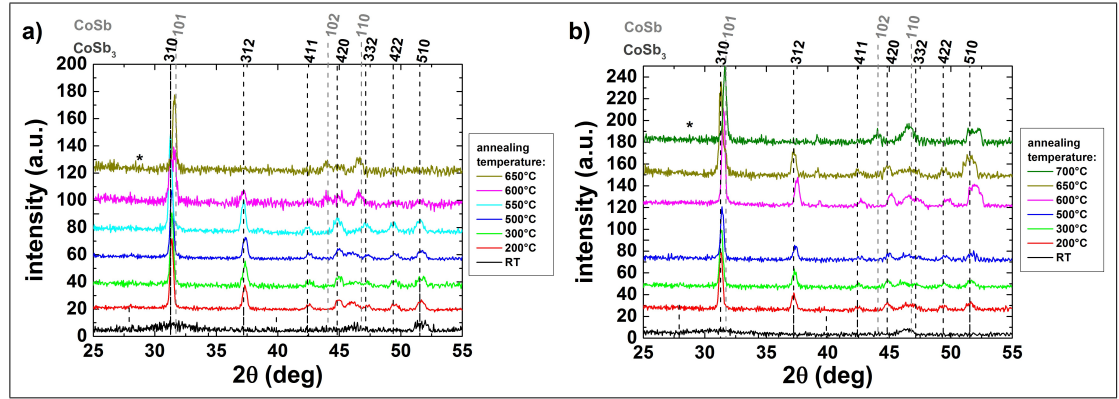
Figure 7.4: XRD scans of films deposited at room temperature and post-annealed at different temperatures. a) Films with initial Sb content of 75 at.% and b) films with initial Sb content of 77 at.%. The initial samples are amorphous. For high annealing temperatures decomposition of the $CoSb_3$ skutterudite phase into CoSb and Sb is observed. The position of the main peak of the Sb phase is marked with asterisk.

lattice constant. At higher annealing temperatures the additional Sb would leave its position and the lattice constant could approach the literature value. The same effect was found by Smalley et al. [95] for MERM deposited $CoSb_3$ thin films and by Schüpp et al. for sputtered films [58]. Smalley et al. explained the decrease of the lattice constant by healing of defects and claimed that the excess of Sb occupies for low temperatures first the voids in the structure. Schüpp et al. also explained the shift with Sb leaving the film. To get a better understanding XRD scans were performed at the synchrotron DESY in Hamburg and afterwards a Rietveld refinement was performed. In contrast to the work of Smalley et al. the refinement became worse by incorporation of Sb in the voids and their results could not be confirmed. However, due to the low film thickness the signal to noise ratio and the overall intensity is very low and little incorporation of Sb into the voids could not reliably refined.

A peak shift to lower angles and therefore the indication of a beginning decomposition occurs for this series not until 650 °C. The corresponding film has a Sb content of around 73 at.%, which agrees well with the value, where the decomposition starts for the other series. The CoSb phase is found for annealing temperatures of 650 °C or higher. Films with excess Sb seems to be more thermally stable. For both series the $CoSb_3$ phase is vanished completely for temperatures higher than 650 °C. The obtained decomposition temperature of both series lies between 550 °C and 650 °C and is therefore lower than the reported value for bulk samples (table 4.1), but in agreement to the range given in literature for thin films (475 °C - 610 °C) [58, 92]. Nevertheless, the obtained XRD results suggest that the general maximum working temperature should not exceed 500 °C.

In fig. 7.5 the typical surface structure of films with the skutterudite phase is shown for different annealing temperatures. The roughness of all films is comparably low and increases with higher annealing temperatures. The strongest increase is caused by cracks that form for annealing at temperatures larger than 300 °C. The films are deposited on SiO$_2$(100 nm)/Si(100) or glass substrates and the cracks are due to the mismatch of the thermal expansion coefficient of film and substrate. If decomposition occurs (600 °C or higher) the grains start to disaggregate into smaller units (agglomerates) and the films get discontinuous. It is believed that these smaller agglomerates correspond to the CoSb phase and the remaining large grains to the CoSb$_3$ phase (see fig. 7.5, 600 °C). These films were further investigated by TEM and EELS mapping was performed. With this method it could be revealed, that the Co:Sb ratio of the agglomerates is much larger than for the larger grains. Based on that, there is some confidence, that the agglomerates consist of CoSb grains.
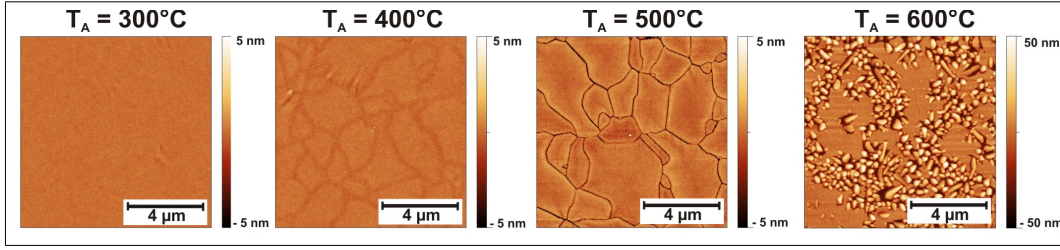


Figure 7.5: AFM study of typical surface structures of CoSb$_3$ films on SiO$_2$(100nm)/Si(100) substrate obtained after annealing at different annealing temperatures $T_A$ (300 °C to 600 °C). For an annealing temperature of 500 °C cracks develop due to thermal stress. Above 600 °C particles form due to decomposition processes.

In analogy to the previous chapter the grain size was investigated with EBSD. The SEM image with an overlaid EBSD image of a sample prepared on a glass substrate is shown in fig. 7.6. The film was annealed at 500 °C. Since different colors correspond to different crystal orientation, it is obvious that cracks occur exactly at the grain boundaries [152]. The grain size lies between 3 µm and 10 µm depending on the used substrate and the film composition. It is much larger than for films deposited at elevated temperatures (grains smaller than 1 µm, see last section). The large grain sizes are expected to yield a larger thermal conductivity, because of less grain boundary scattering of phonons. The annealing temperature has a weak influence on the grain size of the film. It was shown in another study, that the grains do not grow further at higher annealing temperatures [149]. The crystallization should be already finished during the ramping process, since a slow heating rate of 10 K/min was used in that case. Afterwards only defect healing and outgassing of Sb is observed.
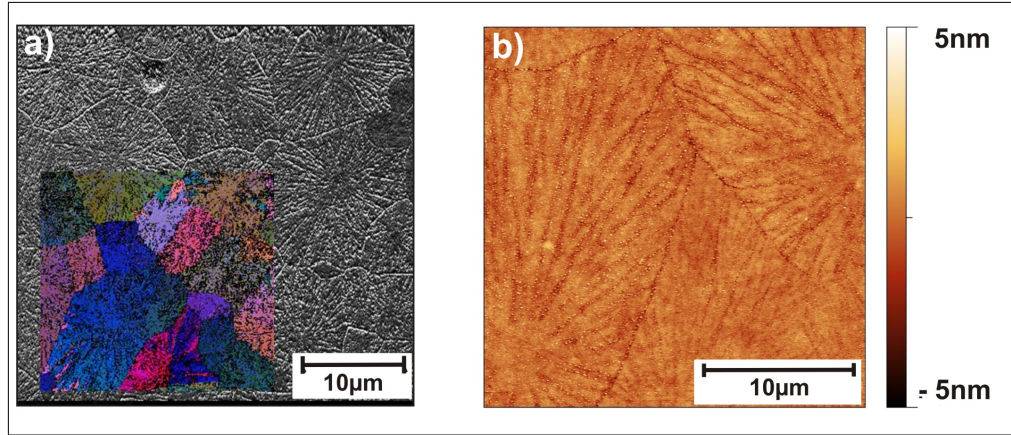
Figure 7.6: a) SEM with overlaid EBSD image of a CoSb$_3$ film annealed at 500 °C [152]. b) AFM image of the same film. The comparison shows, that the SEM contrast corresponds mainly to the surface topology.

Films annealed at different temperatures show a nearly exponential increase of resistivity with increasing annealing temperature, which is independent of composition. This could be due to a better crystal structure by healing of defects with higher temperature. Since the material is semiconducting where defects will dope the material, an increase in resistivity is expected for this case [95]. Additionally the increased roughness, crack formation, or composition changes could also cause a higher resistivity. The resistivity values are between $1\,\mathrm{m\Omega cm}$ and $25\,\mathrm{m\Omega cm}$ and therefore smaller than for the films deposited at elevated temperatures. Additional information are given in chapter 8.1.2 and in the figures 8.7 and 8.8.

**Structural properties of Co-Sb films prepared by MERM**

CoSb$_y$ films with different composition were deposited on Si(100) with the modulated elemental reactant method (MERM) (see ch. 6.2 and 6.3) and afterwards annealed at 400 °C under nitrogen atmosphere. The chosen overall thickness of a Co/Sb double layer was $1\,\mathrm{nm}$. These films differ only slightly from films prepared by codeposition at room temperature followed by post-annealing and will therefore not discussed in detail here. The surface morphology and the grain sizes exhibit no significant differences and single phase skutterudite films could also be found for films with an excess of Sb compared to the stoichiometric 75 at.% of CoSb$_3$. Therefore the basic results found by Johnson et al. [95, 96] were reproduced. Noteworthy here is, that a Se contamination in the range of 1 at.% - 2 at.% was found in these films and it is believed, that the Se atoms occupy the Sb sites of the skutterudite host lattice (see chapter 10.2 and 12.2). An electrical characterization was therefore not performed.

### 7.1.3 Influence of different deposition parameters on the film properties

**Codeposited films on heated substrates with different deposition rate**

Two ways are described in chapter 4 to improve the intrinsic properties of skutterudites: (i) incorporation of guest ions to reduce the thermal conductivity or (ii) substitution of Co by Fe to control the charge carrier density. The realization of both approaches using codeposition of thin skutterudite films is challenging. As the filling fraction of guest ions or the substitution level of Co or Sb need to be controlled accurately, the rates of the incorporated elements need to be much lower than the rate used for Sb. For Yb as filling ion with an intended filling fraction of 10%, its deposition rate has to be ∼100 times smaller than for Sb. Typical MBE deposition rates are in the range of 1 Å/s, which results in a Yb rate of 0.01 Å/s. This value is at the limit of controllable rates. To investigate the influence of the deposition rate on the properties of CoSb$_3$ films two different Sb rates were investigated: 0.3 Å/s and 1.2 Å/s. The corresponding Co rates were calculated according to equation 6.1.
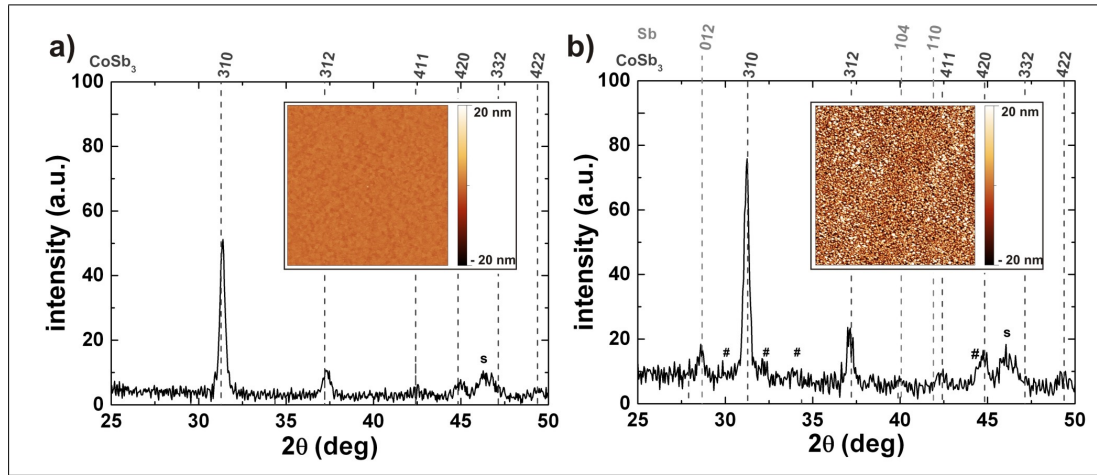


Figure 7.7: a) XRD (2$\theta$) scan for a Co-Sb film deposited with a low rate (Sb: 0.3 Å/s) and the corresponding (10x10) µm$^2$ AFM image. Only the skutterudite phase can be detected. b) The results for a film deposited with high rates (Sb: 1.2 Å/s), but same composition. The presence of the Sb and the CoSb$_2$ phase can clearly be seen. CoSb$_2$ is indicated with #, substrate peaks with s.

XRD (2$\theta$)-scans and AFM images of films deposited at 200 °C with those rates are compared in fig. 7.7. Both films have a Sb content of 77 at.% and the used substrate was SiO$_2$(100nm)/Si(100). The film deposited at 0.3 Å/s is very smooth and no impurity phases were observed by XRD. The films deposited with a Sb rate of 1.2 Å/s

75

show a very rough surface with an island like morphology and it was not possible to achieve films without impurity phases. Especially the formation of the Sb phase seems to be supported. There are two possible explanations for these results. The larger rates are achieved by increasing the temperature of the source materials, leading to incoming atoms with higher energy and thus a larger surface mobility, which might support a Sb cluster formation. Furthermore, the larger rate might lower the possible time for desorption of Sb atoms from the surface, these atoms get embedded and the Sb phase forms additionally.

The influence of the deposition rate on the phase formation is weaker for postannealed films. However, based on our experience, the formation of the Sb phase in post-annealed films is more often observed for higher Sb deposition rates.

To summarize, it is necessary to find a balance for the chosen deposition rates between good quality single phase films and a well reproducible and controllable rate of the fillers or dopands when the codeposition approach is used. Therefore all $CoSb_3$ films with Yb as incorporated filling ion (chaper 11) or films with substitution of Co by Fe (chaper 10) were deposited with a moderate Sb rate of $0.77\,\text{Å/s}$ or by the MERM method, for which the deposition rate has a much weaker influence on the phase formation. The binary skutterudite films were all deposited with a Sb rate of $0.3\,\text{Å/s}$ to obtain best-quality single phase films. Furthermore, the obtained results are important for using other deposition methods as sputtering or pulsed laser deposition (PLD), which are usually performed with higher rates and do basically introduce a larger amount of energy. Here the used rates and the introduced energy have to be kept as low as possible.

### Influence of annealing time on RT deposited films

For this study, which was performed together with the Master student M. Friedemann [147], a $CoSb_3$ film series with an initial Sb content of 75 at.% (within error bars) and one with a little bit excess of Sb (77 at.%) were codeposited at room temperature on a Si wafer with 100nm $SiO_2$ and afterwards post-annealed. Changes in the film properties by varying the annealing time were investigated. For an annealing temperature of $300\,^{\circ}C$, annealing times between $0.5\,h$ and $3\,h$ were chosen, while for $500\,^{\circ}C$ annealing times between $0.25\,h$ and $3\,h$ were applied. Since it was shown in chapter 6.3 and 7.1.2 that a small excess of Sb is favourable, the results are mainly discussed for the sample with 77 at.% Sb.

In fig. 7.8 the change of the Sb content due to annealing are shown for both annealing temperatures. The Sb content was determined by RBS after the annealing process. The films with excess Sb were annealed at $300\,^{\circ}C$ for different annealing times, however no change of the Sb content could be observed. For an annealing temperature of $500\,^{\circ}C$ there is a drop in the Sb content after a very short annealing procedure of $0.25\,h$ from 77 at.% to values about 75.5 at.%. For longer annealing times the Sb content does not decrease further and stays stable at this value. The samples with
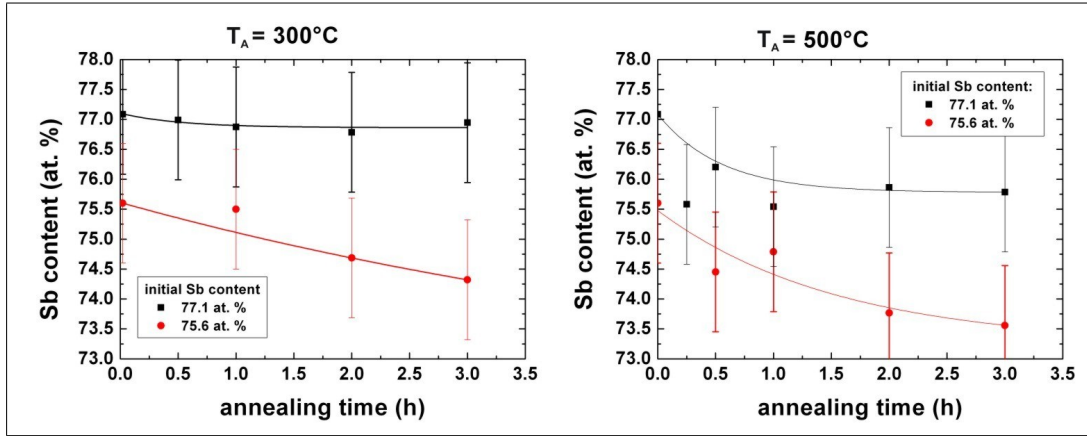
Figure 7.8: Sb loss due to the annealing process at 300 °C and 500 °C in dependence on annealing time [147]. The differences in composition are smaller for the sample with little bit higher Sb content. The shown lines are only guides to the eye.

a Sb content of 75 at.% confirm, that films without Sb excess are thermally less stable. The Sb content decreases continuously with annealing time for both annealing temperatures and no relaxation was observed.

The XRD investigation reveal the skutterudite phase with the same quality in all annealed samples, independent of annealing time or temperature (not shown).

The surface of the Sb rich films annealed at 300 °C (not shown) exhibit a flat surface without distinct changes compared to the initial samples. The rms roughness is in the range below 0.5 nm and for an annealing time of 2 h and 3 h a few cracks are observed. The films annealed at 500 °C have already after 15 min of annealing a plate like structure separated by pronounced cracks. The crack formation becomes slightly enhanced for longer annealing times (fig. 7.9). The lateral grain size can be indirectly estimated by AFM. Since it is known from EBSD measurements that one plate corresponds to one crystal grain, the change in lateral grain size with annealing time can be distinguished. Therefore the maximum possible distance was averaged for five grains and an average grain size of about 2.87 µm is determined. No systematic change with annealing time could be found. The main differences are observed at the grain boundaries. In fig. 7.9 an overview of the region around the cracks (grain boundaries) is shown in the AFM images. However, TEM investigations are required to get further insights on the underlying processes.

The AFM images of the films with 75 at.% Sb reveal no changes for films annealed at 300 °C, but the surfaces of the films annealed at 500 °C differ a lot in comparison to the films with Sb excess. In addition to the plate like structure a lot of particles are located on the surface. As an example, the AFM image of the film annealed at 500 °C for 2 h is added to fig. 7.9. The lateral grain size is with values up to 6.26 µm also much larger.
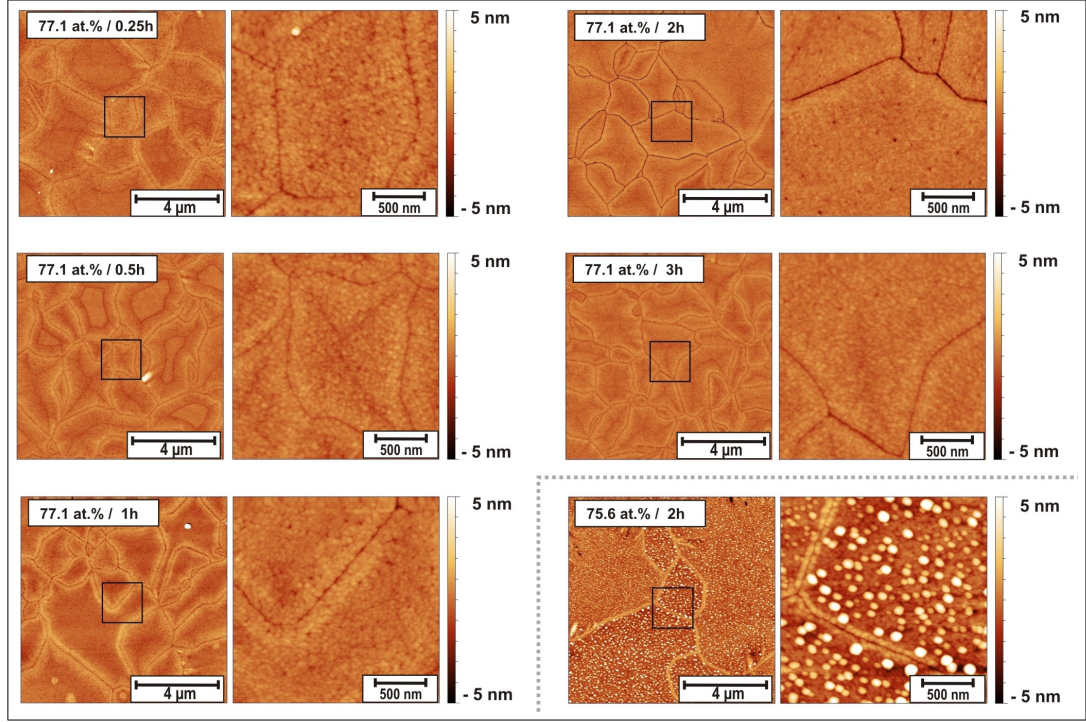
Figure 7.9: AFM images in dependence on the annealing time for CoSb$_3$ films with Sb excess (77 at.%) [147]. The annealing temperature was 500 °C. Additionally, one example is added for the series with lower Sb content (75 at.% Sb, annealing time 2 h).

The electrical properties are presented in fig. 7.10 and they are consistent with the structural properties. The resistivity of the Sb rich samples exhibits for an annealing temperature of 300 °C no dependence on annealing time. Annealing at 500 °C leads to an increase in resistivity with longer annealing times. But a relaxation of the resistivity to ∼30 mΩcm is indicated after 2 h. Since no change in composition and phase formation are detected for annealing times longer than 0.5 h, a healing of lattice defects or effects proceeding at the grain boundaries could be the origins. It is to note, that the data point for 1 h might be an artifact and need to be verified.

The resistivity of the films with 75 at.% Sb is also independent of annealing time when annealed at 300 °C, but the magnitude is larger compared to the films with Sb excess. This can be explained by the larger roughness of these films and the self-doping of the Sb rich samples caused by the additional Sb. The resistivity of the films (with 75 at.% Sb) annealed at 500 °C exhibit roughly a linear increase with annealing time. There is no saturation reached in the investigated annealing time range, which matches very well with the continuous change in Sb content observed by RBS.
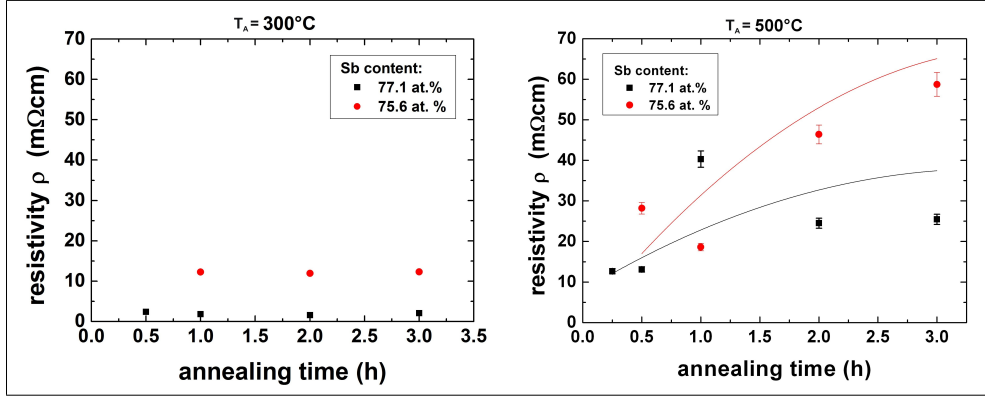
Figure 7.10: Resistivity changes obtained after annealing with various annealing times and temperatures [147]. For an annealing temperature $T_A$ of 300 °C no changes are observed. For 500 °C the resistivity of the Sb rich sample saturates after 2 h, while for the other sample no saturation is observed. The drawn lines are a guide to the eye.

To summarize, both samples show different characteristics after annealing with different annealing times. The Sb rich samples (77 at.%) reveal a large change in properties during the first half hour of annealing and after that the structural properties saturate. Only small changes in surface morphology at the grain boundaries can be found afterwards. For the samples with lower Sb content (75 at.%) no saturation of the investigated properties occur. Therefore it can be concluded, that an excess of Sb is needed to achieve CoSb$_3$ films with stable properties during temperature cycling, which is a requirement for a possible thermoelectric usage.

## 7.2 Structural properties of FeSb$_3$ thin films

Nearly all information given in chapter 7.1.2 for annealed or MERM synthesized CoSb$_3$ films are also valid for FeSb$_3$ films. The main difference for FeSb$_3$ is that the FeSb$_3$ skutterudite phase is a metastable phase (see fig. 4.13). Therefore it is only possible to achieve this phase by using non-equilibrium processes as thin film deposition techniques. The stabilization of FeSb$_3$ thin films was successfully achieved by Johnson et al. [97, 103] by using the modulated elemental reactant method (MERM, see ch. 6.2). In this work, it could be shown, that single phase FeSb$_3$ films can be also achieved by codeposition at room temperature followed by a post-annealing step (see ch. 7.2.2). This study was performed together with the Master student C. Schmidt [138]. In the following "FeSb$_3$ films" is used as short form for single phase Fe-Sb films exhibiting the skutterudite phase, while the exact composition might deviate.

### 7.2.1 Crystallization behaviour

Analog to chapter 7.1.1, the DSC method was used to characterize the phase formation of a MERM deposited Fe-Sb thin film with a Sb content of 76 at.% in dependence of the heating temperature. The measurement was performed in the same way as presented there for $CoSb_3$. The achieved DSC difference curve is shown in fig. 7.11. To relate the occurring peaks to the corresponding phase formation, XRD ($\theta/2\theta$) scans were performed and it could be shown that the first peak at $150.7\,°C$ belongs to the crystallization temperature of the $FeSb_3$ skutterudite phase, which is in rough agreement to literature (see table in fig. 4.12 (a)). In contrast to the DSC investigation of $CoSb_3$, two stronger and relatively broad peaks were found at about $300\,°C$ and $400\,°C$. At $300\,°C$ the skutterudite phase starts already to decompose and the formation of the Sb phase with a (001) texture is observed. The peak appearing at $2\theta \sim 32°$ could not be identified and might correspond to the (101) reflection of $FeSb_2$.
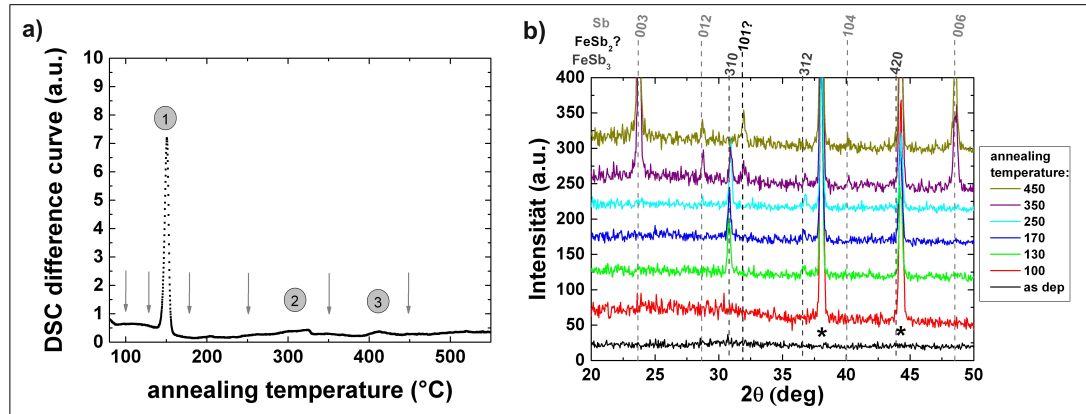


Figure 7.11: a) DSC curve of a Fe-Sb film deposited via MERM method at room temperature. The initial Sb content was 76 at.% Sb. The curve reveals three exothermic transition processes at $161\,°C$, $\sim300\,°C$ and $\sim400\,°C$. Similar samples were annealed at temperatures indicated by the arrows. b) Corresponding XRD ($\theta/2\theta$) scans of these samples. Substrate peaks are marked with asterisk.

However other reflections of this phase are not detected. The decomposition temperature is therefore much lower than for $CoSb_3$, since the phase is metastable and the energy needed to induce the decomposition into more stable phases is smaller than for $CoSb_3$. It is therefore necessary to keep the films below $300\,°C$ during annealing, which is also the maximum possible working temperature of the $FeSb_3$ films. An annealing temperature slightly smaller than $300\,°C$ were used for further investigations, since this value is suitable for achieving single phase films with good crystallinity

and a low number of defects. For temperatures larger than 400 °C only the Sb phase and the unknown phase can be detected by XRD. The FeSb$_3$ phase has completely vanished.

### 7.2.2 Structural properties of post-annealed Fe-Sb films prepared by codeposition

Based on the results shown in the last section, FeSb$_y$ films with a thickness of ∼40 nm were codeposited on SiO$_2$(100nm)/Si(100) at room temperature and afterwards annealed for one hour in UHV at the following annealing temperatures: 150 °C, 200 °C, 250 °C, and 300 °C. The composition of the Fe-Sb films was controlled as described in chapter 6.3.

| Annealing temp. (°C) | Sb content (at.%) | | | | | |
|---|---|---|---|---|---|---|
| | 70-71 | 72-73 | 74-75 | 76-77 | 78-79 | 80-81 |
| 150 | - | FeSb$_2$ | FeSb$_2$ | - | FeSb$_3$ | FeSb$_3$ - |
| 200 | - | FeSb$_2$ | FeSb$_3$+ FeSb$_2$ | FeSb$_3$ | FeSb$_3$ | - - |
| 250 | FeSb$_2$ | FeSb$_2$// FeSb$_2$+Sb | FeSb$_3$+ FeSb$_2$ | FeSb$_3$ | FeSb$_3$ | - |
| 300 | FeSb$_2$ | FeSb$_2$+Sb | FeSb$_3$+ FeSb$_2$ | FeSb$_3$ FeSb$_3$(+Sb) | - | - |

Table 7.3: Phase formation of annealed FeSb$_y$ films [138].

The phase formation of the codeposited films was investigated by XRD in dependence on the annealing temperature and on the Sb content of the films, which is summarized in table 7.3. Additionally obtained XRD scans for two film series with different initial composition (Sb content of 76 at.% and 78 at.%) are exemplarily shown in fig. 7.12 (a) and (b). The FeSb$_3$ skutterudite phase could only be found for a Sb content larger than 75 at.%. This is in agreement to the results found for CoSb$_3$ (see table 7.2) and to the literature [97].
While the initial films are amorphous, the skutterudite phase is already observed for films annealed at 150 °C as can be seen also for the Sb rich series (78 at.% Sb) in fig. 7.12 (b). This is fairly in agreement to the crystallization temperature of 150.7 °C found by DSC. For annealing temperatures of 150 °C, 200 °C and 250 °C, single phase skutterudite films were achieved in a Sb composition range between 76 at.% and 80 at.% as shown in table 7.2. The given upper limit corresponds for all annealing temperatures to the synthesized sample with the largest Sb content and
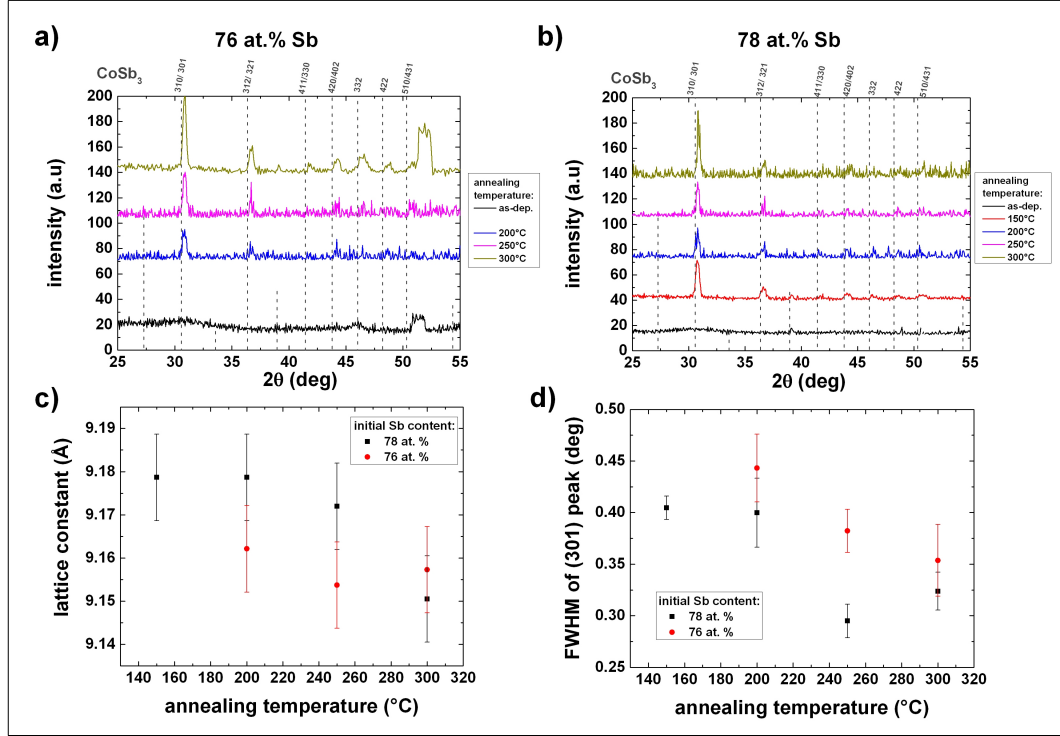
Figure 7.12: a,b) XRD ($\theta/2\theta$) scans of two FeSb$_3$ film series with different initial stoichiometry in dependence of the annealing temperatures. c) In both cases a shift of the (310) peak and thus a change in lattice constant is observed. d) Change of the full width half maximum (FWHM) of the (301) reflection for both series in dependence of the annealing temperature.

thus the onset where additionally the Sb phase is formed was not investigated. For an annealing temperature of 300 °C it was possible to get films with the skutterudite phase in the composition range between 76 at.% and 77 at.%. For 76 at.% single phase films were achieved, for 77 at.% also indications for the formation of the Sb phase are revealed. These results can be also seen in the scans of both series in fig. 7.12. The peaks occurring in the XRD scans of the annealed films can all be attributed to the skutterudite phase. Only the film with Sb excess annealed at 300 °C give additionally some indications for the Sb phase by an increased background around 28.7° ((012) reflex of Sb). Thus the range for the formation of single phase skutterudite might decrease with annealing temperature as also found for CoSb$_3$ films.

With increasing annealing temperature the peak positions are slightly shifted towards higher angles for both series. The corresponding change in lattice constant can be calculated by using equation 5.1 and is shown in fig. 7.12 (c). The change of lattice

constant for the series with 76 at.% Sb is within the error bars. For the films with higher Sb content a stronger decrease is observed and can be explained by healing of defects and Sb evaporation resulting in a relaxation towards the smaller equilibrium lattice constant as described in chapter 7.1.2 for CoSb$_3$. The better crystal quality is also indicated by the lowered FWHM shown in fig. 7.12 (d). The average lattice constant for films annealed at 300 °C is 9.15 Å and was extracted by using the (301) and (321) peak positions. This value is larger than the lattice constant of CoSb$_3$, as expected. However, it is smaller than the reported lattice constant of 9.2383 Å (see table in fig. 4.12 (a)), which is also in agreement to the discrepancy observed for the lattice constant of CoSb$_3$ compared to literature values. These differences could occur due to the different deposition methods, different purity of the used elements, different composition or annealing parameters. In the cited work the annealing was performed under nitrogen atmosphere at 137 °C [98]. Information about duration, ramping times and exact stoichiometry are not given.

The films are very smooth and the rms roughness is below 1 nm. The average roughness for all films annealed at 300 °C is 0.7 nm. This value is comparable to the CoSb$_3$ films annealed at similar temperatures. A systematic increase of roughness with annealing temperature is not found here, which is due to the relatively low annealing temperatures. If the skutterudite phase is formed, a fine grained surface structure can be found as shown in fig. 7.13 (a). In some cases the plate-like structures known from CoSb$_3$ are also obtained for FeSb$_3$ films after annealing at 300 °C (fig. 7.13 (b)). A grain size of 1.32 µm could be extracted from this image, which is in the same range as found for annealed CoSb$_3$ films.
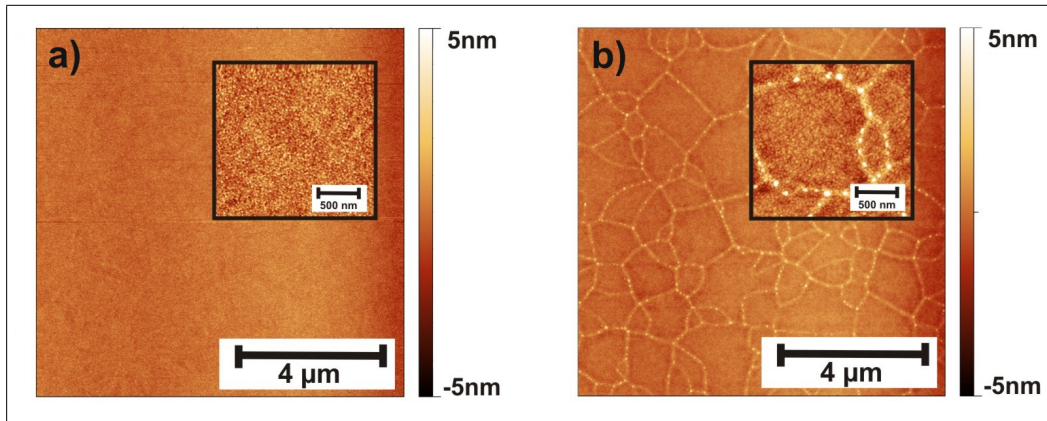


Figure 7.13: Typical surface morphology of FeSb$_3$ films investigated by AFM [138]. a) film annealed at 250 °C and a Sb content of 77.5 at.% and b) film annealed at 300 °C and a Sb content of 77 at.%.

The resistivity and the Seebeck coefficient do not change noteworthy with increasing annealing temperature, which is in contrast to the results found for $CoSb_3$. However, the resistivity values (average $0.8\,m\Omega cm$) are much smaller and the Seebeck coefficients (average $39\,\mu V/K$) are much larger than for the investigated $CoSb_3$ films. The thermoelectric properties will be discussed in detail in chapter 8.2.

To conclude, it was demonstrated for the first time, that single phase $FeSb_3$ films can be synthesized by codeposition. This implies, that eventually occurring preordering processes during the codeposition (which are excluded by using the MERM method) do not result in nucleation sites for the more stable impurity phases like $FeSb_2$. Single phase $FeSb_3$ films could be prepared, if a small excess of Sb is provided. Furthermore $FeSb_3$ films were also prepared in this study by using the MERM method. The structural properties of these films are similar and the basic results given in the literature [97, 103] could be reproduced.

### 7.2.3 Influence of the heating rate on the film properties

To investigate the influence of the heating rate on the structural properties, a $FeSb_3$ film with a Sb content of $(79 \pm 2)$ at.% was codeposited at room temperature on a Ohara "'S-TIH23'" special glass substrate ([153], see chapter 9) and broken into several pieces. Based on the results of chapter 7.2.2, an annealing temperature of $280\,^{\circ}C$ was chosen, since decomposition processes can not be excluded for higher temperatures. This annealing temperature was reached by using three different heating rates ($94\,K/min$, $10\,K/min$, and $3\,K/min$) and kept constant afterwards for $1\,h$. The medium rate of $10\,K/min$ is the standard heating rate usually used for annealing in this work.

The XRD investigation shows for all annealed samples the formation of the skutterudite phase. Minor phases were not detected, but the background caused by the glass substrate decreases the signal-to-noise ratio and thus the sensitivity for small amounts of impurity phases is also decreased.

The AFM images are similar for the different heating rates (fig. 7.14 top row). No cracks occur since the thermal expansion coefficients of film and substrate are in the same range (see chapter 9). The structures observed on the surface are also found on the blank substrates and caused by polishing. The different heating rates have therefore no visible influence on the film morphology.

To get information about the grain structure and grain sizes, EBSD was performed. The band contrast maps are presented in the bottom row of figure 7.14. Band contrast maps reveal a bright contrast for rastered points, where a crystalline structure is clearly observed, and a dark contrast for points, where no crystalline structure is detected (like amorphous regions or grain boundaries). The images are comparable to the EBSD images achieved for $CoSb_3$. No amorphous regions can be found and the grain boundaries exhibit a thickness smaller than $50\,nm$.
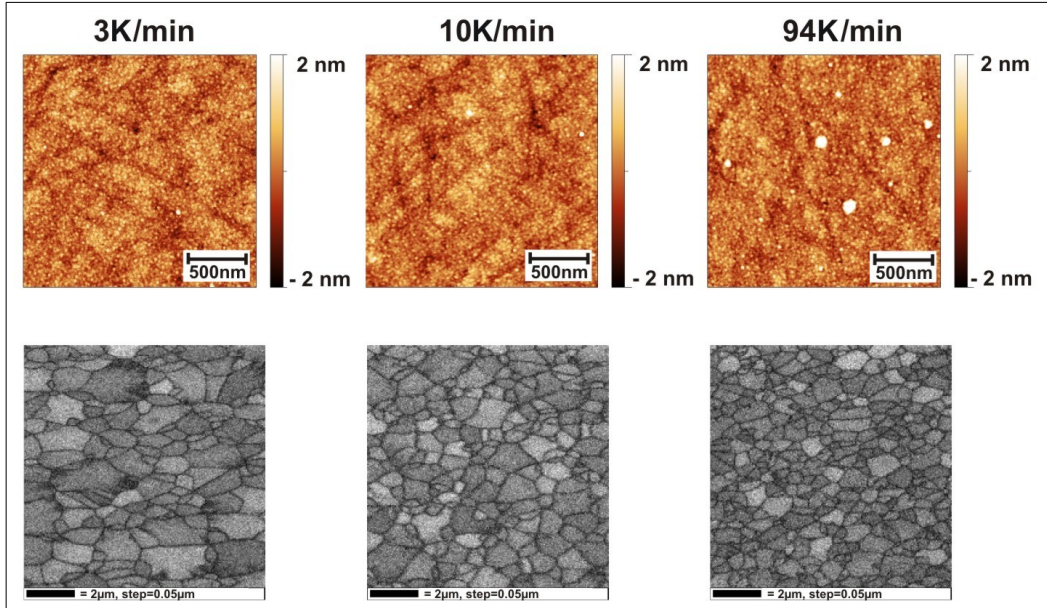
Figure 7.14: top row) AFM images of FeSb$_3$-films with a Sb content of 79 at.% obtained after annealing at 280 °C by using different heating rates [138]. No differences can be found. bottom row) EBSD band contrast maps of these films. A bright color corresponds to a good identification of a crystal structure, hence grain boundaries occur black. It can be seen, that the grain size is decreasing for faster annealing [138].

A clear dependence on the heating rate is observed by analyzing the grain size. With increasing heating rate the grain size decreases (see fig. 7.14) [138]. Because of position drifts in vertical direction during the EBSD measurement, which was proven by recording a SEM picture before and after the EBSD measurement, it was found, that only the horizontal grain size can be analyzed accurately. The average horizontal grain size was extracted by measuring the size of several grains in the image. For a heating rate of 94 K/min, 10 K/min, and 3 K/min a grain size of 0.9 µm, 1.1 µm, and 1.6 µm was obtained, respectively. It is therefore possible to adjust the grain size of skutterudite thin films by the heating rate of the annealing process. If the heating rate is large, the crystallization temperature is passed very fast and the crystal growth starts from many different nucleation sides simultaneously. The growth is then limited by collisions of the growing grains. If the heating rate is lower, only a few grains start to grow. The grains can grow further and reach larger size, before they collide with others. Since the annealed FeSb$_3$ films behave in most cases exactly like the annealed CoSb$_3$ films, there is some confidence that different heating rates should yield also for CoSb$_3$ different grain sizes.
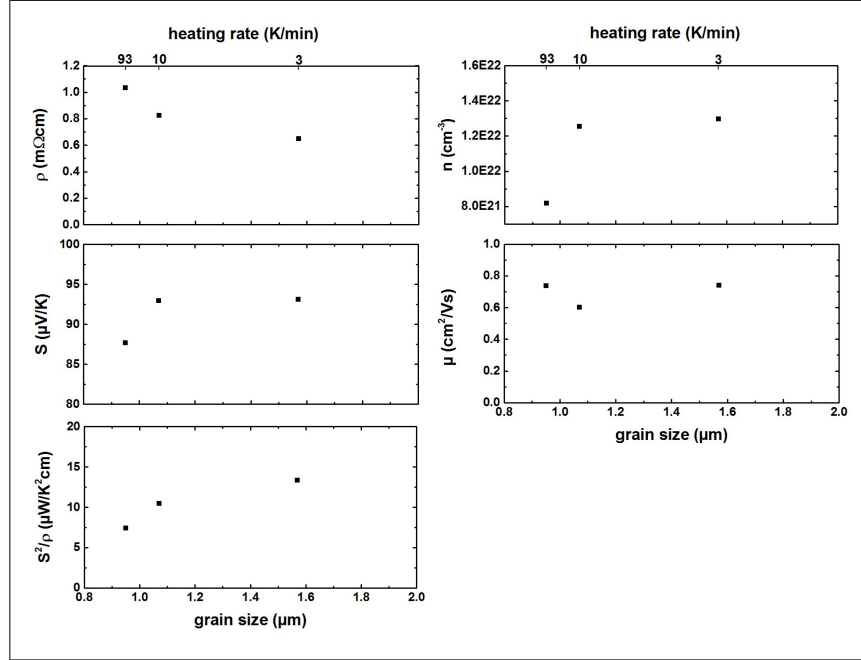
Figure 7.15: Thermoelectric properties in dependence of grain size (or heating rate). For increasing grain size the resistivity $\rho$ is decreased, the Seebeck coefficient $S$ increased and therefore the power factor $S^2/\rho$ enhanced. Hall measurements reveal a constant mobility and an increased charge carrier density.

Additionally, these films were thermoelectrically pre-characterized at room temperature. The data is presented in figure 7.15. The resistivity decreases with increasing grain size by 50 %. Since a larger grain size yield also a lower fraction of grain boundaries, the lower resistivity could be caused by decreased scattering leading to an increase in mobility. Other possibilities are a lower number of trapping states or barrier effects for the charge carriers occurring at the grain boundaries, which would be indicated by a higher number of charge carriers. Therefore Hall measurements were performed and reveal a constant mobility and an increase of the charge carrier density (see fig. 7.15), which supports the second explanation. A more detailed discussion about the influence of the grain boundaries on the electronic properties are for instance given by Suzuki et al. [23].

By changing the heating rate the Seebeck coefficient is only slightly affected and shows an increase of 6.3 % for larger grain sizes. The Seebeck coefficient exhibits only a weak dependence on grain size, grain boundaries, doping or charge carrier density for these films and its magnitude is dominated by the fact, if the skutterudite phase is formed or not (see chapter 8).

To summarize, it is possible to enhance the power factor (fig. 7.15) by a controlled adjustment of the heating rates and thus the grain size of the film. A larger grain size is connected with a lower resistivity and a larger Seebeck coefficient. How the thermal conductivity $\kappa$ and therefore $ZT$ is influenced by the different grain sizes has to be investigated by future measurements, but it is expected that $\kappa$ is increased with larger grain size and a balance has to be found between large power factor and low $\kappa$ for achieving high $ZT$ values.

# 8 CoSb$_3$ and FeSb$_3$ composition series

## 8.1 CoSb$_y$ composition series

### 8.1.1 Films deposited at elevated temperatures

To investigate the influence of the composition on the thermoelectric properties, series of CoSb$_y$ films with a Sb content between 70 at.% and 80 at.% were codeposited on SiO$_2$(100nm)/Si(100) at three different substrate temperatures (175 °C, 200 °C, and 230 °C). "*CoSb$_3$ films*" is again used for single phase skutterudite films independent of the exact composition.

**Film structure and composition**

The influence of different substrate temperatures during deposition on the structural properties was already discussed in chapter 7.1.2 and it was found that the composition range, for which only the CoSb$_3$ phase is formed, becomes more narrow with higher substrate temperature. Additionally, the grain size decreases with substrate temperature and therefore the thermal conductivity should decrease.
The formed crystalline phases are for all investigated deposition temperatures strongly dependent on the Sb content and in the range between 70 at.% to 80 at.% the following systematic changes are observed by using XRD. For a Sb content lower than 72 at.% the CoSb$_2$ or an amorphous phase can be found. With increasing Sb content up to 74 at.% usually a mixture of different phases, mainly CoSb$_2$ and CoSb$_3$, are observed. The CoSb$_3$ phase is only revealed for films with Sb content in the narrow range between ∼75 at.% and ∼76 at.%. For larger Sb content a mixture of the CoSb$_3$ and the Sb phase occurs. Details can be found in table 7.1. These results are in agreement with the phase diagram (fig. 4.11). It is to note that at 175 °C single phase CoSb$_3$ films are obtained even for Sb deficient samples in the range between 72 at.% and 75 at.% (s. chapter 7.1.2).
A clear dependency between surface morphology and Sb content is observed by AFM for all deposition temperatures (fig. 8.1). The surface becomes in general more rough with larger difference of the Sb content from the stoichiometric 75 at.%. Films with this stoichiometry exhibit the smoothest surface, which is in agreement with results reported for PLD deposited films [83]. For large deviations of the Sb content, island-like or column-like structures can be found. A strong island growth is usually connected with the detection of the Sb phase as a secondary major phase. Extracting
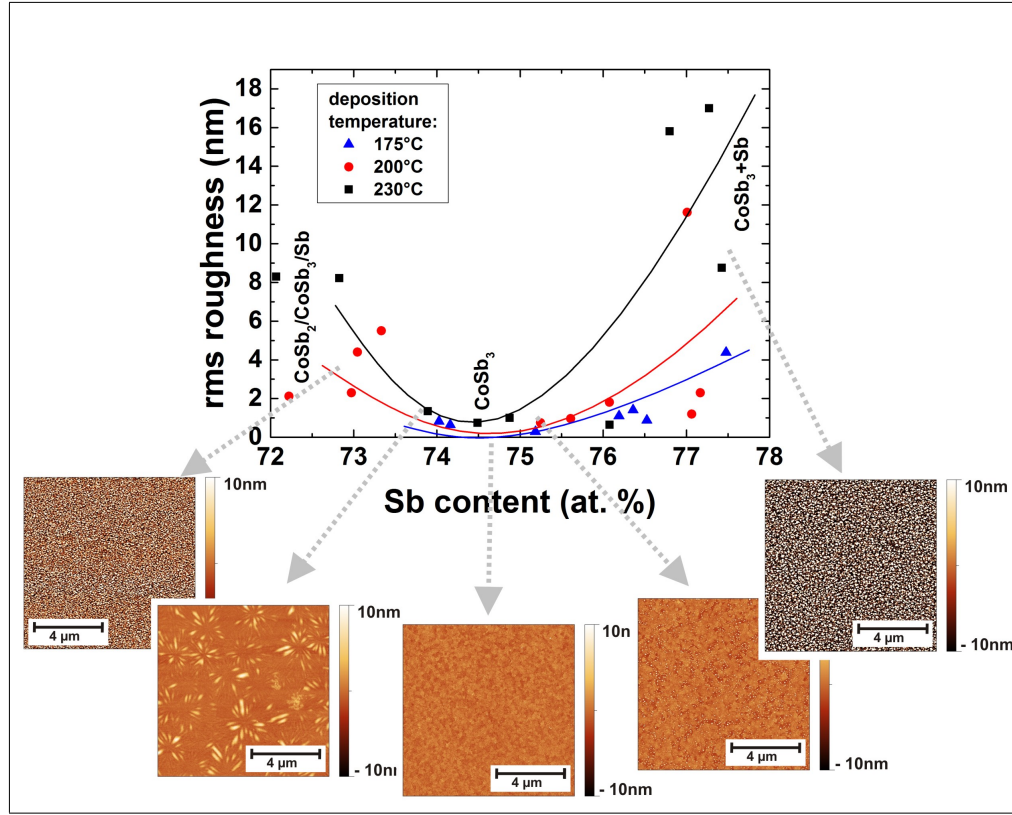
Figure 8.1: Typical AFM images in dependence of the Sb content of the films are shown. The surface morphology is strongly influenced by the Sb content and the corresponding crystalline phases. A minimum in roughness occurs for single phase skutterudite films with ∼75 at.% Sb.

the rms roughness this dependence can be confirmed and a minimum around a Sb content of 75 at.% is observed for all substrate temperatures (fig. 8.1). Furthermore, the change in morphology becomes larger with increasing substrate temperature, providing more energy for diffusion processes und thus stronger grain growth.

**Thermoelectric measurements at room temperature**

In this chapter the changes of the (thermo)electric properties with composition are discussed for films deposited on heated substrates. However as will be discussed in chapter 9.2, the SiO$_2$/Si substrates are not suitable for accurate electrical investigation and only trends can be shown. Glass substrates are the better choice.

All electrical properties measured at room temperature are summarized in fig. 8.2 as function of the Sb content for the different substrate temperatures during deposition. The corresponding ranges, where single phase skutterudite films occur, are also included. Since the sample series deposited at 200 °C and 230 °C show the same behaviour, these series will be discussed first. The third series deposited at 175 °C show a different behaviour and is described afterwards.

In fig. 8.2 (a) the dependence of the resistivity $\rho$ on the composition of the deposited CoSb$_y$ films is shown. For a deposition temperature of 200 °C and 230 °C a maximum in resistivity is observed close to a Sb content of 75 at.%. This value corresponds to the exact stoichiometry of the CoSb$_3$ skutterudite phase and therefore films with a low number of crystal defects are achieved. Since the CoSb$_3$ phase is semiconducting, the largest resistivity is observed for these films. If the stoichiometry differs from this value, vacancies or additional atoms on interstitial lattice sites act as n-type dopands and increase the charge carrier density [95, 74, 22]. Thus the resistivity drops. Savchuk et al. [22] described n-type doping in Sb deficient films due to Co atoms on interstitial sites or the presence of Sb vacancies. Co substituting the Sb sites is not expected, since the formation energy is relatively large. Smalley et al. [95] reported for annealed Sb deficient CoSb$_3$ films deposited by MERM also an n-type doping due to defects. For Sb rich samples they found an incorporation of Sb into the voids yielding n-type, which overcompensates the p-type doping by Co vacancies [95]. An complete occupation of each void would correspond to an Sb content of 76.5 at.% [58], for which the resistivity of the films in this study has already decreased to its initial value for low Sb content. For larger deviations from 75 at.% the concentration of this defects increases, thus degeneration should occur and metallic like behaviour should be observed. If additional phases are formed for even larger deviations of the Sb content from the compensated semiconducting state, these phases could provide additional current paths that short-circuits the semiconducting phase. It was for instance reported that the formation of impurity phases lowers $n$, increases $\mu$, and lowers $S$ [23]. In the work of Suzuki at al. [23] it is for instance hypothesized, that the formation of the semimetallic Sb phase leads to the observed changes due to the contribution of holes and electrons to the conduction process.

The effective charge carrier density was determined by Hall measurements to confirm the doping effect due to vacancies or interstitials. Details about the measurements and the calculations can be found in chapter 5.2. The measurements for the composition series deposited at 200 °C and at 230 °C reveal for all films p-type conduction (indicated by the superscript "+" in the label of fig. 8.2 (c)). This is in agreement with literature, where CoSb$_3$ is described in most cases as p-type semiconducting material (see chapter 4.1.3 or [22]). As expected, a minimum of the effective charge carrier density could be found for the same stoichiometry where the maximum of $\rho$ was observed (fig. 8.2 (c)) confirming the self-doping for deviations from a Sb content of 75 at.%. However, a change of sign to n-type behaviour by larger deviations from
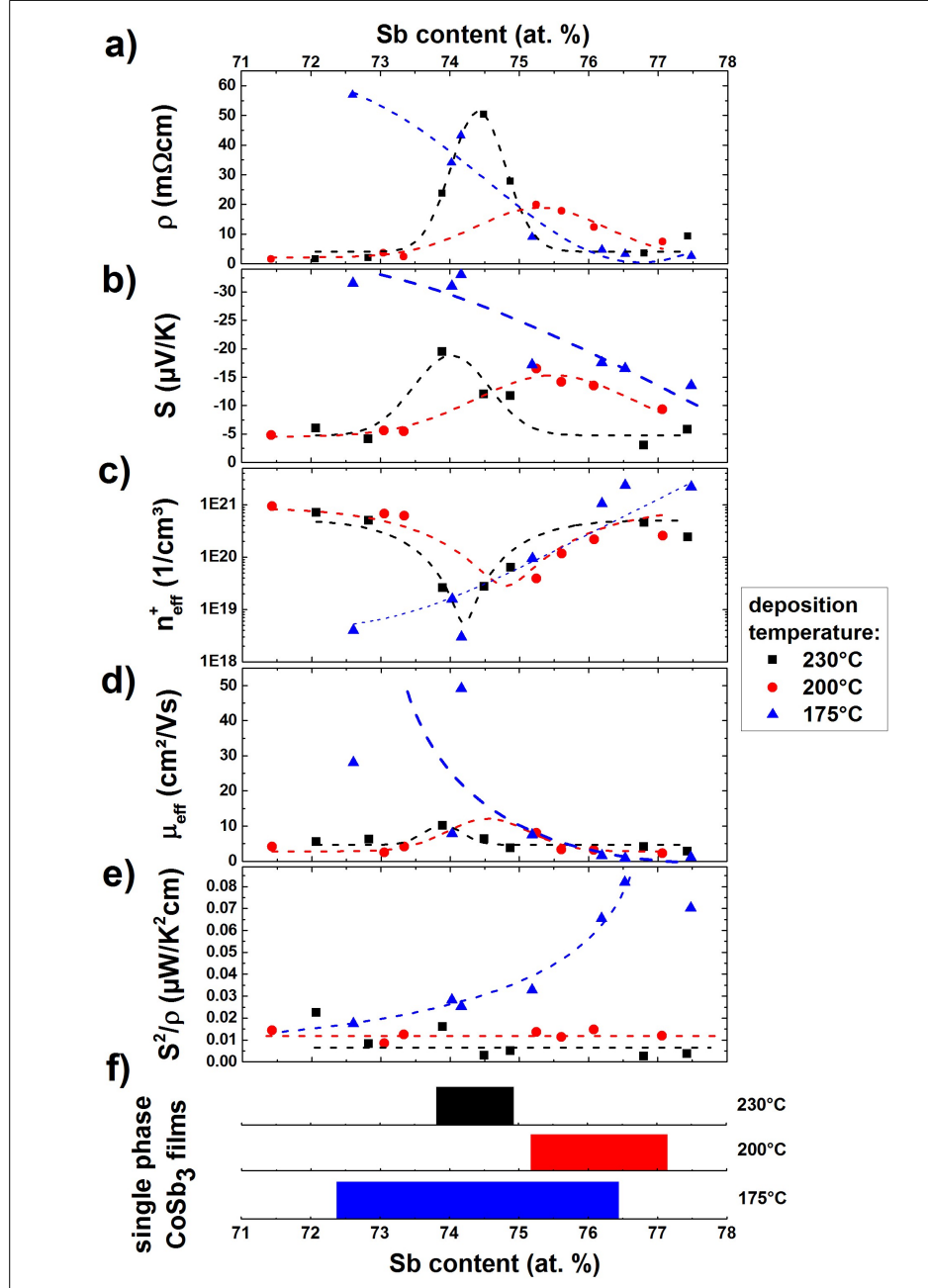
Figure 8.2: Thermoelectric properties in dependence on the Sb content for CoSb$_y$ films deposited at different substrate temperatures. The resistivity $\rho$, the Seebeck coefficient $S$, the power factor $S^2/\rho$, the effective charge carrier density $n_{eff}$ and the effective mobility $\mu_{eff}$ is presented. The superscript "+" in the label of the effective charge carrier density indicates p-type conduction (positive Hall constant). Additionally the bar diagrams at the bottom indicate the composition range for single phase skutterudite films (XRD). The dashed lines are only a guide to the eye.

the stoichiometric composition as reported in [74] was not observed here. Apparently, the doping by vacancies and interstitials is not large enough to compensate the intrinsic p-type character with an effective charge carrier density in the range of $10^{19}\,\mathrm{cm}^{-3}$.

Additionally, the effective Hall mobility was determined with equation 5.6. The absolute values are very low and nearly independent on the Sb content (fig. 8.2 (d)). The large values for the charge carrier densities indicate a lot of ionic impurities, at which scattering occurs. A weak maximum of the mobility is observed for $\sim$75 at.% Sb and therefore at the same position where the minimum in charge carrier density was found. The scattering at ionic impurities is lowest for these films with accurate stoichiometry, since they exhibit the lowest number of defects. As explained in chapter 4.1.3, grain boundary scattering, point defect scattering and phonon scattering contribute additionally to the very low mobility values for CoSb$_3$ thin films at room temperature and temperature dependent measurements of the mobility are necessary to identify the dominating scattering process.

Samples with a high resistivity and a low charge carrier density should have a large absolute value of the Seebeck coefficient (equ. 3.14, fig. 2.1 (b)). Therefore the absolute value of $S$ should also reveal a maximum around 75 at.% of Sb for the films deposited at 200 °C and 230 °C. This behaviour is indeed obtained and shown in fig. 8.2 (b). However, the Seebeck coefficient has negative sign and reaches with -20 µV/K relatively low absolute values at room temperature. In literature typical room temperature values of 150 µV/K/-300 µV/K are reported for p/n-type CoSb$_3$ (ch. 4.1.3). The observed negative sign of the Seebeck coefficient is in disagreement to the positive sign of the Hall constant. This indicates that two types of charge carriers (electrons and holes) contribute to the transport mechanism in CoSb$_3$. Since the two species of charge carriers compete for the Seebeck effect, the low absolute values can be explained.

The power factor $S^2/\rho$ was calculated. Since the maxima of both measurements compensate each other, the values of the power factor are nearly independent on composition and comparably small (see fig. 8.2 (e)).

All these results give indications that the single phase films deposited at 200 °C and 230 °C are degenerated semiconductors. A contribution of several different charge carrier types is most likely, since the sign of the Seebeck coefficient and of the Hall constant is different. The Hall measurement shows holes as major charge carriers and the Seebeck coefficient electrons, which is only possible if both types of charge carriers are present and differ in there effective mass. Additionally, a correlation between the discussed results and the phase formation can be found. The range of the Sb content, where single phase skutterudite films are obtained, is marked in fig. 8.2 (f) for each deposition temperature and the observed extrema of the transport coefficients are always observed within this range. Since the single-phase range is smaller for films deposited at 230 °C, the corresponding maximum is also sharper. In other publi-

cations it was also reported that the maximum Seebeck coefficient is obtained for single phase films [92, 23]. Thus additional parasitic phases worsen the thermoelectric properties. The differences of the absolute values for a deposition temperature of 230 °C compared to films deposited at 200 °C (higher resistivity, higher Seebeck, lower charge carrier density, lower mobility) are caused by the structural differences of both series discussed in chapter 7.1.2.

Films deposited at 175 °C reveal a different behaviour, which can only be explained by the phase formation. Films deposited at higher deposition temperatures exhibit the CoSb$_2$ phase for a Sb content lower than 74 at.% and the Sb phase for a Sb content larger than 77 at.%. In both cases the resistivity drops drastically. Since the CoSb$_2$ phase is not formed at 175 °C, only a decrease for Sb rich samples can be found. Films with lower Sb content than 75 at.% do not exhibit this drop. Down to a Sb content of 70 at.% single phase skutterudite films are obtained and for these films the maximum in resistivity is observed. This process is not yet understood. Sb vacancies as well as Co interstitials should dope the material and the resistivity should be reduced [74, 22]. If these films exhibit different properties due to amorphous Co rich parts or nanoinclusions of other phases, which are not detectable by XRD, has to be investigated by EBSD or TEM. Nevertheless the absolute value of the resistivity is in the same order of magnitude as found for the other sample series deposited at higher temperatures. By increasing the Sb content, the material gets doped and the resistivity decreases. This can be confirmed by the results obtained for the effective charge carrier density, which is smallest for low Sb content and increases by doping of the material with increasing Sb content. The doping influences also the Hall mobility, which decreases with increasing Sb content by scattering at the larger number of ionic impurities in the doped samples. The films exhibit p-type conduction and reveal also relatively low absolute values of the Hall mobility, which is in agreement to the results achieved for the other films series.

The coupling between Seebeck coefficient, resistivity, and charge carrier concentration is also observed for films deposited at 175 °C. The Seebeck coefficient is negative and the absolute value shows the same dependence as the resistivity and decreases with increasing Sb content. $S$ is larger than for the series deposited at higher deposition temperatures and the maximum absolute value achieved is about -33 µV/K. The reason for the larger Seebeck coefficients is not yet understood, but might be caused by the formation of different phases and by the structural differences discussed in chapter 7.1.2.

The calculated power factor increases with increasing Sb content and is in contrast to the other sample series not constant. The decrease of resistivity with higher Sb content is steeper than that one observed for the Seebeck coefficient and therefore both measurements do not fully compensate each other. The maximum power factor is with ~0.08 µW/K$^2$cm the largest one of all three series.
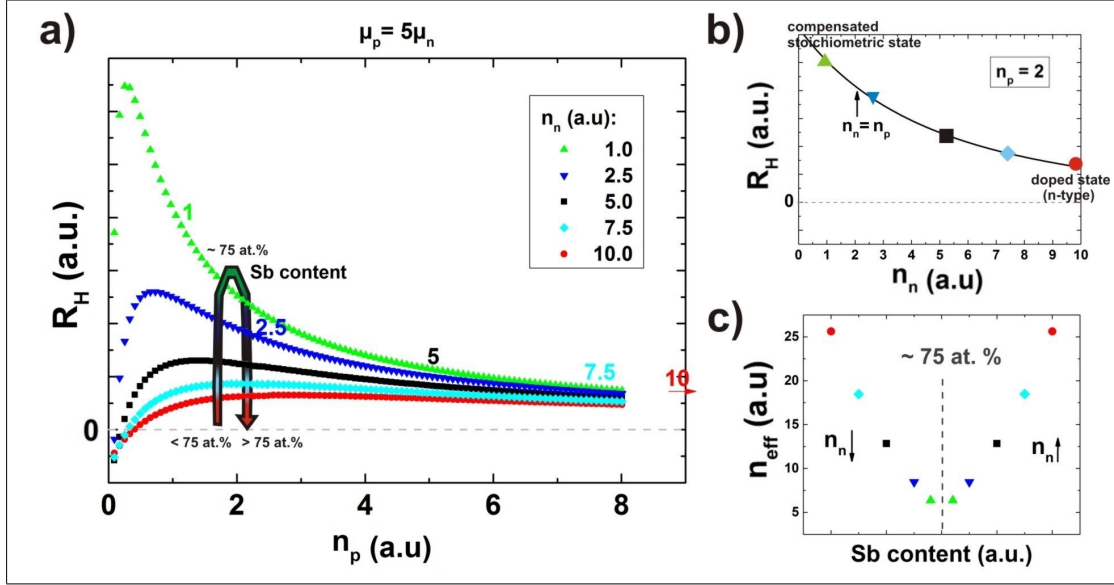
Figure 8.3: a) Hall constant $R_H$ in dependence on the intrinsic hole concentration $n_p$ for different dopings (electron concentration $n_n$). The mobility of the holes is chosen larger than for electrons as expected for CoSb$_3$ [60]. The arrow should indicate the change of $n_n$ with changed Sb content (for $n_p = 2$) and the added numbers mark the point for the same concentration of holes and electrons ($n_p = n_n$), where the Seebeck coefficient should change signs. b) Hall constant as function of doping level $n_n$ for a constant $n_p = 2$. c) The effective charge carrier concentration $n_{eff}$ in dependence of the Sb content (and therefore various $n_n$) is roughly determined ($n_p = 2$).

To give a possible explanation for the revealed curves, especially for the discrepancy between the sign of the Seebeck coefficient and of the Hall constant, the later was qualitatively calculated with equation 5.7 for the presence of electrons and holes:

$$R_H = \frac{n_p\mu_p^2 - n_e\mu_n^2}{e(n_p\mu_p + n_n\mu_n)^2}.$$

The hole mobility of CoSb$_3$ is about five times larger than the mobility of electrons [60], therefore the ratio of both mobilities were chosen as $\mu_p = 5\mu_n$. Additionally, it is expected, that the hole concentration is in the same range as the doping concentration of the electrons ($\sim 10^{19}$ cm$^{-3}$). The Hall constant $R_H$ was calculated with this assumptions and is shown in fig. 8.3 (a) as function of the hole density $n_p$ for different electron concentrations $n_n$ caused by doping. Due to the larger hole mobility, the Hall constant can be positive, even though the electron density $n_n$ (or doping level) is larger than the intrinsic hole density. The point, where the charge carrier

density is equal for both carrier types, is marked by the number of the corresponding doping level $n_n$ above each curve. In chapter 10.1 is determined, that the species with the larger charge carrier density dictates the sign of the Seebeck coefficient. Thus the Seebeck coefficient is tending to be negative as long the system is on the left side of these points, while the Hall constant is already positive due to the larger hole mobility. This behaviour is in agreement to the experimental results. In case of intrinsic excitation the concentration of the holes will be steadily increased with temperature and the Seebeck coefficient should become for moderate n-type doping finally positive.

Now the effect of n-type doping should be simulated exemplarily for a constant intrinsic hole concentration of $n_p = 2$, which can be demonstrated best by the additional plot of the Hall constant $R_H$ as function of the electron concentration (or doping level) $n_n$ shown in fig. 8.3 (b). $R_H$ decreases with increasing doping concentration $n_n$. It is now assumed, that deviation from the stoichiometric Sb content of ~75 at.% with lowest number of defects (like vacancies or interstitials) yield a n-type doping as reported in the literature [95, 74, 22]. This implies, that a low and a large Sb content (for instance 70 at.% and 80 at.%) results in a large doping ($\widehat{=} n_n$ of 10 in the present example shown in fig. 8.3 (c)). The change of $R_H$ with composition can be investigated with this assumptions. Starting for low Sb content in the doped state with an initial value of $n_n = 10$ (red circle fig. 8.3 (b)), the doping level $n_n$ decreases first with increasing Sb content and $R_H$ increases. The lowest doping level and thus the largest $R_H$ is reached for the stoichiometric Sb content with the lowest number of defects ($n_n = 1$, green triangle). This corresponds to a Sb content around 75 at.%, for which the maximum of resistivity and the minimum of charge carrier density was observed (fig. 8.2). By further increasing the Sb content, the electron density increases again due to the increasing number of defects for higher Sb content and $R_H$ decreases. Finally the doped state indicated by the red circle is reached again. This composition dependence is also indicated by the colored arrow in fig. 8.3 (a). The crossing points of the arrow with the $R_H$ curves of different doping level correspond to the points marked with the same symbol in fig. 8.3 (b), respectively.

For these points the effective charge carrier concentration $n_{eff}$ was calculated using equation 5.5. The result is shown in fig. 8.3 (c) in dependence of the Sb content. The determined function agrees qualitatively with the measured curve shown in fig. 8.2 (c). It is to note, that the values of the effective charge carrier density observed in the experiments are larger than the real charge carrier density of the sample, since the used formula 5.5 to calculate $n_{eff}$ is not valid for bipolar conduction. This can be seen for instance by comparing $n_n + n_p$ with $n_{eff}$ in the given model (e.g. doped state marked with red dot in fig. 8.3 (b) and (c): $n_n + n_p = 10 + 2 = 12$ and $n_{eff} \sim 25$). The largest error occurs for low hole concentration close to the compensation point, where the Hall constant changes sign ($n_p < 1$). In that case equation 5.7 has to be used. Since the properties of both types of charge carriers ($n_n$, $\mu_n$, $n_p$ and $\mu_p$) cannot be measured individually, only this qualitative discussion is possible.

For the given example with $n_p = 2$ it has to be noted further, that a switch from negative to positive Seebeck coefficients would occur for the films with the lowest number of defects and therefore the lowest electron density ($n_n$=1). $n_p$ becomes in that case larger than $n_n$, what can be also seen nicely in fig. 8.3 (a) and (b), and a positive Seebeck coefficient should be obtained. Even though this change was reported in literature [74], it was not observed for the films presented in this work. The electron density of the investigated samples was always higher than the hole density.

**Low temperature transport measurements for the Co-Sb composition series deposited at 230 °C**

The temperature dependence of the resistivity was investigated for films deposited at 230 °C. Furthermore an additional Hall and resistivity measurement was performed in the range between 225 K and 250 K and compared to room temperature measurements. The achieved results are shown in table 8.1. The effective charge carrier density at room temperature is slightly increased compared to the one measured at 230 K and remains positive (p-type conduction). The largest relative increase occurs for the sample with 74.5 at.%. This is reasonable, since this sample is close to the stoichiometric composition of CoSb$_3$ (75 at.% Sb), exhibits only the CoSb$_3$ skutterudite phase, has the highest resistance and the lowest charge carrier density at room temperature (s. table 8.1), and it is therefore expected, that it should exhibit the strongest semiconducting character of all samples (largest temperature coefficient of resistivity, largest band gap, etc.).

This claim can be confirmed by temperature dependent resistivity measurements, which are presented in fig. 8.4 (a). The room temperature values are added and agree well with the measurements in the cryostat. Only the sample with 74.9 at.% differs and was therefore remeasured at room temperature giving the same result. This discrepancy is not yet understood. It can be seen, that all films exhibit a negative slope typical for semiconductors. For the lowest Sb content the resistivity is

| Sb content (at.%) | $n_{230K}$ (cm$^{-3}$) | $n_{RT}$ (cm$^{-3}$) | $\rho_{RT}$ (mΩcm) | $\alpha_T$ (K$^{-1}$) | Slope$_{200K}$ (K) | $E_{gap}$ (meV) |
|---|---|---|---|---|---|---|
| 72.82 | 4.9E20 | 5.0E20 | 2.0 | -0.0030 | 103.3 | 17.8 |
| 73.89 | 6.4E19 | 2.6E20 | 23.5 | -0.0020 | 90.9 | 15.7 |
| 74.48 | 7.0E18 | 2.7E19 | 50.3 | -0.0052 | 116.0 | 20.0 |
| 74.87 | 6.0E19 | 6.4E19 | 27.8 | -0.0056 | 126.1 | 21.7 |
| 76.79 | 4.0E20 | 4.5E20 | 3.5 | -0.0043 | 104.0 | 17.9 |

Table 8.1: Extracted low temperature electric parameters: Sb content, effective charge carrier density $n_{230K}$ at 230 K and $n_{RT}$ at room temperature, resistivity $\rho$ at room temperature, temperature coefficient $\alpha_T$, slope of the $\ln \rho$ over $1/T$ function around 200 K, and the corresponding band gap width $E_{gap}$.
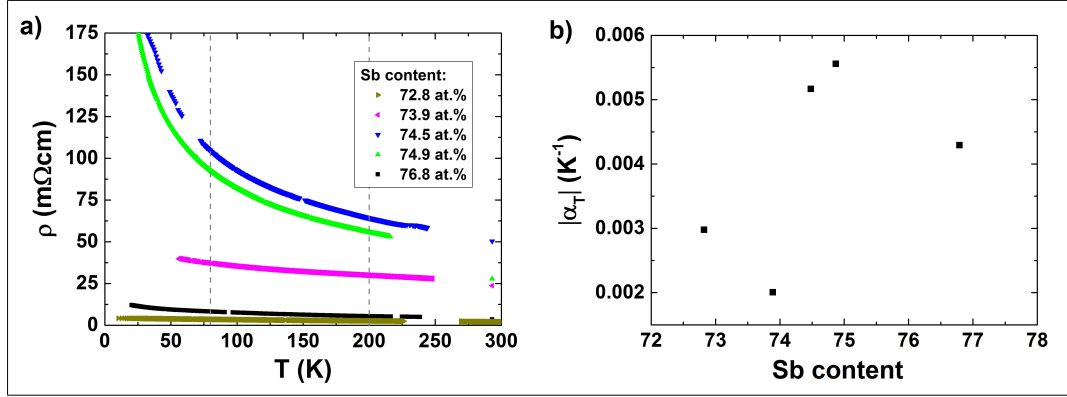
Figure 8.4: a) The temperature dependence of the resistivity $\rho$ for Co-Sb films with different Sb content deposited at 230 °C. For a Sb content close to 75 at.% semiconducting behaviour is observed. b) The extracted absolute value of the linear temperature coefficient $\alpha_T$ was obtained from the slope between 80 K and 200 K and is shown in dependence on the Sb content of the films. The corresponding region is marked with the dashed lines in (a).

nearly constant. The deviation from the stoichiometric Sb content of ∼75 at.% yield lots of defects and the formation of different phases resulting in large charge carrier densities, degeneration, subbands or additional current paths. With increasing Sb content the number of defects is decreasing first and thus the resistivity and also the relative change with temperature is increasing. The most pronounced semiconducting behaviour is indeed found for a Sb content around 75 at.%, for which the lowest number of defects occurs. For even larger Sb amount the number of defects increases again, the material gets doped, and for the highest investigated Sb content of 76.8 at.% the resistivity becomes also nearly constant, which is typical for degenerated semiconductors. These visual results are supported by extracting the linear temperature coefficient $\alpha_T$, which is calculated from the average slope between 80 K and 200 K and defined in the following as

$$\alpha_T = \frac{1}{\rho(200K)} \frac{\rho(200K) - \rho(80K)}{200K - 80K}.$$

The calculated values are negative as expected for semiconducting behaviour and are also included in table 8.1 for the individual samples. In figure 8.4 (b) the dependence of the absolute value of $|\alpha_T|$ on the Sb content of the film is shown and the largest values are obtained close to the desired 75 at.% of Sb. The obtained results support the discussions given for the room temperature resistivity measurements. Furthermore it is to note, that it is possible to cover the whole range of resistivity curves reported in literature for CoSb$_3$ (see fig. 4.9) only by varying the composition.

The bandgap width or the existing excitation levels can be investigated by plotting the logarithm of $\rho$ over $T^{-1}$ (see table 3.1) and performing a linear regression. Thereby it is assumed, that there is only phonon scattering and that the semiconductor is non-degenerated, which could be the case for the films with the largest temperature coefficient and for temperatures above 200 K. Above this temperature the curves are indeed approaching a linear slope, from which the bandgap width is determined (not shown). The obtained values are listed in table 8.1 and they are all in the same range. Since the temperature dependences of the different samples are quite different, this is surprising and counts for a similar band structure with various doping level for the individual samples. However, the values are relatively low in comparison to the given literature values of the occurring bandgaps, which are usually larger than 50 m$e$V (see table table 4.1). Therefore high temperature measurements of resistivity and mobility are needed to verify, if really a linear behaviour is observed and if the acoustic phonon scattering is the dominating scattering process. The obtained values for the bandgap should be better understood as lower limit. It is to note that the onset of intrinsic excitation is reported in literature in a temperature range between 300 K and 600 K (see chapter 4) and a linear dependence is usually not observed in this temperature range.

Below a temperature of 200 K, no linear behaviour can be observed in the plots of $\ln \rho$ over $T^{-1}$ and the resistivity data cannot be explained by band excitation. At low temperatures it is typical for highly doped semiconductors to find variable range hopping (VRH) based on localized electrons [43, 45, 44]. The theory predicts a linear dependence between $\ln(\rho)$ over $T^{-1/4}$ (table 3.1). These plots are shown for all samples in fig. 8.5 (a). All samples exhibit for low temperatures (right side of the graph) a linear behaviour shown by the additionally plotted linear fits (red). Towards higher temperatures (left side) the curve gets more and more bended and the absolute value of the slope increases steadily. The temperature $T_{dev}$ at which the change from linear to the more bended curve occurs, differs for the different compositions. This temperatures was determined by both, the estimation where the linear fit differs from the measured curve and additionally by the change of the first derivative of the measured curve. The dependence of this temperature on the Sb content of the films is shown in the figure 8.5 (b) and a maximum around 160 K is found for films close to the stoichiometric Sb content of 75 at.%. Here, films with the lowest number of defects and thus lowest doping level are observed. If the defect/doping concentration is small, the number of excitation levels in the gap is smaller and the width of the bandgap is largest. The energy available at low temperature is therefore not enough to excite charge carriers into the conduction band and between the doping states VRH can occur up to larger temperatures. The observed values for these films are even larger than typically reported values in literature [154, 155]. If the defect/doping concentration is increased by deviations from the stoichiometric Sb content, more and more impurity states might be generated in the gap and the probability to excite

charge carriers to the conduction band is increased for these samples resulting in a lower $T_{dev}$. This claim is supported by the plot of the deviation temperature $T_{dev}$ as function of the effective charge carrier density $n_{eff}$ shown in fig 8.5 (c). The higher $n_{eff}$, the lower $T_{dev}$. For even higher doping the formation of an additional subband in the gap could occur and no VRH is observed at all. The formation of such a subband is likely for a narrow bandgap semiconductor like CoSb$_3$ but very complicated to investigate. Another aspect to explain the temperature dependence of the resistivity at low temperatures could be grain boundary scattering with variable barrier height as discussed by Kajikawa [47]. In this work it is explicitly mentioned that results of various studies former attributed to a combination of VRH and grain boundary scattering [155] can be better explained in their model.
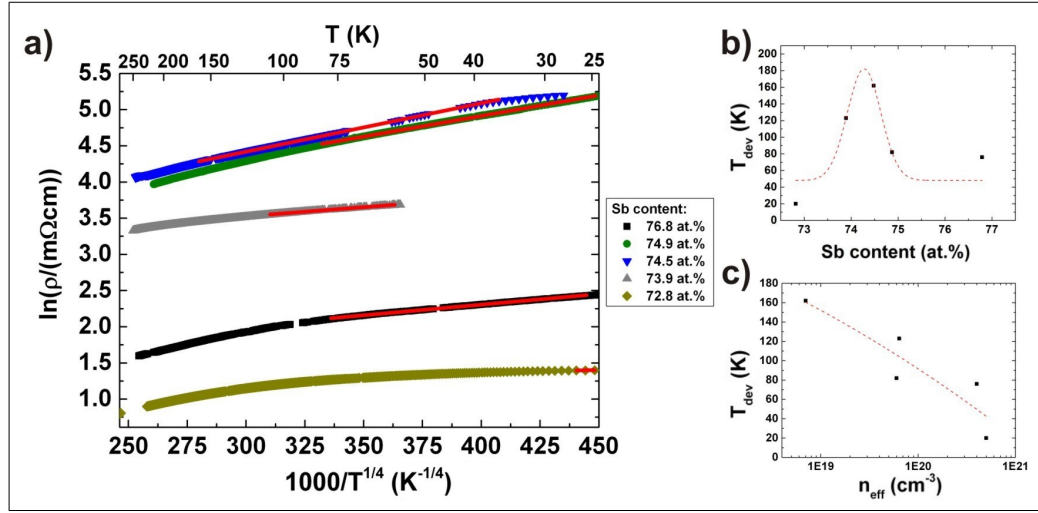


Figure 8.5: a) The logarithm of $\rho$ in dependence of $T^{-1/4}$ for Co-Sb films with different Sb content deposited at 230 °C. A linear dependence indicates variable range hopping (VRH). The corresponding temperature regimes are fitted by a linear function (red curves). b)+c) The temperature $T_{dev}$, where the slope begins to differ from linear behavior, is shown in dependence of b) the charge carrier density and c) the Sb content.

Hall measurements could be performed over the entire low temperature range only for a few samples (not shown), however the interpretation is very challenging. The narrow band gap is very sensitive to changes in defect density and thus charge carrier density, which gives easily rise to bipolar conduction with overlapping transport properties of electrons and holes [95]. Furthermore, small changes of the skutterudite lattice structure have a strong influence on the band gap [61], which could be

already induced by the fabrication technique [95]. It is therefore hardly possible to analyze the Hall constant, charge carrier density, and mobility in this temperature range qualitatively and the literature values reported for the bandgaps differ significantly. Some reported studies explain the observed temperature dependence of the charge carrier density by an impurity band [38], other have used a two acceptor and one donor level system with a deep acceptor level [156]. When intrinsic conduction is reached at higher temperatures and the transport mechanism becomes hole dominated, a more detailed investigation is possible.

In summary, the discussed low temperature measurements for the samples deposited at 230 °C agree well with the electrical and structural investigations at room temperature. The results reveal a very strong influence of small changes in the Sb content on the electric properties at low temperatures, which demands a stable Sb content of the films during heat cycling in the final thermoelectric devices. VRH is indicated as dominating conduction process at low temperatures. An analysis of the Hall measurements at low temperatures is complicated, especially for bipolar transport and eventually formed impurity bands. A more detailed discussion is given for instance by Arushanov et al. [156]. Furthermore, the investigation of resistivity at higher temperatures and the investigation of the Seebeck coefficient in the entire temperature range between 4 K and 800 K are necessary to get deeper insights into the interaction of crystal structure, band structure, and electric properties.

## 8.1.2 Annealed films

CoSb$_y$ films with a Sb content between 69 at.% and 86 at.% were codeposited at room temperature on SiO$_2$(100nm)/Si(100) and post-annealed to investigate the thermoelectric properties of annealed films in dependence of the Sb content. One series was annealed at $T_A = 300$ °C and one at $T_A = 500$ °C. The transport parameter of both composition series show similarities compared to the film series deposited at elevated temperatures. However, the structural differences of both types of films differ significantly (see ch. 7.1.2) resulting also in pronounced differences of the thermoelectric properties.

### Film structure and composition

As mentioned in chapter 7.1.2, the composition range, where the skutterudite phase is formed, is for annealed films larger (table 7.2). It starts at 74 at.% Sb and ends at values between 78 at.% and 82 at% Sb, depending on the annealing temperature. Films with lower Sb content exhibit a mixture of the CoSb$_3$ skutterudite phase and the CoSb$_2$ phase, films with larger Sb content show a mixture of CoSb$_3$ and Sb. The AFM images obtained for the different compositions are presented in fig. 8.6 for an annealing temperature of 500 °C. The Sb deficient films reveal a smooth surface with rod like structures. For a Sb content larger than 74 at.% only the skutterudite phase
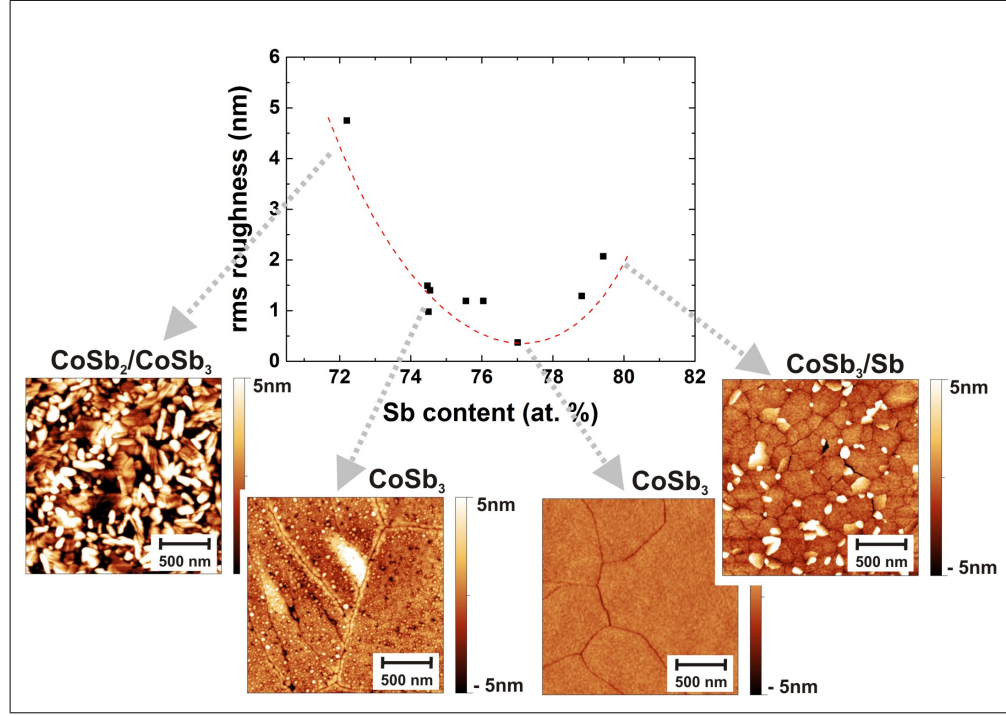
Figure 8.6: The rms surface roughness is presented in dependence of the Sb content of Co-Sb films annealed at 500 °C. Additionally, the AFM images and the corresponding crystalline phases are added.

can be detected. These films exhibit a smooth surface with many distortions and a lot of small cracks, holes, and particles can be found. The roughness is smaller than 1.5 nm. With increasing Sb content the number of particle and the roughness decreases. Above 77 at.% Sb a fine-grained surface structure distorted by several cracks is observed for the skutterudite films. If the Sb phase is additionally formed (around 80 at.%), some parts start to tilt and to peel off from the substrate. The surfaces of films annealed at 300 °C exhibit less changes in dependence of the composition and stay very smooth (not shown). These visual impressions can be confirmed by the dependence of the rms roughness on the Sb content and a pronounced minimum can be found for films annealed at 500 °C, which is shown in fig. 8.6.

All annealed films are over the entire composition range much smoother compared to films deposited at elevated temperatures. The larger composition range for obtaining single phase films and the smoother surfaces make annealed films more promising for thermoelectric applications than films deposited at elevated temperatures. This is supported by improved thermoelectric properties, which will be discussed in the next section.

**Thermoelectric properties at room temperature**

In fig. 8.7 the electric and thermoelectric properties are shown in dependence on the Sb content for annealing temperatures of 300 °C and 500 °C. The Sb content was measured by RBS after the annealing process. The basic results agree with the composition series of films deposited at elevated temperatures (compare fig. 8.2).

The resistivity for both annealing temperatures exhibits also a peak for a Sb content of about 75 at.%. However, the width of the resistivity peak is much smaller than the composition range, where single phase skutterudite films are observed (fig. 8.7 (a) and (f)). This range lasts for instance up to a Sb content of 82 at.% for films annealed at 500 °C, while the resistivity drops already for a value of 76.5 at.%. The absolute resistivity values of the annealed samples are smaller compared to the measured values for films deposited at elevated temperature (compare fig. 8.2). Possible explanations are less scattering due to the smaller grain size (less grain boundary scattering) and smoother surfaces (less surface scattering). The Hall measurements indicate indeed an increased scattering. First there is no significant difference of the effective charge carrier density between films of both preparation types. A minimum around 75 at.% Sb is also observed for the annealed films (fig. 8.7 (c)) and the absolute values are even slightly decreased compared to the films deposited at elevated temperatures (fig. 8.2 (c)). Therefore the decrease of resistivity is caused by a higher mobility (less scattering), which can be seen by comparing fig. 8.7 (d) and fig. 8.2 (d).

The Seebeck coefficients are comparable to the values found for the films deposited on heated substrates and reveal also a negative sign in contrast to the positive Hall constants, which is again an indication for two species of carriers. The absolute value of $S$ is less sensitive to the Sb composition than the resistivity and a broad maximum is observed (73 at.% - 80 at.%, s. fig. 8.2 (b)). It is believed that the increase is strongly connected to the formation of single phase skutterudite films. Since single phase skutterudite films can be observed for post-annealed films in a much broader composition range, the maximum of $S$ is also much broader than the one observed for the films deposited at elevated temperatures. Impurity phases yield a decrease of the Seebeck coefficient, as already mentioned in the last section [92, 23]. The relation between $S$ and single phase films was less obvious for films deposited at elevated temperatures, since the respective composition range of single phase films there is as narrow as the peak width of the resistivity caused by self-doping due to a non-stoichiometric Sb content. Therefore the peaks of the Seebeck coefficient and that one of the resistivity could be both explained only by a change of the Sb content (fig. 8.2).

The different characteristic of $S$ and $\rho$ with respect to the Sb content and the phase formation influences the power factor ($S^2/\rho$) strongly. The Seebeck coefficient is enlarged for single phase skutterudite films and nearly independent to compositional changes. The resistivity is also increased for single phase skutterudite films, but de-
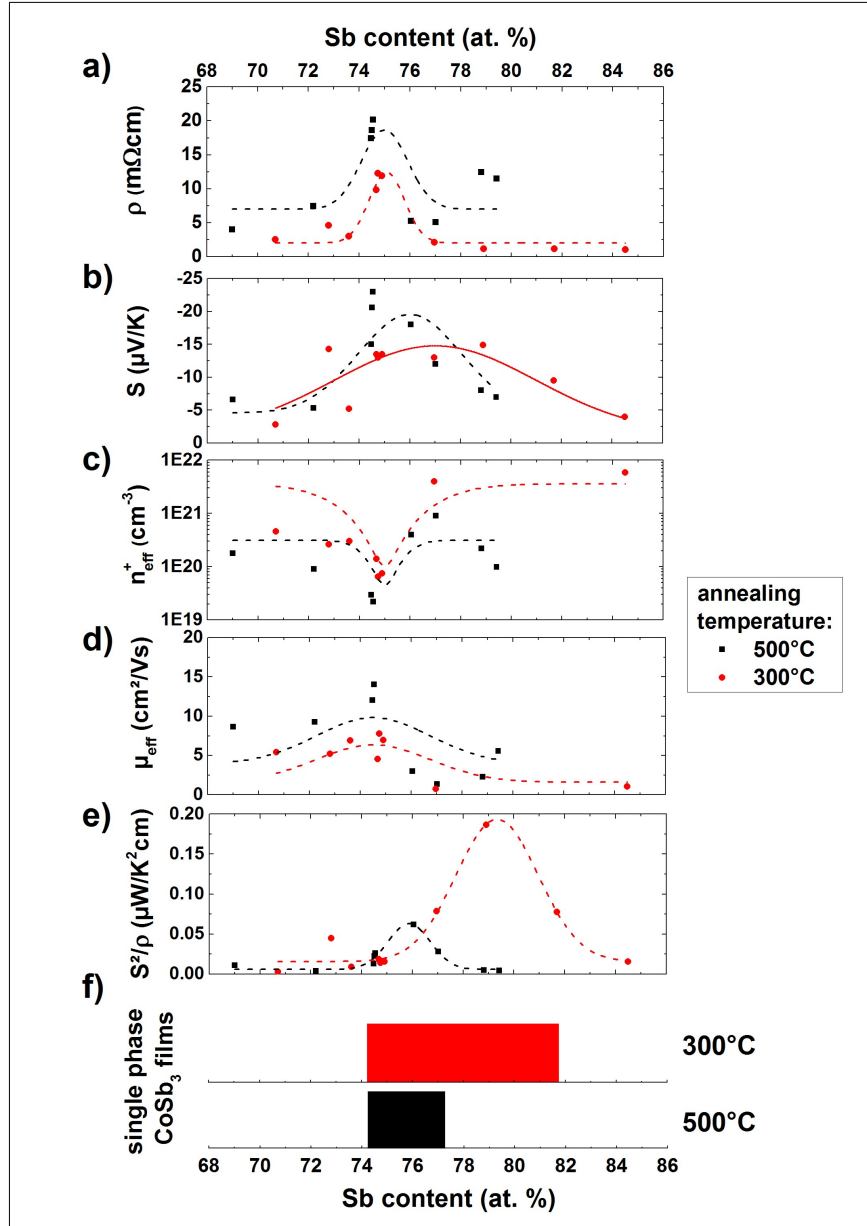
Figure 8.7: (a - e) Thermoelectric properties of annealed Co-Sb films in dependence of the Sb content. The films were deposited at room temperature and post-annealed at different temperatures. The superscript "+" in the label of the effective charge carrier density indicates p-type conduction (positive Hall constant). Besides the thermoelectric transport parameter, the composition range for the formation of single phase skutterudite films is marked in (f) by the bars. It is to note, that the shown composition range is much larger compared to the results of the films deposited at elevated temperatures (compare fig. 8.2) and thus the observed peaks are less sharp. The dashed lines are a guide to the eye.

pends strongly on the Sb content or better the corresponding change of the charge carrier density. For the Co-Sb films with a Sb content larger than 75 at.% the resistivity drops due to doping with Sb, while the Seebeck coefficient is still high. The peak of the Seebeck coefficient is therefore not fully compensated by the resistivity peak (as found for the films deposited on heated substrates) and thus the power factor shows a pronounced maximum between 75 at.% and 82 at.% Sb (s. fig. 8.2 (e)). The power factor of the annealed samples is additionally improved by the lower resistivity due to less scattering at grain boundaries and surface. The exact maximum position is shifted for the different annealing temperatures and the larger value of $\sim 0.2\,\mu W/K^2 cm$ is achieved for films annealed at 300 °C. It should be further referenced to chapter 9.2, where it is shown, that the Seebeck coefficient of the films is actually about 50 % larger. On the SiO$_2$/Si(100) substrate lower values were measured due to the influence of this substrate on the measurement. The real power factor should therefore exhibit even larger values.

Comparing the different annealing temperatures, it can be concluded that a better crystallinity occurs by annealing at higher temperatures. The healing of defects at larger temperatures causes less parasitic doping states and therefore a lower charge carrier density, which results further in an increase of resistivity, mobility and Seebeck coefficient. However the overall power factor is decreased. These results are in agreement to the structural properties and especially to the relaxation of the lattice constant due to the annealing process presented in chapter 7.1.2 for post-annealed films.

**Low temperature electric properties**

Low temperature measurements were performed for the single phase skutterudite films only. For this study, the films were structured by lithography using a mask for a six point resistivity/Hall measurement structure. The lithography procedure was performed in cooperation with the Leibniz-Institut für Festkörper- und Werkstofforschung Dresden (IFW) and an image of the final film structure is shown in fig. 8.9 (b). Some difficulties appeared by contacting these structures and therefore not all samples could be measured. It is therefore recommended to use instead the van der Pauw method in combination with the contacting method presented in fig. 5.2 (c) for the measurements of skutterudite thin films.

In fig. 8.8 (a) an overview of the temperature dependence of the resistivity for the samples annealed at 300 °C is shown. It can be seen that the samples, showing the largest resistivity at room temperature, also reveal the largest resistivity over the entire temperature range and the largest temperature coefficient. This supports the results obtained for the films deposited at elevated temperatures. The strongest semiconducting behaviour is found for the films with a Sb content close to the stoichiometric Sb content for CoSb$_3$ of $\sim$ 75 at.%. The determined temperature coefficients
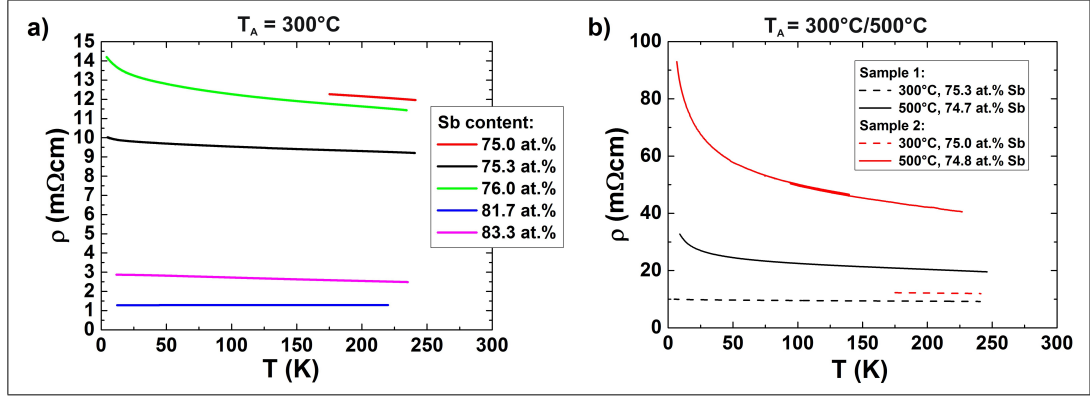
Figure 8.8: Temperature dependence of the resistivity for room temperature deposited films with post-annealing step: a) for films with different composition annealed at 300 °C and b) for two selected samples to demonstrate the resistivity change due to annealing at different temperatures (300 °C and 500 °C). The Sb content was obtained after annealing via RBS.

of these samples are about $0.0006\,\mathrm{K}^{-1}$ for an annealing temperature of 300 °C, and therefore lower compared to samples deposited at 230 °C with comparable Sb content (see table 8.1). If the Sb content is lower or higher than 75 at.%, the resistivity and the temperature coefficient drop as described before. The character of degenerated semiconductors is found for all samples indicated by the very low temperature coefficient.

Furthermore, the influence of the used annealing temperature on the temperature dependence of the resistivity is shown for two samples with a Sb content around 75 at.% in fig. 8.8 (b). Besides the larger resistivity by a better crystallinity/healing of defects, which was already discussed for annealed films in chapter 7.1.2, the temperature coefficient is also drastically increased with increasing annealing temperature ($0.0028\,\mathrm{K}^{-1}$ for 500 °C). The defect healing decreases the charge carrier density and lowers the amount of impurity states distorting the band gap. Thus a stronger semiconducting character with larger temperature coefficient is obtained. It is further to note, that the obtained curves shown in fig. 8.8 (b) demonstrate how sensitive the electric properties are on slight changes in the Sb content around 75 at.% and on the defect concentration. The obtained curves cover nearly the whole band width of curves found in other publications (fig. 4.9), as already found for films deposited at elevated temperature. Both samples annealed at 500 °C have for instance exactly the same composition, but the temperature dependence of the resistivity reveal large differences. Therefore, it has to be guaranteed that the thermal treatment does not change the composition or causes further defect healing. However, it was shown in chapter 6.3 that the Sb content changes during the annealing process. It is therefore

necessary to investigate the stability of the composition during thermal cycling processes. Nevertheless, the results obtained in chapter 7.1.3 are very promising, where a stabilization of the film properties could be achieved in case of slightly Sb rich samples and annealing times longer than 2 h.
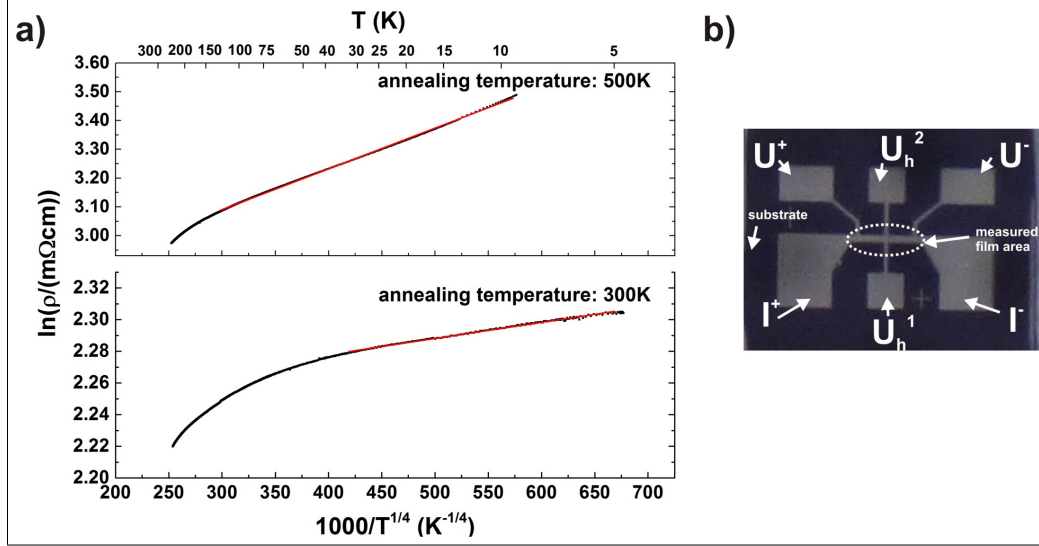


Figure 8.9: a) The logarithm of the resistivity $\rho$ of an annealed CoSb$_3$ film is plot over $1/T^{1/4}$ for two different annealing temperatures (with different scale). The initial film was deposited at room temperature with a Sb content of $\sim 74$ at.%. If variable range hopping (VRH) is present, a linear dependence should occur. b) The used 6 point film structure for the measurements of the resistivity and the Hall voltage: $I^+$ and $I^-$ are the contacts for the applied current, $U^+$ and $U^-$ the contacts for measuring the voltage along the film stripe and $U_H^1$ and $U_H^2$ the contacts for measuring the Hall voltage perpendicular to the film stripe.

Additionally the intrinsic properties as bandgap width and conduction mechanisms were investigated. By plotting $\ln \rho$ over $1/T$, the linear regression around 200 K reveals a larger slope for the samples annealed at higher temperatures. The corresponding energy gap for an annealing temperature of 300 °C was in the range of 3 meV - 4 meV and for 500 °C in the range of 8 meV. These values are doubtful as described for the samples deposited at elevated temperatures and the linear dependence have to be confirmed by high temperature measurements. Such low values might be an indication for degeneration or for the formation of subbands.

For the films deposited at elevated temperatures variable range hopping (VRH) was observed as dominant conduction mechanism at low temperature. For the annealed

films the situation is less clear. Several samples could not be measured down to the necessary temperature; some show a clear linear dependence in the corresponding plot of $\ln \rho$ over $1/T^{\frac{1}{4}}$ (see table 3.1), others do not. The plots for a sample with a Sb content around 75 at.% are exemplarily shown in fig. 8.9 (a). A clear linear dependence can be found for both annealing temperatures (for 300 °C linear up to ∼30 K, for 500 °C up to ∼74 K). The Hall constant was also measured for these films around 225 K and the data is roughly in agreement with the room temperature measurements. An decrease of the charge carrier density with increasing temperature could be found. This behaviour is typical for variable range hopping or subbands [44, 45], however this conduction mechanism is not expected for this temperature range. An increase of $n_{eff}$ could also be found close to a compensation point of holes and electrons or if the mobilities of the contributing charge carrier types exhibit different temperature dependences. Furthermore, special features of the band structure have to be taken into account [73]. Extended Hall investigations at lower temperatures are required to clarify the origin of the decrease with temperature.

## 8.2 FeSb$_y$ composition series

For this study, which was performed together with the Master student C. Schmidt, Fe-Sb films were deposited on SiO$_2$/Si wafers at room temperature by codeposition and the Sb content was varied between 70 at.% and 81 at.% [138]. Pieces of each wafer were afterwards post-annealed at various temperatures (T$_A$ = 150 °C, 200 °C, 250 °C, and 300 °C). However, the Fe distribution over the whole wafer was not homogeneous and thus the composition was determined after annealing for each sample with RBS.

### Film structure and composition

As already described in chapter 7.2.2, the FeSb$_3$ phase is only formed for a Sb content higher than 75 at.%. The composition limit above which the pure Sb phase is additionally formed could not be investigated. However, for an annealing temperature of 150 °C single phase skutterudite films are found up to 80 at.% Sb. An overview is given in table 7.3.
The change of the surface structure in dependence on the Sb content was again investigated by AFM. Films annealed at temperatures below 250 °C are completely smooth and no noteworthy changes of the surface morphology were observed. Therefore only films annealed at 250 °C or 300 °C will be discussed. Characteristic AFM images are shown in fig. 8.10 for selected films, which were annealed at 300 °C. The shown results agree basically with the annealed CoSb$_y$ composition series shown in fig. 8.6 and all investigated films are relatively smooth. For low Sb content (70 at.%) the FeSb$_2$ phase is formed and rod like structures can be seen on the surface. With increasing
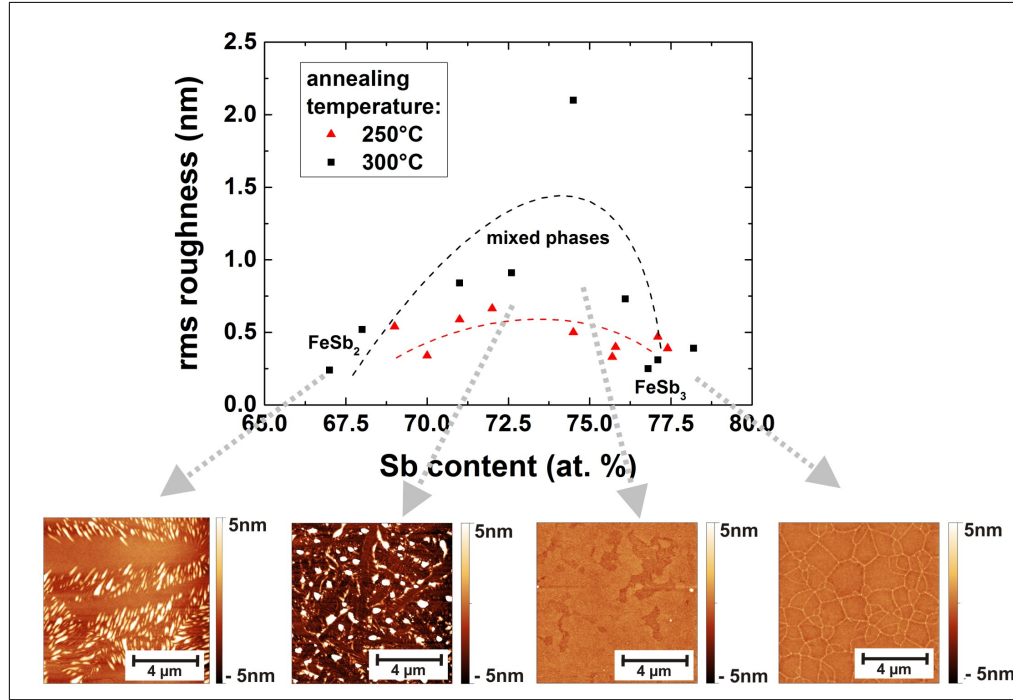
Figure 8.10: The rms surface roughness of Fe-Sb films as function of the Sb content for films annealed at 250 °C and 300 °C. In addition the phases detected by XRD and typical AFM images of films annealed at 300 °C are added. The dashed lines are only a guide to the eye.

Sb content, first particles occur and if the composition reaches nearly 75 at.% two regions could be distinguished. This is in agreement with the XRD results, where the FeSb$_3$ skutterudite and the FeSb$_2$ phase is detected. For these films SEM combined with EDX was performed, but the different regions could not be related to a specific phase. If the Sb content of the annealed films is larger than 76 at.%, the FeSb$_3$ phase is formed and the surface changes to a smooth grain structure. The typical surface cracks, which were already observed for annealed CoSb$_3$ films, were also found in some cases for films annealed at 300 °C.

The extracted rms roughness confirms these observations and the curves achieved for an annealing temperature of 250 °C and 300 °C are included in fig. 8.10. For single phase FeSb$_2$ and FeSb$_3$ films minimum values are observed, while the transition region with particles and inhomogeneous regions reveal larger roughness. The rms roughness is increasing slightly with annealing temperatures and all films exhibit values below 2 nm, which is also lower than the investigated CoSb$_y$ films. However, for the comparison the lower annealing temperatures for the Fe-Sb films have to be kept in mind.

109

**Thermoelectric measurements at room temperature**

Even though the structural properties of the annealed Fe-Sb and the annealed Co-Sb films are comparable, the thermoelectric properties differ drastically (see fig. 8.11 for FeSb$_y$ and fig. 8.7 for CoSb$_y$ films).

The resistivity of the Fe-Sb films at room temperature is much smaller than for the Co-Sb films and reveal only a weak dependence on the Sb content (fig. 8.11). Only a drop from about $1\,\mathrm{m\Omega cm}$ to about $0.5\,\mathrm{m\Omega cm}$ is observed for a Sb content of 75 at.% [138]. The formation of single phase FeSb$_3$ skutterudite films could be the reason. This low magnitude and the independence on compositional changes could indicate a heavily doped or degenerated semiconductor as well as metal like behaviour. To the best of my knowledge, no band structure calculations are published for FeSb$_3$ and therefore it is not known, if FeSb$_3$ is semiconducting. The valence electron count gives 68, which should be related to metallic like behaviour (VEC, see chapter 4.1). In a cooperation L. Hammerschmidt [157] calculated the band structure by DFT/PBE, which results in p-type metallic behaviour with the Fermi energy in the valence bands. Furthermore, the calculations predict a huge difference for spin up and down. While spin up exhibits extremely flat valence bands, for the other orientation the Fermi energy crosses only a linear band similar to that one found for CoSb$_3$. Ignoring the linear band due to its low density of states, pseudogaps in the range between $0.5\,e$V (indirect gap) and $1\,e$V (direct gap at $\Gamma$ point) can be found for this orientation. On the contrary, Möchel et al. [98] published temperature dependent resistivity measurements for FeSb$_3$ prepared by MERM and obtained semiconducting character with a gap of $16.3\,\mathrm{m}e$V. The corresponding curve was shown in fig. 4.12 (b) and their room temperature resistivity value is about four times larger than the observed values of the films investigated here.

The performed Hall measurements deliver deeper insights and confirm p-type conduction. The effective charge carrier concentration reveals large values in the order of $10^{22}\,\mathrm{cm}^{-3}$, while the effective Hall mobility is around $0.5\,\mathrm{cm}^2/\mathrm{Vs}$ and extremely small. The charge carrier density increases slightly with increasing Sb content, but no obvious dependence of the mobility on the Sb content can be found. The low resistivity is caused by the large carrier concentration and the FeSb$_3$ films should therefore reveal a metallic-like temperature dependence. Future work has to be done to improve the low mobilities. Therefore it is first necessary to identify the contributing scattering mechanism by temperature dependent measurements. In a second step methods have to be found to influence the scattering processes. One possible approach to get further insights might be also the synthesis and investigation of samples with different grain size (see chapter 7.2.3) to identify and vary the contribution of the grain boundary scattering.

The measured Seebeck coefficient is shown in fig. 8.11 (b). It has a positive sign and increases with increasing Sb content, especially for a Sb content larger than 75 at.%, for which single phase skutterudite films are formed [138]. The maximum value at
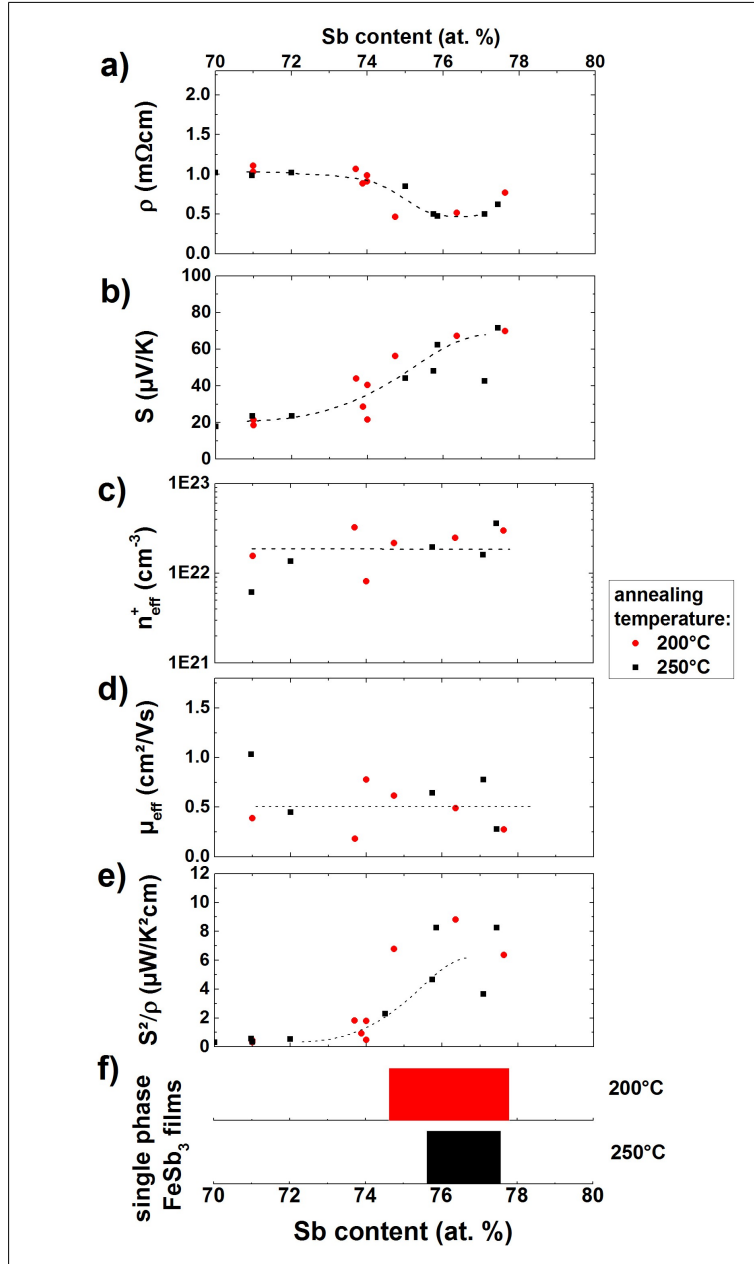
Figure 8.11: (a - e) Thermoelectric properties of Fe-Sb films with different Sb content at room temperature. The films were deposited at room temperature and post-annealed at 200 °C and 250 °C. The dashed lines are only a guide to the eye and the superscript "+" in the label of the effective charge carrier density indicates p-type conduction (positive Hall constant). The composition range of single phase skutterudite films is marked in (f) by the bars. Films with larger Sb content would be needed to determine the achievable maximum power factor $S^2/\rho$.

room temperature is $\sim$70 µV/K and therefore much higher than the maximum absolute value obtained for Co-Sb films is observed. Since Hall constant and Seebeck coefficient give both a positive sign, hole conduction dominates in these films. In case of CoSb$_3$ films, holes and electrons compete and the resulting thermal voltage is smaller. However, the large Seebeck coefficients are surprising, since band structure calculations, VEC and the obtained electric properties reveal rather metallic behaviour than semiconducting properties and thus a small Seebeck coefficient $S$. The large differences for spin up and spin down density of states determined by band structure calculation could be one reason for the large $S$. On the other hand, the films reveal a small Hall mobility. In combination with the large charge carrier density amorphous regions in the films could be an explanation. However this was not confirmed by EBSD measurements. An additional possibility are energy filtering effects at the grain boundaries. Anno et al. [33] reported for instance large Seebeck coefficients up to 600 µV/K in CoSb$_3$ thin films and explained them by taking only electrons into account which could pass the energy barriers emerging due to the grain boundaries. Future investigations including temperature dependent measurements are necessary to clarify this contrary results and to show how the intrinsic properties of the skutterudite crystallites play together with the properties caused by the structure (thin film, grain size, grain boundaries, etc). Furthermore, the contribution of the charge carriers for spin up and down have to be elucidated.

Using resistivity and Seebeck coefficient to calculate the power factor $S^2/\rho$ at room temperature, a maximum value of about $10\,\mu W/K^2cm$ is achieved for a Sb content of 77 at.% (fig. 8.11 (e)), which is 100 times larger than the value obtained for CoSb$_3$ films in this study. This room temperature value is in the range of the results given in literature references for optimized skutterudite based thermoelectric materials [27] and as shown for instance in fig. 4.9. The measurements have to be extended to higher temperatures and the thermal properties have to be characterized to evaluate the potential of these FeSb$_3$ thin films. Furthermore, it has to be kept in mind that the real Seebeck coefficient of the film is about 50 % larger (see chapter 9.2), since the obtained values are lowered by the influence of the SiO$_2$/Si(100) substrate on the measurements. Thus the achieved power factor of the Fe-Sb films at room temperature is already very promising. However, no investigation of the Seebeck coefficient or the power factor of FeSb$_3$ can be found in literature and these promising combination of $\rho$ and $S$ at room temperature was not yet reported.

To summarize, Fe-Sb thin films show the properties of a strongly doped p-type semiconductor with large Seebeck coefficient. They exhibit better thermoelectric properties (power factor) at room temperature than the CoSb$_3$ films, where two types of charge carrier compete. The optimum of the power factor with respect to the composition is not reached in this study, since it is still increasing with increasing Sb content (fig. 8.11). To estimate the real potential of these films, it is further necessary to characterize the thermal conductivity and thus determine the achievable $ZT$ value.

# 9 Influence of various substrates on the film properties

Besides the optimization of the thermoelectric properties, the thermal stability of the film material plays an important role especially for thin films and has also to be guaranteed for the skutterudite films. Thermoelectric materials have to resist high working temperatures and large temperature changes. In typical applications frequently performed heating cycles are usual and could cause strain, thermal fatigue, cracks, and the formation of different crystal phases [158].

By using thermoelectric thin films, one has therefore to pay also attention to the different thermal and mechanical properties of film and substrate and their interplay. If the linear thermal expansion coefficient $\gamma$ of film and substrate differ from each other, the heating process could induce cracks, bendings, defects or material loss due to thermal stress [159, 160, 161, 162, 163, 164]. As shown in fig. 7.5, the $CoSb_3$ films deposited at room temperature on $SiO_2/Si(100)$ reveal typically pronounced surface cracks after annealing at temperatures above $400\,°C$. If the thermal expansion coefficient of substrate and film is nearly the same, this crack formation in the film is expected to be avoided. The reported thermal expansion coefficients of $CoSb_3$ bulk samples are in a range between $8.5 \cdot 10^{-6}\,K^{-1}$ and $9.1 \cdot 10^{-6}\,K^{-1}$ [98, 165], thus substrates with a thermal expansion coefficients close to these values should be used. $SiO_2/Si(100)$ substrates exhibit a much lower thermal expansion coefficient $\gamma_s = 2.6 \cdot 10^{-6}\,K^{-1}$ compared to bulk $CoSb_3$ and it is therefore expected that the deposited Co-Sb film on these substrates exhibits the observed cracks. A detailed investigation of the influence of different substrates with various expansion coefficients on the film structure is given in chapter 9.1.

In general, substrates for thermoelectric films have to fulfill further requirements: thermal stability up to the working temperature of the thermoelectric material, low surface roughness, electrical insulating and low thermal conductivity. If the thermal stability of the substrate is not given up to the device working temperature, the substrate starts to decompose, to exhibit phase formations or to react with the film. The film itself is also affected and the functioning can not be guaranteed. If the roughness is in a comparable range to the film thickness, strong surface scattering or discontinuous films were achieved. Conductive substrates (thermally and electrically) would worsen the thermoelectric film properties. A large electric conductivity compared to the film could compensate the thermal voltage. If the substrate exhibits on the other side a larger thermal conductivity than the film, it would shortcut the

film thermally, which has to be kept in mind for the optimization of the thermal conductivity of a thermoelectric thin film. A reasonable lower thermal conductivity of the film compared to the substrate would be useless. Furthermore, conductive substrates could influence the measurements of the transport parameters as will be discussed in chapter 9.2.

## 9.1 Substrate influence on the film morphology

To investigate a possible influence of the substrate on the structural properties and the morphology of the film, $CoSb_3$ thin films were codeposited at room temperature on selected substrates with various thermal expansion coefficient $\gamma_s$ around the bulk value of $CoSb_3$. An overview of the used substrates is given in table 9.1. It is to note that the different special glass substrates "S-LAL13", "S-LAM51", "S-LAM3" and "S-TIH23" produced by the OHARA GmbH are thermally stable up to more than $700\,°C$ [153] and were renamed as $SG_\gamma$ (index $\gamma$ indicates the corresponding thermal expansion coefficient, see table 9.1). This is also the case for the special ceramic substrate "TS-10SX" (also OHARA Gmbh) renamed as $SC_{11}$ in the following. The focus of this study was lying on the influence of the different substrate expansion coefficients $\gamma_s$ on the film morphology. Therefore also substrates were investigated, whose thermal conductivities are not suitable for thermoelectric measurements and applications. These ones are marked red in table 9.1. All investigated substrates are electrically insulating, thermally stable in the interesting temperature range and sufficiently smooth (roughness well below $1\,nm$).

| Substrates | $\gamma_s$ ($10^{-6}$ K$^{-1}$) | $\kappa_s$( W/mK) | Sb (at.%) | Group | $d_s$(mm) |
|---|---|---|---|---|---|
| fused silica (FS) | 0.5 | 1.84 | 74 | I | 1.5 |
| silicon (100 nm SiO$_2$/Si) | 2.6 | 147.9 | 77/74 | I/II | 0.5 |
| sapphire Al$_2$O$_3$(0001/11$\bar{2}$0) | 5.0 | 18 | 78 | I | 0.5 |
| special glass (SG$_\gamma$) | 7.2$^b$/8.0$^c$/9.4$^d$/10.6$^e$ | <1 | 74 | II | 1.0 |
| special ceramics (SC$_{11}$) | 11.0$^f$ | 2 | 78 | I | 1.0 |
| magnesium ox. MgO(001) | 14.0 | 30 | 78 | I | 0.5 |
| CoSb$_3$ bulk | $\approx 9$ [98, 165] | <1 [38, 39] | | | |

Table 9.1: Chosen substrates and their thermal expansion coefficients $\gamma_s$, their thermal conductivity $\kappa_s$, the Sb content of the corresponding film, the defined sample group and the substrate thickness $d_s$. All substrates are electrically insulating. The red entries mark not suitable thermal conductivities with respect to thermoelectric applications. Furthermore literature values for CoSb$_3$ bulk samples are added.

$^{b-f}$ produced by Ohara with the following product names[153]:
$^b$ S-LAL13 / $^c$ S-LAM51 / $^d$ S-Lam3 / $^e$ S-TIH23 / $^f$ TS-10X

The film preparation via room temperature codeposition followed by a post-annealing step (see chapter 6.2) is a proper method to achieve smooth, single phase $CoSb_3$ films and was therefore used for this investigation. Due to the size of the sample holder, only a limited number of different substrates could be mounted at the same time and two deposition runs have to be performed resulting in two sample series, series I and series II (see table 9.1). The $SiO_2$(100nm)/Si(100) substrate was used in both runs as reference sample, since films on this substrate are well characterized by former investigations and possible differences of both series can be easily identified.

### Structural characterization

To validate the right film stoichiometry of both series RBS measurements were performed. The as-deposited films of the first series (I) have a Sb content between $(77 \pm 1)$ at.% and $(78 \pm 1)$ at.%, which is more than the stoichiometric 75 at.% of $CoSb_3$. The films of the second deposition series (II) exhibit a slightly reduced Sb content of $(74 \pm 1)$ at.%.
To investigate the formed crystalline phases, XRD measurements with a constant incident angle of $\omega = 10°$ were performed (see ch. 5.1). The obtained XRD scans are shown in fig. 9.1 for different Co-Sb films on the reference substrate $SiO_2$/Si(100)



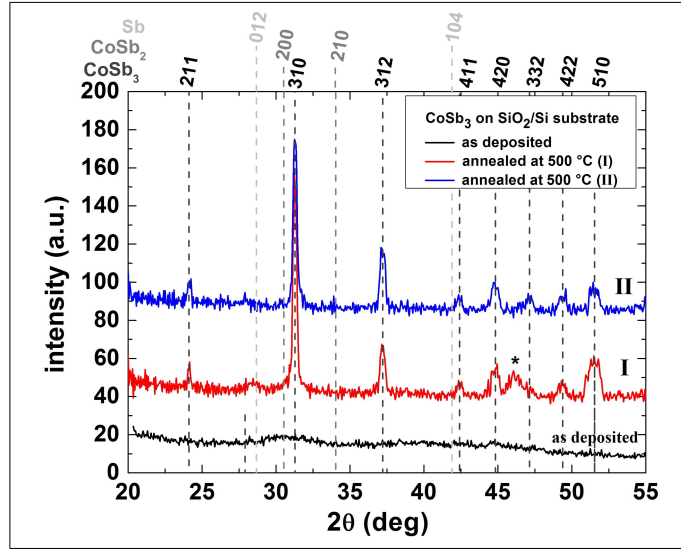Figure 9.1: XRD pattern of different Co-Sb films prepared on the reference substrate $SiO_2$/Si(100) [152]. Additionally to an exemplary as-deposited film (bottom), the pattern for an annealed film of series I (top) and II (middle) are shown. Substrate peaks are marked by asterisk.

representative for all other films of the particular series. The as-deposited films reveal no peaks and are therefore x-ray amorphous. The films were afterwards annealed to form crystalline phases. In the scans obtained after annealing at 500° several peaks are observed for the films of both series, which can be attributed to the skutterudite phase. Besides the skutterudite major phase, the pattern of the Sb rich film (series I) gives indications for the existence of metallic Sb as minor phase. Weak reflections belonging to the $CoSb_2$ phase can be found for the film of series II, which is in agreement with the lower Sb content. Similar results were also obtained on the other substrates of each deposition series. It is to note that there are no indications for an introduced film texture by using the single crystalline substrates $Al_2O_3(0001/11\bar{2}0)$ and MgO(001).

The surface structure was investigated by AFM. All as-deposited samples showed a very smooth surface with a roughness smaller than 1 nm and the found surface morphology gives also no indication for different film growth on the single crystalline substrates. The AFM images of the annealed films prepared on the different substrates are presented in fig. 9.2. The images of the Sb-rich films (sample series I) can be found in the top row ((a) - (d)) of fig. 9.2 and exhibit a cracked surface, while the Sb-deficient film (sample series II) are presented in the bottom row ((e) - (i)) and reveal star-shaped structures with cracks. Since these differences occur also on the reference substrate ((a) and (e)), the origin of the different surface morphology is the difference in composition and phase formation.

First the changes of series I are discussed with increasing $\gamma_s$. The $SiO_2(100nm)/Si(100)$ substrates exhibit a thermal expansion coefficient of $\gamma_s = 2.6 \cdot 10^{-6} \, K^{-1}$ and the expected cracked film surface is observed (fig. 9.2 (a)). For $Al_2O_3(0001)$ substrates with a somewhat larger expansion coefficient of $5 \cdot 10^{-6} \, K^{-1}$ only minor changes of the surface morphology compared to the reference substrate of series I can be found (fig. 9.2 (b)). The expansion coefficient of the ceramic substrate, $SC_{11}$, is close to that one of bulk $CoSb_3$. The film surface is therefore very smooth and the number of cracks decreases drastically (fig. 9.2 (c)). A further increase of $\gamma_s$ up to $14 \cdot 10^{-6} \, K^{-1}$ (MgO(100), fig. 9.2 (d)) causes again a large number of cracks and reveal similarities to the surface morphology observed for the film of series I prepared on $SiO_2/Si(100)$. The investigation of the surface morphology for series II yield the same results. For the series of the special glass substrates with $\gamma_s$ values between $7.3 \cdot 10^{-6} \, K^{-1}$ and $10 \cdot 10^{-6} \, K^{-1}$, the number of cracks is rapidly diminished in comparison to the film on the reference sample of series II (fig. 9.2 (e)). The smoothest surface was found for $SG_{10.6}$, for which nearly no cracks were observed at the film surface (fig. 9.2 (i)). The smoothest films of both series are therefore observed for a substrate thermal expansion coefficient $\gamma_s$ close to that one of bulk $CoSb_3$, as expected [152]. Furthermore the thermal expansion coefficients of the special glasses are between that ones of $Al_2O_3$ and $SC_{11}$ of series I and the results of both deposition series agree well, which is illustrated in fig 9.2 by the bight yellow arrow.
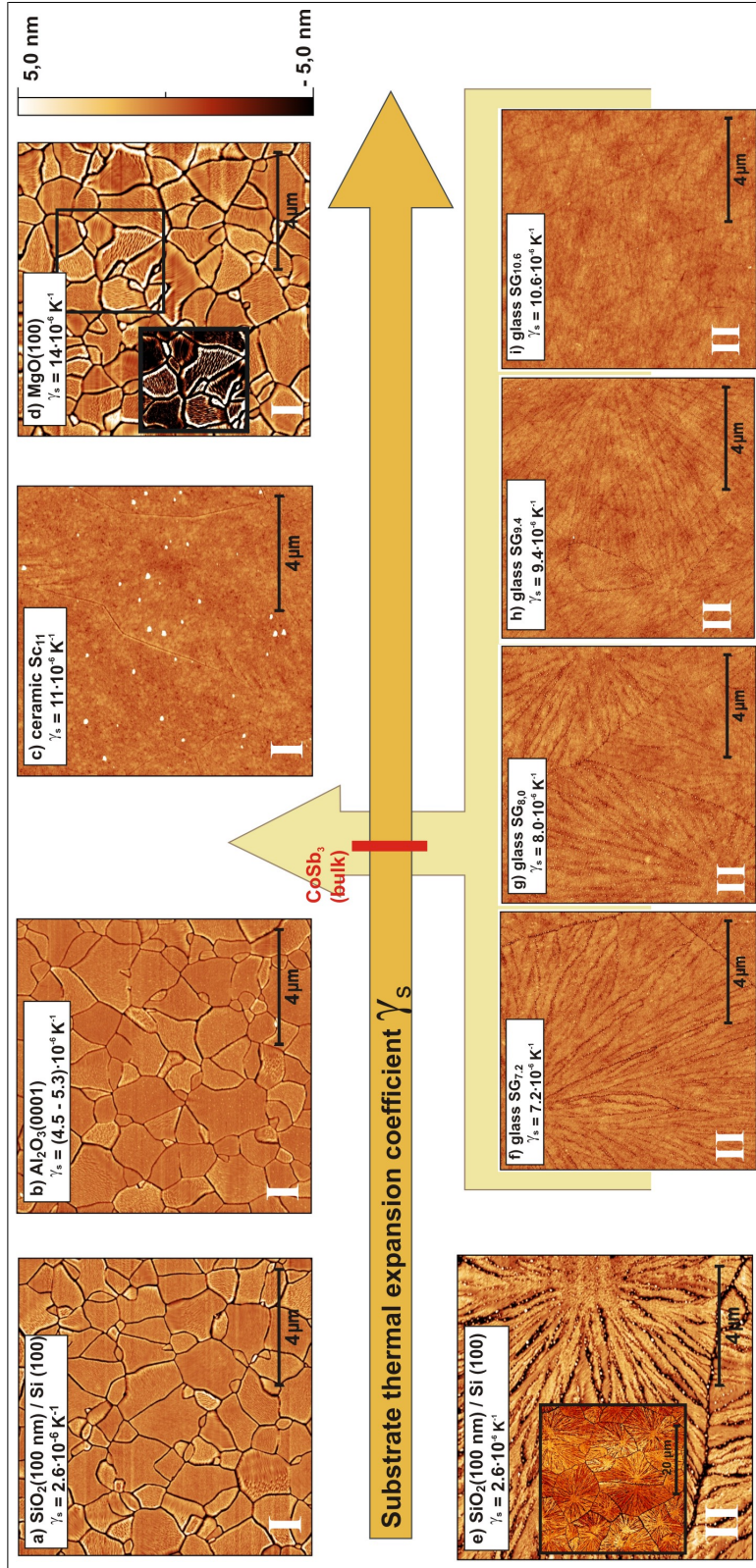
Figure 9.2: (a – i) AFM images of Co-Sb films on various substrates with different thermal expansion coefficient $\gamma_s$ (top row: series I; bottom row: II). The images were obtained after annealing at 500 °C. Additionally the expansion coefficient of CoSb$_3$ (bulk, [98, 165]) is indicated in red color. The films prepared on the reference substrates SiO$_2$/Si(100) are shown in the images a) and e). Both series exhibit a different type of surface morphology due to differences in their composition [152]. The smoothest film is shown in i) and was prepared for series II on the SG$_{10.6}$ glass substrate. The bright yellow arrow should roughly indicate, which range of $\gamma_S$ is covered by the different glass substrates SG$_\gamma$ of series II in comparison to series I.

The visual impressions, concerning the crack formation, can be quantified by extracting the rms-roughness of the film surfaces taken from the $10 \times 10\,\mu m^2$ sized area of the AFM images. The dependence of the rms-roughness (including cracks and surface roughness) on the thermal expansion coefficient of the substrate is summarized in fig. 9.3. The extracted rms-values of both sample series reveal the expected minimum value, where the thermal expansion coefficients of the film and the substrate are similar [152]. For the films, where cracks are absent, individual grains can not be identified in AFM images and the grain sizes were determined by EBSD (not shown). The determined grain size is only slightly increased compared to the cracked films and no drastic changes can be found [152].
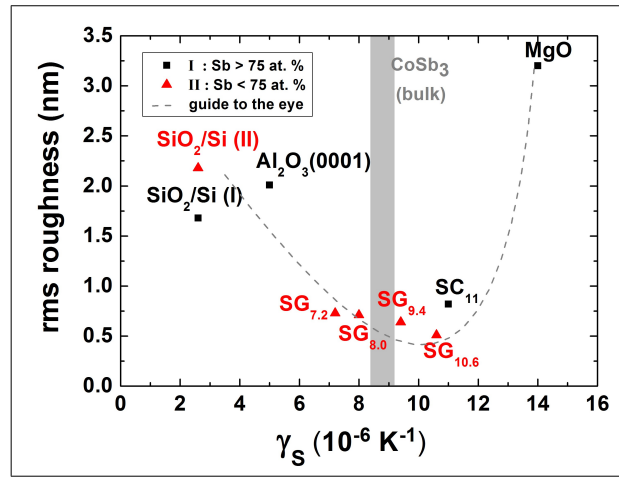


Figure 9.3: The rms-roughness of the Co-Sb thin films as function of the thermal expansion coefficient $\gamma_s$ of the used substrates [152]. A minimum of the rms-roughness is obtained for $\gamma_s$ - values, which are close to $\gamma$ of CoSb$_3$ bulk samples (marked as gray stripe, [98, 165]).

## Stress measurements

The $\sin \chi^2$ method was applied in order to determine the residual film stress in these samples [166]. This investigation can support the idea that the change in surface morphology and in rms-roughness is caused by thermally induced stress due to the mismatch of the thermal expansion coefficient of film and substrate.

For this method the shift of the peak position of the (503) skutterudite peak is measured in dependence of the tilting angle $\chi$ and in different directions by additional rotation of the sample around ($\phi$) [108]. The corresponding changes of interplanar distances were calculated from the peak shift by the Bragg equation (equ. 5.1). If

the biaxial stress model can be used, a linear dependence of the interplanar distance and $\sin \chi^2$ should be observed. This is only the case in absence of shear stress contributions. In that case the film stress can be easily calculated using the isotropic Young´s modulus ($Y_{mod} = 160$ GPa [167]) and the Poisson ratio ($\nu = 0.193$ [167]) of bulk $CoSb_3$ [108]. The measured dependence of the interplanar distance on $\sin \chi^2$ can be exemplarily seen in fig. 9.4 (a) for a $CoSb_3$ film on $Al_2O_3$ for two directions ($\phi_1$ $=0°$ and $\phi_2 =90°$). A linear dependence on the tilting angle is observed. In addition no difference between both rotation angles are found.
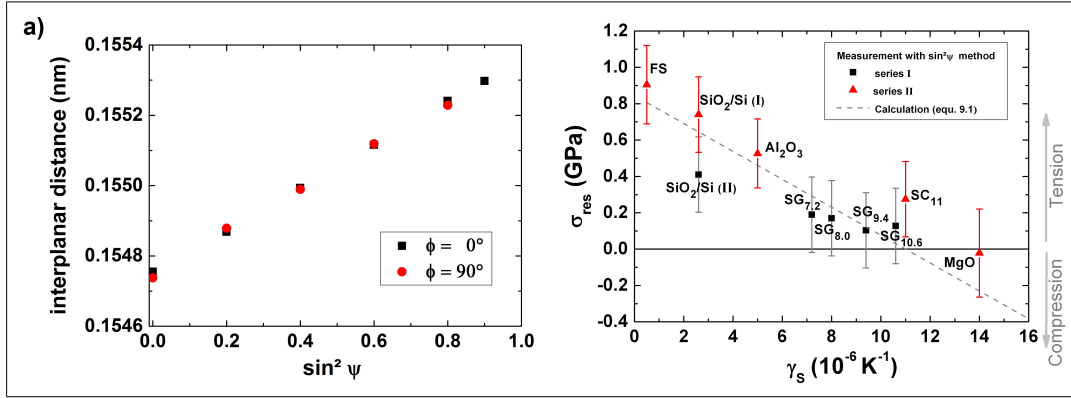


Figure 9.4: a) Strain measurement with the $\sin^2 \chi$ method for a $CoSb_3$ film deposited on $Al_2O_3$ (0001). The interplanar lattice distance was calculated using the peak position of the (503) peak in the XRD pattern, which was measured under different tilting angles $\chi$; b) Calculated residual stress for the films on the different substrates, using the slope of the strain measurements [152].

Similar curves are also observed for the films on the other substrate and out of the slope of this curve the residual film stress $\sigma_{res}$ can be calculated [108]. The determined values are shown in fig. 9.4 (b) as a function of the substrate thermal expansion coefficient $\gamma_s$. Tensile stress ($\sigma_{res} > 0$) is observed for $\gamma_s$ lower than $11 \cdot 10^{-6}\,\mathrm{K}^{-1}$. In this region $\sigma_{res}$ is decreasing with increasing $\gamma_s$ for both series, which is consistent with the reduction of the mismatch between the thermal expansion coefficient of the substrate $\gamma_S$ and of the film $\gamma_F$. For substrates with suitable expansion coefficients, the stress approaches very small values, which goes along with the change from cracked to smooth surfaces obtained for these films. For MgO(100) with the highest thermal expansion coefficient, the XRD peaks shift towards lower angles, which indicates compressive stress with $\sigma_{res} < 0$. This substrate has therefore a larger expansion coefficient than the film. Despite the fact that compressive stress is measured, the surface exhibits a large number of cracks usually indicating tensile

stress. Nevertheless, the film reveal in contrast to the other films bendings towards the grain boundaries, which is better visualized in the inset of fig. 9.2 (d) revealing a bright contrast of the bendings. This could be an indication for a different process of crack formation under compressive stress. In combination with the large error bars of the stress measurements, further investigations are needed to understand the results for MgO(100) completely.

The large error bars are caused by the relatively low $2\theta$-value of $\sim 59.62°$ for the used (503) reflection. $2\theta$ angles larger than $100°$ are typical for this method, since the observed peak shifts are better resolvable in this angle range and the error becomes smaller. However, this was not feasible as the peak intensities at higher angles were too low for the thin films. The used peak delivers good results only for strong peak shifts and therefore high stresses (here $> 200\,\text{kPa}$). For lower stress the shifts become too small and deviations from the linear behavior occur.

For thermally induced stress due to the different thermal expansion coefficients of film and substrate, a simple expression for $\sigma_{res}$ can be given [159]:

$$\sigma_{res} = Y_{mod}(\gamma_f - \gamma_s)(T_C - T_{meas}), \tag{9.1}$$

where $Y_{mod}$ is the Young´s modulus of the film, $\gamma_f$ and $\gamma_s$ the thermal expansion coefficient of film and substrate, $T_C$ the temperature during phase formation, and $T_{meas}$ the measuring temperature. This equation was used to fit the measured data of the residual film stress and the corresponding curve is additionally plotted in fig. 9.4 (b). By using $Y_{mod}= 160\,\text{GPa}$, $T_C = 500\,°\text{C}$ (annealing temperature), and $T_{meas} = 20\,°\text{C}$, the best fit was achieved for $\gamma_f \sim 11 \cdot 10^{-6}\,\text{K}^{-1}$ [152].

It is further to note that only the residual stress of the cracked surface could be measured here. The initial tensile stress is larger, but the rough agreement of experimental values and calculation confirms that the thermally induced stress is connected to the difference in the thermal expansion coefficients between film and substrate. This is also expressed by the change of the film morphology by approaching the $\gamma$ value of bulk CoSb$_3$ [152].

**Resistivity measurements**

The room temperature resistivity of the films deposited on different substrates was measured after annealing at $500\,°\text{C}$. For both series, the lowest resistivity was observed for the smooth films without cracks (fig. 9.5) [152]. Less charge carrier scattering due to the absence of cracks could be the origin of the decrease and was also indicated by mobility measurements (not shown). Besides the larger thermal stability, a proper substrate choice results therefore also in better thermoelectric properties. Comparing both series, a big difference of the absolute resistivity value can be found, which can be attributed to the composition dependence shown in chapter 8.1.2. Film series II is closer to the exact stoichiometry of semiconducting CoSb$_3$ and reveals
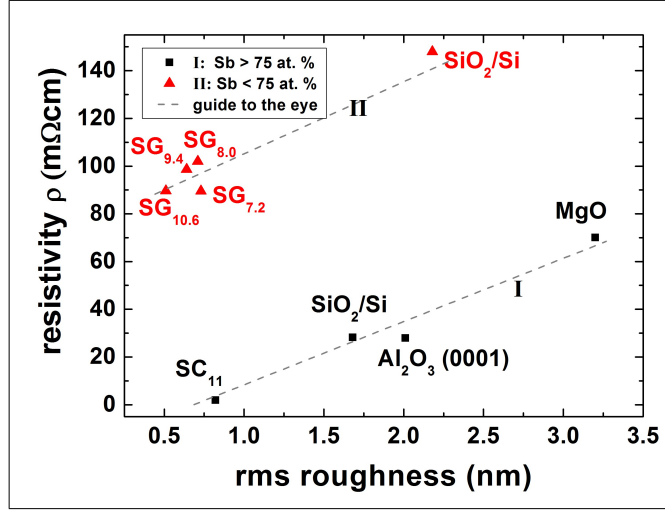
Figure 9.5: Resistivity in dependence on the rms-roughness of the films and the chosen substrate for both deposition series [152]. If the thermal expansion of film and substrate is comparable, a low rms-roughness and a low resistivity is observed for both series. The difference between the absolute values of both series is due to the different composition.

therefore a larger resistivity. For the investigated films, the influence of different composition is larger than the influence of an optimized surface morphology.

## Summary

Differences of the thermal expansion coefficient of film and substrate generate strong stress and cracks in the films and can be reduced by a proper substrate choice [152]. For substrates with a expansion coefficient $\gamma_s$ between $9 \cdot 10^{-6}\,\mathrm{K}^{-1}$ and $11 \cdot 10^{-6}\,\mathrm{K}^{-1}$ the cracks vanish and the induced thermal stress becomes very small. Suitable substrates are the Ohara special glass $SG_{9.4}$ with $\gamma_s = 9.4 \cdot 10^{-6}\,\mathrm{K}^{-1}$, $SG_{10.6}$ with $\gamma_s = 10.6 \cdot 10^{-6}\,\mathrm{K}^{-1}$ and the special ceramic $SC_{11}$ with $\gamma_s = 11 \cdot 10^{-6}\,\mathrm{K}^{-1}$. Another possible candidate should be $ZrO_2$, with a thermal expansion coefficient around $9.2 \cdot 10^{-6}\,\mathrm{K}^{-1}$ [168]. All other requirements needed for the usage as thermoelectric substrate are also fulfilled for each of these substrate types. This investigations implies that the thermal expansion coefficient of the $CoSb_3$ films has also to be in this range [152].

## 9.2 Substrate influence on thermoelectric properties and measurements

Low temperature and high temperature Seebeck measurements were performed for $CoSb_3$ films on four different substrates: fused silica, Ohara special glass $SG_{10.6}$, thermally oxidized $SiO_2$(100nm)/Si(100) and $ZrO_2$(100). As described in chapter 9.1 only the Ohara special glass and $ZrO_2$ are suitable candidates, which fulfill all requirements needed for thermoelectric applications. This investigation should give especially an assessment, if the results presented in chapter 8 for the measured Seebeck coefficient of Co-Sb and Fe-Sb films on $SiO_2$(100nm)/Si(100) are reliable. An individual sample series was performed for both temperature ranges (low and high temperature), since the sample holder has a limited size and all setups need a little bit different sample geometry. Before the deposition process was performed, the substrates were broken into smaller pieces with the right shape to avoid possible damage of the deposited films by the breaking procedure. The Co-Sb films were codeposited at room temperature onto the different substrate pieces and annealed at 450 °C under UHV conditions after short exposure to air. This procedure was repeated for both sample series and yields comparable film composition and microstructure within each series, but possible differences in the structural and transport properties compared to each other. The Seebeck coefficient of both series were characterized afterwards together with the Master students J. Franke and D. Reinhardt [136, 137]. The measured data curves are shown in fig. 9.6.

### Low temperature Seebeck measurements for Co-Sb films on different substrates

The measurements of the Seebeck coefficient at low temperature is shown in fig. 9.6 (a). Both, the magnitude and the trend of the measured curves are very similar for the samples on fused silica, Ohara special glass, and $ZrO_2$, while the measurements for the film on $SiO_2$(100nm)/Si(100) reveal much smaller absolute values and the observed minimum occurs at lower temperatures [137].
The smaller absolute values can be explained by the influence of the larger thermal conductivity of Si on the measurements of the Seebeck coefficient. The $SiO_2$/Si(100) substrate does thermally shortcut the film impeding the development of the desired temperature gradient. This is observed in the experiment by an obvious increase of the cold side temperature of the setup, which should be constant. This temperature increase does not occur for the other substrates. A large amount of heat is directly transfered through the Si from the hot to the cold side and the actual thermal gradient in the film is therefore much lower than the measured one, which yields a lower Seebeck coefficient.
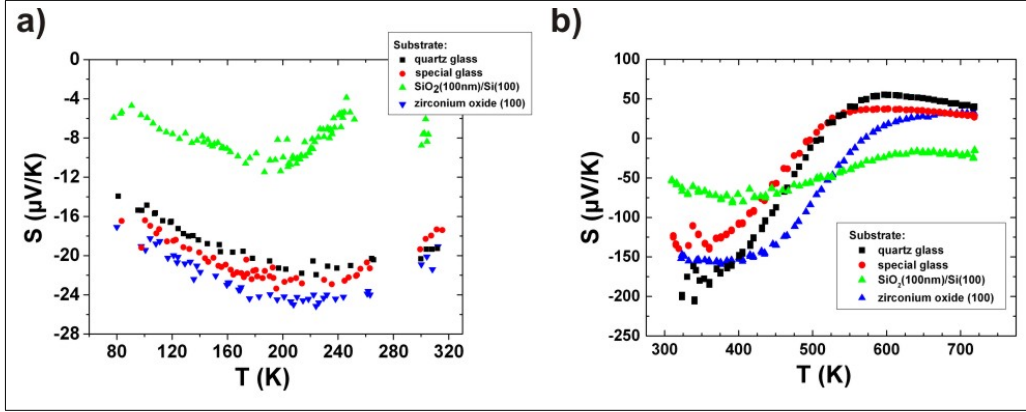
Figure 9.6: Low temperature and high temperature measurements of the Seebeck coefficient of Co-Sb films on different substrates [136, 137]. For each temperature regime (low and high temperature) an individual sample series was deposited.

This can be demonstrated by simple simulations with the program Energy 2D of The Concord Consortium [169] as shown in fig. 9.7 for films on fused silica and on $SiO_2(100nm)/Si(100)$. The simulations are presented for the geometry of the room temperature setup (fig. 5.5), since this setup was used for all Seebeck measurements of the composition series (ch. 8). The size ratios of the room temperature setup (fig. 5.5)) and of the sample were taken analog to the realistic experimental geometry. The volume of the film is negligible compared to the volume of the substrate. The film temperature and the temperature at the bottom side of the substrate should therefore coincide. Additionally interlayers (ZS in fig. 9.7) with adjustable thermal conductivity $\kappa_{ZS}$ were placed between the copper blocks and the sample to simulate the different thermal coupling and the temperature drop in the thermal glue (used for insulation, blue in fig. 5.5 (a)). A high thermal conductivity of the interlayer ($\kappa_{ZS} = 10\,\mathrm{W/Km}$) represents a good thermal coupling, while lower values correspond to worse coupling. The simulations were performed in such a way that the initial temperature was chosen equal to 293 K and the heater at the left side of the sample was switched on for a fixed time of 240 s. The used heater power was chosen comparable to the experimental one.

As it can be seen in fig. 9.7 (a), the measured thermal gradient ($T_{TC2}$ - $T_{TC1}$) and the gradient present in the film ($T_{F2}$ - $T_{F1}$) are equal for the fused silica substrate and reveals a good thermal coupling [137]. Nearly all of the temperature drop in the film occurs over the slit, as it should be for ideal measurements [133]. The cold side temperature ($T_{TC2}$) is not affected. The simulation for the film on $SiO_2(100nm)/Si(100)$ with good thermal coupling are shown in fig. 9.7 (b) and reveal different results. First it can be seen that the cold Cu block ($T_{TC2}$) is also heated as observed in the ex-
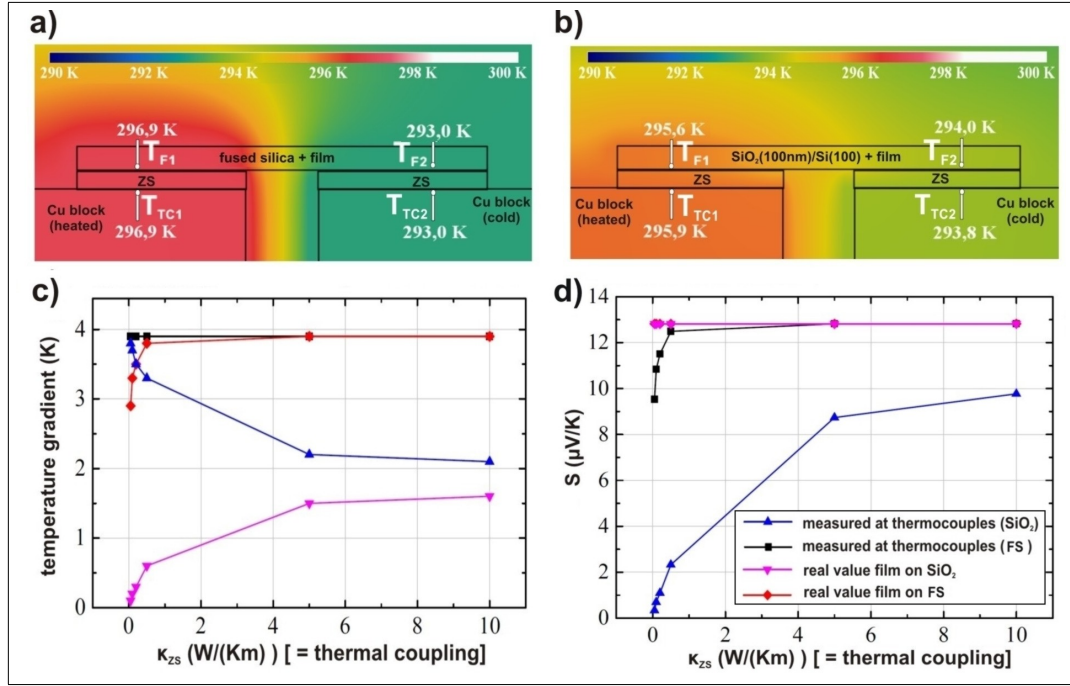
Figure 9.7: Simulations of the temperature development during the measurements of the Seebeck coefficient with the room temperature setup [137]. The initial temperature was 293 K and heating of the left sample side was performed for 240 s. The introduced interlayer ZS should simulate the thermal coupling between copper block and substrate by varying its thermal conductivity $\kappa_{ZS}$. a) for a film on fused silica substrate (FS) and good coupling ($\kappa_{ZS} = 10$ W/Km) b) for a film on SiO$_2$(100nm)/Si(100) and $\kappa_{ZS} = 10$ W/Km. c) The extracted temperature gradient at the thermocouples ($T_{TC2} - T_{TC1}$) and the real film gradient ($T_{F2} - T_{F1}$) are shown for both substrates in dependence of $\kappa_{ZS}$ [137]. d) The corresponding Seebeck coefficient for an assumed Seebeck coefficient of 13 µV/K for the film [137]. The shown legend belongs also to the curves shown in (c).

periments. A lot of heat is only transferred and not used to achieve the temperature gradient [137]. Additionally a vertical temperature drop occurs over the interface and the gradient in the film is lower than the measured one. This effect is getting even stronger, if the thermal coupling to the substrate becomes worse.

The influence of this coupling was further investigated by changing the thermal conductivity $\kappa_{ZS}$ of the interlayer stepwise and performing the simulation procedure for each case. The results are given in fig. 9.7 (c) for both substrates. For the fused silica the measured and the real gradient differ only for very bad coupling ($\kappa_{ZS} < 1$ W/Km), while for SiO$_2$(100nm)/Si(100) no agreement of the gradients can be found in the in-

vestigated range [137], however the difference becomes smaller for good coupling. In practice, a good thermal coupling must be ensured for reasonable measurements. By assuming for instance a Seebeck coefficient of $13\,\mu V/K$ for the film, which is close to the experiment, the measured Seebeck coefficient on fused silica differs again only for very bad coupling from the real film value (fig. 9.7 (d)), while the values measured for the films on $SiO_2(100nm)/Si(100)$ are lower for each configuration. This explains rather well the lower absolute values found in the experiment for films on $SiO_2(100nm)/Si(100)$ compared to the other investigated substrates. For the geometry of the low-temperature measurement head, similar results are achieved. However the underlying mechanism is slightly different and details can be found in other studies [137].

Furthermore, it is to note that the measured temperature curves for the films on $SiO_2(100nm)/Si(100)$ change with time. The Seebeck coefficient of the same sample became in later investigations for example positive at room temperature ($\sim 100\,\mu V/K$) and the minimum shifts to even lower temperatures [137]. The films on the other substrates were also remeasured and the initial curves could be reproduced. This is in agreement to the work of Kumar et al. [64], who reported for MgO and $SiO_2/Si$ substrates oxidation at the substrate interface. It is claimed that Sb reduces MgO and the thermally oxidized $SiO_2/Si$ substrate provides good diffusion paths for oxygen. Oxidation was not observed in this work for quartz (single crystalline $SiO_2$) and glass substrates. Quartz exhibits less diffusion channels and larger energy barriers, while for glass substrates usually additional constituents are added, which occupy the interstices impeding also oxygen diffusion [64].

## High temperature measurements

The high temperatures measurements for the films on different substrates were performed in a home-built setup and confirm the low temperature measurements. Details regarding the setup can be found elsewhere [136, 170]. In fig. 9.6 (b) the measured Seebeck coefficients for temperatures between $300\,K$ and $700\,K$ are shown for the different samples. The absolute values do not match to the low temperature measurements, since both series were deposited separately and could exhibit different composition and microstructure. Nevertheless, the obtained curves confirm that the film on $SiO_2(100nm)/Si(100)$ exhibits a different character compared to the films on the other investigated substrates. Close to room temperature the same trends were observed as for the low temperatures measurements. The Seebeck coefficient measured for the film on the $SiO_2(100nm)/Si(100)$ substrate reveal smaller absolute values caused by the larger thermal conductivity of Si. However, the Seebeck coefficient of the other samples reveal for higher temperature a sign change due to the onset of intrinsic excitation as expected from literature for lightly n-doped $CoSb_3$ (see fig. 4.6), while the Seebeck coefficient of the film on $SiO_2(100nm)/Si(100)$ stays nega-

tive, even though the basic shape is quite similar [136]. These observation cannot be explained by the thermal shortening of the film due to the larger thermal conductivity of Si and might be related to pores (so-called pin holes) in the thermally oxidized $SiO_2$ interlayer. These pores give electrical connection between the Si and the film, which affects the measurement especially in the high temperature regime, where the resistivity of the Si decreases by intrinsic excitation [136]. The breakthrough of the oxide is usually observed in this temperature range. Another explanation might be also the expected oxidation at the substrate interface, which was already discussed for the low temperature Seebeck measurements.

## Summary

The temperature dependent measurements demonstrate clearly that Si(100) with $100\,nm$ thermally oxidized $SiO_2$ is not usable as substrate for thermoelectric thin films for many reasons. Possible oxidation at the interface to the film could influence strongly the film properties in time and it is reported that this will worsen the power factor [64]. Occurring pin holes in the oxide will yield wrong values for the measured transport coefficients at high temperatures. Furthermore, their influence is random and can not be controlled. Substrates with large thermal conductivity (which is also the case for $SiO_2(100nm)/Si(100)$) affect the measurements of the Seebeck coefficients and much lower absolute values are determined.

These results denote caution by the interpretation of the transport parameter found for the composition series (chapter 8). Since the thermoelectric measurements were performed immediately after deposition, no altering by oxidation is expected for these samples. Furthermore, only low- and room temperature measurements are presented, where the influence of the Si due to pinholes should be rather low and the oxidation process is not supported. It is therefore believed that occurring trends can be still demonstrated, even though the absolute values have to be taken with caution. This is especially the case for the Seebeck coefficient due to the thermally shortening of the film. However, the $SiO_2(100nm)/Si(100)$ substrates are similar for all the samples and should give therefore about the same quantitative change of the Seebeck coefficient. To estimate the change of the absolute value due to the thermal shortening, several Co-Sb and Fe-Sb films were simultaneously deposited on the Ohara special glass $SG_{10.6}$ (see ch. 9.1) and on the $SiO_2(100nm)/Si(100)$ substrate. The observed underestimation of the Seebeck coefficient on $SiO_2(100nm)/Si(100)$ at room temperature was for this films about 50 %, which can be also seen in fig. 9.6 (a). This would count for a correction of the power factor presented in chapter 8 by a factor of 2.25.

# 10 $Fe_xCo_{1-x}Sb_3$ - controlled doping by substitution of Co with Fe

The thermoelectric figure of merit $ZT$ and especially the power factor $S^2/\rho$ depend on the charge carrier density as shown in fig. 2.1 (b), yielding semiconductors as most suitable material group for thermoelectrics. Conventional thermoelectric materials exhibit charge carrier densities in the range of $10^{19}\,cm^{-3}$ to $10^{20}\,cm^{-3}$. For the optimization of the power factor it is necessary to adjust the charge carrier density by controlled doping. One possibility to adjust the charge carrier density of $CoSb_3$ is to substitute Co by other elements like Fe or Ni. Fe has one electron less than Co and will create holes in the system, which results in a more p-type conductivity. On the other hand, Ni will introduce electrons leading to n-type doping. In this chapter the substitution of Co by Fe will be discussed for thin films. The $Fe_xCo_{1-x}Sb_3$ films were therefore synthesized by codeposition of all three elements or alternatively by using the MERM method (see ch. 6.2). The study was performed together with the Master student A. Dalla [171].

In chapter 8 it was shown that pure $CoSb_3$ is bipolar and exhibit two types of charge carrier, while $FeSb_3$ is dominated by hole conduction. By investigating the electric properties of films with different Fe substitution level $x$, additional insights into the individual properties of the different charge carrier types can be given and also a more realistic estimation of the charge carrier densities in the bipolar Co-Sb films.

## 10.1 Properties of codeposited $Fe_xCo_{1-x}Sb_3$ films

### Deposition and structural properties

In case of the codeposited films, it is more complicated to control the composition. As explained in chapter 6.3 the calibration function of the film composition compared to the nominal composition is needed due to the change of the Sb sticking coefficient for codepositions. For the deposition of $Fe_xCo_{1-x}Sb_3$ with a specific $x$, the Sb rate $\Phi_{Sb}$ was kept constant. The corresponding Co rate $\Phi_{Sb}$ was calculated with respect to the chosen Sb rate via calibration curve and equation 6.1. Afterwards the Fe rate was calculated by using in equation 6.1 the nominal ratio of Co to Fe $((1\text{-}x)/x)$ and the determined Co rate. In contrast to the usual rates used for Co to achieve a ratio of Sb:Co around 3:1 (about $0.1\,\text{Å/s}$), much smaller rates have to be used if additional Fe is introduced to keep the ratio of Sb:(Fe+Co) constant at about 3:1.

Therefore a calibration curve over a wide range of the Sb:Co ratio is needed, which is shown in fig. 10.1 (a). The observed curve reveals a surprisingly linear behaviour over the whole composition range. Furthermore, the calibration of the effusion cell temperature to control the Fe rate has also to be performed in a wide range and is shown in fig. 10.1 (b). It exhibits the known exponential character, caused by the temperature dependence of the vapour pressure (Clausius-Clapeyron-equation, [172]).
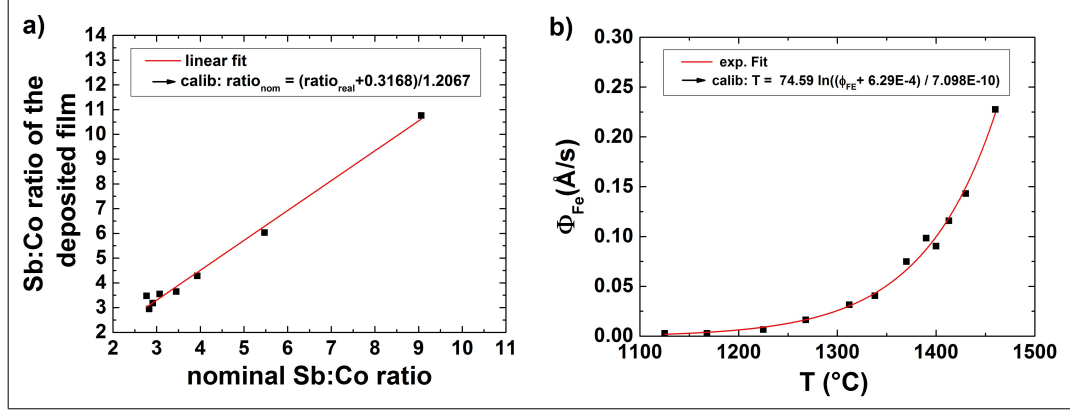


Figure 10.1: Used calibration curves for deposition of Fe$_x$Co$_{1-x}$Sb$_y$ films. a) The calibration curve for the desired Co to Sb ratio $((1-x)/y)$ in the final film. Since the Sb rate is kept constant, the corresponding nominal ratio has to be adjusted by changing the Co flux. b) The calibration curve to determine the needed effusion cell temperature for a specific Fe rate.

To demonstrate the substitution of Co by Fe in MBE grown Co-Sb thin films, samples with different nominal Fe content $x$ (0.05, 0.1, 0.2, 0.3, and 0.5) were deposited at room temperature on SiO$_2$(100 nm)/Si(100) substrates and post-annealed at 450 °C. The composition of the ~40 nm thick Fe$_x$Co$_{1-x}$Sb$_3$ was verified by RBS and the phase formation was investigated via XRD. All samples exhibit a Sb content of (77 ± 1) at.%. The Fe content $x$ varies between 0.06 and 0.49, however the error is especially for low values of $x$ relatively large, since the Fe and the Co peak overlap in the RBS spectra due to the small differences of their atomic mass.

The skutterudite phase is the major phase in all investigated samples (fig. 10.2) and despite the relative large Fe content of some films no other phases could be detected. A peak shift of all peaks towards lower angles is observed with increasing Fe content, which corresponds to an enlarged lattice parameter. This is an indication that Fe actually substitutes Co in the skutterudite crystal. The peak shape reveals nearly no changes, only the film with the largest Fe content of $x = 0.49$ gives some weak indications for a peak shoulder. It is therefore believed that all samples are homogeneous
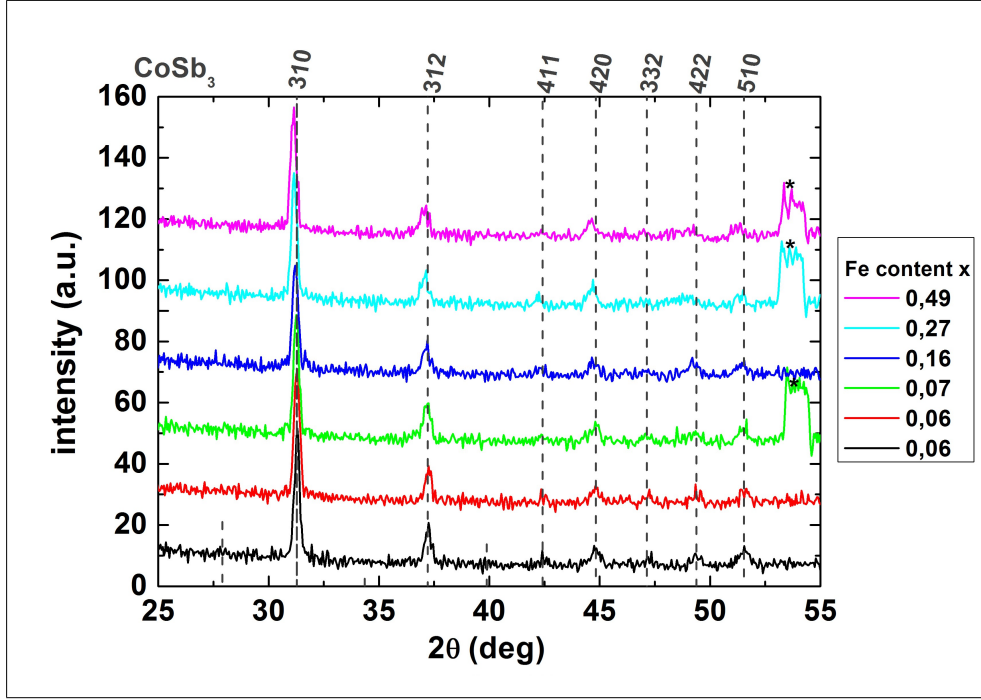
Figure 10.2: XRD spectra of $Fe_xCo_{1-x}Sb_3$ with different Fe content $x$. The skutterudite phase is the only detected phase and with increasing Fe content, a peak shift occurs. The asterisk marks substrate peaks.

with respect to the Fe distribution. If separation of Fe rich and Fe deficient regions with different lattice constants would be present, peak broadening, peak shoulders or side maxima would be observed.

The patterns were analyzed in detail by Rietveld refinement to extract the lattice constant $a$. The resulting refinement is shown for $x = 0.49$ in fig. 10.3 (a) and the extracted lattice constant in dependence of the Fe content in fig. 10.3 (b). Here a linear slope following Vegards law [173] is roughly observed, which is also in agreement to the literature [174]. The film with $x = 0.49$ seems to deviate from the linear function. If the substitution limit is reached, deviations from linear behaviour were also reported in literature, which is usually the case for bulk samples with $x > 0.15$ [175, 176]. The achieved substitution level for the MBE grown films is larger than 0.3 and therefore considerably above the bulk value. Where exactly the deviation from the linear behaviour starts in the present case, has to be investigated in future studies, since the chosen step size of $x$ is relatively large.

Another possibility to explain the increasing cross plane lattice constant might be stress induced by the Fe atoms. To exclude the influence of stress on the lattice

parameter, $\sin^2\chi$ measurements were performed for three films of another series with various Fe content. Details about the method are given in chapter 5.1 and 9.1. The investigated films with a Fe content of $x = 0.02$, $0.14$, and $0.37$ reveal all the same residual stress with respect to the error bars and a stress induced peak shift can be excluded.

The influence of Fe substitution on the surface morphology was investigated via AFM. All films reveal a smooth surface with a rms-roughness below $0.5\,\text{nm}$ (not shown). The typical plate-like structure with weak cracks can be found, which was already presented in fig. 7.5. For the largest Fe content of $x = 0.49$ the cracks are more pronounced than for the other samples. However, the extracted rms-roughness reveal no systematic dependence on the Fe content.
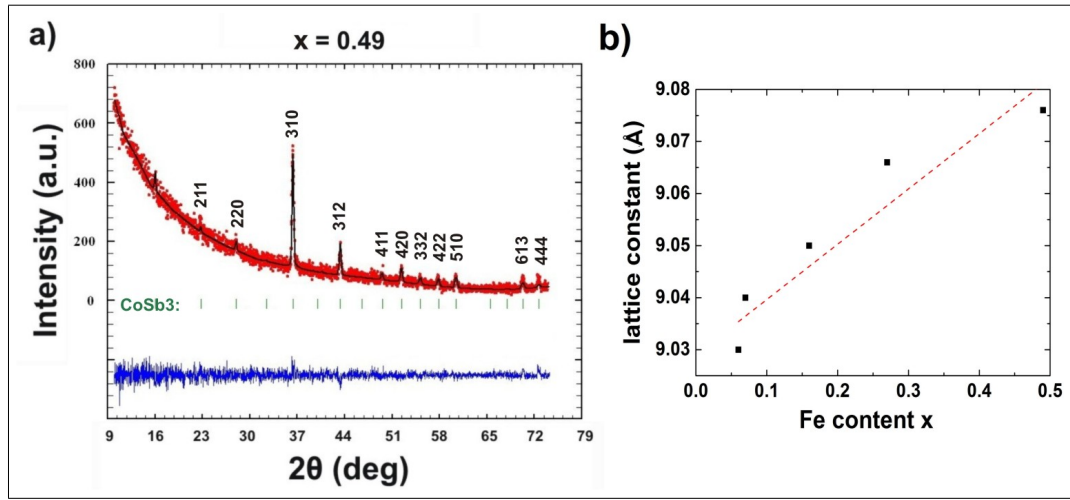


Figure 10.3: a) Rietveld refinement of the XRD pattern of a $Fe_{0.49}Co_{0.51}Sb_{3.35}$ thin film, which was measured with the wavelength of the Co $K_\alpha$ radiation to avoid fluorescence. b) Extracted lattice constant of the skutterudite phase in dependence of the Fe content $x$.

## Thermoelectric properties

Room temperature resistivity, Hall, and Seebeck measurements were performed for the $Fe_xCo_{1-x}Sb_3$ films with different Fe content $x$. With increasing Fe content the material is expected to become p-doped, which means the system should change from the bipolar character of $CoSb_3$ (see chapter 8.1) to a hole dominated p-type system analog to the pure $FeSb_3$ system (see chapter 8.2). These assumptions can be confirmed by the results of the measurements shown in fig. 10.4.
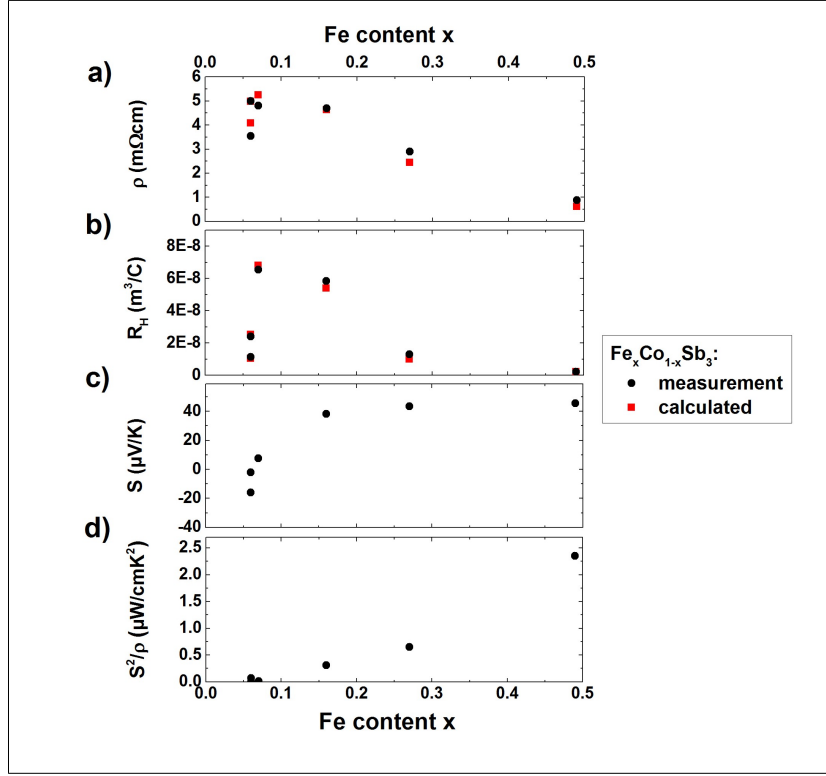
Figure 10.4: Electric properties, Seebeck coefficient and power factor of annealed (450 °C) $Fe_xCo_{1-x}Sb_3$ films in dependence of the Fe content $x$. The measurements were performed at room temperature and are shown in black. The red squares are the calculated values for a possible refined configuration of $n_p$, $\mu_p$, $n_e$ and $\mu_n$, since holes and electrons contribute to the transport coefficients in these samples.

The resistivity is basically decreased with increasing $x$ due to the doping with Fe (fig. 10.4 (a)). If more holes are introduced the charge carrier density should increase and the resistivity becomes smaller. However, the resistivity is for low substitution level first increasing. The origin of this effect cannot be clarified and could be related to the band structure [73]. Another possibility would be electron-hole scattering yielding smaller mobilities compared to the undoped samples. For larger doping the hole conduction dominates, the electron contribution can be neglected, and the resistivity drops.

The Hall constant exhibits positive sign, which is in agreement to a p-type conduction. A maximum is observed for relatively low $x$ and the measured curve (fig. 10.4 (b)) has very similar character to the qualitatively discussed curves shown in fig. 8.3 (a),

where the Hall constant was calculated with increasing hole density $n_p$ for a given constant doping density of electrons ($n_n$) of the same magnitude. With increasing Fe content in the present samples, $n_p$ should indeed increase and thus the basic discussions given there for CoSb$_3$ with light holes and heavy electrons can be confirmed. With increasing Fe content, more and more holes are introduced until the samples become completely hole dominated with negligible contribution of the electron. This is the case for large Fe content. $R_H$ decreases continuously beyond the maximum ($x > 0.07$), which corresponds to an increase of the charge carrier density. This increase confirms together with the structural results (single phase skutterudite films and linear increase of lattice constant with $x$) the successful substitution of Co by Fe in MBE grown Fe$_x$Co$_{1-x}$Sb$_3$ thin films. It is therefore shown, that substitution of Co is also in skutterudite thin films a possible tool to adjust the charge carrier concentration. The n-type doping $n_n$ of the films caused by defects should be comparable to the hole density $n_p$ for low Fe content ($x < 0.07$) and the samples reveal bipolar character in this regime. If both carrier types compensate each other finally, the Hall constant becomes zero. This is expected for the present series for even lower Fe content or pure CoSb$_3$ films, which is indicated by the strong decrease of $R_H$ for low Fe content. This is a further proof for the bipolar behaviour observed for CoSb$_3$. The Seebeck coefficient $S$ reveals a change of sign with increasing Fe content, as expected. For low Fe content the Seebeck coefficient is still negative as also obtained for CoSb$_3$. In this range the higher number of heavy electrons dominate over the light holes as discussed in chapter 8.1.1. $S$ becomes positive for $x$ between 0.06 and 0.07 (fig. 10.4 (e)) and increases continuously with further increasing Fe content until the saturation might be reached for $x = 0.49$. Even larger doping should decrease the Seebeck coefficient according to the second term of equation 3.14. The absolute values obtained for the Seebeck coefficient match well with the discussion above. For the bipolar regime around $x = 0.07$, the electrons and holes have an opposed contribution to $S$ and thus the absolute values of these samples are low, which was also be found for undoped CoSb$_3$ (see chapter 8.1). With strong substitution of Co by Fe mainly holes contribute to $S$ and larger values comparable to that ones of FeSb$_3$ are observed (s. ch. 8.2).

The power factor increases strongly with Fe content $x$ and is improved by the fact that the resistivity drops by doping, while the influence of the parasitic electrons becomes less, yielding a larger Seebeck coefficient. The optimum of the power factor is not yet reached and even larger Fe contents should be favorable (as long the alloy is stable and no FeSb$_2$ is formed).

By assuming that the electron contribution for the largest substitution level can be neglected, one possible configuration of the electron concentration $n_n$, the electron mobility $\mu_n$, the hole carrier concentration $n_p$, and the hole mobility $\mu_p$ could be developed for the samples to explain the data. Since only the resistivity and Hall measurements are the base of this analysis, the solution is undetermined (4 unknown

parameter, 2 measurements). However several additional constraints can be taken into account. $n_p$ has for instance to increase with increasing Fe content. To calculate and refine the measured resistivity $\rho$ and the measured Hall constant $R_H$ from the four parameters, equation 5.7 and 5.8 were used. Using the assumption, that the sample with the largest Fe content is completely p dominated, the measured Hall constant is mainly defined by $n_p$ and the mobility is $\mu_p$. From this start values, $n_p$ is decreased for the other samples with lower $x$ and together with the other parameters iteratively ($\mu_p$, $n_n$ and $\mu_n$) refined, until they agree as good as possible with the measured data of $\rho$ and $R_H$. The calculated values for $\rho$ and $R_H$ from the determined configuration of the parameters are added as red squares to the graphs shown in fig. 10.4. It can be seen that all values can be approximated well.

The refined parameters are finally summarized in dependence of the Fe content in table 10.1. The hole carrier concentration $n_p$ varies in that case over two orders of magnitude by doping ($10^{19}\,cm^{-3}$ - $10^{21}\,cm^{-3}$), while the hole mobility $\mu_p$ is lower than $20\,cm^2/Vs$. In fig 10.5 (a) and (b) both parameters are shown for various Fe content. $n_p$ seems to increase exponentially for doping by Fe and $\mu_p$ drops rapidly with increasing Fe content (ionized impurity scattering).

The electron concentration is about $\sim 10^{19}\,cm^{-3}$ and decreases with larger Fe content (fig. 10.5 (a)). This effect might be explained by a shift of the Fermi energy introduced by the doping with Fe. The electron mobility $\mu_n$ was determined in the range of $\sim 7\,cm^2/Vs$ and nearly no changes are observed for different $x$. The determined values are about half of the values found for $\mu_p$ and confirm the lower mobility expected for electrons.

For the discussion above, it has to be kept in mind that the refined values are only one possible undetermined configuration. However, the parameters obtained by this procedure show that the electron concentration for the two samples with the lowest $x$ is larger than the hole concentration (table 10.1 or fig. 10.5 (a)). Exactly these two samples have a negative sign of the Seebeck coefficient and the positive Hall constant of both samples is only observed due to the different mobilities. All other sam-

| Fe content $x$ | $n_p$ ($10^{19}$ cm$^{-3}$) | $\mu_p$ (cm$^2$/Vs) | $n_n$ ($10^{19}$ cm$^{-3}$) | $\mu_n$ (cm$^2$/Vs) |
|---|---|---|---|---|
| 0.06 | 5.00 | 14.5 | 9.75 | 8.24 |
| 0.06 | 5.00 | 14.5 | 6.75 | 7.84 |
| 0.07 | 5.53 | 17.5 | 3.25 | 6.84 |
| 0.16 | 8.50 | 14.0 | 2.25 | 6.84 |
| 0.27 | 54.30 | 4.5 | 1.50 | 6.84 |
| 0.49 | 284.00 | 3.5 | 1.15 | 6.84 |

Table 10.1: Possible configuration of the electric parameters for $Fe_xCo_{1-x}Sb_3$ thin films with various $x$. $n_p$ is the hole density, $\mu_p$ the hole mobility, $n_n$ the electron density, and $\mu_n$ the electron mobility.
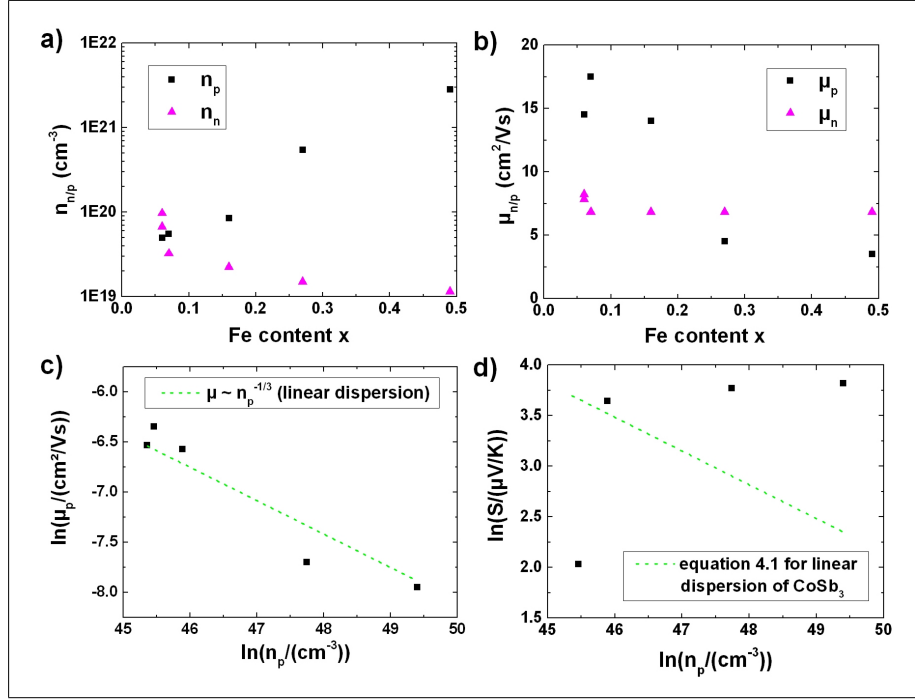
Figure 10.5: a) The dependence of the hole $(n_p)$ and the electron concentration $(n_n)$ as function of the Fe content $x$ for one possible configuration extracted from the measured data of annealed $Fe_xCo_{1-x}Sb_3$ films. b) The corresponding mobilities $(\mu_p$ and $\mu_n)$ of the different carrier types. c) The determined hole concentration in dependence of the hole mobility. The green line demonstrates the expected dependence for a linear dispersion. d) Seebeck coefficient in dependence of the hole concentration. The expected $S$ for the linear valence band of $CoSb_3$ calculated with equation 4.1 is included as green line.

ples reveal positive sign of the Seebeck coefficient and the absolute values becomes larger with increasing difference between $n_n$ and $n_p$. Therefore this configuration could explain the thermoelectric results found for $CoSb_3$ (bipolar), $FeSb_3$ (p-type) and $Fe_xCo_{1-x}Sb_3$ (transition region) qualitatively quite well, and especially the fact, why the Hall constant of $CoSb_3$ is positive and the Seebeck coefficient is negative. Unfortunately these four parameters cannot be measured individually and the used equations are averaging also over various electrons or holes with different effective mass themselves originating from different or nonparabolic bands. A quantitative analysis is very difficult.

It was further investigated if the special features of the bandstructure (chapter 4.1.2) with a linear dispersion of the valence band can be verified, which should be possible

fore hole dominated samples with larger $x$. Therefore the Fermi energy has to lie in the gap or close to the valence band and no impurity band should be formed, which can not be excluded due to the very large hole density.

First the hole mobility is investigated in dependence on the hole concentration. $n_p$ should be proportional to $\mu_p^{-1/3}$ for the linear band (see ch. 4.1.2). To extract the exponent, $\ln(n_p)$ over $\ln(\mu_p)$ was plotted as shown in fig. 10.5 (c) and the slope of the determined values are close to the expected -1/3. The linear fit reveals a value of -0.4. Since for parabolic bands a much larger slope of -2/3 is expected [63], the agreement could indicate the influence of the linear band structure.

Additionally, the connection of the Seebeck coefficient and the hole density was investigated. The results shown in fig. 10.5 (d) reveal no agreement of the obtained data with the prognosed relation for the linear band given in equation 4.1. Only a single value is in agreement with the theory (film with $x = 0.16$). For lower hole densities the electrons might have an additional influence lowering the Seebeck coefficient. For larger doping, the Fermi energy could already lie in the valence band or an impurity band might form. Furthermore, the influence of the large Fe substitution on the band structure is unknown and will be investigated in a future study. Indications for a decreasing slope of the linear band with increasing $x$ were for instance obtained by low temperature measurements (not shown). Calculations of Hammerschmidt [157] reveal further a very flat valence band for $FeSb_3$ and it is not known, if a gradual transition from $CoSb_3$ to $FeSb_3$ exists.

In summary, the pure undoped $CoSb_3$ thin films of this study, which were prepared by MBE technique, are not favourable for thermoelectric applications or future nanostructured approaches like multilayer or patterned structures since the bipolar properties yield to low Seebeck coefficients. A controlled doping for example by substitution of Co by Fe (or Ni) can be also performed for thin films and is necessary to achieve a dominating charge carrier type and thus an enhancement of the power factor to typical values of thermoelectric materials.

## Temperature dependent transport measurements

Low temperature resistivity and Hall measurements with the van der Pauw method, as well as low temperature Seebeck measurements were performed for the samples with different Fe content. The measured curves are shown in fig. 10.6 and the obtained curves match in most cases to the room temperature measurements.

The resistivity is plotted in dependence of the temperature in fig 10.6 (a) for all samples, which are hole dominated ($S$ and $R_H$ positive, $x \geq 0.07$). In the bipolar regime close to the compensation ($x < 0.07$) an analysis is difficult. A semiconducting behaviour with negative temperature coefficient can be found for the investigated samples with the lowest Fe content of $x = 0.07$ and $x = 0.16$. The slope becomes a little bit smaller for the sample with $x = 0.16$. Extracted bandgaps are in the range
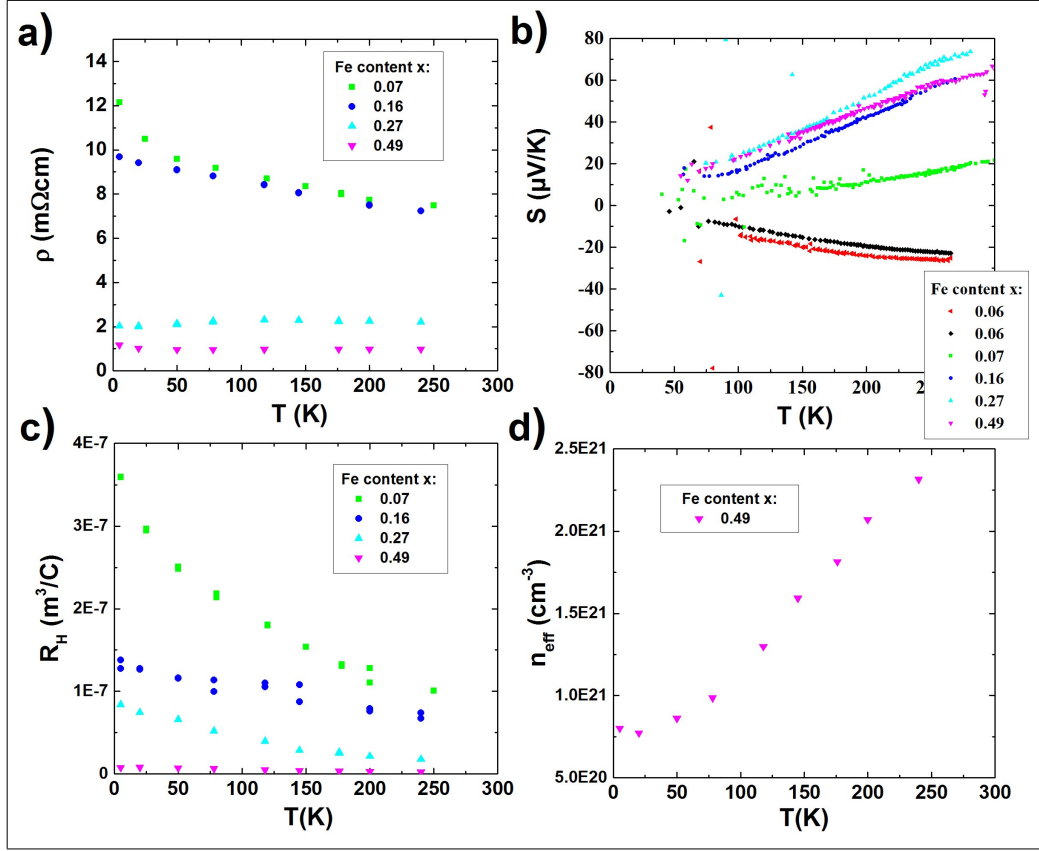
Figure 10.6: Temperature dependence of the transport coefficients of selected Fe$_x$Co$_{1-x}$Sb$_3$ films in dependence of $x$: a) resistivity, b) Seebeck coefficient, c) Hall constant, and d) effective charge carrier concentration of the sample with $x = 0.49$.

of $5\,\mathrm{m}e\mathrm{V}$. The resistivity of the samples with the substitution level of 0.27 and 0.49 exhibit nearly no temperature dependence. A high substitution level of Fe yields quickly to degeneration or subbands, which is also supported by the small bandgap of CoSb$_3$. This should be the reason, why equation 4.1 is not valid for most of the samples as discussed in the last section.

The Hall investigation at low temperatures is critical to interpret, since the additional influence of the electrons is difficult to estimate. The Hall constant is decreasing with temperature and for all samples positive over the entire temperature range (fig. 10.6 (c)). The samples show therefore p-type conduction. Assuming only holes (what could be true for $x$=0.49), the decrease of the Hall constant indicates the generation of holes with increasing temperature. An increase of the effective charge carrier density from $0.8 \cdot 10^{20}\,\mathrm{cm}^{-3}$ to $2.3 \cdot 10^{21}\,\mathrm{cm}^{-3}$ is calculated for the sample with

$x = 0.49$ by using equation 5.5 valid in the single band model (fig. 10.6 (d)). The relatively small increase might be also an indication for a degenerated semiconductor or metallic like behaviour.

The temperature dependence of the Seebeck coefficient is shown in fig. 10.6 (b) for different Fe content $x$. For low $x$ the Seebeck coefficient remains negative over the entire temperature range. It exhibits the typical shape found in literature for n-type doped $CoSb_3$ with a minimum somewhat above room temperature due to the onset of intrinsic excitation (see figures 4.5, 4.6 and 4.9). For larger Fe content the Seebeck coefficient is in agreement to the Hall constant positive for the measured temperature range. In these samples the hole concentration is always larger than the electron concentration. $S$ rises steadily and no indications for a saturation can be seen. The maximum of $S$ occurring for the onset of intrinsic conduction was not observed in the investigated temperature range and should be reached at higher temperatures. The observed values for the Seebeck coefficient in these films are at the lower limit of the literature values shown in fig. 4.5, 4.6 and 4.9, but the influence of the Si substrate on the measurements have to be kept in mind (see ch. 9.2). High temperature measurements are needed to optimize the Fe doping with respect to the largest Seebeck coefficient or rather with respect to the largest power factor.

## Thermal properties - Raman measurements

To characterize the influence of the introduced Fe atoms on the vibrational modes of $CoSb_3$, Raman measurements were performed for this sample series. First a pure $CoSb_3$ film with a Sb content of 75 at.% was measured. The film was deposited at room temperature and the Raman spectra obtained after annealing at $500\,°C$ is shown in fig. 10.7. For the single phase $CoSb_3$ films the spectra published by Nolas et al. [177] could be reproduced and according to this publication 7 active Raman modes can be observed (4 $F_g$, 2 $E_g$ and 1 $A_g$), which do all belong to vibrations of Sb atoms. A peak analysis of the measured spectra was performed and can be seen as red (overall fit) and green (individual modes) lines. The $F_g$ and the $E_g$ modes are observed for both polarization directions, while the $A_g$ modes only occur for parallel polarization. This is clearly visible for the $A_g$ mode around $179\,cm^{-1}$. If the second $A_g$ mode at $\sim150\,cm^{-1}$ is really observed, is not confirmed, since both spectra exhibit at this position no clear difference. Therefore the corresponding peak is marked with a question mark in the VV spectra. The very narrow peaks at low wave numbers are artifacts due to the used laser.

This study should show the changes in the vibrational modes by going from $CoSb_3$ to $FeSb_3$. Since all the modes belong to Sb vibrations [177, 178], the changes due to the incorporated Fe atoms could not be directly observed. The achieved Raman spectrum is presented in fig.10.8 for different Fe content $x$. Additionally, the single phase $CoSb_3$ film without Fe substitution is included. The discussed footprint of
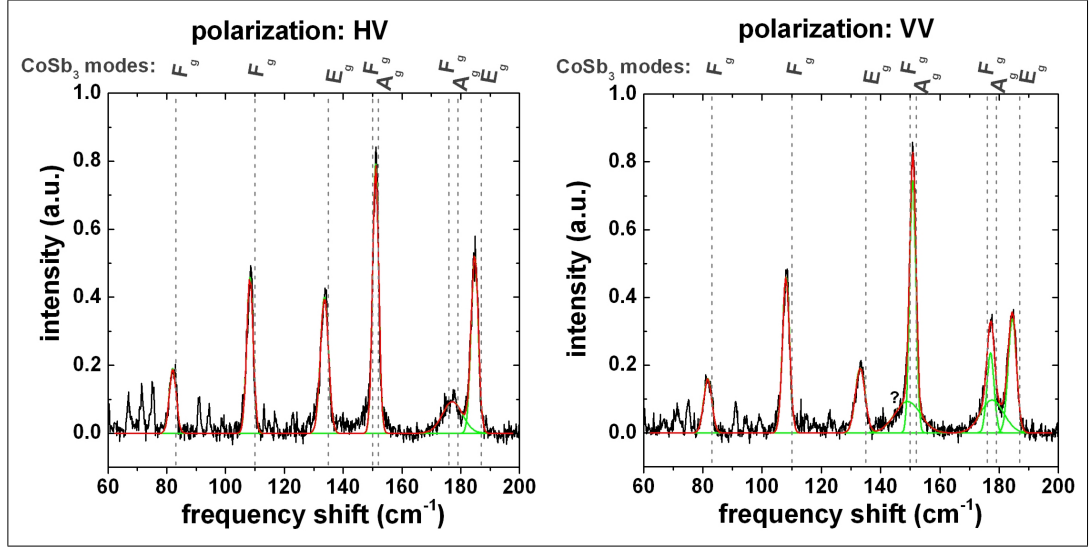
Figure 10.7: Raman measurements of an annealed $CoSb_3$ thin film without Fe substitution. HV are measurements in perpendicular and VV in parallel polarization. The added modes were found by Nolas et al. [177] and agree well with these measurements. The $A_g$ modes are only visible in VV polarization. The $A_g$ mode at $\sim 150\,cm^{-1}$ can not be identified clearly, which is indicated by a question mark.

$CoSb_3$ can be obtained also for the Fe containing films. Additional peaks or features do not occur. There is for example no indication for the pure Sb phase, which yields to peaks at $112.5\,cm^{-1}$ and $150.5\,cm^{-1}$ [179]. With increasing Fe substitution level the peaks shift to lower wave numbers, but the basic features are mainly conserved (fig. 10.8). This is expected, since the Fe atoms only substitute Co and do not change the crystal structure or the Sb rectangles itself. Fe atoms increase the lattice constant, which gives rise to different distances between the Sb atoms affecting the bond strength. Furthermore, each Sb atom is bonded to a transition metal (Fe or Co). If the Fe content $x$ is larger, more bonds between Fe and Sb occur, which could also yield changed vibrational modes. Both processes weaken the bonds and a shift of the Raman peaks to lower frequency is observed. The shift of the individual peaks were extracted and can be found in fig. 10.9 in dependence of the mode symmetry. The shifts are nearly linear. For all $E_g$ modes a comparable slope was found, which differs from that one of the $F_g$ modes. The underlying structural changes and the symmetry changes of the individual vibrational modes yielding to shifts in the Raman spectrum are difficult to investigate and beyond the scope of this work.
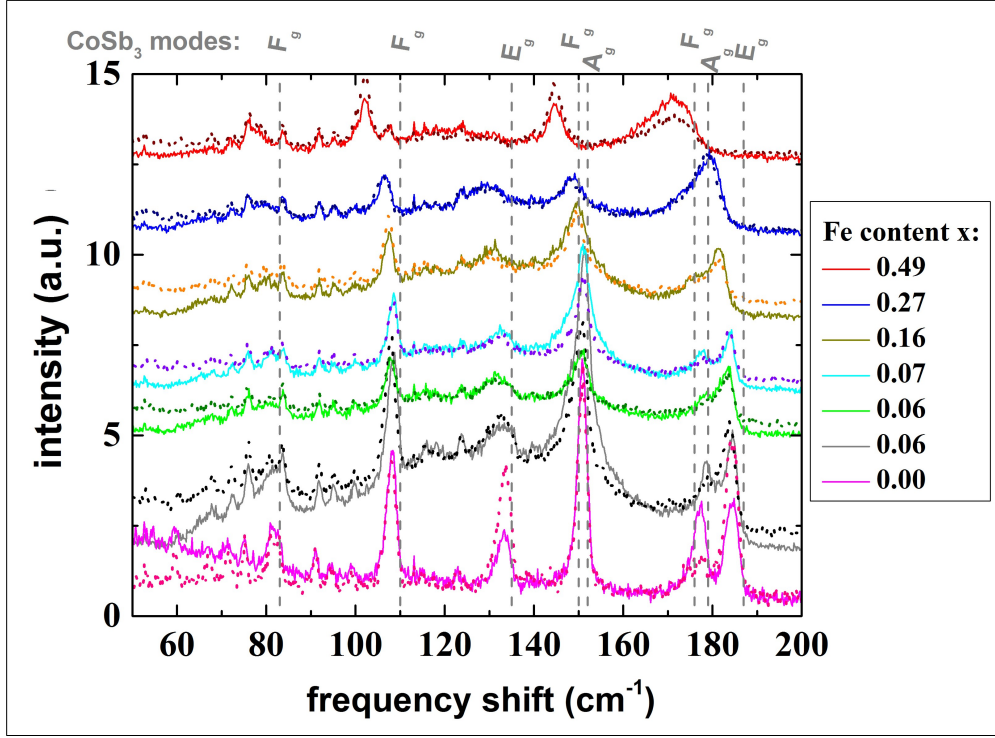
Figure 10.8: Raman measurements of $Fe_xCo_{1-x}Sb_3$ films with different Fe content $x$. The solid lines are measured in parallel polarization (VV), the dashed ones in perpendicular (HV). With increasing $x$, a peak shift towards lower wave numbers is observed. The sharp peaks at low wave numbers are parasitic effects of the laser.

With increasing Fe content, the signal intensity decreases and the peaks become washed out. The first reason for this change could be the increasing charge carrier density with larger Fe content, which shields the incident laser beam and increases the noise background of the measurement strongly. Additionally, the mass difference between Fe and Co yield to mass scattering of phonons and a decreased thermal conductivity. This might also influence the vibrational modes of the Sb atoms, if the Fe content is large enough. Furthermore, it can be recognized that the $E_g$ mode at $139\,cm^{-1}$ vanishes nearly completely. The origin of this effect is unknown and the consideration of the symmetry properties of this mode could not give an answer. Further investigations are needed here to distinguish if the peak really disappears or if it is not observable due to the larger signal-to-noise ratio and a strong peak broadening.
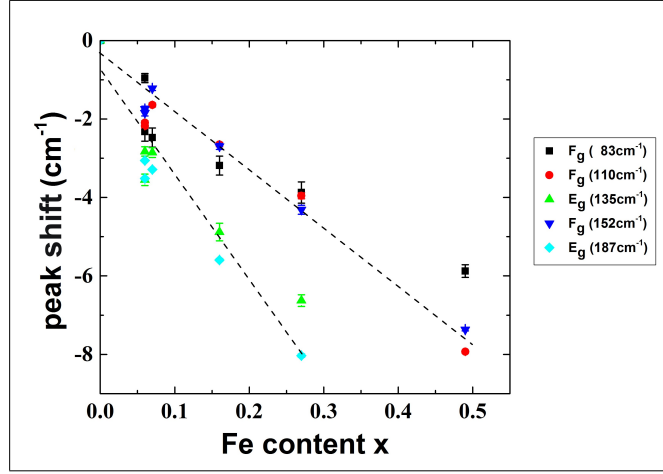
Figure 10.9: Shift of the individual Raman peaks in dependence of the Fe content $x$ for $Fe_xCo_{1-x}Sb_3$ thin films. The speak shift is almost linear and reveals for modes with different symmetry ($E_g$ or $F_G$) different slopes.

To conclude, the filling with Fe shifts mainly the Raman peaks due to weakening of the bonds. The skutterudite structure is conserved and the substitution of Co by Fe can be also confirmed by Raman. For large Fe content, the peak width of the vibrational modes is influenced, which could indicate distorted vibration due to mass scattering yielding a suppressed thermal conductivity.

It is further to note that Raman measurements for pure $FeSb_3$ films were unfortunately not possible, since the huge charge carrier density in these films screen the laser beam and therefore the necessary excitation of the sample.

## 10.2 Properties of $Fe_xCo_{1-x}Sb_3$ films deposited via MERM

The deposition with the MERM method is easier to handle. First, the needed double layer units Co/Sb (unit A) and Fe/Sb (unit B) have to be calibrated individually as described in chapter 6.3. Afterwards superlattices with a well defined sequence of A and B were deposited at room temperature and post-annealed to achieve ∼50 nm thick crystalline $Fe_xCo_{1-x}Sb_3$ films with different $x$. To achieve for instance $x = 0.5$ the sequence AB has to be repeated several times, for achieving $x = 0.4$ the repeating sequence is ABABA and so on. This is illustrated in fig. 10.10. The challenge of this method is to find a possible and controllable sequence for each $x$ value wanted, since the sequence and the unit thickness has to be chosen in a way that the individual layers of the sequence unit mix homogeneously before crystallization. This is especially for very small $x$ values complicated, where the number of B units is low. In

this work films with a Fe content of $x = 0$, 0.2, 0.25, 0.33, 0.4, 0.5, 0.75, and 1 were prepared via the MERM method on Si(100) and on fused silica substrates.

To check the initial state of the as-deposited films, XRR and RBS measurements were performed and the results are summarized in the table shown in fig. 10.11 (b). The film thickness was extracted from the XRR measurements by analysis of the Kiessig fringes and the extracted value is in agreement with the nominal thicknesses of $\sim 50$ nm. For some layers ($x = 0.2$, 0.25, 0.33, 0.75) a weak Bragg peak related to a multilayer period of about 1 nm ($\hat{=} 2\theta$ of 8.83° for Cu $K_\alpha$ radiation) is observed. The multilayer period accords in that case to the thickness of the Co/Sb (unit A) and Fe/Sb (unit B) double layers. In fig. 10.11 (a) a measured XRR scan is presented exemplarily for the film with $x = 0.33$ (repeating sequence = AAB) and the Bragg peak is observed for an angle of $2\theta = 8.539°$. The multilayer period calculated by dividing the overall thickness extracted from the Kiessig fringes by the number of deposited units agrees in the range of the error bars with the value determined by the position of the Bragg peak (fig. 10.11 (b)), giving a cross check for both measurements. The Bragg peak could not be detected for all films since the multilayer period of 1 nm is at the lower resolvable limit and extremely flat and sharp interfaces are needed.

The composition was checked by RBS. The multilayers cannot be resolved with this method, only the overall composition can be determined. In fig. 10.11 (b) the results are summarized and compared with the nominal values. Since this deposition was performed in a HV chamber without wall cooling, parasitic Se from the chamber wall is found in the films with an average content of 5.5 at.% and a maximum value of
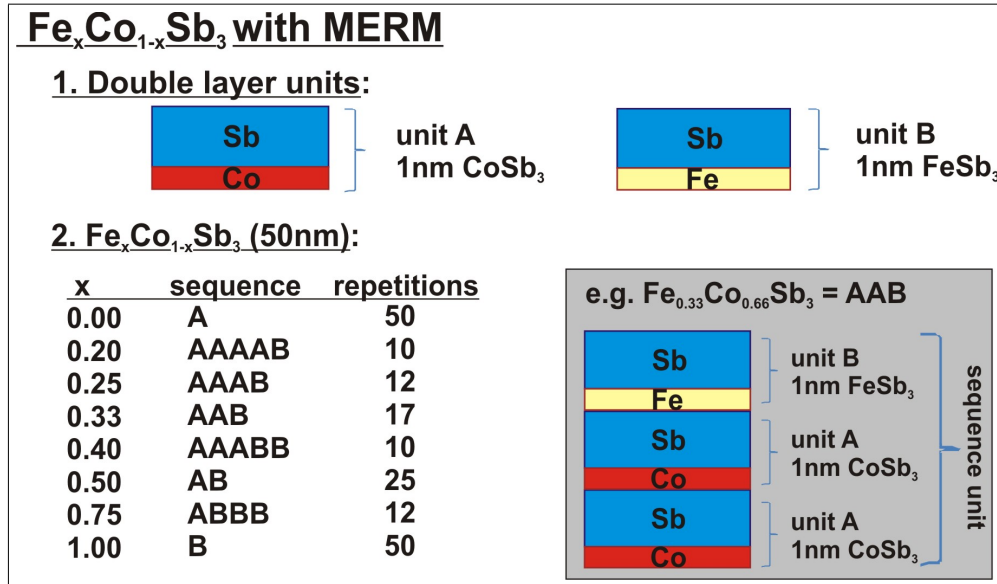


Figure 10.10: Illustration of the layer stacks used to deposited $Fe_xCo_{1-x}Sb_3$ films with the MERM method

a)



b)

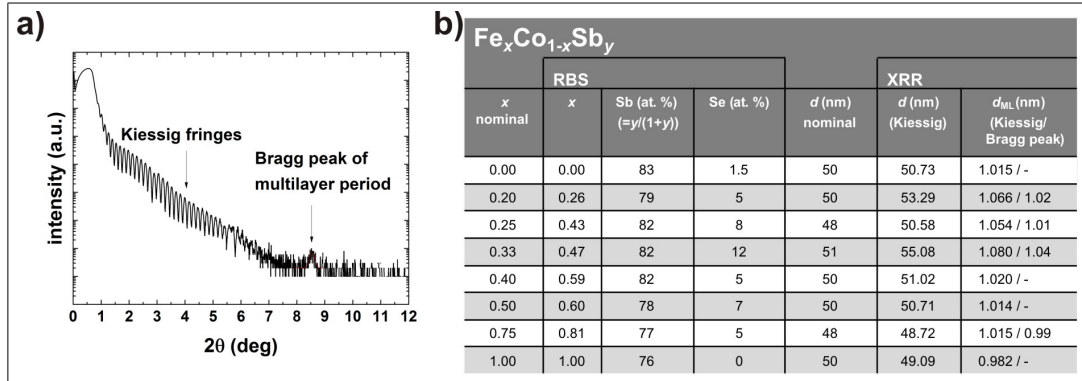| $Fe_xCo_{1-x}Sb_y$ | | | | | | |
|---|---|---|---|---|---|---|
| **RBS** | | | | | **XRR** | |
| $x$ nominal | $x$ | Sb (at. %) (=y/(1+y)) | Se (at. %) | $d$ (nm) nominal | $d$ (nm) (Kiessig) | $d_{ML}$ (nm) (Kiessig/ Bragg peak) |
| 0.00 | 0.00 | 83 | 1.5 | 50 | 50.73 | 1.015 / - |
| 0.20 | 0.26 | 79 | 5 | 50 | 53.29 | 1.066 / 1.02 |
| 0.25 | 0.43 | 82 | 8 | 48 | 50.58 | 1.054 / 1.01 |
| 0.33 | 0.47 | 82 | 12 | 51 | 55.08 | 1.080 / 1.04 |
| 0.40 | 0.59 | 82 | 5 | 50 | 51.02 | 1.020 / - |
| 0.50 | 0.60 | 78 | 7 | 50 | 50.71 | 1.014 / - |
| 0.75 | 0.81 | 77 | 5 | 48 | 48.72 | 1.015 / 0.99 |
| 1.00 | 1.00 | 76 | 0 | 50 | 49.09 | 0.982 / - |

Figure 10.11: a) XRR-curve of a $Fe_{0.47}Co_{0.53}Sb_{4.5}$ multilayer film deposited with MERM with occurring Kiessig fringes and Bragg peak. b) Overview of the parameters for $Fe_xCo_{1-x}Sb_y$ films deposited with MERM method. The composition was determined by RBS and a contamination with Se from heated chamber walls was observed. The film thickness $d$ and the multilayer thickness $d_{ML}$ were extracted from XRR measurements.

12 at.% observed for the sample with $x = 0.47$. The Se contamination was in the following neglected and the average Sb content with respect to the sum of Fe and Co is 80 at.% ($\widehat{=} y/(y + 1)$). The achieved values for $x$ are slightly larger than the nominal ones.

DSC measurements of the initial samples and XRD of the annealed ones were performed to prove, if the layered films mix during the annealing process homogeneously by diffusion and if they crystallize in a single phase. If different phases and inhomogeneous crystal structures occur, several crystallization events in the DSC measurements are expected. The DSC results are shown in fig. 10.12 (a). All but one sample (AAAB) revealed only one significant crystallization event around 170 °C, analog to the results obtained for Co-Sb and Fe-Sb films (chapter 7.1.1 and 7.2.1). Single phase skutterudite films are therefore expected. Some smaller events corresponding to the formation of the pure Sb phase are also observed between 300 °C and 400 °C (see chapter 7.1.1).

For $x = 0$ the crystallization temperature of $CoSb_3$ is observed (161.4 °C). With increasing Fe content the crystallization temperature of the skutterudite phase (main peak) increases first, reaches the maximum value of 202.9 °C for $x = 0.47$ (AAB) and decreases again, revealing finally the crystallization temperature of $FeSb_3$ of about 150 °C. This shift of the crystallization temperature can have different origins. First, the films have slightly different initial states, which is indicated by the appearance of the Bragg peak in the XRR measurements only in some samples. These differences could contribute to slightly different processes of interdiffusion and crystallization
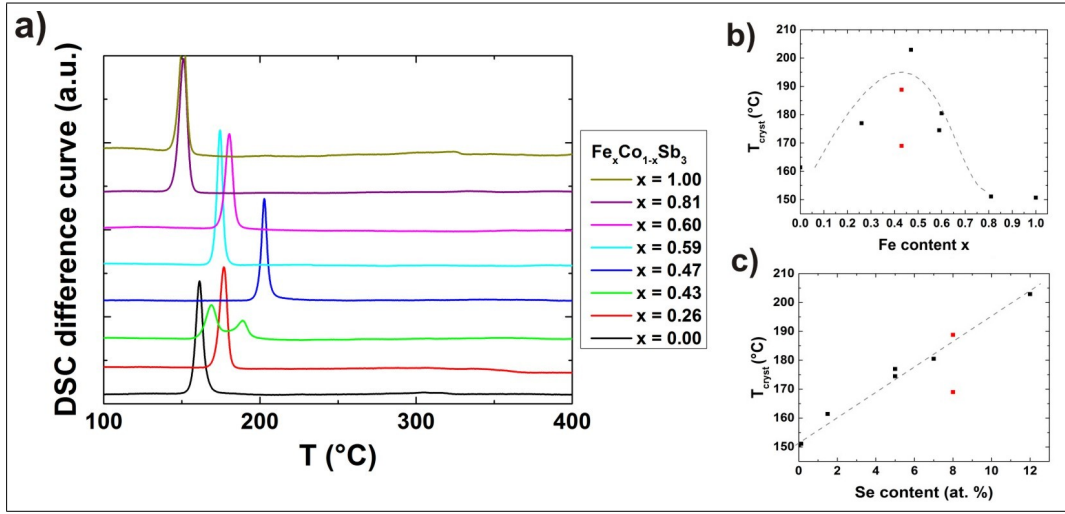
Figure 10.12: a) DSC investigation of MERM deposited $Fe_xCo_{1-x}Sb_y$ films with various Fe content $x$. Only the sample with $x = 0.43$ exhibits two exothermic peaks. Crystallization temperature in dependence of b) the Se and c) the Fe content. The data points of the sample with $x = 0.43$ are marked in red. The dashed lines are only a guide to the eye.

during the annealing process. The incorporation of Fe could also affect the inter-diffusion and crystallization (changed atom species, changes lattice constant). The strongest influence is expected for films with a Fe content of $x \sim 0.5$, which should exhibit the largest disorder. Another contribution might arise from the variation of the Sb content and the presence of the parasitic Se, which could also impede the diffusion. The crystallization temperature is plotted in fig. 10.12 (b) in dependence of the Fe content $x$ and in fig. 10.12 (c) in dependence of the Se content. Both transition temperatures found for the AAAB samples are marked in red in the diagrams, since it is not clear if and which of these peaks could be attributed to the skutterudite phase formation. Even though the crystallization temperature might exhibit a maximum for a Fe content around $x = 0.45$, the more obvious dependence is observed for the variation of the Se content. To clarify the origin of the shift, it is necessary to deposit samples without Se. In that case only a decrease of the transition temperature with Fe incorporation was reported [93]. It is to note further that for different Sb content no systematic influence was observed.

For most samples a single crystallization event was observed by DSC, however the presence of the skutterudite phase has to be confirmed. The MERM deposited $Fe_xCo_{1-x}Sb_y$ films were therefore first annealed in UHV at $450°$ for $1\,h$ and XRD was performed afterwards. The observed peaks can be attributed for all samples
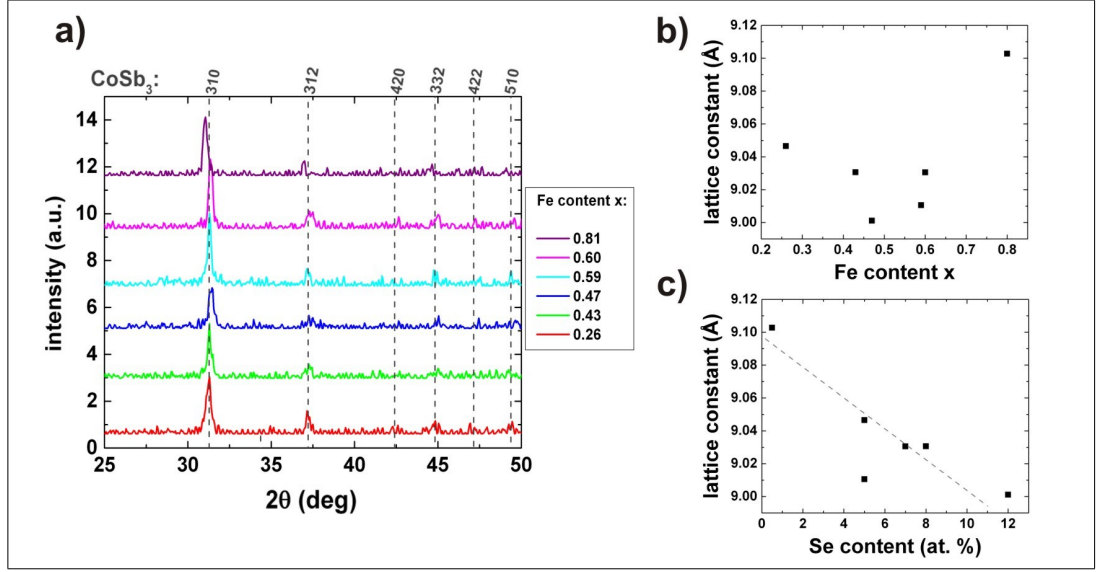
Figure 10.13: XRD pattern of different MERM deposited $Fe_xCo_{1-x}Sb_y$ films with various $x$ obtained after annealing at 450 °C. The peak position of the (310) reflex was used to calculate the lattice constant, which is shown as function (b) of the Fe content and (c) of the Se content. The dashed line is only a guide to the eye.

to the skutterudite phase (fig. 10.13). Other phases are not observed. An increasing Fe content yield usually a systematic peak shift and an increased lattice constant [174, 175, 176]. While the increasing lattice constant was shown for codeposited $Fe_xCo_{1-x}Sb_3$ (fig. 10.3), it is not observed for MERM deposited films and even a tendency for a decreased lattice constant is found, which can be seen in fig. 10.13 (b). Since the crystallization temperature is influenced by the Se content, the lattice constant was also investigated as function of the Se content and decreases with increasing Se content as shown in figure 10.13 (c). This indicates the incorporation of Se into the skutterudite lattice, compensating the lattice expansion due to the substitution of Co by Fe, which could also be an explanation for the strong influence of the Se content on the crystallization temperature. Most likely, the Se atoms substitute the Sb atoms in the lattice [180, 181, 182]. Since the atomic radius of Se is much lower than for Sb, the lattice parameter is decreased. It is to note, that the XRD patterns for the samples with the largest Se content ($x = 0.43$ and $x = 0.47$) give also indications for peak shoulders.

To summarize the DSC measurements indicate, that a homogeneous Fe-Co-Sb-Se skutterudite film could be achieved by MERM deposition. The substitution of Co by Fe could not be shown due to the Se contamination. It is believed, that the Se atoms are also incorporated into the skutterudite crystal structure and exhibit a stronger influence on the structure properties than the Fe.

# 11 Filled CoSb$_3$ thin films

CoSb$_3$ in its cubic skutterudite phase exhibits high power factors $S^2/\rho$ due to its band structure (ch. 4.1.2 and 4.1.3). However, the thermal conductivity is mainly based on the lattice contribution and relatively large [19]. If electro-positive guest ions are introduced to the voids of the CoSb$_3$ host lattice, these ions will change the phononic dispersion relation and therefore decrease the thermal conductivity. This approach was introduced in detail in chapter 4.1.3. In this study 40 nm thick Yb$_z$(CoSb$_3$)$_4$ films were deposited, and the Yb content $z$ was varied between $0<z<1$. Structural, electrical and thermal properties of these films were investigated.

## Film deposition and structural properties

The 40 nm thick Yb$_z$(CoSb$_y$)$_4$ films are deposited by codeposition at room temperature on SiO$_2$(100nm)/Si(100) substrate (see chapter 6.2). Co was evaporated by an

| Sample no. | Annealing temperature | Yb content $z$ | Yb filling fraction $z_{FF}$ | Sb content (at.%) | Phases (by XRD) |
|---|---|---|---|---|---|
| 1 | 300 | 0.04 | 0.01 | 76.4 | CoSb$_3$ |
|   | 500 | 0.05 | 0.04 | 75.7 | CoSb$_3$ |
| 2 | 300 | 0.08 | 0.09 | 77.1 | CoSb$_3$ |
|   | 500 | 0.08 | 0.05 | 76.3 | CoSb$_3$ |
| 3 | 300 | 0.12 | 0.18 | 76.4 | CoSb$_3$ |
|   | 500 | 0.14 | 0.13 | 75.8 | CoSb$_3$ |
| 4 | 300 | 0.23 | 0.27 | 77.9 | CoSb$_3$ |
|   | 500 | 0.29 | 0.12 | 77.1 | CoSb$_3$ |
| 5 | 300 | 0.52 | 0.48 | 78.6 | CoSb$_3$ |
|   | 500 | 0.45 | 0.13 | 77.1 | CoSb$_3$ |
| 6 | 300 | 0.60 | 0.51 | 79.3 | CoSb$_3$ |
|   | 500 | 0.67 | 0.10 | 77.7 | CoSb$_3$ |
| 7 | 300 | 1.15 | 0.68 | 76.0 | CoSb$_3$(+amorph.?) |
|   | 500 | 1.16 | 0.57 | 76.1 | CoSb$_3$(+amorph.?) |

Table 11.1: Structural properties of annealed Yb$_z$(CoSb$_y$)$_4$ films. The Yb content $z$ and the Sb content of the host lattice $(y/1+y)$ was determined by RBS. The phases formed in the films, and the filling fraction $z_{FF}$ was investigated by XRD combined with Rietveld refinement.

electron gun evaporator, Sb and Yb by effusion cells (see chapter 6.1). The Co and the Sb flux were first calibrated to deposit films with a Sb content of 75 at.% (see ch. 6.3). Both fluxes were kept constant for the following depositions, and the Yb flux was varied to achieve films with different Yb content $z$. The as-deposited samples were cut into different pieces and one of these pieces was afterwards post-annealed under UHV conditions for 1 h at 300 °C and another one for 1 h at 500 °C to form the skutterudite phase.

To validate the film stoichiometry, RBS measurements were performed afterwards. An overview over the annealed samples and the resulting Yb and Sb content is presented in table 11.1. It is to note that the Sb content is given with respect to the amount of Co in the film and corresponds therefore to the Sb content of the Co-Sb host lattice. The Yb content is neglected for the calculations. Thus the overall Sb content of the film is therefore slightly lower. Nearly all films containing Yb reveal an increased Sb content, which can be seen in fig. 11.1 for the as-deposited samples and might be related to a larger sticking coefficient of Sb in the presence of Yb. An exception is observed for the film with $z = 1.15$, which reveals also a different behaviour for all other investigations.
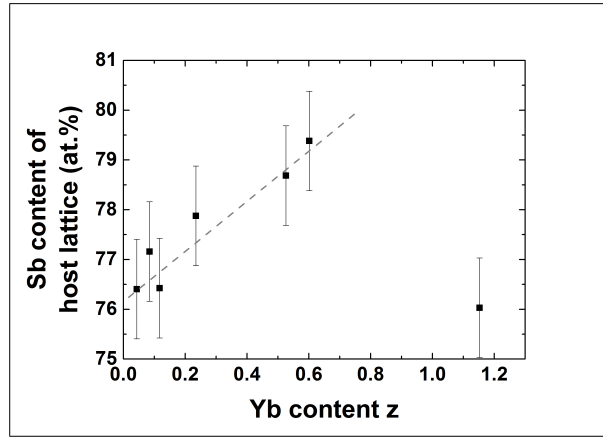


Figure 11.1: The Sb content of the Co-Sb host lattice $(y/(y+1))$ for the as-deposited Yb$_z$(CoSb$_y$)$_4$ films is shown in dependence of the Yb content $z$. Since the Co and the Sb flux were kept constant for all depositions, the presence of Yb might change the Sb sticking coefficient.

To make sure, that the Yb is situated in the voids of the structure, XRD scans followed by Rietveld refinement were performed. The scans are shown in fig. 11.2 separated into the results obtained for the films after annealing at 300 °C and after annealing at 500 °C. All observed peaks can be related to the skutterudite phase and

no indications for minor phases are seen. Due to much lower multiplicities of these phases, the detection limit of the minor phases is quite low. Their mass fraction is already larger than 5%, if peaks of these phases are clearly distinguishable from the noise. The highly symmetric cubic skutterudite crystal structure has a large multiplicity, therefore smaller amounts give already a larger peak intensity. The mass fraction of minor phases investigated by Rietveld refinement of the XRD patterns is for all samples lower than 10%. The incorporation of Yb into the voids of the $CoSb_3$ host lattice can be confirmed by the (211) reflection. The intensity of the this peak is very sensitive to the filling with guest ions and will be suppressed for a high filling fraction. Indeed the intensity of this peak is decreasing with increasing Yb content. For films annealed at 300 °C (fig. 11.2 (a)) the (211) reflection vanishes nearly completely for large Yb content $z$. This visual impression can be also confirmed by performing Rietveld refinement and the filling fraction $z_{FF}$ can be determined. A Yb filling fraction $z_{FF} = 1$ denotes, that each void of the host lattice is filled with one Yb guest ion. The extracted filling fractions $z_{FF}$ are also shown in table 11.1. The values are in the same range as the stoichiometric Yb content $z$ determined by RBS. The error of the extracted filling fraction is relatively large and the thermal parameter (mean displacement) of the individual atoms could not be determined. For an accurate refinement a $\theta$ - $2\theta$ scan over a wide range and a large number of peaks with good signal-to-noise ratio is necessary. Due to the small film thickness and the limited beam intensity this could not be fulfilled. For $2\theta$-values above 60° it was not possible to resolve further reflexes. Nevertheless, the good agreement of the Yb content $z$ and the extracted filling fraction $z_{FF}$ give confidence that most of the introduced Yb is sitting in the voids of the host lattice. Furthermore, it is noteworthy that the achieved filling fractions are much larger than the known bulk limit for equilibrium synthesis methods of ~0.2 [85, 183]. In fig. 11.3 (a) the extracted lattice parameter is presented in dependence of the Yb filling fraction. Up to a filling fraction of 0.5, a slight increase of the lattice parameter is observed, which is for example also reported for Nd and Th filled films [71, 72]. Above this filling fraction the lattice parameter increases strongly. This behaviour is not observed so far and the origin is unknown. However, it is to note here that different Sb contents also influence the lattice parameter and both contributions might overlap here.

The films annealed at 500 °C reveal a different behaviour (fig. 11.2). First the (211)-peak is decreasing with increasing $z$ and approaches a constant intensity for all samples with $z > 0.14$. The reached constant intensity belongs to an extracted filling fraction of 0.12. During the annealing process at 500 °C most of the Yb is removed from the voids until an equilibrium filling fraction of 0.12 is reached. To where this Yb atoms move could not yet be clarified and the RBS investigation of these films reveal that the total Yb content is maintained and that no Yb is evaporated (see table 11.1). The formation of different phases containing Yb was also not observed by XRD. Therefore, TEM investigations are necessary to identify, where the Yb is
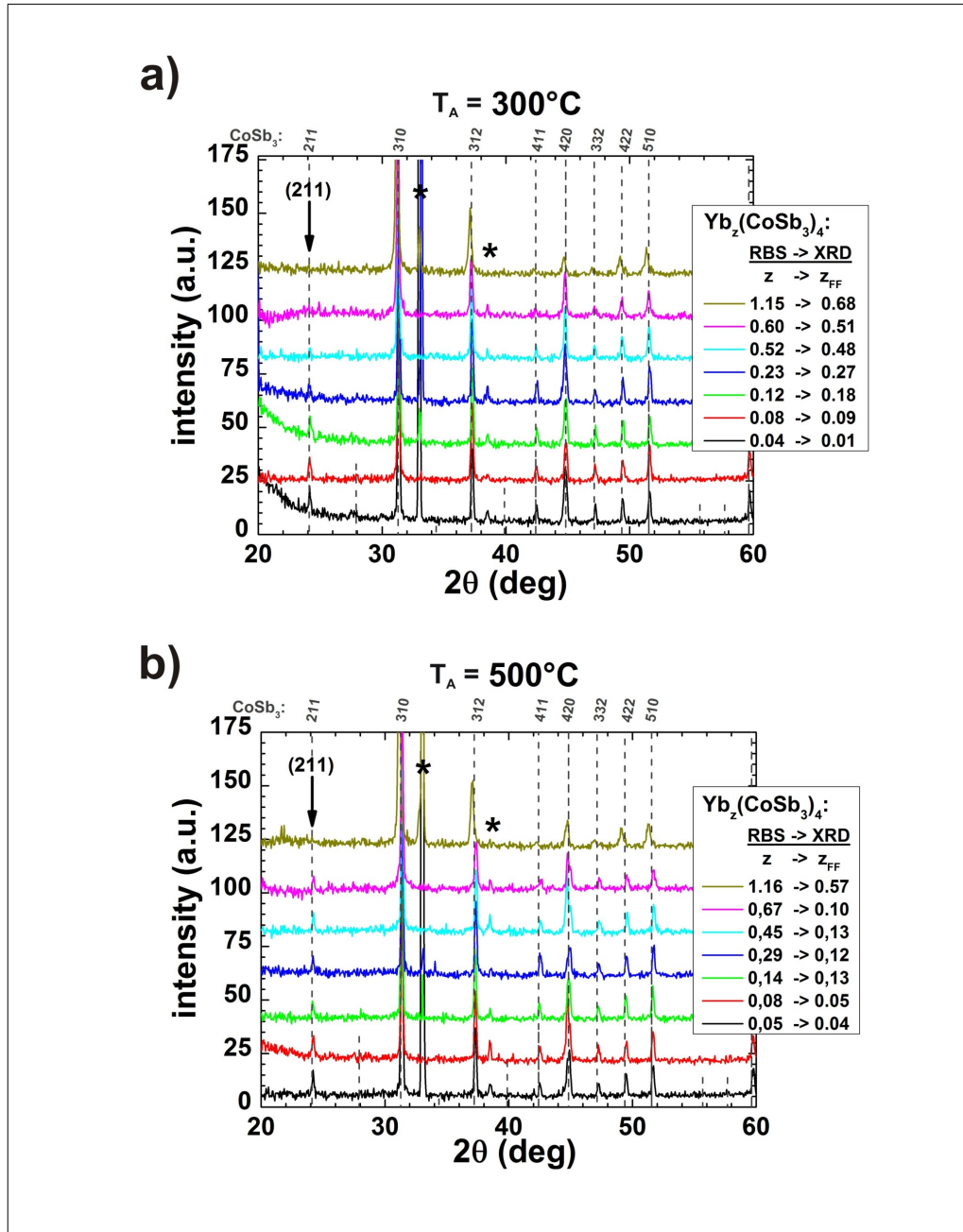
Figure 11.2: Comparison of the XRD scans of Yb$_z$(CoSb$_y$)$_4$ films obtained after annealing at (a) 300 °C and (b) 500 °C. In all films the CoSb$_3$ phase is detected as major phase. The intensity of the (211) peak of the CoSb$_3$ phase is sensitive to the Yb filling fraction $z_{FF}$, which was extracted out of the presented patterns by Rietveld refinement. Substrate peaks are marked with asterisk.

situated. It is to note that the sample with the largest Yb content of $z = 1.16$ exhibit in contrast to the other investigated samples a much lower intensity of the (211) peak corresponding to a surprisingly large filling fraction of $z_{FF} = 0.57$. The investigation of the lattice parameter for these samples reveals no clear dependency and a broad distribution is observed for low filling fraction (fig. 11.3 b)). This distribution could be related to the occurring error of the calculated lattice constant, but could be also attributed to a different Sb content or to the additional change of the lattice constant by heating Sb rich samples to 500 °C (see chapter 7.1.2). For the sample with the large filling fraction of $z_{FF} = 0.57$ an unusual large increase of the lattice constant is observed in comparison to the results achieved at 300 °C.
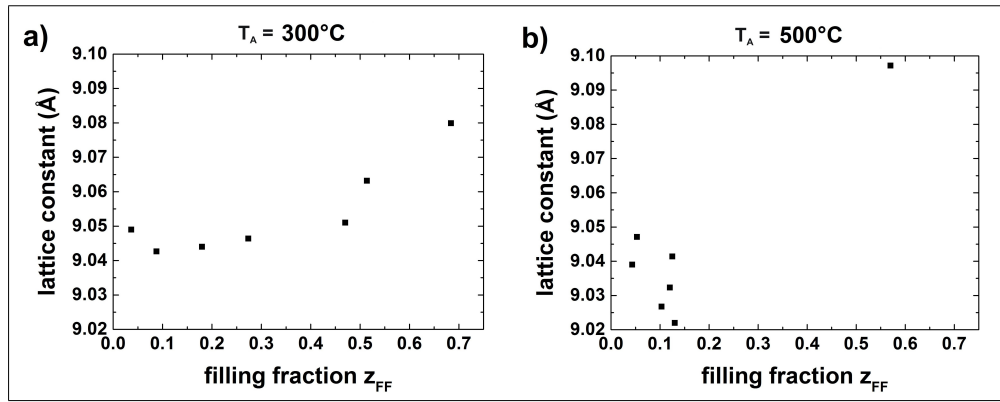


Figure 11.3: The revealed lattice constant in dependence of the filling fraction $z_{FF}$ is presented for the films annealed at (a) 300 °C and (b) 500 °C. For 300 °C an increase of the lattice constant is observed, while for 500 °C no systematic dependence can be found.

Accounting to the results achieved by RBS and XRD, the samples can be divided into different groups (see comparison of fig. 11.2 (a) and (b)). If the initial filling fraction of the as-deposited films was lower than 0.12 there is nearly no difference between the XRD scans obtained after annealing at 300 °C and 500 °C. The filling fraction is equal for both annealing temperatures. This is true for the samples listed in table 11.1 as number 1, 2, and 3. For higher initial Yb content, the (211) peak drops after annealing at 500 °C to a constant intensity related to a equilibrium filling fraction of $z_{FF} = 0.12$, which is valid for the samples 4, 5, and 6. Only sample 7 with the largest filling fraction of 0.68 at 300 °C exhibits still a high filling fraction of $z_{FF} = 0.57$ after annealing at 500 °C. Therefore, this film is an exception and the reason for this behaviour is not clarified yet. One possible explanation could be the very good stoichiometry with respect to the Sb content. However, this sample confirms that

149

larger filling fractions than 0.12 can be maintained at higher temperatures. For the other samples a way to conserve the large amount of the incorporated Yb has to be found.

AFM images of the surface morphology can be found in fig. 11.4 for three different Yb$_z$(CoSb$_3$)$_4$ films. Even though all films are relatively flat (maximum rms-roughness $\leq 2$ nm), the Yb filling fraction has a strong influence on the surface morphology. With increasing Yb content the surface type changes from the typical plate like structure ($z < 0.2$, fig. 11.4 (a)) to a homogeneous grained surface without cracks ($z > 0.7$, e.g. fig. 11.4 (c)). In between there is a transition range where different surface structures can be found. For the sample with $z = 0.45$ a mixture of both types occur as shown in fig. 11.4 (b). However, also completely different surface structures can be found in this range, which are not shown. Possible reasons for the observed changes in morphology are for instance inhomogeneous Yb incorporation with different lattice constants, introduced stress by the additional Yb, additional Yb situated at the grain boundaries or a changed crystallization process. Further studies are needed. Furthermore, it is to note that a comparison of the AFM images in fig. 11.4 (a) and (b) leads to the assumption that the incorporation of Yb might yield smaller lateral grain sizes, which has also to be verified by EBSD measurements.
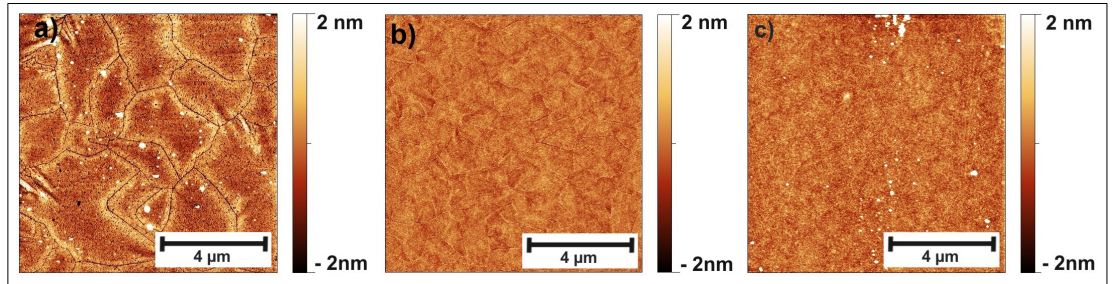


Figure 11.4: AFM images of Yb$_z$(CoSb$_y$)$_4$ films obtained after annealing at $500\,^{\circ}$C. Three different surface types are revealed due to the change of the Yb content $z$: (a) $z = 0.14$, (b) $z = 0.45$, and (c) $z = 1.15$.

## Electrical properties at room temperature

The concept behind the filling with guest ions is to decrease the thermal conductivity without drastically changing the electrical properties of the material. Van der Pauw and Hall measurements were performed to extract the resistivity, the Hall mobility, and the charge carrier concentration of the annealed films. For the films of this study, it can be shown that the introduction of Yb has a large influence on the resistivity and

the charge carrier concentration. All measurements were done at room temperature and the results are shown in fig. 11.5 in dependence of the Yb filling fraction $z_{FF}$ for both annealing temperatures. Samples without Yb filling produced with the same parameters were additionally added for comparison as red symbols.

The resistivity of the samples reveals for both annealing temperatures a decrease with increasing filling fraction $z_{FF}$ (fig. 11.5 (a)), which is mainly caused by an increase of the charge carrier concentration. The introduction of Yb dopes the material heavily and the charge carrier concentration increases strongly compared to non-filled $CoSb_3$. The effective charge carrier concentration $n_{eff}$ was determined with equation 5.5 from the Hall measurements and is shown in fig. 11.5 (b). The observed values are larger than $10^{21}$ cm$^{-3}$ indicating metallic behaviour as also expected from the valence electron count for larger filling fractions (VEC = 74 for $z_{FF} = 1$, see chapter 4.1.1). An additional charge compensation would be required for large filling fractions as
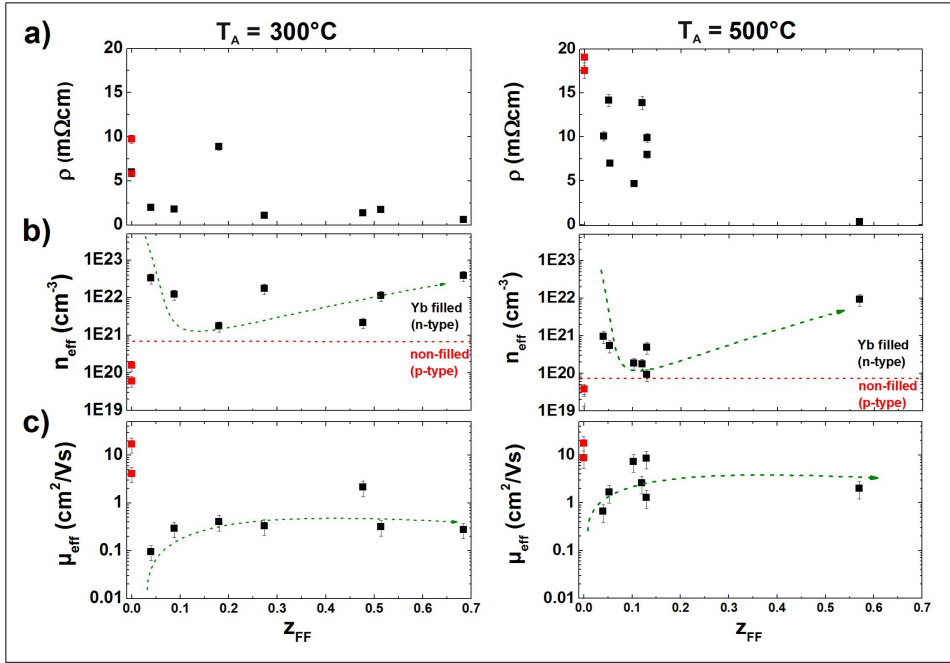


Figure 11.5: Results of the electric measurements of $Yb_z(CoSb_3)_4$ thin films performed at room temperature. For both annealing temperatures, (a) the resistivity $\rho$ , (b) the Hall mobility $\mu_{eff}$ and (c) the effective carrier concentration $n_{eff}$ is shown in dependence on the Yb filling fraction $z_{FF}$. Yb dopes the material strongly. A switch from p- to n-type conduction and metal-like carrier densities are observed. The green arrows should illustrate one possible model to explain the data for low filling fractions.

described in chapter 4.1.1, which can be realized for instance by the substitution of Co with Fe. The samples annealed at 500 °C exhibit a larger resistivity and in average an order of magnitude lower effective charge carrier concentration, which is due to the defect healing during the annealing process (see ch. 7.1.2).

It is important to note that the Yb filling changes the conduction from p-type to n-type. Yb delivers two additional electrons to the system, resulting in n-type doping. By considering two types of carriers as found for CoSb$_3$, there are two possible models to interpret the dependence of the effective charge carrier concentrations on the filling fraction shown in fig. 11.5 (b). The first model is a heavy doping with electrons in the order of $10^{21}$ cm$^{-3}$ by the introduction of Yb. The initial hole concentration in the CoSb$_3$ host structure is negligible in comparison to the amount of electrons after filling and the fluctuations of $n_{eff}$ are mainly caused by measurement errors and various Sb content. Especially such high charge carrier densities are related to large errors. This model agrees well for the results of the films annealed at 500 °C. However huge effective carrier concentrations were observed for films annealed at 300 °C with low filling fractions, which are difficult to explain only by measurement errors and could be caused by compensation of p and n-type charge carriers. Both carrier types cancel each other out and very low Hall voltage would be obtained as already found for Fe$_x$Co$_{1-x}$Sb$_3$ films (fig. 10.4). The calculated effective charge carrier concentration exhibits in that case a singularity explaining the strong increase for low filling fraction. The concentration of n-type carriers is further increased for larger filling fraction, which is usually connected with a minimum of the effective charge carrier concentration followed again by an increase for the electron dominated regime. The basically expected curve shape corresponding to the second model is illustrated by the green arrows in fig. 11.5 (b) and (c). The used equation for the calculating the effective charge carrier density is in that case only usable in the electron dominated regime beyond the minimum. Close to the compensation it is not valid and delivers this unrealistic large values. Furthermore, this second model would agree to the thermoelectric investigations of the CoSb$_3$ composition series, which was discussed in chapter 8.1, and also to the results found for the Fe$_x$Co$_{1-x}$Sb$_3$ film series with different Fe content discussed in chapter 10.1. The synthesized CoSb$_3$ films are bipolar exhibiting an excess of heavy electrons in combination with light holes. The Hall constant is positive. By substitution with Fe, the films become hole dominated and the electron contribution can be neglected. By filling with Yb, the compensation point is passed (singularity of the effective charge carrier concentration, Hall constant reveal sign change) and the films become electron dominated for larger filling fractions.

The effective mobility $\mu_{eff}$ are presented in fig. 11.5 (c). The values are larger for films annealed at 500 °C due to less defects. The non-filled films show the highest effective mobilities for both annealing temperatures and a rapid drop can be found for films with Yb due to the scattering of the charge carriers at the introduced ionic

impurities (Yb ions). In the first model the low effective mobilities observed for small filling fractions might be explained by an enhanced electron-hole scattering. In the second model these low values are related to the compensation of both carrier types. The effective mobility has to approach zero, where the singularity in the effective charge carrier concentration occurs, since the used equations to calculate $n_{eff}$ and $\mu_{eff}$ would not be valid for this bipolar regime.

Even though it can not be verified with the present series which model is valid for low filling fractions, it can be concluded that the Yb filling yields a n-type doping and metal-like charge carrier densities. This charge has to be compensated, otherwise the benefit of a lower phononic thermal conductivity by filling will be lowered by a strongly increased electronic thermal conductivity.

## Thermal properties

The incorporation of fillers should lower the thermal conductivity of the skutterudite thin films and was investigated by time resolved X-ray diffraction (TRXRD), asynchronous optical sampling (ASOPS), and Raman scattering. With the first method the overall thermal conductivity is investigated, while the others give mainly information about the phononic contribution. ASOPS is thereby most sensitive to acoustic phonon modes and Raman spectroscopy to optical modes. The main effect of the fillers should be a lowered acoustic contribution to the phononic thermal conductivity. However, since the electric properties and therefore the electronic thermal conductivity are also changed, at least the TRXRD should be also influenced by the larger charge carrier density. As discussed below, it can be shown with all methods that the Yb ions influence the thermal properties, however an absolute value for the thermal conductivity could not be determined.

### Time resolved X-ray diffraction

Time resolved XRD (TRXRD) was performed for the $Yb_z(CoSb_3)_4$ films annealed at $300°$, since these samples exhibit a wider variation of the filling fraction than the films annealed at $500°$ and thus a possible influence of the fillers on the thermal conductivity can be better investigated. Films with a filling fraction of $z_{FF} = 0$, 0.08, 0.27 and 0.68 were investigated. For these measurements, an additional Au film with a thickness of 20 nm - 30 nm was deposited on top of the skutterudite film, which is illustrated in fig. 11.6 (a). The sample was afterwards heated by laser pulses and the following cooling process of the Au film is a measure for the thermal conductivity of the film underneath. The change of temperature due to the laser pulse is detected by XRD. Thermal expansion yields an increase of the lattice parameter in the heated sample and thus a change of the peak positions in the XRD diffraction pattern (see fig. 11.6 (b)). If the evolution of the peak shift is investigated with time, temperature changes can be detected, which is shown for the Au film in figure 11.6 (c). Analyzing
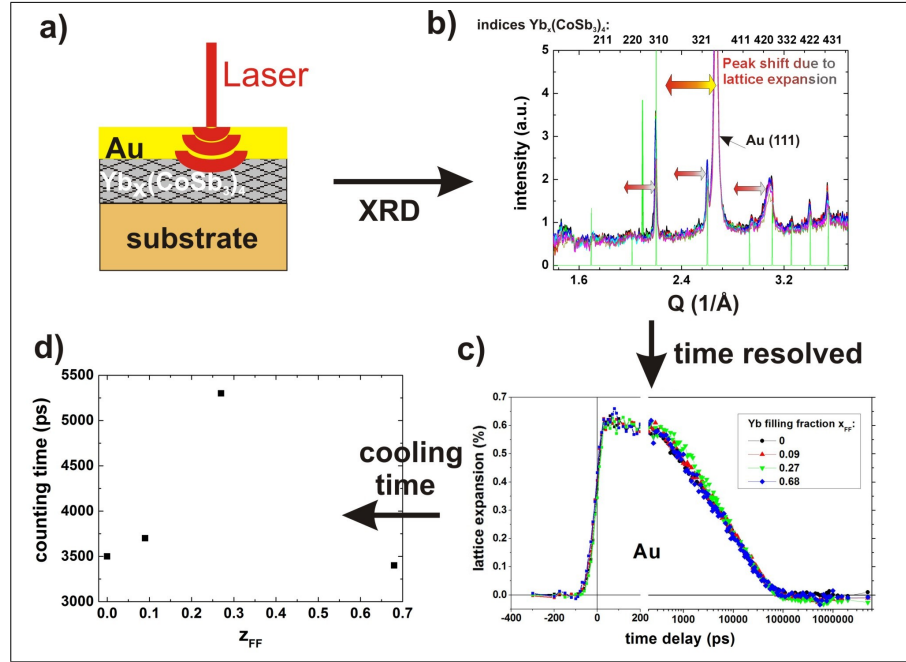
Figure 11.6: Principle of the time resolved XRD measurements. a) A laser pulse heats the Au film on top of the Yb$_z$(CoSb$_3$)$_4$ film. b) The temperature increase yield to a lattice expansion detected by XRD. c) Time resolved XRD enables the investigation of the cooling process. d) The cooling constant is extracted by a fit of the exponential decay of the Au cooling curve shown in dependence of the filling fraction $z$ of the skutterudite layer.

the shift of specific peaks corresponding to different phases (here Au and skutterudite phase), enables the characterization of temperature changes in the individual layers. From the observed cooling curves of a layer, specific time constants of the cooling process can be extracted (see fig. 11.6 (d)), which are connected to the thermal transport processes and the thermal conductivities of the underlying layers. Interface dominated cooling has an exponential temperature decay, while bulk dominated heat conduction follows a power law [141].

In the present case, the laser heat is dissipated in the first 10 nm - 20 nm (mainly the Au-film) and after ~100 ps a homogeneous temperature is reached in the Au film and the lattice expansion is constant (see fig. 11.7 (a)). A weak lattice expansion is also observed for the skutterudite film (see fig. 11.7 (b)) in this time regime, which is believed to be related to heat conduction by electrons. After 300 ps the Au film starts to cool down (lattice expansion decreases, 300 ps - 500 ps) by conduction of heat through the CoSb$_3$ film. This can be also seen as additional change of the
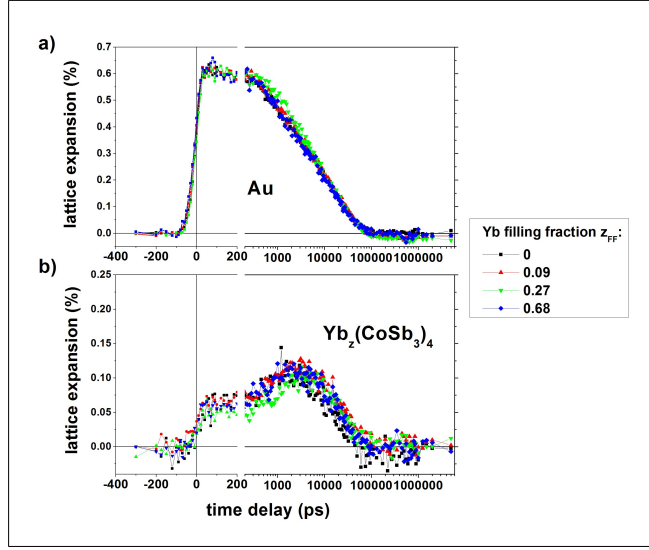
Figure 11.7: Results of time resolved XRD for the film system $Au/Yb_z(CoSb_3)_4$/substrate. The skutterudite $Yb_z(CoSb_3)_4$ layer was annealed at $300\,°C$. a) A laser pulse heats the top Au film at 0 and yield a sharp lattice expansion. b) Later the heat is transferred through to the $Yb_z(CoSb_3)_4$ film underneath, indicated by the additional change of lattice expansion in this film after 200 ps. After 10000 ps both layers relax to room temperature. Different Yb filling fractions $z_{FF}$ are compared.

lattice expansion of the skutterudite phase in figure 11.7 (b). After 10000 ps both films relax towards room temperature and the initial temperature and thus the initial lattice parameter is reached again after $\sim$50 ns.

The filling fraction $z_{FF}$ of the $Ybz(CoSb_3)_4$ influences the cooling process of the Au layer in the time range between 500 ps - 5000 ps. An analysis of the first exponential decay to extract the cooling constant for this process was performed for these samples and the determined values are shown in fig. 11.6 (d). The cooling time of the Au layer increases with the filling fraction $z_{FF}$. Usually a larger cooling time is related to a lower thermal conductivity of the underlying film. The highest cooling time and therefore the lowest thermal conductivity of the skutterudite film is observed for the sample with a filling fraction $z_{FF} = 0.27$. It is therefore believed that the Yb filling lowers the thermal conductivity as expected. The sample with the unusual high filling fraction has again a lower cooling time, which is not understood. Additional samples with different filling fractions have to be investigated with this method. For a quantitative calculation of the thermal conductivity, a fit of the temperature curves by modeling the heat flux in the individual layers is necessary.This calculations are in progress for the measured data. First measurements were also performed for

films annealed at 500 °C, however it was not possible to extract the time constant, because the cooling time is about 8 ns and therefore already in a time regime, which is dominated by the SiO$_2$ layer of the substrate. To overcome this limitations given by the substrate, it is necessary for future measurements to choose suitable substrates with much larger thermal conductivity than the skutterudite film itself.

## Investigation of acoustic phonons by asynchronous optical sampling (ASOPS)

High-speed asynchronous optical sampling (ASOPS) is a femtosecond pump-probe laser spectroscopy technique to generate and detect coherent acoustic phonons in a material for the investigation of thermal properties like the speed of sound. This technique was performed for selected Yb$_z$(CoSb$_3$)$_4$ films with different filling fraction (annealing temperature 300 °C; $z_{FF}$ = 0, 0.08, 0.27 and 0.68) to investigate the influence of the filling fraction on the acoustic phonons [184]. The basic principle is explained in the following, details can be found elsewhere [142, 143]. An ultrashort pump pulse will be absorbed in the film and non equilibrium carriers are generated. When these carriers relax fast, isotropic stress is created and yield to a longitudinal acoustic phonon pulse propagating in the film with the speed of sound and getting reflected at interfaces and surfaces. This pulse modifies locally the optical constants (reflectivity), which can be detected by a time delayed probe pulse.

The measured time dependence of the relative reflectivities is shown in fig. 11.8 (a) after subtracting the decaying background of the excited charge carriers. All samples
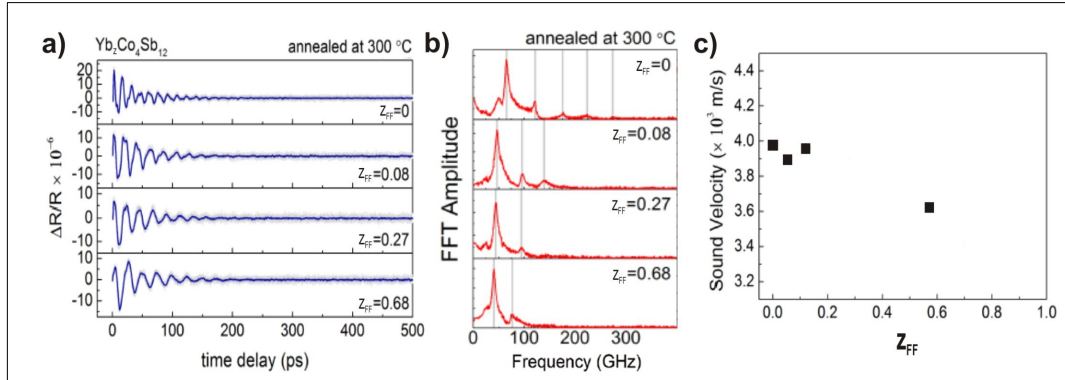


Figure 11.8: Asynchronous optical sampling (ASOPS) of Yb$_z$(CoSb$_3$)$_4$ films, which were annealed at 300 °C [184]. a) measured change of reflectivity with time in dependence of the filling fractions $z_{FF}$. Damped oscillations are observed. b) Fast Fourier transformation (FFT) of the data, resulting in equidistant peaks. c) The sound velocity of the films in dependence of the filling fraction $z_{FF}$.

exhibit damped oscillations [184]. The FFT analysis of this data can be found in fig. 11.8 (b), for which equidistant peaks are revealed [184]. These peaks are caused due to the limited film thickness. The pulse get reflected at the surface and at the bottom interface of the skutterudite film and standing waves are created by interference. For the unfilled sample peaks corresponding up to the 5th order can be observed. With increasing filling fraction the observed signal from high order resonances get more and more damped and for the film with the largest filling fraction only the first and second order is detectable. This suppression of the high frequency peaks is an indication for a stronger scattering of the phonons by incorporation of the rattler ions and therefore a decreased thermal conductivity. Additionally, a peak shift between the films with different filling fractions $z_{FF}$ can be found, which is mainly caused by differences in film thickness. The frequency $f$, where a peak occurs, is related to the mode number $m$ by:

$$f_m = \frac{m v_l}{2d}. \tag{11.1}$$

$v_l$ is the longitudinal sound velocity and $d$ the film thickness. Using this equation, $v_l$ can be determined in dependence of the Yb filling fraction $z_{FF}$ (s. fig. 11.8 (c)) [184]. For moderate filling fractions, the sound velocity remains nearly constant and has a magnitude of about $4000\,\mathrm{m/s}$. This value is in the range of existing literature values achieved for bulk $CoSb_3$ . A slight decrease with filling might occur, but the deviation should be mainly related to the errors made by the determination of the film thickness. To increase the accuracy, the measurement of the thickness has to be improved. For the highest filling fraction, a clear decrease of $v_l$ is observed. Since the discrepancy between Yb content $z$ and filling fraction $z_{FF}$ is very large for this sample, it has to be confirmed in future work if this strong decrease is only related to the Yb filling. Furthermore, the results of TRXRD measurements indicate in contrast an increase of the overall thermal conductivity for this sample. Since the results achieved by ASOPS reveal a lower speed of sound and a strong damping of acoustic phonon modes, the increased electronic thermal conductivity due to the large charge carrier density for this sample must overcompensate the decreased phononic contribution of the thermal conductivity.

To summarize, filling with Yb has two effects for decreasing the phononic thermal conductivity: i) an enhanced scattering of acoustic phonons and ii) indications for a decrease of the speed of sound [184]. While enlarged scattering occurs already for low filling fractions, a reduced speed of sound is only found for large filling fractions and has to be confirmed in future studies. The tendency of a decreasing thermal conductivity with increasing filling fraction, which was also observed by TRXRD, can be confirmed.

## Raman spectroscopy

The annealed Yb$_z$(CoSb$_3$)$_4$ films were investigated by Raman spectroscopy to investigate changes of the optical modes due to the filling with Yb. Again only the results for films annealed at 300 °C are shown. The Raman measurements were performed with the same parameter as used for the Fe$_x$Co$_{1-x}$Sb$_3$ films (see ch. 5.4, green laser, 532 nm, 2 mW, different polarization). The footprint of pure CoSb$_3$ (see fig. 10.7) is also found for Yb filled films [177]. The measured curves are presented in figure 11.9 and the modes of pure CoSb$_3$ are marked. All modes belong to vibrations of Sb atoms and the oscillations of the filling ions could not be directly observed. However, these oscillation have a strong influence on the Sb vibrational modes. With increasing filling fraction a peak shift towards smaller wave numbers and a broadening of the peaks is observed. In the work of Nolas et al. [177] it is claimed, that the shift is due to an increase of the lattice constant and the broadening due to a distortion of the Sb modes by the rattling of the guest ions. In this work a more systematic investigation of these effects is possible due to the larger number of available filling fractions.
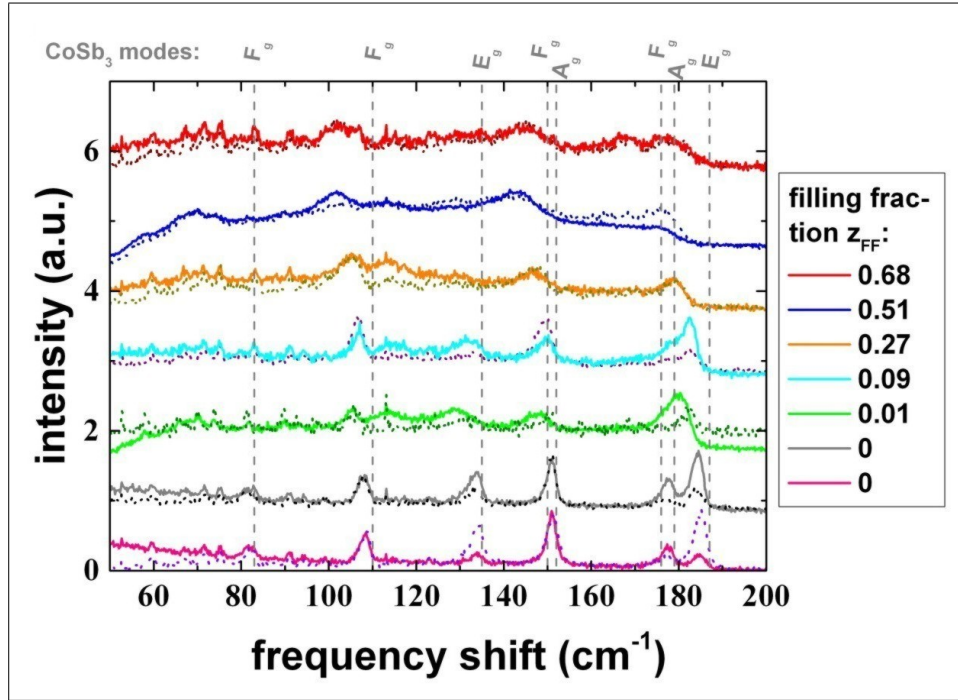


Figure 11.9: Raman spectra for Yb$_z$(CoSb$_3$)$_4$ films with different Yb filling fractions $z_{FF}$ and different polarization (parallel-solid line, perpendicular-dotted line). The measured spectra were obtained after annealing at 300 °C. The sharp peaks at low wave numbers are parasitic effects of the used laser.
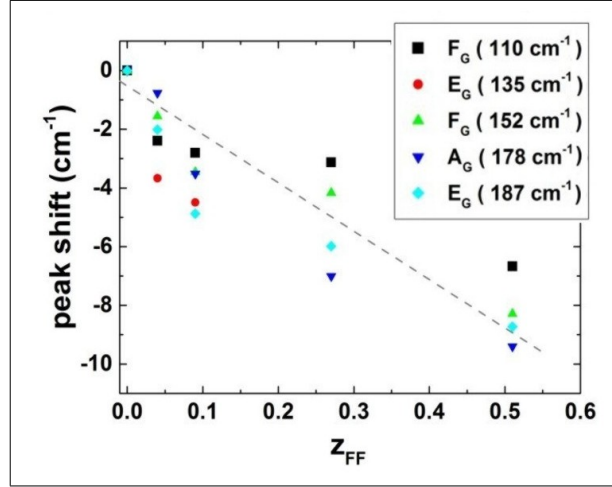
Figure 11.10: The Raman peaks shift to smaller wave numbers with increasing filling fraction.

The signal-to-noise ratio is again decreased with larger filling fraction due to the increase in charge carrier density and thus the stronger shielding of the laser beam. This causes a lowered intensity of the obtained modes, however the $E_G$ mode at $\sim 135\,\mathrm{cm}^{-1}$ reveals a much larger decrease and does nearly vanish, as already observed for the $Fe_xCo_{1-x}Sb_3$ films with increasing $x$. The symmetry change responsible for this change has to be further investigated.

The shift of the individual peaks is shown in fig. 11.10 as function of the filling fraction $z_{FF}$ and a linear behaviour is roughly observed. The overall shift is in the same range as found for the $Fe_xCo_{1-x}Sb_3$ shown in fig. 10.9. This agrees to the claim that the shift of the Raman peaks is related to a change of the lattice constant, since the increase of the lattice constant due to the Yb filling is also in the same range as for the increase by Fe substitution of Co (fig. 11.3 and 10.3). In contrast to the peak shift of $Fe_xCo_{1-x}Sb_3$, all modes exhibit the same shift. This indicates that the filling with Yb has a different influence on the Sb modes than the substitution with Fe. Fe might change the symmetry of the vibrational modes (s. ch. 10.1), while the filling with Yb only yields a homogeneous extension of the lattice constant and the symmetry of the Sb modes is not changed.

# 12 Examples for nanostructured thin film approaches

## 12.1 CoSb₃ thickness series

Two different thickness series in the range between 2 nm and 150 nm were codeposited on SiO$_2$(100nm)/Si(100) at 200 °C. The films of the first series exhibits a Sb content of 74.5 at.% - 76.0 at.% and the films of the second series a Sb content of 73.0 at.% - 74.5 at.%.
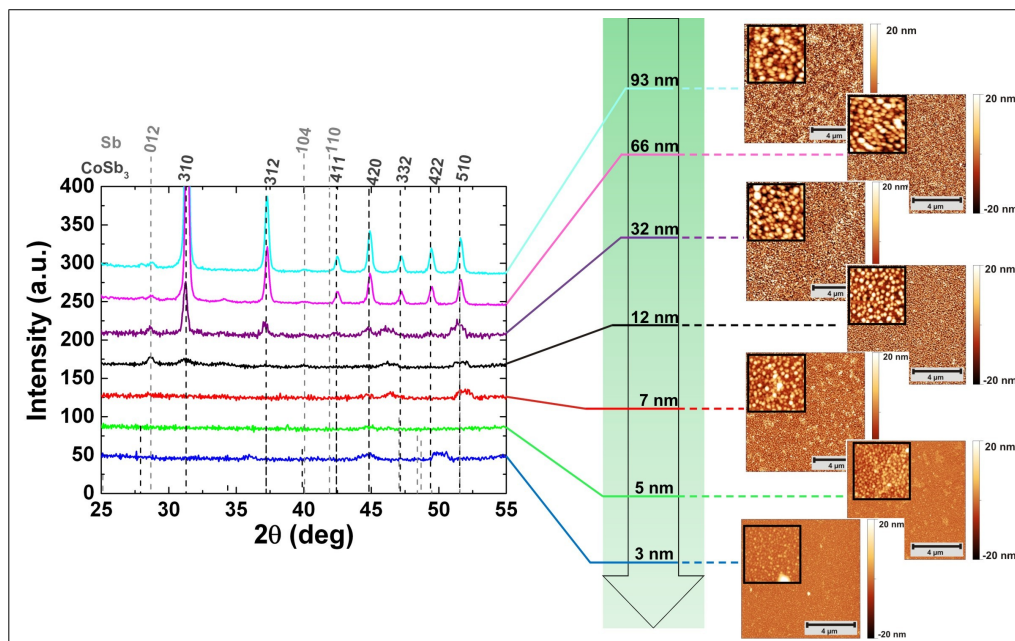


Figure 12.1: XRD investigation of CoSb$_3$ films with different film thickness and the corresponding AFM images. The films are deposited at 200 °C and exhibit a Sb content close to 75 at.%. However, the large deposition rate yield rough surfaces and Sb as minor phase. Below 10 nm the film signal is too low to identify peaks in the XRD pattern.
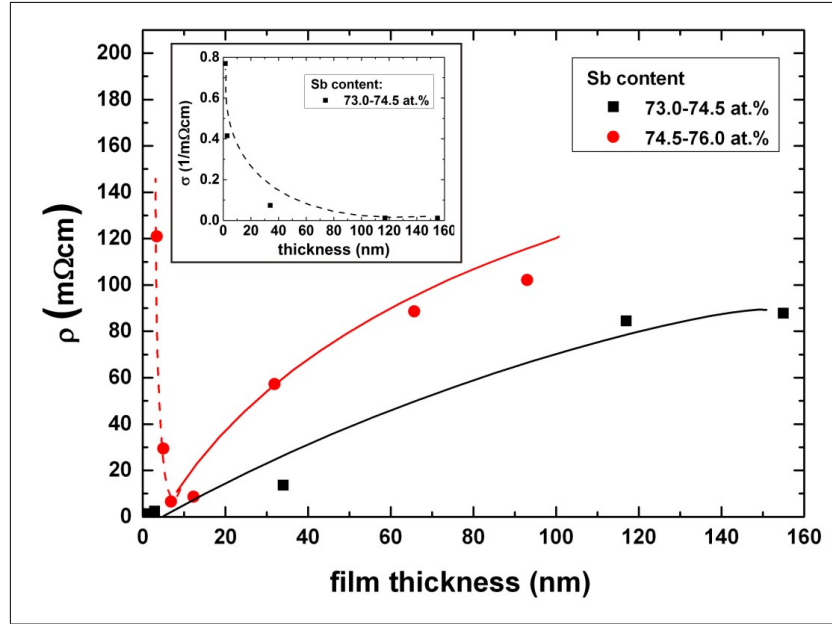
Figure 12.2: The resistivity of two CoSb$_3$ thin film series with different Sb content is plotted as function of the film thickness. The films were deposited at 200 °C. The inset shows the thickness dependence of the conductivity for the series with lower Sb content. The lines are only a guide to the eye.

The XRD measurements of the first series (74.5 at.% - 76 at.% Sb) are shown in fig. 12.1. The skutterudite phase is revealed as major phase and the Sb phase as minor phase down to a film thickness of 12 nm. The signal coming from the investigated film is for smaller thicknesses too weak to identify crystalline phases.

All films exhibit a strongly grained surface, which can be seen in the AFM images presented in fig. 12.1. Roughness and grain size increase with increasing film thickness. However, the thinnest films with a thickness of 3 nm and 5 nm exhibit probably a discontinuous surface, since there are no indications in the AFM image for material in between the islands, which can still be found in the AFM images for films of 7 nm thickness or thicker. The observed minor phases and the grained surfaces are caused by the relatively high deposition rate of $\Phi_{Sb} = 1.2$ Å/s (see chapter 7.1.3).

Film thickness and morphology should have a strong influence on the electric properties for several reasons. The electrical conductivity could be increased due to quantum confinement, which was introduced in chapter 2.2; the enlarged surface-to-bulk ratio could yield charge carrier generation at the surfaces, surface states or scattering due to the surface roughness. Therefore van der Pauw and Hall measurements were performed at room temperature to determine resistivity, charge carrier density and

Hall mobility in dependence of the film thickness. The measured resistivity for the different film series are shown in fig. 12.2. The resistivity for films with a Sb content around 75 at.% (red curve) decreases with decreasing film thickness and reaches its minimum value of 6.6 mΩcm for 7 nm thick film. For thinner films the resistivity of this series increases rapidly, which can be attributed to the discontinuous film surface found by AFM. The decrease of resistivity is mainly caused by an increase of the (effective) charge carrier density from $2 \cdot 10^{19}$ cm$^{-3}$ (90 nm) up to $1.25 \cdot 10^{21}$ cm$^{-3}$ (7 nm), shown in fig. 12.3 (a) for the same series. This could be caused by quantum confinement, a surface state and/or by charge carrier generation at the surface. Based on these measurements, it can not distinguished which of these effect dominates. Deeper insights might be given by a model, where the density and the mobility of the charge carriers were treated separately for the surface and the film [185, 186]. Compared to the large change of the effective charge carrier density, only a slight change of the effective Hall mobility of this series from 4 cm$^2$/Vs to 1 cm$^2$/Vs can be observed with decreasing thickness, which might be related to surface scattering due to the enlarged surface-to-bulk ratio. Nevertheless, bipolar conduction is expected for these films and both, $n_{eff}$ and $\mu_{eff}$ have to be taken with caution.

For the series with a Sb content between 73.0 at.% - 74.5 at.% similar results are obtained. For this series CoSb$_3$ is also observed as major phase by XRD and the films exhibit a strongly grained surface. However, the lower Sb content yield CoSb$_2$ as additional minor phase and a lower resistance, which is in agreement to the results found for the composition series in chapter 8.1.1. Again a decrease of the resistivity with decreasing thickness is observed. For these series continuous films down to a
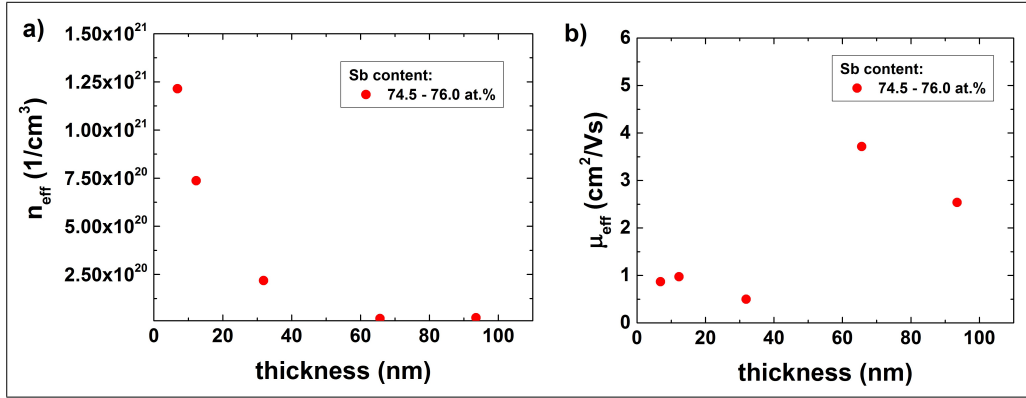


Figure 12.3: a) Effective charge carrier density and b) effective Hall mobility in dependence of the film thickness for CoSb$_3$ films with a Sb content of ∼ 75 at.% deposited at 200 °C. A single band model is used to determine both parameter from resistivity and Hall measurements.

thickness of 1.3 nm could be deposited, even though the surface structure found by AFM (not shown) does not differ noteworthy from the series discussed first. Therefore, the resistivity reveal a strong decrease for thicknesses well below 5 nm, which is better visualized in the inset of fig. 12.2 showing the electrical conductivity over the thickness of these films.

To conclude it could be shown, that the lowered dimension of thin films could enhance the electric properties as foreseen by Dresselhaus et al. [6, 7]. The simplest explanation to interpret the measured data would be a charge carrier generation at the surfaces and thereby a decrease of mobility due to the generated ionic impurities. In practice a contribution of several different effects is expected, and different models have be taken into account (e.g. [185, 186]).

## 12.2 $Fe_xCo_{1-x}Sb_3$ gradient films

The charge carrier density of $CoSb_3$ can be controlled by substitution of Co with Fe atoms as presented in chapter 10. Another effect of the incorporation of Fe is a decrease of the thermal conductivity by mass scattering due to the mass difference of Co and Fe [20]. Since the speed of sound of $CoSb_3$ and $FeSb_3$ differs [98], also multi-layer systems of both skutterudites should be promising. A much stronger influence on the thermal conductivity is expected for inhomogeneous samples, where the Fe content of the film varies due to nanostructuring. This could be achieved by the synthesis of a $Fe_xCo_{1-x}Sb_3$ gradient layer, where the Fe content $x$ is gradually changed. To investigate the feasibility of this approach, a $Fe_xCo_{1-x}Sb_3$ cross plane gradient film with varying $x$ from 0 (bottom interface) to 0.5 (surface) was deposited on a Si(100) substrate by MERM at room temperature (see chapter 6.2). This method is used, since it is much more challenging to deposit a film with gradient and desired stoichiometry by codeposition of all elements. However, the depositions have to be performed at room temperature and a post-annealing step is required for crystallization. The nominal stacking sequence to achieve the gradient is illustrated in fig. 12.4 and is based on the principle used to achieve $Fe_xCo_{1-x}Sb_3$ with constant $x$, which was discussed in chapter 10.2.

However, the incorporation of Fe yields doping of the material (see ch. 10) and the variation range of $x$ need to be chosen with respect to the associated increase of the charge carrier density and thus with respect to the thermoelectric properties. The best thermoelectric power factor at room temperature was achieved for a Fe content of $x = 0.49$ (s. chapter 10). Therefore, the average value $\bar{x}$ of the gradient film should be around this value or at least in the hole dominated regime ($x > 0.1$, fig. 10.4). The nominal $\bar{x}$ for the present layer stack is 0.3, which is clearly in the hole dominated regime, but slightly lower than the maximum value of $x = 0.49$.
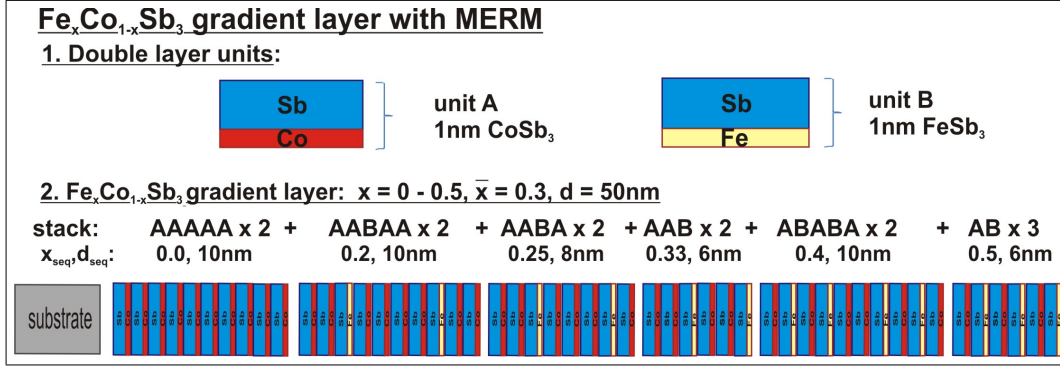
**Fe$_x$Co$_{1-x}$Sb$_3$ gradient layer with MERM**

**1. Double layer units:**

| Sb | } | unit A |
|----|---|--------|
| Co |   | 1nm CoSb$_3$ |

| Sb | } | unit B |
|----|---|--------|
| Fe |   | 1nm FeSb$_3$ |

**2. Fe$_x$Co$_{1-x}$Sb$_3$ gradient layer:  x = 0 - 0.5, x̄ = 0.3, d = 50nm**

| stack: | AAAAA x 2 + | AABAA x 2 | + AABA x 2 | + AAB x 2 + | ABABA x 2 | + AB x 3 |
|--------|-------------|-----------|-----------|-------------|-----------|----------|
| x$_{seq}$,d$_{seq}$: | 0.0, 10nm | 0.2, 10nm | 0.25, 8nm | 0.33, 6nm | 0.4, 10nm | 0.5, 6nm |

substrate

Figure 12.4: Layer stack of a Fe$_x$Co$_{1-x}$Sb$_3$ gradient film prepared by the modulated elemental reactant method (MERM). The Fe content $x$ varies from 0 at the substrate interface to 0.5 at the film surface.

The overall composition of the as-deposited film was checked by RBS. The measured spectrum is shown in fig. 12.5 (a). Besides the expected elements Co, Fe, and Sb, a contamination with 5 at.% of Se was found in the film, which is caused by heated side walls. The Simnra simulation [106, 107] of the measured data is included in fig. 12.5 (a) and also the contribution of the individual elements. The performed simulation is based on a homogeneous Fe$_x$Co$_{1-x}$Sb$_3$ film with constant $x$. This assumption reveals deviations from the measured curve especially in the energy range of the overlapping contributions of Co and Fe, which is shown in fig. 12.5 (b) in detail. The composition was extracted from the performed simulation and the results are summarized in figure 12.5 (a) in the inserted table. The contribution of the Se contamination was thereby neglected. The film has a slightly larger Sb content than the nominal stack and $\bar{x}$ is with 0.43 also higher than expected.

Different pieces of this as-deposited sample were annealed in UHV for one hour at 200 °C, 300 °C and 400 °C, respectively. The thermal stability of the gradient by this heat treatment is a second important aspect for the feasibility of the synthesis of Fe$_x$Co$_{1-x}$Sb$_3$ gradient films. First it is necessary that the films crystallize during the annealing process before the gradient can be compensated by diffusion processes. In chapter 10 it was shown that all Fe$_x$Co$_{1-x}$Sb$_3$ crystallize usually in a single event between 150 °C and 210 °C. These temperatures are relatively low, resulting in a high probability that the films crystallize before the gradient is completely vanished. Furthermore, the gradient and the skutterudite phase need to endure temperatures up to 500 °C afterwards. For high temperatures, a gradient usually yield diffusion and thus a homogenization of the film. Therefore, the bonding energy of the formed Fe$_x$Co$_{1-x}$Sb$_3$ crystals has to be high enough and the bonds strong enough in comparison to the applied heat energy. The performed RBS measurements indicate that both

requirements are fulfilled, since no changes of the RBS spectra were obtained with increasing annealing temperature (not shown). This implies also, that the amount of Se stays constant and no outgassing of Se occurs during the annealing process.
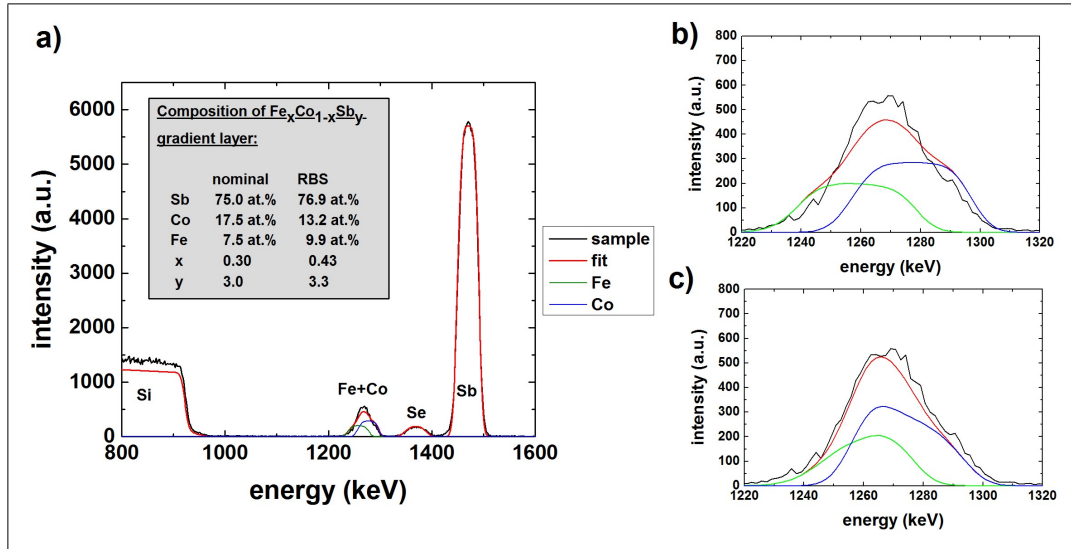


Figure 12.5: a) RBS spectra of the as-deposited $Fe_xCo_{1-x}Sb_y$ gradient film and the simulated data using only a single layer with constant $x$. The overall composition determined with this approach is given in the table (inset). b) Shows an enlarged part of the Fe and Co contribution fitted by the single layer approach. c) Simulation repeated by using the depth profile information obtained by SNMS.

The XRD scans of the annealed films can be found in fig. 12.6 for different annealing temperatures and all films reveal the skutterudite phase. Parasitic phases and especially phases attributed to the Se contamination are not detected. A small peak shift towards higher angles is observed for different annealing temperatures and can be attributed either to defect healing (ch. 7.1.2) or to changes in the lattice constant by rearrangements of the Fe atoms. The peaks are symmetric and the (310) peak shows for instance within the usual deviations no significant broadening compared to pure $CoSb_3$ films. A distribution of different lattice constants, as one could expect for the strong variation of $x$, is therefore not observed. The position of the (301) peak was extracted for the film annealed at $400\,^{\circ}C$ by fitting a Gaussian function and corresponds to a lattice constant of $9.0723\,\text{Å}$, which is larger than the obtained value for $CoSb_3$ (chapter 7.1.2). A similar increase was also observed for homogeneous $Fe_xCo_{1-x}Sb_3$ films with different $x$ (shown in fig. 10.3 (b)). By using the corresponding linear function of this increase, the lattice constant of the gradient film
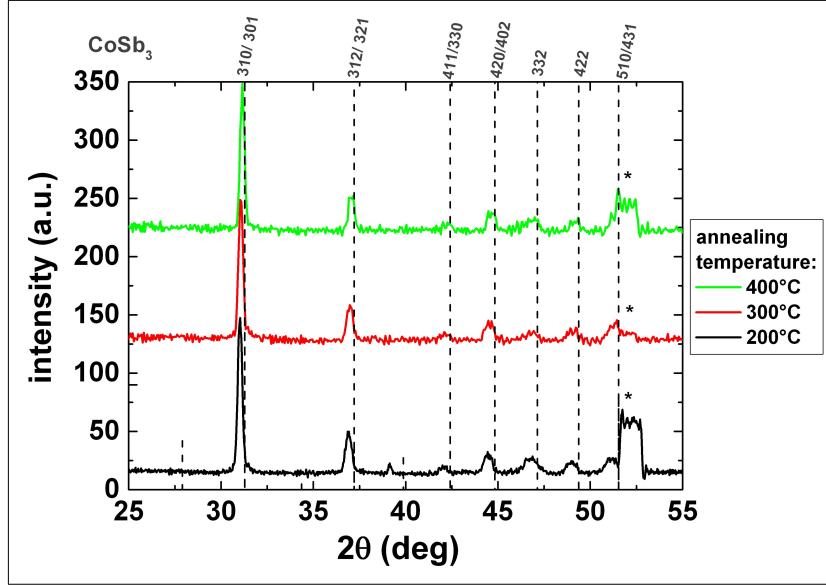
Figure 12.6: XRD pattern of room temperature deposited Fe$_x$Co$_{1-x}$Sb$_3$ gradient films obtained after annealing at different temperatures. Single phase skutterudite films are observed. Substrate peaks are marked by asterisk.

(9.0723 Å) would yield to a substitution level of $x = 0.41$, which is in good agreement to the determined $\bar{x}$ of 0.43 using RBS. Thus, the XRD investigations support in contrast to the RBS results the formation of a homogeneous film with a constant lattice parameter and constant $x$ more.

To answer the question, if the gradient is still present after the post-annealing of the films, the depth profile of the individual elements was determined by secondary neutral mass spectrometry (SNMS). The measured curve of the as-deposited sample is plotted in fig. 12.7 (a). The extracted average composition is close to the results of the RBS measurements ($\sim$8 at.% Fe, $\sim$12 at.% Co and $\sim$80 at.% Sb; $x = 0.4$).

The measured curves exhibit some artifacts close to the surface (sharp peaks), which could be caused by the measurements itself or by some surface oxidation. The parasitic Se content is about 4 at.% and constant over the whole film thickness, while Sb reveals a minimum of 76 at.% for a depth region around 25 nm and increases afterwards again to the initial 80 at.%. Underneath the surface region (first 5 nm) the Fe and the Co concentration is nearly equal (around 8 at.%). This matches quite well with the nominal layer stack, where Fe and Co should have the same concentration at the top surface of the film. By analyzing the Co profile it can be found, that the Co content increases continuously in the first 25 nm up to 13.5 at.% and exhibits only weak changes for larger depth. Finally some disturbances occur close
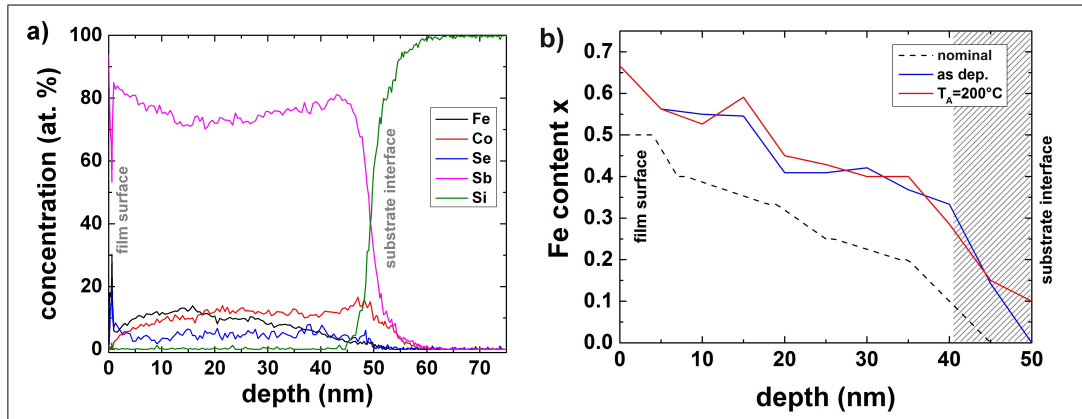
Figure 12.7: a) Elemental depth profile of the as-deposited $Fe_xCo_{1-x}Sb_3$ gradient film obtained by secondary neutral mass spectroscopy (SNMS). b) Extracted depth profile of the Fe content $x$ for the nominal layer stack, the as-deposited gradient film, and the gradient film annealed at $200\,°C$.

to the substrate interface. Fe starts to decrease linearly in concentration for a film depth larger than 15 nm and reaches values lower than 1 at.% close to the substrate interface. A gradient in $x$ can be therefore clearly observed by the depth profile of Co and Fe. For the nominal layer stack there should be no Fe between 40 nm and 50 nm in the depth profile. However, the detected Fe amount in a depth of 40 nm is still 5 at.% and decreases slowly. Therefore diffusion of Fe must have occurred in this depth region during deposition. The observed SNMS depth profile was used to simulate the RBS data again by using several layers. The resulting fit is shown in fig. 12.5 (c) and approaches the experimental data much better than the former used homogeneous film approach presented in fig. 12.5 (b). The RBS and the SNMS measurements agree well and the obtained depth profile can be verified.

The SNMS spectra obtained after annealing at the different temperatures reveal no significant differences in comparison to the as-deposited sample and the Fe gradient is maintained. In figure 12.8 the comparison of the individual elemental depth profiles are shown in dependence of the used annealing temperatures. In these plots, it is more clear, that no changes occur in the elemental distribution by annealing. The distribution of Sb becomes slightly more homogeneous with a Sb concentration of around 79 at.%. Neither diffusion processes of Co or Fe are observed that compensate the gradient, nor the Se diffuses to the top surface or evaporates. The bonding energy in the skutterudite phase is therefore larger than the energy, which can be obtained by rearrangements, diffusion processes, compensation of the gradient or formation of different phases. It could not be clarified, whether Se has an influence on the stabilization of the gradient, if it contributes to the skutterudite lattice or where
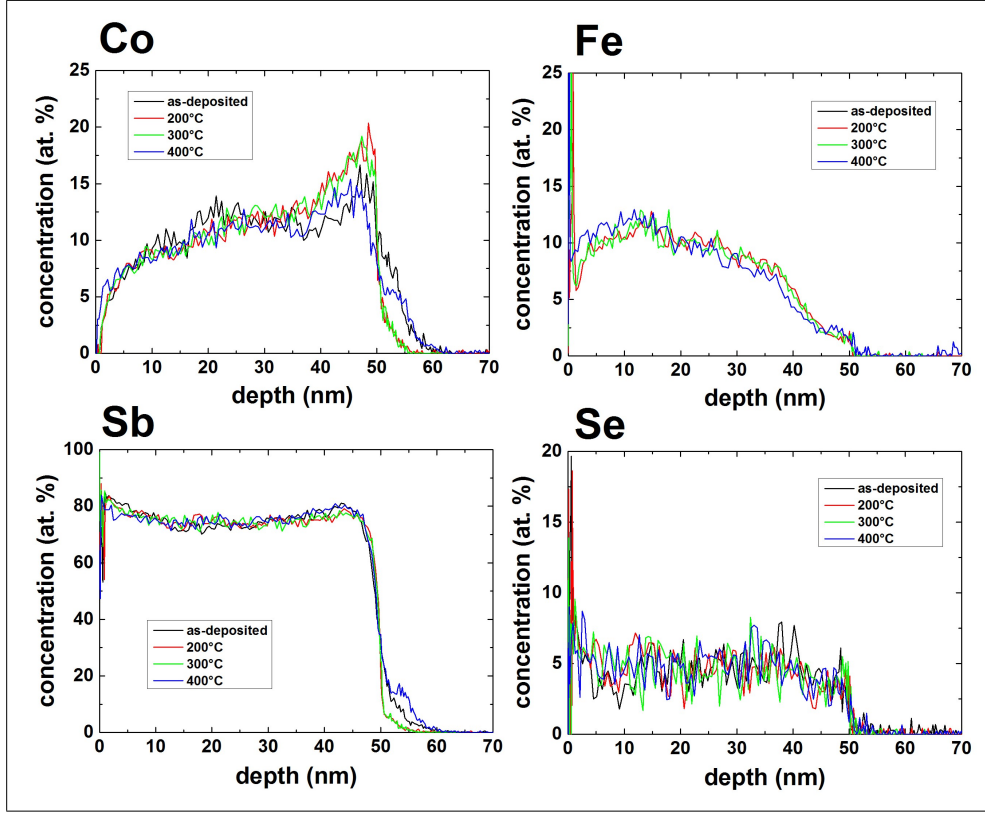
Figure 12.8: Depth profile of the individual elements in a $Fe_xCo_{1-x}Sb_3$ gradient films obtained after annealing at different temperatures. Nearly no changes are observed due to the annealing process and the gradients of Co and Fe are clearly observed. The Se contamination coming from the heated side walls exhibits also an homogeneous profile.

exactly it is situated. However, the maintained profile of Se is in contrast to its high vapor pressure and indicates the incorporation in the skutterudite lattice as already prognosed in chapter 10.2. Additionally it is to note that the Co profile of the annealed samples becomes more linear with depth and a constant region for a larger depth than 25 nm is not observed any more. This change is not yet understood. Since the constant range occurs only for the as-deposited sample, some rearrangements due to crystallization might be an explanation for this change. Measurement errors or inhomogeneous parts of this sample are also possible.

The change of $x$ with increasing depth is shown in fig. 12.7 (b) for a better comparison of the nominal layer stack with the deposited gradient film. The profiles are shown for the nominal layer stack, the as-deposited gradient film and the crystallized film

annealed at $200\,°C$. The linear change of $x$ could be realized in the samples with good accuracy. The investigated films are Fe rich, which yields an constant offset of $x$ of about 0.1 compared to the nominal stack. In the depth range between $40\,nm$ and $50\,nm$ (gray shadowed in the figure), there is no Fe in the nominal profile. However, Fe has diffused in this region and the prepared samples are even closer to a linear profile over the entire thickness range than the nominal one.

To conclude, all results are very promising for future thermoelectric $Fe_xCo_{1-x}Sb_3$ gradient films or multilayer structures, since the gradient can be stabilized up to the necessary working temperatures and the films surface is kept very flat (not shown). If these structures can yield to an enhancement of thermoelectric properties, has to be investigated by future studies and was not performed due to the unknown contribution of the parasitic Se. It is to note that XRD reveals no noteworthy differences between gradient films and homogeneous $Fe_xCo_{1-x}Sb_3$ films, and the mechanism why only a single lattice constant is observed for films with varying Fe content or how the stress due to the distorted lattice parameter is relaxed, was not investigated.

# 13 Summary and Outlook

The present work proves the feasibility to deposit single phase skutterudite thin films by MBE technique. Their structural and thermoelectric properties were investigated by taking the thermal stability and the substrate choice into account. The realization of controlled doping by substitution as well as the incorporation of the guest ions was successfully demonstrated. This work is therefore a good starting point for designing skutterudite based thin film structures. Two successful examples for such structures are given: i) a thickness series, where a strong decrease of the resistivity was observed for films with a thickness lower than 10 nm, and ii) a $Fe_xCo_{1-x}Sb_3$ gradient film, for which the gradient was maintained even at an annealing temperature of 400 °C.

**Deposition and structural properties of the skutterudite films**

For the deposition of the skutterudite films, three deposition methods were used: i) codeposition at room temperature with post annealing step, ii) codeposition at elevated temperatures, and iii) modulated elemental reactant method (MERM). Room temperature deposited films are amorphous and an annealing step is necessary to get them crystalline. The determined crystallization temperatures of $CoSb_3$ and $FeSb_3$ are 161.3 °C and 150.7 °C. Films deposited at elevated temperatures above 170 °C crystallize therefore immediately during deposition.

To achieve thermally stable single phase skutterudite films a little excess of Sb compared to the stoichiometry of $CoSb_3$ ($FeSb_3$) is needed for all different deposition methods and the Sb content must be controlled accurately. For the codeposition, it has to be taken into account, that the sticking coefficients of Sb is larger than for a deposition of pure Sb. Additionally a decrease of the Sb content by thermal evaporation is observed during the annealing process of films deposited at room temperature. The used deposition rates have also to be chosen well. It could be shown that a large rate is supporting the formation of other phases (especially the Sb phase) and a balance between the controllability of the individual fluxes and the film quality has to be found.

The codeposition at elevated temperatures was only investigated for Co-Sb films. It exists only a small composition range, where single phase $CoSb_3$ films can be obtained (74 at.% - 77 at.% Sb) and the formation of parasitic minor phases is supported with increasing deposition temperatures. The single phase $CoSb_3$ films exhibit a relatively smooth surface, however strong island growth is observed if the stoichiometry differs

from the given composition range. The grain size of the single phase films was extracted by EBSD and TEM and a clear decrease by increasing deposition temperature is shown ($175\,°$C: $0.72\,\mu$m, $230\,°$C: $0.02\,\mu$m).

Compared to that, the post-annealed $CoSb_3$ and $FeSb_3$ skutterudite films (codeposited at room temperature or MERM) reveal a larger composition range for single phase skutterudite films (75 at.% - 82 at.% Sb). An increase in annealing temperature results in a relaxation of the lattice constant and in a stronger semiconducting behaviour of the resistivity, which can be attributed to healing of defects. The film surface is very smooth and the roughness is smaller than for the elevated films, which is independent of the annealing temperature. The determined grain size is between $3\,\mu$m and $10\,\mu$m and can be controlled by choosing different heating rates. Larger heating rates yield smaller grain sizes. Decomposition is finally observed for $CoSb_3$ above $600\,°$C and for $FeSb_3$ above $300\,°$C, which corresponds to the maximum working temperature, respectively.

## Thermoelectric properties of $CoSb_3$ and $FeSb_3$ thin films

The thermoelectric properties of $CoSb_3$ are investigated for the combination of skutterudite film and $SiO_2$(100nm)/Si(100) substrate. Semiconducting behaviour is observed for stoichiometric $CoSb_3$ films independent of the used deposition method. Deviations from 75 at.% Sb yield self-doping, and degeneration or metallic behaviour is observed due to the very small bandgap rather quickly. The Seebeck coefficient is strongly influenced by the formation of impurity phases and reveal enlarged values for single phase skutterudite films. The composition range of single phase films for samples deposited at elevated temperatures is very small and the narrow maximum of the resistivity and Seebeck coefficient compensate each other with respect to the power factor, which results in a very low value of $0.08\,\mu$W/K$^2$cm. The annealed films exhibit in contrast a broader composition range of single phase films with enlarged Seebeck coefficient. The Seebeck coefficient is therefore still increased for single phase Sb rich films, while the resistivity is already lowered by self-doping, which results in a larger power factor of $0.2\,\mu$W/K$^2$cm. The relatively low power factors observed in both cases are caused by bipolar conduction. The contribution of heavy electrons and light holes close to the compensation point yield a negative Seebeck coefficient and a positive Hall constant. This bipolar behavior was confirmed by the Hall investigation of $Fe_xCo_{1-x}Sb_3$ and by the investigation of Yb filled $CoSb_3$. The low temperature measurements of the semiconducting samples reveal small bandgaps of around $20\,$m$e$V. However, this value has to be confirmed by high temperature measurements. Additionally the conduction mechanism for temperatures below $150\,$K could be related to variable range hopping.

$FeSb_3$ films deposited on $SiO_2$(100nm)/Si substrate reveal different properties. As expected from the valence electron count, this material exhibits metallic behavior

with large charge carrier density. Nevertheless, the Seebeck coefficient of these films reveal surprisingly large values, which is not understood. Thus the achieved power factor at room temperature of $9\,\mu W/K^2 cm$ is very promising and much larger than the reported values for $CoSb_3$ thin films. The conduction in these films is dominated by holes and no bipolar contribution was identified. However, a way to increase the small mobilities has to be found to enhance the power factor further.

In general, several parameters to optimize the thermoelectric properties of binary skutterudite films have been found: i) the chosen deposition method, ii) the chosen annealing/deposition temperature, iii) the heating rate of the annealing process, and vi) the composition of the film. The best results regarding the power factor at room temperature were achieved for films with a Sb content of $\sim$78 at.%, which have been first deposited at room temperature (codeposition or MERM) by using low deposition rates, and which were afterwards post-annealed with very small heating rates. For $CoSb_3$ additional doping is necessary to overcome the bipolar regime. If these parameters are also preferred for high $ZT$ values, has to be investigated by measurements of the thermal conductivity. Here smaller grain sizes (and thus higher heating rates) are expected to be more suitable for a low thermal conductivity and a balance to the optimum power factor has to be found.

**Influence of the substrate**

The influence of the substrate was also investigated. Suitable substrates need to be insulating, must exhibit a low thermal conductivity and their thermal expansion coefficient should be between $9 \cdot 10^{-6}\,K^{-1}$ and $11 \cdot 10^{-6}\,K^{-1}$ to avoid surface cracks. Possible candidates are special glasses, special ceramics and for instance $ZrO_2$.

Substrates with large thermal conductivity will influence the measuring procedure and reveal wrong values of the Seebeck coefficient $S$. The obtained $S$ of skutterudite films on $SiO_2(100nm)/Si(100)$ are for instance underestimated to about 50 % and should be understood as lower limit. Thus the given values of the power factors need also to be corrected. Furthermore, the $SiO_2$ layer might also yield oxidation of the film from the bottom and it can exhibit pores, which give an electrical connection to the Si at higher temperatures. In future studies this substrate should not be used.

**$Fe_xCo_{1-x}Sb_3$ thin films**

To optimize the thermoelectric properties of the films controlled doping is necessary, which was shown for the $CoSb_3$ films by substitution of the Co atoms in the lattice by Fe. The successful realization of the substitution is confirmed by XRD, Hall measurements, and Raman spectroscopy for films deposited at room temperature followed by a post-annealed step. Noteworthy is that the achieved maximum substitution level of 0.49 is larger than the expected equilibrium value of 0.08 for bulk samples [58].

### $Yb_z(CoSb_3)_4$ thin films

Another necessary step for suitable thermoelectric properties in skutterudites is the incorporation of fillers, which could be also demonstrated for the MBE grown thin films. Yb filled $CoSb_3$ films were deposited at room temperature and post-annealed. The successful realization of the incorporation was shown by XRD combined with Rietveld refinement. For the films annealed at 300 °C an unusual large filling fraction of 0.68 could be realized, which is much larger than the achievable values of 0.2 for equilibrium synthesis techniques [85, 183]. Unfortunately most of the samples show a decrease towards the equilibrium value after annealing at 500 °C. A larger value could only be maintained for one sample, with a Sb content of the host lattice very close to the stoichiometric 75%. It is a very promising result to keep such a large filling fraction at these temperatures. Furthermore, the influence of the filler on the thermal properties was verified by time resolved XRD, Raman spectroscopy and asynchronous optical sampling. All three methods indicate a decrease of the thermal conductivity with increasing filling fraction, even though no absolute value could be determined. It is to note that all Raman peaks shift equally for the different modes, which is in contrast to the films with different Fe substitution level. Thus the filling might only expand the lattice, and does not introduce a symmetry change as it is believed for the substitution with Fe.

### Outlook

In future studies, the filling and the substitution approach have to be combined to achieve p-type and n-type thin films with larger $ZT$. Filling fraction and substitution level have to be adjusted in such a way that the thermal conductivity is strongly lowered by the filler, while the films are additionally still in the semiconducting regime (valence count $\sim 72$). The main challenge to achieve this goal is to determine the thermal conductivity. The extrinsic properties have also to be optimized. For instance the grain size must be controlled to achieve the best combination of low thermal conductivity and small electric mobility.

The optimized individual films can be afterwards used for the variety of possible nanostructuring approaches. There are for instance filled and non-filled $CoSb_3/FeSb_3$ multilayers, $Fe_xCo_{1-x}Sb_3$ multilayer, $Fe_xCo_{1-x}Sb_3$ gradient layers, multilayer/gradient layers with varying grain sizes, multifilled films, geometrical modulated films created by lithography or by deposition on nanoperforations with different geometrical parameters...

# Bibliography

[1] J. M. Ziman. *Prinzipien der Festkörpertheorie.* Akademie Verlag, Berlin, 1974.

[2] R. Pelster, R. Pieper, and I. Hüttl. Thermospannungen - viel genutzt und fast immer falsch erklärt! *Physik und Didaktik in Schule und Hochschule 1/4*, pages 10–22, 2005.

[3] M. Brignone. Development of a Thermoelectric Generator for a 1.4l Gasoline Engine: Results and Future Needs. talk, 11th European Conference on Thermoelectrics, Noordwijk, 2013.

[4] J. Sommerlatte, K. Nielsch, and H. Böttner. Thermoelektrische Multitalente. *Physik Journal*, 6(5):35–41, 2007.

[5] M. S. Dresselhaus, G. Chen, M. Y. Tang, R. Yang, H. Lee, D. Wang, Z. Ren, J.-P. Fleurial, and P. Gogna. New Directions for Low-Dimensional Thermoelectric Materials. *Adv. Mater.*, 19(8):1043–1053, 2007.

[6] L. D. Hicks and M. S. Dresselhaus. Thermoelectric figure of merit of a one-dimensional conductor. *Phys. Rev. B*, 47(24):16631–16634, 1993.

[7] L. D. Hicks and M. S. Dresselhaus. Effect of quantum-well structures onthe thermoelectric figure of merit. *Phys. Rev. B*, 47(19):12727–12731, 1993.

[8] L. Yu-Ming, O. Rabin, S. B. Cronin, J. Y. Ying, and M. S. Dresselhaus. Semimetal-semiconductor transition in $BiSb_x$ alloy nanowires and their thermoelectric properties. *Appl. Phys. Lett.*, 81(13):2403–2405, 2002.

[9] D. M. Rowe. *Thermoelectrics Handbook: Macro to Nano.* CRC Handbook, Taylor and Francis, 2006.

[10] R. Venkatasubramanian, E. Siivola, T. Colpitts, and B. O'Quinn. Thin-film thermoelectric devices with high room-temperature figures of merit. *Nature*, 413:597–602, 2001.

[11] T. Harris, H. Lee, D. Z. Whang, J. H. Huang, Z. F. Ren, B. Klotz, R. Dowding, M. S. Dresselhaus, and G. Chen. Thermal Conductivity Reduction of SiGe Nanocomposites. *Mater. Res. Soc. Symp. Proc.*, 793, 2003.

[12] A. M. Rao, X. Ji, and T.M. Tritt. Properties of nanostructured one-dimensional and composite thermoelectric materials. *MRS Bulletin*, 31:218, 2006.

[13] H. Linke. Thermoelectric Quantum Systems or Energy Filtering in Thermoelectrics. talk, thermoelectric winter school, Bremen, 2010.

[14] J. M. O. Zide, D. Vashae, Z. X. Bian, G. Zeng, J. E. Bowers, A. Shakouri, and A. C. Gossard. Demonstration of electron filtering to increase the Seebeck coefficient in $In_{0.53}Ga_{0.47}As/In_{0.53}Ga_{0.28}Al_{0.19}As$ superlattices. *Phys. Rev. B*, 74(20), 2006.

[15] F. R. Harris, S. Standridge, C. Feik, and D. C. Johnson. Design and Synthesis of $[(Bi_2Te_3)_x(TiTe_2)_y]$ Superlattices. *Angewandte Chemie International Edition*, 42(43):5296–5299, 2003.

[16] W. Kim, J. Zide, A. Gossard, D. Klenov, S. Stemmer, A. Shakouri, and A. Majumdar. Thermal conductivity reduction and thermoelectric figure of merit increase by embedding nanoparticles in crystalline semiconductors. *Phys. Rev. Lett.*, 96(04):5901, 2006.

[17] Y.-M. Lin and M. S. Dresselhaus. Thermoelectric properties of superlattice nanowires. *Phys. Rev. B*, 68(7):5304, 2003.

[18] M. Christensen, N. Lock, J. Overgaard, and B. B. Iversen. Crystal Structures of Thermoelectric n- and p-type $Ba_8Ga_{16}Ge_{30}$ Studied by Single Crystal, Multitemperature, Neutron Diffraction, Conventional X-ray Diffraction and Resonant Synchrotron X-ray Diffraction. *J. Am. Chem. Soc.*, 128(49):15657–15665, 2006.

[19] A. Leithe-Jasper and W. Schnelle. Gefüllte Skutterudite - Physik und Chemie von Eisen-Antimoniden der Alkali-, Erdalkali- und Seltenerd-Metalle. 2006. Tätigkeitsbericht MPI Dresden.

[20] G. S. Nolas, D. T. Morelli, and Terry M. Tritt. SKUTTERUDITES: A Phonon-Glass-Electron Crystal Approach to Advanced Thermoelectric Energy Conversion Applications. *Annual Review of Materials Science*, 29:89–116, 1999.

[21] G. A. Slack. *CRC Handbook of Thermoelectrics (ed. D. M. Rowe)*. CRC PRESS, 1995.

[22] V. Savchuk, A. Boulouz, S. Chakraborty, J. Schumann, and H. Vinzelberg. Transport and structural properties of binary skutterudite $CoSb_3$ thin films grown by dc magnetron sputtering technique. *J. Appl. Phys. D: Appl. Phys.*, 92(9):5319–5326, 2002.

[23] A. Suzuki. Pulsed Laser Deposition of Filled Skutterudite $LaFe_3CoSb_{12}$ Thin Films. *Jpn. J. Appl. Phys.*, 42(5A):2843–2849, 2003.

[24] A. Shakouri. Recent Developments in Semiconductor Thermoelectric Physics and Materials. *Annu. Rev. Mater. Res.*, 41:399–431, 2011.

[25] F. L. Curzon and B. Ahlborn. Efficiency of a Carnot engine at maximum power output. *Am. J. Phys.*, 43(22), 1975.

[26] D. M. Rowe and C. M. Bhandari. *Modern Thermoelectrics*. Hold Saunders Ltd, 1983.

[27] G. Rogl, D. Setman, E. Schafler, J. Horky, M. Kerber, M. Zehetbauer, M. Falmbigl, P. Rogl, E. Royanian, and E. Bauer. High-pressure torsion, a new processing route for thermoelectrics of high ZTs by means of severe plastic deformation. *Acta mater.*, 60(5):2146–2157, 2012.

[28] D. Narducci. Do we really need high thermoelectric figures of merit? A critical appraisal to the power conversion efficiency of thermoelectric materials. *Appl. Phys. Lett.*, 99(10):2104, 2011.

[29] G. J. Snyder and E. S. Toberer. Complex thermoelectric materials. *Nature Mat.*, 7:105–114, 2008.

[30] J.-F. Li, W.-S. Liu, L.-D. Zhao, and M. Zhou. High-performance nanostructured thermoelectric materials. *Asia mater.*, 2(4):152–158, 2010.

[31] D. I. Bilc, S. D. Mahanti, and M. G. Kanatzidis. Electronic transport properties of PbTe and $AgPb_mSbTe_{2+m}$ systems. *Phys. Rev. B*, 74(12):2232, 2006.

[32] T. M. Tritt. *Recent Trends in Thermoelectric Materials Research III*. Gulf Professional Publishing, 2001.

[33] H. Anno, T. Sakakibara, Y. Notohara, H. Tashiro, T. Koyanagi, H. Kaneko, and K. Matsubara. Preparation and thermoelectric properties of $CoSb_3$ thinfilms on GaAs(100) substrate. *IEEE, Proceedings ICT XVI International Conference on Thermoelectrics*, pages 338–342, 1997.

[34] T. E. Humphrey, M. F. O´Dwyer, and H. Linke. Power optimization in thermionic devices. *J. Phys. D: Appl. Phys.*, 38(12):2051–2054, 2005.

[35] K. Kopitzki. *Einführung in die Festkörperphysik*. B.G. Teubner, Stuttgart, 3rd edition, 1993.

[36] L. S. Stilbans. *Physic of Semiconductors*. Sovetskoe Radio, Moscow, 1967.

[37] N. W. Ashcroft and N. D. Mermin. *Festkörperphysik*. Oldenburg-Verlag, München, Wien, 2nd edition, 2005.

[38] D. Mandrus, A. Migliori, T. W. Darling, M. F. Hundley, E. J. Peterson, and J. D. Thompson. Electronic transport in lightly doped $CoSb_3$. *Phys. Rev. B*, 52(7):4926–4931, 1995.

[39] D. T. Morelli, T. Caillat, J.-P. Fleurial, A. Borshchevsky, J. Vandersande, B. Chen, and C. Uher. Low-temperature transport properties of p-type $CoSb_3$. *Phys. Rev. B*, 51(15):9622–9628, 1995.

[40] J. Leszczynski, V. Da Ros, B. Lenoir, A. Dauscher, C. Candolfi, P. Masschelein, J. Hejtmanek, J. Tobola, R. I. Smith, C. Stiewe, and E. Müller. Electronic band strcture, magnetic transport and thermodynamic properties of In-filled skutterudites $In_xCo_3Sb_{12}$. *J. Phys. D: Appl. Phys.*, 46(49):5106, 2013.

[41] A. F. Ioffe. *Physics of Semiconductors*. Soviet Academy of Science, Moscow, 1957.

[42] V. I. Fistul. *Heavily Doped Semiconductors*. Plenum Press, New York, 1969.

[43] H. Ibach and H. Lüth. *Festkörperphysik: Einführung in die Grundlagen*. Springer-Verlag, Berlin, Heidelberg, 7th edition, 2009.

[44] B. T. Rissom. *Elektrische Transporteigenschaften von epitaktischen und polykristallinen Chalkopyrit-Schichten*. Dissertation, FU Berlin, 2007.

[45] S. Schuler. *Transporteigenschaften und Defekte in polykristallinen $CuGaSe_2$-Schichten und Heterostrukturen*. Dissertation, FU Berlin, 2002.

[46] H. Ibach and H. Lüth. *Festkörperphysik: Einführung in die Grundlagen*. Springer-Verlag, Berlin, Heidelberg, 3rd edition, 1993.

[47] Y. Kajikawa. Conduction model covering non-degenerate through degenerate polycrystalline semiconductors with non-uniform grain-boundary potential heights based on an energy filtering model. *Journ. Appl. Phys.*, 112(12):3713, 2012.

[48] E. S. Toberer, L. L. Baranowski, and C. Dames. Advances in Thermal Conductivity. *Annu. Rev. Mater. Res.*, 42:179–209, 2012.

[49] P. G. Klemens. Thermal Resistance due to Point Defects at High Temperatures. *Phys. Rev.*, 119(2):507–509, 1960.

[50] E. S. Toberer, A. Zevalkink, and G. J. Snyder. Phonon engineering through crystal chemistry. *J. Mater. Chem.*, 21:15843–15852, 2011.

[51] D. Jänsch. *Thermoelektrik: Eine Chance für die Automobilindustrie.* Expert Verlag, Renningen, Germany, 2008.

[52] K. Salzgeber, P. Prenninger, A. Grytsiv, P.Rogl, and E. Bauer. Skutterudites: Thermoelectric Materials for Automotive Application? *Journ. Electron. Mat.*, 39(9):2074–2078, 2010.

[53] J.-P. Fleurial, K. Johnson, J. Mondt, J. Sakamotol, J. Snyder, C.-K. Huang, R. Blair, G. Stapfer, T. Caillat, W. Determan, P. Frye, B. Heshmatpour, M. Brooks, and K. Tuttle. Development of Segmented Thermoelectric Multicouple Converter Technology. *Proc. Aerospace Conference, IEEE*, 2006.

[54] J. P. Fleurial, T. Caillat, and A. Borshchevsky. Skutterudites: An Update. In *Proceedings of 16th International Conference of thermoelectrics, Dresden, Germany, 1997. IEEE Catalog No. 97th 8291, pp. 1-11.*

[55] T. Caillat, A. Borshchevsky, and J.-P. Fleurial. Properties of single crystalline semiconducting $CoSb_3$. *J. Appl. Phys.*, 80(8):4442–4449, 1996.

[56] C. Stiewe. *Nanostrukturierte $CoSb_3$-Skutterudite - Neue Materialien für die Thermogeneratorik.* Dissertation, Justus-Liebig-Universität Gießen, 2009.

[57] H. Anno, K. Hatada, H. Shimizu, K. Matsubara, Y. Notohara, T. Sakakibara, H. Tashiro, and K. Motoya. Structural and electronic transport properties of polycrystalline p-type $CoSb_3$. *J. of Appl. Phys.*, 83(10):5270–5276, 1998.

[58] B. Schüpp, I. Bächer, M. Hecker, N. Mattern, V. Savchuk, and J. Schumann. Crystallization behavior of $CoSb_3$ and $(Co,Fe)Sb_3$ thin films. *Thin solid films*, 434(1):75–81, 2003.

[59] G. Rogl and P. Rogl. Mechanical Properties of Skutterudites. *Sci. Adv. Mat.*, 3(4):517–538, 2011.

[60] J. O. Sofo and G. D. Mahan. Electronic structure of $CoSb_3$: A narrow-band-gap semiconductor. *Phys. Rev. B*, 58(23):15620–15623, 1998.

[61] L. Hammerschmidt, S. Schlecht, and B. Paulus. Electronic structure and the ground-state properties of cobalt antimonide skutterudites; Revisited with different theoretical methods. *Phys. Status Solidi A*, 210(1):131–139, 2013.

[62] B. C. Sales, D. Mandrus, B. C. Chakoumakos, V. Keppens, and J. R. Thompson. Filled skutterudite antimonides: Electron crystals and phonon glasses. *Phys. Rev. B*, 56(23):15081–15089, 1997.

[63] D. J. Singh and E. Pickett. Skutterudite antimonides: Quasilinear bands and unusual transport. *Phys. Rev. B*, 50(15):11235–11238, 1994.

[64] S. R. S. Kumar, D. Cha, and H. N. Alshareef. Lattice dynamics and substrate-dependent transport properties of (In, Yb)-doped $CoSb_3$ skutterudite thin films. *J. Appl. Phys.*, 110(8):3710, 2011.

[65] S. Katsuyama, Y. Shichijo, M. Ito, K. Majima, and H. Nagai. Thermoelectric properties of the skutterudites Co1-xFexSb3 system. *J. Appl. Phys.*, 84(12):6708–6712, 1998.

[66] G. Rogl, A. Grytsiv, E. Bauer, P. Rogl, and M. Zehetbauer. Structural and physical properties of n-type skutterudite $Ca_0.07Ba_0.23Co_3.95Ni_0.05Sb_{12}$. *Intermetallics*, 18(3):394–398, 2010.

[67] P. N. Alboni, X. Ji, J. He, N. Gothard, and Terry M. Tritt. Thermoelectric properties of $La_{0.9}CoFe_3Sb_{12}$-$CoSb_3$ skutterudite nanocomposites. *J. Appl. Phys.*, 103(11):3707, 2008.

[68] G. Rogl, A. Grytsiv, P. Rogl, E. Bauer, M. Kriegisch, S. Puchegger, and M. Zehetbauer. On The Skutterudite $Pt_4Sn_{4.4}Sb_{7.6}$. *Int. J. Modern. Phys. B*, 24(06-07):711–721, 2010.

[69] L. Xi, W. Zhang, L. Chen, and J. Yang. Filled Skutterudites: from Single to Multiple Filling. *Journ. of the Korean Ceramic Society*, 47(1):54–60, 2010.

[70] J.-L. Mi, M. Christensen, E. Nishibori, V. Kuznetsov, D. M. Rowe, and B. B. Iversen. Multitemperature synchrotron powder diffraction and thermoelectric properties of the skutterudite $La_{0.1}Co_4Sb_{12}$. *J. Appl. Phys.*, 107(11):3507, 2010.

[71] V. L. Kuznetsov, L. A. Kuznetsova, and D. M. Rowe. Effect of partial void filling on the transport properties of $Nd_xCo_4Sb_{12}$ skutterudites. *J. Phys.: Condens. Matter*, 15(29):5035, 2003.

[72] B. C. Sales, B. C. Chakoumakos, and D. Mandrus. Thermoelectric properties of thallium-filled skutterudites. *Phys. Rev. B*, 61(4):2475–2481, 2000.

[73] F. Timmermann. Untersuchung thermoelektrischer Transporteigenschaften von dünnen $Fe_xCo_{1-x}Sb_3$-Schichten. Master thesis, Technische Universität Chemnitz, Fakultät für Naturwissenschaften, OFGF, 2014.

[74] W.-S. Liu, B.-P. Zhang, J.-F-Li, and L.-D. Zhao. Effects of Sb compensation on microstructure, thermoelectric properties and point defect of $CoSb_3$ compound. *J. Phys. D: Appl. Phys.*, 40(21):6784–6790, 2007.

[75] D. Jung, M-H. Whangbo, and S. Alvarez. Electronic structure of $CoSb_3$: A narrow-band-gap semiconductor. *Inorg. Chem.*, 29(12):2252–2255, 1990.

[76] J. W. Sharp, E. C. Jones, R. K. Williams, P. M. Martin, and B. C. Sales. Thermoelectric properties of $CoSb_3$ and related alloys. *J. of Appl. Phys*, 78(2):1013–1018, 1995.

[77] Y. Wang, X. Xu, and J. Yang. Resonant Oscillation of Misch-Metal Atoms in Filled Skutterudites. *Phys. Rev. Lett.*, 102(17):5508, 2009.

[78] R. Hermann, F. Grandjean, and G. J. Long. Einstein oscillators that impede thermal transport. *Am. J. Phys.*, 73(2):110–118, 2004.

[79] V. Keppens, D. Mandrus, B. C. Sales, B. C. Chakoumakos, P. Dai, R. Coldea, M. B. Maple, D. A. Gajewski, E. J. Freemann, and S. Bennington. Localized vibrational modes in metallic solids. *Nature*, 395:876–878, 1998.

[80] M. M. Koza, M. R. Johnson, R. Viennois, H. Mutka, L. Girard, and D. Ravot. Breakdown of phonon glass paradigm in La- and Ce-filled $Fe_4Sb_{12}$. *Nat. Mat.*, 7:805–810, 2008.

[81] M. Christensen, A. B. Abrahamsen, N. B. Christensen, F. Juranyi, N. H. Andersen, K. Lefmann, J. Andreasson, C. R. H. Bahl, and B. B. Iversen. Avoided crossing of rattler modes in thermoelectric materials. *Nat. Mat.*, 7:811–815, 2008.

[82] J. Dong, O. F. Sankey, and C. W. Myles. Theoretical Study of the Lattice Thermal Conductivity in Ge Framework Semiconductors. *Phys. Rev. Lett.*, 86(11):2361–2364, 2000.

[83] A. Dauscher, M. Puyet, B. Lenoir, D. Colceag, and M. Dinescu. Microstructural investigation of $Ca_xCo_4Sb_{12}$ films prepared by pulsed laser deposition. *Appl. Phys. A*, 79(4-6):1465–1468, 2004.

[84] D. Colceag, A. Dauscher, B. Lenoir, V. Da Ros, R. Birjega, A. Moldovan, and M. Dinescu. Pulsed laser deposition of doped skutterudite thin films. *Science Direct*, 253:8097–8101.

[85] X. Shi, W. Zhang, L. D. Chen, J. Yang, and C. Uher. Theoretical study of the filling fraction limits for impurities in $CoSb_3$. *Phys. Rev. B*, 75(23):5208, 2007.

[86] X. Shi, H. Kong, C.-P. Li, C. Uher, J. Yang, J. R. Salvador, H. Wang, L. Chen, and W. Zhang. Low thermal conductivity and high thermoelectric figure of merit in n-type $Ba_xYb_yCo_4Sb_{12}$ double-filled skutterudites. *Appl. Phys. Lett.*, 92(18):2101, 2008.

[87] J. Y. Peng, P. N. Alboni, J. He, B. Zhang, Z. Su, T. Holgate, N. Gothard, and T. M. Tritt. Thermoelectric properties of (In,Yb) double-filled $CoSb_3$ skutterudite. *J. Appl. Phys.*, 104(05), 2008.

[88] D. Liang, H. Yang, S. W. Finefrock, and Y. Wu. Flexible Nanocrystal-Coate Glass Fibers for High-Performance Thermoelectric Energy Harvesting. *Nano Lett.*, 12(4):2140–2145, 2012.

[89] B. Yu, M. Zebarjadi, H. Wang, K. Lukas, H. Wang, D. Wang, C. Opeil, M. Dresselhaus, G. Chen, and Z. Ren. Enhancement of Thermoelectric Properties by Modulation-Doping in Silicon Germanium Alloy Nanocomposites. *Nano Lett.*, 12(4):2077–2082, 2012.

[90] C. Caylor, A. M. Stacy, B. Bloom, R. Gronsky, T. Sands, W.W. Fuller-Mora, A. Ehrlich, D. Song, and G. Chen. Growth and properties of multilayered skutterudite thin films. *IEEE, Proceedings from the 18th International Conference on Thermoelectrics*, pages 656–661, 1999.

[91] H. Anno, K. Matsubara, Y. Notohara, T. Sakakibara, K. Kishimoto, and T. Koyanagi. Thermoelectric properties of rf-sputtered $CoSb_3$ films. *IEEE, Proceedings from the 15th International Conference on Thermoelectrics*, pages 435–439, 1996.

[92] S. R. S. Kumar, A. Alyamani, J. W. Graff, T. M. Tritt, and H. N. Alshareef. Pulsed laser deposition and thermoelectric properties of In- and Yb-doped $CoSb_3$ skutterudite thin films. *J. Mater. Res.*, 26(15):1836–1841, 2011.

[93] V. Savchuk, J. Schumann, B. Schüpp, G. Behr, N. Mattern, and D. Souptel. Formation and thermal stability of the skutterudite phase in films sputtered from $Co_{20}Sb_{80}$ targets. *Journal of Alloys and Compounds*, 351(1-2):248–254, 2003.

[94] J. C. Caylor, A. M. Stacy, R. Gronsky, and T. Sands. Pulsed laser deposition of skutterudite thin films. *J. Appl. Phys.*, 89(6):3508–3513, 2001.

[95] A. L. E. Smalley, S. Kim, and D. C. Johnson. Effects of Composition and Annealing on the Electrical Properties of $CoSb_3$. *Chem. Mater.*, 15(20):3847–3851, 2003.

[96] H. Sellinschegg, S. L. Stuckmeyer, M. Hornbostel, and D. C. Johnson. Synthesis of Metastable Post-Transition-Metal Iron Antimony Skutterudites Using the Multilayer Precursor Method. *Chem. Mater.*, 10(4):1096–1101, 1998.

[97] J. R. Williams, M. Johnson, and D. C. Johnson. Composition Dependence of the Nucleation Energy of Iron Antimonides from Modulated Elemental Reactants. *J. Am. Chem. Soc*, 123(8):1645–1649, 2001.

[98] A. Möchel, I. Sergueev, N. Nguyen, Gary J. Long, F. Grandjean, D. C. Johnson, and R. P. Hermann. Lattice dynamics in the $FeSb_3$ skutterudite. *Phys. Rev. B.*, 84(6):4302, 2011.

[99] F. Völklein and H. Balles. A Microstructure For Measurement Of Thermal Conductivity Of Polysilicon Thin Films. *J. Microelectromechanical Systems*, 1(4):193–196, 1992.

[100] F. Völklein. Thermal conductivity of thin films-experimental methods and theoretical interpretation. *Proceedings ICT '97. 16th International Conference on Thermoelectrics, Dresden, 1997.*, pages 711–718.

[101] F. Völklein and E. Kessler. Thermal Conductivity and Thermoelectric Figure of Merit of Thin Antimony Films. *Phys. Stat. Sol. B*, 158(2):521–529, 1990.

[102] T. B. Massalski, H. Okamoto, and P. R. Subramanian. *Binary Alloy Phase Diagrams*. ASM Intl., 2nd edition, 1990.

[103] M. D. Hornbostel, E. J. Hyer, J. Thiel, and D. C. Johnson. Rational Synthesis of Metastable Skutterudite Compounds Using Multilayer Precursors. *J. Am. Chem. Soc*, 119(11):2665–2669, 1997.

[104] G. Schatz and A.Weidinger. *Nukleare Festkörperphysik*. B. G. Teubner, Stuttgart, 1992.

[105] M. Daniel. Herstellung und Charakterisierung thermoelektrischer $CoSb_3$-Schichten. Diploma thesis, Technische Universität Chemnitz, Fakultät für Naturwissenschaften, OFGF, 2009.

[106] Program code by M. Mayer, Max Planck Institute für Plasmaphysik (IPP), Garching.

[107] M. Mayer. SIMNRA, a Simulation Program for the Analysis of NRA, RBS and ERDA. *Proceedings of the 15th International Conference on the Application of Accelerators in Research and Industry, American Institute of Physics Conference Proceedings 475*, page 541, 1999.

[108] L. Spieß, R. Schwarzer, H. Behnken, and G. Teichert. *Moderne Röntgenbeugung*. Vieweg und Teubner Verlag, Deutschland, 2005.

[109] K.-H. Jost. *Röntgenbeugung an Kristallen*. Akademie-Verlag, Berlin, 1975.

[110] W. A. Rachinger. A Correction for the $\alpha_1$ $\alpha_2$ Doublet in the Measurement of Widths of X-ray Diffraction Lines . *J. Sci. Instrum.*, 25(7):254–255, 1948.

[111] JCPDS-International Center of Diffraction Data. 1999.

[112] H. Krischner and B. Koppelhuber-Bitschnau. *Röntgenstrukturanalyse und Rietveldmethode*. Vieweg Verlag, Braunschweig/Wiesbaden, 5th edition, 1994.

[113] R. A. Young. *The Rietveld Method*. Oxford University Press Inc., New York, 1995.

[114] J.J. Rodriguez-Carvajal. FULLPROF, A program for Rietveld refinement and pattern matching analysis. *Abstract of the Satellite Meeting on Powder Diffraction of the XV Congress, Int. Union of Crystallography, Talence,France*, page 127, 1990.

[115] FULLPROF, http://www.ill.eu/sites/fullprof/index.htmlo (03.07.2014, 03:05 Uhr).

[116] S. N. Magonov and M.-H. Whangbo. *Surface Analysis with STM and AFM*. VCH, Weinheim, New York, Basel, Cambridge, Tokyo, 1996.

[117] R. Wiesendanger. *Scanning Probe Microscopy and Spectroscopy*. Cambridge Univ. Press, Cambridge, 1994.

[118] Free and Open Source software, www.gwyddion.net (15.06.2014, 20.35).

[119] A. Frick and C. Stern. *DSC Prüfung in der Anwendung*. Carl Hanser Verlag, München Wien, 2006.

[120] W. Hemminger and G. Höhne. *Grundlagen der Kalorimetrie*. Akademie-Verlag, Berlin, 1980.

[121] G. Höhne, W. Hemminger, and H.-J. Flammersheim. *Differential Scanning Calorimetry-An introduction for Practioners*. Springer Verlag, Berlin, 1996.

[122] Netzsch Hompage, Funktionsprinzip einer Wärmestrom-DSC, www.netzsch-thermal-analysis.com/de/landing-pages/funktionsprinzip-einer-waermestrom-dsc.html (04.07.2014, 13.35).

[123] Specs Surface Nano Analysis GmbH, INA-X system and descriptions, http://www.specs.de/cms/front_content.php?idcat=131 (04.07.2014, 14:19 Uhr).

[124] D. Lipinsky. *Sekundärionen und Neutralteilchenmassenspektrometrie an oxidischen Dünnschichtsystemen*. Deutscher Universitäts Verlag, Wiesbaden, 1995.

[125] A. Lakatos, G. A. Langer, A. Csik, C. Cserhati, M. Kis-Varga, L. Daroczi, G. L. Katona, Z. Erdelyi, G. Erdelyi, K. Vad, , and D. L. Beke. Nanoscale investigations of shift of individual interfaces in temperature induced processes of Ni-Si system by secondary neutral mass spectrometry. *Appl. Phys. Lett.*, 97(23):3103, 2010.

[126] W. Schäfer and G. Terlecki. *Halbleiterprüfung: Licht und Rasterelektronenmikroskopie.* Hüthig Verlag, Heidelberg, 1986.

[127] K. Wetzig and D. Schulze. *In situ Scanning Electron Microscopy in Material Research.* Akademie Verlag, Berlin, 1995.

[128] K. G. Lickfeld. *Elektronenmikroskopie.* Eugen Ulmer Verlag, Stuttgart, 1979.

[129] M. v. Heimendahl. *Einführung in die Elektronenmikroskopie: Verfahren zur Untersuchung von Werkstoffen und anderen Festkörpern.* Viehweg, Braunschweig, 1970.

[130] F. J. Humphreys. Grain and subgrain characterisation by electron backscatter diffraction. *Journ. of Mat. Sci.*, 36(16):3833–3854, 2001.

[131] Oxford Instruments,http://www.oxford-instruments.com/products/microanalysis /ebsd/ebsd-post-processing-software (27.06.2014, 12:19 Uhr).

[132] F. Timmermann. Implementierung einer PID-Temperatursteuerung mitels LabView. Spezialisierungspraktikum, Technische Universität Chemnitz, Fakultät für Naturwissenschaften, OFGF, 2013.

[133] E. Compans. Dynamic method for in situ measurements of the thermoelectric power of vapor quenched thin films. *Rev. Sci. Instrum.*, 60(8):2715, 1989.

[134] J. Martin, T. Tritt, and C. Uher. High temperature Seebeck coefficient metrology. *J. Appl. Phys.*, 108(12):1101, 2010.

[135] T. Markstein. Weiterentwicklung des Tieftemperatur-Seebeck-Messstandes und erste Testmessungen. Diploma thesis, Technische Universität Chemnitz, Fakultät für Naturwissenschaften, OFGF, 2012.

[136] J. Franke. Charakterisierung von $CoSb_3$ Schichten bei hohen Temperaturen. Master thesis, Technische Universität Chemnitz, Fakultät für Naturwissenschaften, OFGF, 2013.

[137] D. Reinhardt. Bestimmung des Seebeck-Koeffizienten von $CoSb_3$-Schichten auf unterschiedlichen Substraten. Master thesis, Technische Universität Chemnitz, Fakultät für Naturwissenschaften, OFGF, 2014.

[138] C. Schmidt. Herstellung und Charakterisierung von $FeSb_3$-Dünnschichten. Bachelor thesis, Technische Universität Chemnitz, Fakultät für Naturwissenschaften, OFGF, 2013.

[139] efunda Inc., http://www.efunda.com/designstandards/sensors/thermocouples/ thmcple_theory.cfm?Orderby=Seebeck0C#sensitivity (23.06.2014, 08:05 Uhr).

[140] R. B. Roberts. The absolute scale of thermoelectricity. *Philos. Mag.*, 36(1):91–107, 1977.

[141] D. Issenmann, N. Wehmeier, S. Eon, H. Bracht, G. Buth, S. Ibrahimkutty, and A. Plech. Determination of nanoscale heat conductivity by time-resolve X-ray scattering. *Thin Solid Films*, 541(0):28–31, 2013.

[142] R. Gebs, G. Klatt, C. Janke, T. Dekorsy, and A. Bartels. High-speed asynchronous optical sampling with sub-50fs time resolution. *Optics Express*, 18(6):5974–5983, 2010.

[143] A. Bartels, R. Cerna, C. Kistner, A. Thoma, F. Hudert, C. Janke, and T. Dekorsy. Ultrafast time-domain spectroscopy based on high-speed asynchronous optical sampling. *Rev. Sci. Intrsum.*, 78(3):5107, 2007.

[144] J. R. Ferraro, K. Nakamoto, and C. W. Brown. *Introductory Raman Spectroscopy*. Academic Press, Amsterdam, Boston, 2nd edition, 2003.

[145] H. Sellinschegg, J. R. Williams, G. Yoon, and D. C. Johnson. The Synthesis of Metastable Skutterudites and Crystalline Superlattices. *Mat. Res. Soc. Symp.*, 626, 2000.

[146] H. Hortenbach. *Surfactant-gesteuertes Wachstum von Siliciden*. Dissertation, Technische Universität Chemnitz, 2003.

[147] M. Friedemann. Untersuchung zur Stabilität von $CoSb_3$-Schichten in Abhängigkeit verschiedener Temperzeiten und -temperaturen. Spezialisierungspraktikum, Technische Universität Chemnitz, Fakultät für Naturwissenschaften, OFGF, 2013.

[148] H.-A. Durand, K. Nishimoto, K. Ito, and I. Kataoka. Hyperthermal beams for the fabrication of thermoelectric thin films. *Applied Surface Science*, 154-155:387–392, 2000.

[149] N. Jöhrmann. Strukturuntersuchung dünner Eisen-Platin- und Cobalt-Antimon-Schichten mit elektronenmikroskopischen Methoden. Diploma thesis, Technische Universität Chemnitz, Fakultät für Naturwissenschaften, Analytik an Festkörperoberflächen, 2012.

[150] M. Henzler and W. Göpel. *Oberflächenphysik des Festkörpers*. Teubner-Verlag, Stuttgart, 1994.

[151] K. Dransfeld and P. Kienle. *Elektrodynamik und spezielle Relativitätstheorie*. Oldenbourg-Verlag, 2nd edition, 2002.

[152] M. Daniel, M. Friedemann, N. Jöhrmann, A. Liebig, J. Donges, M. Hietschold, G. Beddies, and M. Albrecht. Influence of the substrate thermal expansion coefficient on the morphology and elastic stress of $CoSb_3$ thin films. *Phys. Status Solidi A*, 210(1):140–146, 2013.

[153] Ohara GmbH, http://www.ohara-gmbh.com/bn (10.08.2011, 11:05 Uhr).

[154] J. Zhang, W. Cui, M. Juda, D. McCammon, R. L. Kelley, S. H. Moseley, C. K. Stahle, and A. E. Szymkowiak. Hopping conduction in partially compensated doped silicon. *Phys. Rev. B*, 48(4):2312–2319, 1993.

[155] A. F. Qasrawi. Cd-Doping Effects on the Properties of Polycrystalline $\alpha$-$In_2Se_3$ Thin Films. *Cryst. Res. Techol.*, 37(4):378–390, 2002.

[156] E. Arushanov, K. Fess, W. Kaefer, C. Kloc, and E. Bucher. Transport properties of lightly doped $CoSb_3$ single crystals. *Phys. Rev. B*, 56(4):1911–1917, 1997.

[157] $FeSb_3$ band structure calculations, not published results, Hammerschmidt, Freie Universität Berlin.

[158] E. D. Case. Thermal Fatigue and Waste Heat Recovery via Thermoelectrics. *J. Electron. Mater.*, 41(6):1811–1819, 2012.

[159] J. A. Thornton and D. W. Hoffman. Stress-Related Effects in Thin Films. *Thin Solid Films*, 171(1):5–31, 1989.

[160] J. Kawashima, Y. Yamada, and I. Hirabayashi. Critical thickness and effective thermal expansion coefficient of YBCO crystalline film. *Physica C*, 306(1):114–118, 1998.

[161] D. C. Yoo, J. Y. Lee, I. S. Kim, and Y. T. Kim. Effects of post-annealing on the microstructure and ferroelectric properties of $YMnO_3$ thin films on Si. *J. Cryst. Growth*, 233(1-2):243–247, 2001.

[162] R. G. Elliman, T. D. M. Weijers-Dall, M. G. Spooner, T. Kim, and A. R. Wilkinson. Stress and stress relief in dielectric thin films-the role of hydrogen. *Nucl. Intrum. Methods Phys. Res. B*, 249(1-2):310–313, 2006.

[163] A. A. Volinsky, N. R. Moody, and D. C. Meyer. Stress-Induced Periodic Fracture Patterns In Thin Films. In *Proceeding, 11th International Congress on Fracture, Turin, Italy, 2005*.

[164] K. M. Crosby and R. M. Bradley. Simulations of tensile fracture in thin films bonded to solid substrates. *Philos. Mag. B*, 76(1):91–105, 1997.

[165] G. Rogl, L. Zhang, P. Rogl, A. Grytsiv, M. Falmbigl, D. Rajs, M. Kriegisch, H. Müller, E. Bauer, J. Koppensteiner, W. Schranz, M. Zehetbauer, Z. Henkie, and M. B. Maple. Thermal expansion of skutterudites. *J. Appl. Phys.*, 107(4):3507, 2010.

[166] V. Hauk. *Structural and Residual Stress Analysis by Nondestructive Methods*. Elsevier, Amsterdam, 1997.

[167] X. Yang, P. Zhai, L. Liu, and Q. Zhang. Thermodynamic and mechanical properties of crystalline $CoSb_3$: A molecular dynamics simulation study. *J. Appl. Phys.*, 109(12):3517, 2011.

[168] CrysTec GmbH, http://www.crystec.de/daten/ysz.pdf (02.04.2014, 20:00 Uhr).

[169] C. Xie. Interactive Heat Transfer Simulations for Everyone. *The Physics Teacher*, 50(4):237–240, 2012.

[170] J. Franke. Aufbau und Erprobung eines Messsystems zur Messung elektrischer Transportkoeffizienten bei hohen Temperature. Bachelor thesis, Technische Universität Chemnitz, Fakultät für Naturwissenschaften, OFGF, 2011.

[171] A. Dalla. Fe-Substitution in dünnen $CoSb_3$ Sichten. Master thesis, Technische Universität Chemnitz, Fakultät für Naturwissenschaften, OFGF, 2013.

[172] W. Nolting. *Grundkurs Theoretische Physik 4: Spezielle Relativitätstheorie, Thermodynamik*. Springer, Heidelberg, 8th edition, 2012.

[173] L. Vegard. Die Konstitution der Mischkristalle und die Raumfüllung der Atome. *Zeitschrift für Physik*, 5(1):17–26, 1921.

[174] J. Yang, G. P. Meisner, D. T. Morelli, and C. Uher. Iron valence in skutterudites: Transport and magnetic properties of $Co_{1-x}Fe_xSb_3$. *Phys. Rev. B*, 63(1):4410, 2000.

[175] P. Amornpitosuk, D. Ravot, F. Gascoin, and J. C. Tedenac. Chemistry of Materials a Tool for Skutterudite Based Materials Tailoring. Application to Cobalt Based System. In *Proceeding, ECT 2007, Odessa, Ukrain, 2007*.

[176] J. Peng, J. Yang, X. Song, Y. Chen, and T. Zhang. Effect of Fe substitution on the thermoelectric transport properties of $CoSb_3$-based Skutterudite compound. *Journal of Alloys and Compounds*, 426(1-2):7–11, 2006.

[177] G. S. Nolas, C. A. Kendziora, and H. Takizawa. Polarized Raman-scattering study of Ge- and Sn-filled $CoSb_3$. *J. of Appl. Phys.*, 94(12):7440–7444, 2003.

[178] J. L. Feldman and D. J. Singh. Lattice dynamics of skutterudites: First-principles and model claculations for $CoSb_3$. *Phys Rev. B*, 53(10):6273–6282, 1996.

[179] G. S. Nolas, G. A. Slack, T. Caillat, and G. P. Meisner. Raman scattering study of antimony-based skutterudites. *J. of Appl. Phys.*, 79(5):2622–2626, 1996.

[180] B. Duan, P. Zhai, L. Liu, and Q. Zhang. Thermoelectric properties of Trisubstituted Skutterudite $Co_4Sb_{11}Ge_{1-x-y}Te_xSe_y$ Compounds. *J. Electron. Mater.*, 41(6):1120–1124, 2012.

[181] F. Laufek, J. Navratil, J. Plasil, T. Plechacek, and C. Drasar. Synthesis, crystal structure and transport properties of skutterudite-related $CoSn_{1.5}Se_{1.5}$. *Journal of Alloys and Compounds*, 479(1-2):102–106, 2009.

[182] G. S. Nolas, J. Yang, and R. W. Ertenberg. Transport properties of $CoGe_{1.5}Se_{1.5}$. *Phys. Rev. B*, 68(19):3206, 2003.

[183] X. Shi, W. Zhang, L. D. Chen, and J. Yang. Filling Fraction Limit for Intrinsic Voids in Crystals: Doping in Skutterudites. *Phys. Rev. Lett.*, 95(18):5503, 2005.

[184] C. He, M. Daniel, M. Grossmann, O. Ristow, D. Brick, M. Schubert, M. Albrecht, and T. Dekorsy. Investigation of coherent acoustic phonon dynamics in thin films of $CoSb_3$ and partially filled $Yb_xCo_4Sb_{12}$ skutterudites. *Phys. Rev. B*, 89(17):4303, 2014.

[185] D. Decker, E. Loos, C. Drobniewski, A. Mogilatenko, J. Schumann, G. Beddies, and H.-J. Hinneberg. Structure and properties of $CrSi_2$/Si multilayers. *Microelectronic Engineering*, 76(1-4):331–335, 2004.

[186] C. Drobniewski. Elektrische Messungen an Silicium/Silicid Strukturen. Diploma thesis, Technische Universität Chemnitz, Fakultät für Naturwissenschaften, 2004.

# Acknowledgment

After achieving the diploma in physics I thought, the dissertation is only an extended version of the already mastered task. No additional obligatory lectures, project duration three/four years instead of one and free play to all ideas, since much more time is available. This was only half the truth.

The research directions within the field of skutterudites/thermoelectrics could be chosen by myself based on the new specific knowledge earned from reading more and more papers. And the field is widely spread. New ideas have to be created, new methods have to be tried, experiments planned in systematic way over a long time without loosing the overview of the whole story. Small problems have increased to large chaos over the PhD time, which were hidden during one year diploma time. With the arrangement of my desk and of the stored measurement data I want to mention only the smaller ones. With each year the responsibilities have increased. Besides performing some teaching, projects for Diploma, Master, and Bachelor theses had to be offered and supervised. Suddenly I was responsible for younger students and should help them achieving their diploma, what was one or two years before a milestone in my life. Furthermore a lot of posters, presentations, meetings, reports and talks had to be prepared and finally a talk was given on the European Thermoelectric Conference with lot of experts in the audience. There have been many days or nights in the lab with the feeling nothing will ever work. It is surprising how long this thesis finally got, by spending all that frustrating and in that moment "wasted" hours. However, these hours are necessary to see the whole story behind something. In parallel the private life offered also a lot of challenges. With the work as scientific worker at the university, the first own flat, the first tax declaration, washing clothes permanently by myself, make decisions for insurances and a lot of further tasks arose. The feeling of being now "alone" at home was compensated by frequently visits of my friends especially in the first year of the thesis. The new position gave the financial space for traveling around a bit. Furthermore I got to know a beautiful young lady called Aileen, who has turned my daily routine upside down. The death of my grandparents is also to mention here making especially the last year of working exhausting and much harder.

After this short journey into the past and with the completed thesis in my hands, I can say: me and my live has changed completely during the PhD-time. This time was full of new experiences and delivered a lot of challenges to grow on.

A big contribution to many of these things has Prof. Manfred Albrecht, who gave me the possibility to be a member of his PhD team. Thanks for his support and to give me plenty of rope for pushing the section thermoelectrics with my ideas. Also the possibility to visit conferences and project partners in different parts of the world, was a great support and a big motivation, especially the change of scene by working two month in Eugene was really helpful for refreshing batteries.

I have to thank all the group members. I think it´s on of the most important things to go willingly to the working place and there was no other chance by being member of this group. In this atmosphere it was possible to handle all the challenges and tasks discussed above and nearly everybody was helping if not. Special thanks here to Gunter Beddies, my mentor in thermoelectrics and an example for enthusiasm and scientific curiosity till the last working day.

The ambitious way of working by "my" students is strongly connected with this thesis. Therefore I want to thank Martin Friedemann, Tommy Markstein, Marc Lindorf, Ayham Dalla, Jonny Franke, Felix Timmermann, David Reinhardt, Constance Schmidt, Frank Arnold and Sergey Bogdanov for getting punished and mortified by me without any complains. I wish everybody a successful future.

Thank you Dave (Prof. D. Johnson) and your family for the invitation to this awesome two month in Eugene and the treatment as a family member.

Further acknowledgments to all project partners, coworkers who performed measurements for me, and also to all people who contribute to this work by discussions, proofreading or support in any other way. Thanks to Andreas Liebig, Patrick Matthes, Carsten Schulze, Birgit Hebler, Ute Vales, Beate Mainz, Senoy Thomas, Christian Schubert, Dennis Nissen, Elke Weiße, Richard Willhelm, Rene Heller, Mirreille Maret, Jörn Donges, G. Rogl, Prof. P. Rogl, Devin Merrill, Matthi Alemayehu, Dan Moore, Prof. Beke, Gabor Langer, G. Katona, Z. Aabdin, Nicola Peranio, Prof. Eibl, Nathanael Jöhrmann, Anton Plech, the beamline scientists at ESRF, Chuan He, T. Dekorsy, Ovidio Gordan, Ghazal Tofighi, Prof. Zahn.

I also want to acknowledge the German Research Foundation (DFG) for funding within the priority program SPP 1386 "Nanostructured thermoelectrics".

The final thanks is regarded to all the people who have nothing to do with this thesis, but who make my live each day a little bit more exciting. Hugs for my Dad and my Mom, for my girlfriend Aileen, and for all my friends.

# *Curriculum vitae*

## Personal data:

Name:                                   Marcus Daniel
Professional Title / Position:          Dipl. Phys. / Scientific coworker

Date of birth:                          24.12.1984
Place of birth:                         Karl-Marx-Stadt, Germany
Nationality:                            German
Marital status:                         single

## Work experience and internships:

| | |
|---|---|
| since 11/2009 | **Scientific coworker and Ph.D. student in research group of Prof. Albrecht at faculty of physics, TU Chemnitz** |

tasks:
a) Deposition and characterisation of thermoelectric $CoSb_3$ thin films
b) Construction and setup of thermoelectric measurement system
c) Supervisor of 13 diploma, bachelor and master students
d) Teaching and lab courses

9/2012-11/2012:    Co-worker in research group of Prof. D. Johnson at department of chemistry, University of Eugene, Oregon, USA

## Internships:

12/2008 – 03/2009:    **Student assistant in research group of Prof. Dr. M. Albrecht at faculty of physics, TU Chemnitz**
Tasks:
a) Tutor: general physics
b) XRD- and magnetic measurements in Grenoble and Krakow

12/2007 – 03/2008:    **Part-time job at 3D Micromac AG Chemnitz**
Tasks:    Development of ultra-short pulsed laser-systems for material processing

10/2006 – 01/2007:    **Internship at 3D Micromac AG Chemnitz**
Tasks:
a) Development of ultra-short pulsed laser-systems for material processing
b) integration und adjustment of new components in laser setups
c) Glass-labeling against product piracy

08/2006 – 09/2006:    **Internship in Moscow at the Institute of biochemical physics of the Russian Academy of Science**
Tasks:    Simulations of bounding energies in carbon nanotubes

**Study:**

| | |
|---|---|
| 10/2003 – 09/2009: | **Physics (diploma), TU Chemnitz** |
| | Specialization:      Nanophysics, semiconductor devices and circuits, internet programming |
| | Diploma thesis topic:      Deposition and characterization of thermoelectric $CoSb_3$ thin films |
| 01/2007 – 06/2007: | **Exchange semester at KTH Stockholm** |
| | Specialization:      spintronic, internet programming |

**Education:**

| | |
|---|---|
| 1995 – 2003: | Alexander von Humboldt Gymnasium in Chemnitz |
| | Graduation:      A-level |
| | Grade:      1.4 |
| 1991 – 1995: | Primary school in Chemnitz |

## *List of publications*

**2014:**

C. He, <u>M. Daniel</u>, M. Grossmann, O. Ristow, D. Brick, M. Schubert, M. Albrecht, and T. Dekorsy, *Investigation of coherent acoustic phonon dynamics in thin films of $CoSb_3$ and partially filled $Yb_xCo_4Sb_{12}$ skutterudites*, Phys. Rev. B: 89 (17), 2014

**2013:**

<u>M. Daniel</u>, M. Friedemann, N. Jöhrmann, A. Liebig, J. Donges, M. Hietschold, G. Beddies, and M. Albrecht, *Influence of the substrate thermal expansion coefficient on the morphology and elastic stress of $CoSb_3$ thin films*, Phys. Status Solidi A: 210 (1), 2013

C. Schubert, B. Hebler, H. Schletter, A. Liebig, <u>M. Daniel</u>, R. Abrudan, F. Radu, and M. Albrecht, *Interfacial exchange coupling in Fe-Tb/[Co/Pt] heterostructures*, Phys. Rev. B: 87 (5), 2013

**2012:**

C. Brombacher, C. Schubert, <u>M. Daniel</u>, A. Liebig, G. Beddies, T. Schumann, W. Skorupa, J. Donges, S. Häberlein, and M. Albrecht, *Chemical ordering of FePt films using millisecond flash-lamp annealing*, J. Appl. Phys.: 111 (2), 2012

C. Brombacher, H. Schletter, <u>M. Daniel</u>, P. Matthes, N. Jöhrmann, M. Maret, D. Makarov, M. Hietschold, and M. Albrecht, *FePtCu alloy thin films: Morphology, $L1_0$ chemical ordering, and perpendicular magnetic anisotropy*, J. Appl. Phys.: 112 (7), 2012

R. Brandt, F. Ganss, T. Senn, <u>M. Daniel</u>, M. Albrecht, and H. Schmidt, *Frequency tuning the ultrafast magnetization dynamics of FexPt100-x alloys*, J. Appl. Phys.: 111 (5), 2012

S. Thomas, G. Pookat, S. S. Nair, <u>M. Daniel</u>, B. Dymerska, A. Liebig, S. H. Al-Harthi, R. V. Ramanujan, M. R. Anantharaman, J. Fiedler, and M. Albrecht, *Exchange bias effect in partially oxidized amorphous Fe-Ni-B based metallic glass nanostructures*, J. Phys.: Cond. Matter: 24 (256004), 2012

**2011:**

T. Kosub, C. Schubert, H. Schletter, <u>M. Daniel</u>, M. Hietschold, V. Neu, M. Maret, D. Makarov, and M. Albrecht, *Coercivity enhancement in exchange biased $CoO/Co_3Pt$ bilayers*, J. Phys. D: 44 (015002), 2011

# Selbstständigkeitserklärung

Hiermit erkläre ich, dass ich die vorliegende Arbeit selbstständig angefertigt, nicht anderweitig zu Prüfungszwecken vorgelegt und keine anderen als die angegebenen Hilfsmittel verwendet habe. Sämtliche wissentlich verwendete Textausschnitte, Zitate oder Inhalte anderer Verfasser wurden ausdrücklich als solche gekennzeichnet.

Chemnitz, den April 13, 2015

_____

Marcus Daniel